OPTICAL PHASE SPACE DISTRIBUTIONS FOR COHERENCE TOMOGRAPHY

by

Adam P. Wax

Department of Physics
Duke University

Date: ____________________
Approved:

____
Dr. John E. Thomas, Supervisor

____
Dr. Robert Behringer

____
Dr. Daniel Gauthier

____
Dr. Bob Guenther

____
Dr. Berndt Mueller

Dissertation submitted in partial fulfillment of the
requirements for the degree of Doctor of Philosophy
in the Department of Physics
in the Graduate School of
Duke University

1999

ABSTRACT

(Physics)

OPTICAL PHASE SPACE DISTRIBUTIONS FOR COHERENCE TOMOGRAPHY

by

Adam P. Wax

Department of Physics
Duke University

Date: ______________________________
Approved:

____
Dr. John E. Thomas, Supervisor

____
Dr. Robert Behringer

____
Dr. Daniel Gauthier

____
Dr. Bob Guenther

____
Dr. Berndt Mueller

An abstract of a dissertation submitted in partial
fulfillment of the requirements for the degree
of Doctor of Philosophy in the Department of
Physics in the Graduate School of
Duke University

1999

Abstract

This thesis introduces optical phase space distributions, i.e., the joint position and momentum distribution of a light field. These distributions provide a new conceptual framework for the study of light propagation in multiple scattering media. Since light is predominantly scattered rather than absorbed in many biological tissues, interest in light scattering studies has recently been revived for application to biomedical optical imaging. Thus, improving the understanding of light transport in a multiple scattering medium will impact current biomedical imaging techniques such as coherence tomography.

In this thesis, a method for directly measuring optical phase space distributions using a novel heterodyne imaging scheme is developed. The heterodyne method can be implemented with either coherent or low-coherence-length light. It is shown that the detected voltage is given as the convolution of the Wigner distribution of the light field of interest with that of a reference field when measuring the mean square heterodyne beat signal. It is further shown using Fourier optics theoretical methods that the center position and momentum of the reference field in the heterodyne scheme can be scanned by translating optical elements. Thus, the optical phase space distribution is mapped out in position and momentum as a smoothed Wigner distribution with resolution determined by the spatial width and diffraction angle of the reference field. In addition, implementation of the heterodyne scheme using low coherence length light permits selection of the path length of detected photons, effectively giving timing resolution.

Wigner distributions are shown to obey rigorous transport equations which are derived from the underlying wave equations. Thus, measurement methods based on Wigner distributions can be placed on a firm theoretical footing. The properties of

Wigner distributions are illustrated using measured optical phase space distributions for Gaussian beams from a coherent source as an example. Since Wigner distributions are sensitive to the coherence properties of the light field, optical phase space distributions can be used to characterize the light from a variety of sources. A method of coherence characterization is developed that recovers the parameters of the Gaussian Schell-model, a mathematical description of partially coherent light. This method is applied to characterize the light sources used in the scattering studies presented in this thesis.

Light scattering is investigated in three experiments. These studies employ the heterodyne scheme to measure the optical phase space distribution of light emerging from turbid media. Coherent light from a helium neon laser is used to explore the field transmitted through a turbid medium consisting of 5.7 μm polysyrene spheres in a water-glycerol mixture. The momentum distribution of the transmitted field contains three components: a sharp ballistic peak, a narrow diffractive pedestal and a broad background. The narrow diffractive pedestal is seen to attenuate more slowly than the ballistic light as the concentration of scatterers is increased. The data are in excellent agreement with a theoretical model that explains the behavior of the pedestal by including multiple diffractive scattering and treating large angle scattering as a loss.

Light from broadband superluminescent diodes is used to explore the propagation of low coherence length light in multiple scattering media. Optical phase space distributions are presented for the light transmitted through varying concentrations of polystyrene spheres for different photon path lengths within the medium. It is shown that narrow momentum distributions are obtained for path lengths slightly longer than those of ballistic light. It is believed that this light can be used for biomedical optical imaging. The final study presented in this thesis examines low coherence length light which has been backscattered by a turbid medium. Optical phase space distributions are presented for various photon path lengths within the medium. The data are shown to agree with a theoretical model which is cast in the form of a Wigner distribution for comparison to experiment.

Acknowledgments

First, I would like to thank John Thomas for teaching me how to be a good scientist. He has been a great advisor and friend. We both entered this field at the same time and have learned about it together. John has taught me many laboratory skills over the years but I feel the most important thing I have learned from him is the intangible drive to demand the best from my work - to make sure things are done right. If not for his encouragement, enthusiasm and insight, this thesis project would never have progressed past my first year student fumblings into a full blown research program.

I would also like to thank my high school physics teacher, Lewis Love for introducing me to physics. His enthusiasm opened an exciting new world for me.

Next, I would like to thank the friends I have made here at Duke. First year was tough but thanks to Chris Baird, Bill Brown and Mark Steen, we all got through it and had a few laughs along the way. I will always remember late night studying with Captain Twelvepack and our field trips, including a midnight run to Atlanta and a visit to the fountain at UNC. In more recent years, Martin Hall joined our group and provided both pointed and pointless debate on virtually any subject.

I also would like to acknowledge the other members of the research group. When I first arrived, the senior students, Carl, Alan, Mikey and Zhao were kind enough to give me the guidance I needed to navigate my way through graduate research. As I became a senior student myself, I had the pleasure of sharing the office with Tom, Ken, Lu, Mike and Stephen who all helped me kill the occasional idle moment with fine water cooler talk. More recently, I've shared an office with Samir who has graciously tolerated me as I wrote this thesis. Lastly, as I turn the lab over to the newest students, Frank and Lee, I wish them luck in accomplishing all that lies ahead of them.

Of course, I would like to thank my family. My parents, Bonny and Sandy, have always encouraged me and had faith in me even though I surely pushed the limits of what any parent must endure. My sisters, Kerrin and Bobbi, have also helped me to reach my goals through lending an ear to my troubles and encouraging me to follow my dreams. I would also like to thank my friend Dave Trinin whose been like a brother to me, enjoyed the good times and stuck through the bad times and also introduced me to my fiancee, Jodi. Finally but most importantly, I thank my dear, sweet, Jodi for the encouragement, love and understanding she gave me as I finished out my graduate school career. Without her support, this thesis may never have been finished.

To Jodi, with Love

Contents

List of Figures

List of Tables

Chapter 1

Introduction

Tomographic imaging employs a wave field to obtain information about multiple cross-sectional planes of an object to reconstruct its three dimensional form. The cross-sectional planes can be probed using various types of waves, such as a sound wave or an electromagnetic wave. When an optical field is used as the probe, the coherence properties of the light can be exploited to isolate contributions from each individual plane. This method is termed coherence tomography. Although coherence tomography can be applied to learn about the structure of any object, it has been particularly useful in biomedical imaging applications.

This dissertation provides a new conceptual framework for studying and improving coherence tomography through the measurement of the optical phase space distribution of a light field. An optical phase space distribution describes the joint measurement of the momentum and position of a light field in a plane transverse to its direction of propagation. Phase space distributions are important for coherence tomography because they are sensitive to the phase and amplitude of the optical field emerging from a biological medium. Thus, they provide information not available with conventional intensity measurements.

A simple optical system has been developed that permits direct measurement of the phase space distribution of an optical field. The method is applied to the fundamental study of light propagation in turbid media. A turbid medium is any medium where light is predominantly scattered instead of absorbed, as is the case in many biological tissues. The study presented here will further the use of coherence tomography in biological imaging. As an introduction to this work, I begin by outlining the importance of using optical fields for medical imaging. This is followed by a brief description of the method used to measure optical phase space distributions in this study.

1.1 Motivation

Biomedical imaging techniques seek to detect and diagnose abnormalities within human tissues. Recently, optical methods have received increased attention as a potentially powerful diagnostic tool in medical imaging [1–9]. Although several other modalities exist for imaging parts of the body, such as x-ray imaging, x-ray computed tomography (CT), magnetic resonance imaging (MRI) and ultrasound, each technique possesses specific limitations that optical imaging can avoid. For example, high energy x-rays can ionize tissue making them potentially harmful for routine diagnostics. By contrast, optical radiation is non-ionizing and thus safer for repeated exposures.

Optical imaging is particularly promising because it is quite sensitive to abnormal metabolic processes that may signal tumor formation in some cases [1, 2]. X-ray imaging is not sensitive to these chemical changes in that it only reveals the structural damage caused by them. For this reason, x-rays may not detect small, early tumors, which are the most treatable, nor detect the differences between benign and malignant tumors [3]. Insensitivity to chemical processes also limits the usefulness of ultrasound and MRI. In addition, factors such as the poor spatial resolution of ultrasound and the high cost of MRI equipment necessarily restrict these methods to specific applications.

Optical biomedical imaging techniques rely on the measurement and interpretation of the optical field that has passed through human tissue. This can be much more complex than interpreting x-ray or MRI images because radiation at or near optical frequencies is highly scattered by biological materials. Two approaches can be taken to image in the presence of multiple scattering. The first relies on selectively detecting only ballistic photons, i.e., those that have passed through the tissue without being scattered. This can be accomplished by time-gating [4, 5], or exploiting a source with a short coherence length [6–8], to select out photons with a specific path length within a scattering medium. The second approach is to utilize the photons which have been multiply scattered [9]. The use of scattered photons to learn about the scattering medium is referred to as the inverse problem [3].

In clinical implementations, biomedical optical imaging methods make use of position dependent intensity measurements where light is collected via an optical fiber with a broad angle of acceptance. Thus, potentially useful information contained in the angular distribution and spatially varying phase of the field is ignored. Further understanding and refinement of optical biomedical imaging methods can be gained by measuring joint position and momentum (angular) distributions of light transmitted through biological tissues. These joint position and momentum distributions are termed optical phase space distributions and are well suited for studying the propagation of light in multiple scattering media.

1.2 Optical Phase Space Distributions

We have developed a technique for measuring optical phase space distributions based on heterodyne detection. In heterodyne detection, a weak optical field is mixed with a strong reference beam and the total power is measured. The reference beam, referred to as a local oscillator (LO), is offset in frequency from the signal beam. Mixing the two serves to enhance the signal. The measured beat signal arises from the interference of the signal and LO fields in the plane where they are detected. The spatial overlap of the LO and signal fields determines the beat amplitude,

$$V_B = \int dx \mathcal{E}^*_{LO}(x)\mathcal{E}_S(x), \tag{1.1}$$

where the corresponding y integral has been suppressed. In this expression, $\mathcal{E}$ represents the spatially varying part of the optical field. An important feature of our technique is that we measure the *mean square* beat signal $\left\langle |V_B|^2 \right\rangle$. I will show in Chapter 4 that this offers many advantages from both practical and theoretical standpoints. Of particular importance is that the mean square beat signal can be written elegantly in terms of the Wigner distributions of the signal and LO fields.

In 1932, Wigner [10] introduced a wave-mechanical phase space distribution in quantum mechanics. It was first adapted to describe optical fields by Bastiaans in 1978 [11]. For a wave field varying in one spatial dimension, $\mathcal{E}(x)$ the Wigner phase space distribution is given by [12]

$$W(x,p) = \int \frac{d\epsilon}{2\pi} \exp(i\epsilon p)\langle \mathcal{E}^*(x+\epsilon/2)\mathcal{E}(x-\epsilon/2)\rangle, \tag{1.2}$$

where x is the position, p is a wavevector (momentum), and $\langle \ldots \rangle$ denotes a statistical average. The expression for the mean square beat signal is given by

$$\left\langle |V_B(x_o,p_o)|^2 \right\rangle = \int dx\, dp\, W_{LO}(x-x_o, p-p_o) W_S(x,p), \tag{1.3}$$

where W_{LO} is the Wigner distribution of the LO field and W_S is that of the signal field. The optical phase space distribution is mapped out as a contour plot by scanning the center position x_o and center momentum p_o of the LO Wigner distribution,.

Wigner phase space distributions are important for studying the propagation of light in turbid media because they obey rigorous transport equations. The transport equations are derivable from the underlying wave equations for the optical field as I will demonstrate in Chapter 3. Thus, measurement methods based on Wigner

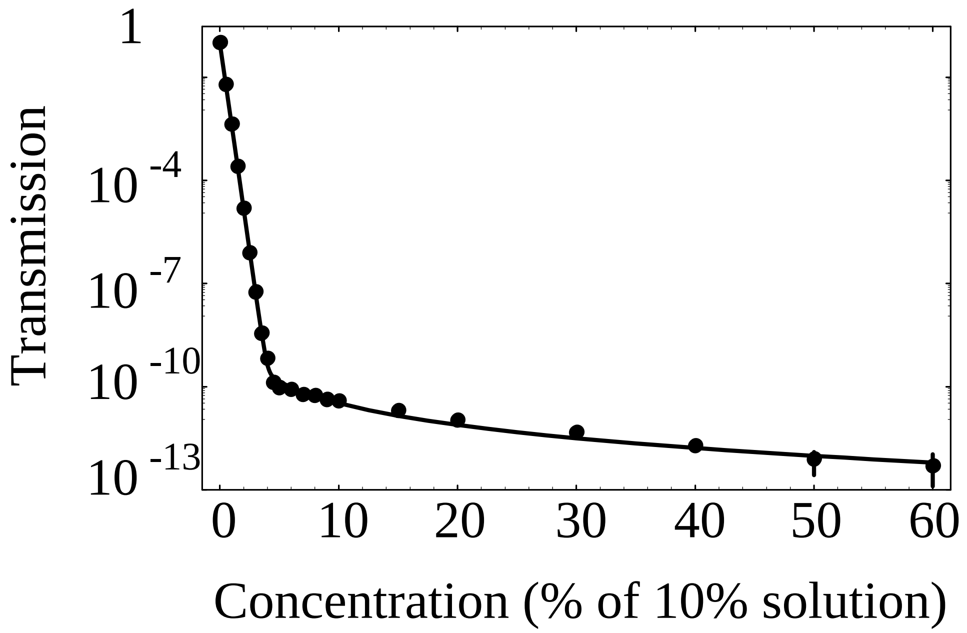

Figure 1.1: Transmission vs. concentration of 10% intralipid solution. Points - data; solid line - theory.

distributions can be placed on a firm theoretical footing. Wigner distributions are also important because they are sensitive to the coherence properties of light. This allows the study of the propagation of optical *coherence* in turbid media. It has been suggested that coherence tomography based on measurement of Wigner phase space distributions may yield new avenues for medical imaging [13].

The method I have developed has an extremely high dynamic range. It can detect signal beams over a range of 130 dB with sub-femtowatt sensitivity [14]. As a demonstration of the dynamic range, Figure 1.1 shows the results of an initial study of simple transmission measurements using optical phase space measurements in the forward direction ($x_o = p_o = 0$). The mean square beat intensity is measured for transmission through varying concentrations of Intralipid solution, a soy emulsion often used in turbid media studies for its tissue-like properties. The points represent measured transmission data (Table A.1). The solid line represents a theoretical model given by Equation 6.20. It is discussed in detail in Chapter 6 (section 6.3). The lowest transmission level detected in this experiment was 2.5×10^{-13} of the incident 0.5 mW signal beam. The measured power at this lowest level is 1.25×10^{-16} W and corresponds to a flux of approximately 300 photons per second.

As Equation 1.3 shows, the measured mean square beat signal is the convolution of the Wigner distribution of the signal field with that of the LO, i.e., the signal Wigner distribution is *smoothed* by the Wigner distribution of the LO. The position resolution of the smoothed Wigner distribution is given by the spatial size of the LO and its momentum resolution is given by the LO diffraction angle. In the case of a gaussian LO beam, the position and momentum width have a minimum uncertainty product and thus cannot be varied independently. Although a smoothed Wigner distribution is coarse grained and therefore contains less information than the true Wigner distribution, optical phase space measurements can still provide substantial sensitivity to the coherence properties of a light field in many cases of practical interest.

Mean square beat signals, as measured in our experiments, are sensitive both to ballistically transmitted light and to light that has been multiply scattered into the mode of the local oscillator [14]. This is in contrast to mean beat signals, which are only sensitive to unscattered, ballistic light. The difference between mean and mean square beat signals has been discussed previously for homodyne detection [15]. Both scattered and unscattered light can be used for biological imaging, but through different approaches. Ballistic light is most desirable for imaging, but is highly attenuated in thick samples. Therefore, scattered light, which is attenuated more slowly, must be used to image through thicker samples. To illustrate the sensitivity of our method to both ballistic and scattered light, Figure 1.2 shows an optical phase space

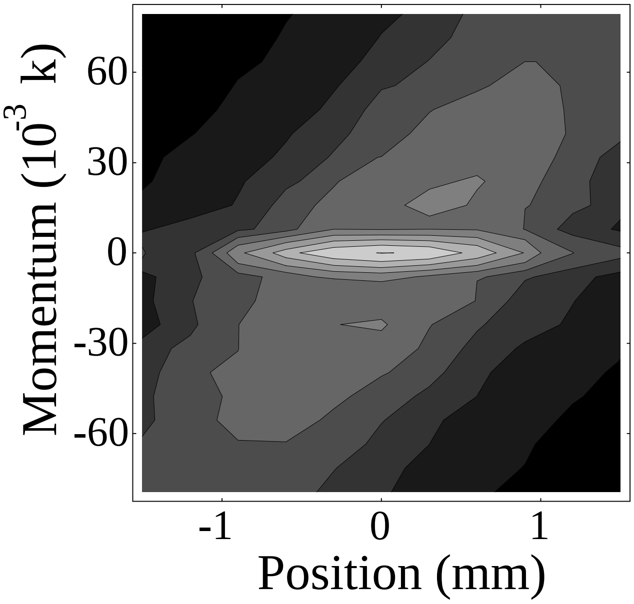

Figure 1.2: Measured optical phase space distribution for light transmitted through a turbid medium.

distribution as a contour plot in position x_o and momentum p_o in units of the optical wavevector k. This plot shows both the ballistic and scattered light emerging from a sample of polystyrene spheres in a water/glycerol mixture The ballistic light is the narrow island in the center of the plot centered at zero transverse momentum. The broad ellipse surrounding it is the scattered light. This example is discussed further in section 6.2.1.

The Wigner distribution of scattered light is of interest because it contains information about the form factor of the scattering object. To exploit this information, it is desirable to isolate low order scattered light which still retains substantial information about the scatterer. Isolation can be accomplished by suppressing multiple or diffuse scattering as much as possible. In comparison to other detection methods that collect light over a broad range of angles, heterodyne detection has high angular resolution. This angular resolution allows selective suppression of multiply scattered light because of its broad angular distribution compared to the narrow angular profile of light arising from low-order scattering. In addition, the heterodyne technique permits the use of either coherent or low-coherence-length light sources, the latter allowing further suppression of diffuse scatter by timing resolution [16]. Thus, this method will complement current studies of low order light scattering [17–19].

Measurements of optical phase space distributions are particularly relevant to current optical coherence tomography (OCT) methods [6–8]. In OCT, the light reflected from a biological sample is measured using a low-coherence-length source. The coherence length of a source is inversely proportional to its bandwidth. Thus, a source with a bandwidth in the range of tens of nanometers will have a coherence length of a few microns. When using a broadband source for interferometry, as in OCT, the optical path of the two beams used must be aligned within the coherence length of the source to yield an interference signal. In OCT, a sample is placed in the path of one of the beams in the interferometer and a variable optical path delay is included in the other. By varying the path length of the reference beam, a specific path length for light reflected from the sample is selectively detected. This results in a depth resolution that depends on the coherence length of the light source. For a coherence length of a few microns, the resolution corresponds to that obtained using time gating and a short laser pulse of a few tens of femtoseconds in duration. Our heterodyne method also can be implemented using a low-coherence-length source and thus can impact OCT in a number of ways.

The optical phase space method can be used to provide additional information about light propagation in biological materials that is missing in OCT measurements. The difference is that our method measures the mean square beat signal compared to the mean beat signal measured in OCT, thus, our method can study scattered light while OCT cannot. In addition, the optical phase space method examines both the spatial and angular distributions of a light field while OCT only measures its position dependent intensity. Finally, our method also provides information about the coherence properties of light fields. Therefore, it can be used to conveniently characterize the coherence properties of the low-coherence-length light sources used in OCT. As new low-coherence-sources are being continually developed for applications such as OCT, a means for quickly and easily characterizing their coherence properties is necessary. Knowledge of the coherence properties of the input light field are a needed reference when interpreting the measurements made in OCT. The method of characterizing the coherence properties of a light source are presented in Chapter 5 as well as example characterizations for coherent and low-coherence-length sources.

The capability to sort the light emerging from a turbid sample by specific phase space parameters makes our system particularly useful for studying several anomalous effects that have been observed with OCT that hinder its capabilities. For example, it has been shown recently that multiple small angle scattering increases the amplitude of the effective probe field over that expected for simple exponential decay of the ballistic light. The probe field contains a distorted wavefront that causes structures small compared to the transverse coherence length of the unscattered input beam to be enhanced compared to large ones [20]. Another example of anomalous behavior seen in OCT is a consequence of using a low coherence length source. The low coherence length light necessarily selects only a certain range of spatial frequencies to be detected. This selection also tends to favor small scale structures over larger ones [21]. A more complete description of OCT methods is presented in section 2.4.3 while the particular applied problems mentioned here are addressed in section 7.4.3 of this thesis.

As an illustration of the capabilities of the optical phase space method, Fig. 1.3 and Fig. 1.4 show the measured Wigner distributions for low-coherence-light

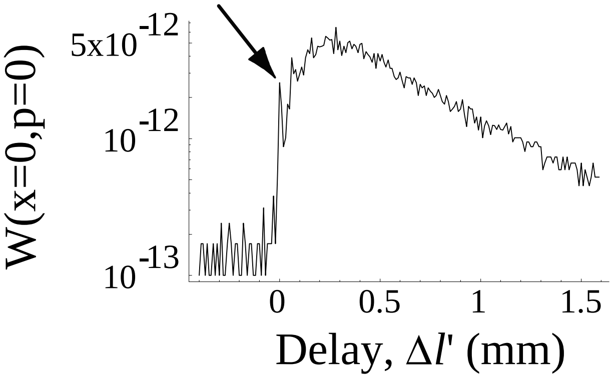

Figure 1.3: Measured optical phase space density for $x = 0$ and $p = 0$ as a function of photon path length. The scatterer concentration is $\rho = 1.5 \times 10^7/\mathrm{cm}^3$.

transmitted through a sample of polystyrene spheres in a water/glycerol mixture. Fig. 1.3 shows the measured optical phase space density for zero transverse position (x_o) and zero transverse momentum (p_o) for different path lengths within the medium. The path lengths are measured relative to the ballistic light at zero delay, indicated by the arrow in the figure. Here we see that the ballistic light is attenuated by a factor of $e^{-27.2} = 1.5 \times 10^{-12}$ compared to a sample with no scatterers. This represents a relatively high attenuation as it approaches the limit of detectable light levels using our method. Although the ballistic light is still present, its peak magnitude is lower than that of the scattered light detected at non-zero path delays. This figure illustrates two key attributes of our method. First, our method can measure both ballistic and scattered light over a large dynamic range. Second, it illustrates that different path lengths can be selectively detected by using a low coherence source. The mechanics and consequences of using a low coherence source in our scheme are discussed in more detail in section 4.1.2.

As a further illustration of the capabilities of our system, Fig. 1.4 shows measured optical phase space distributions in position (x_o) and momentum (p_o) for the same

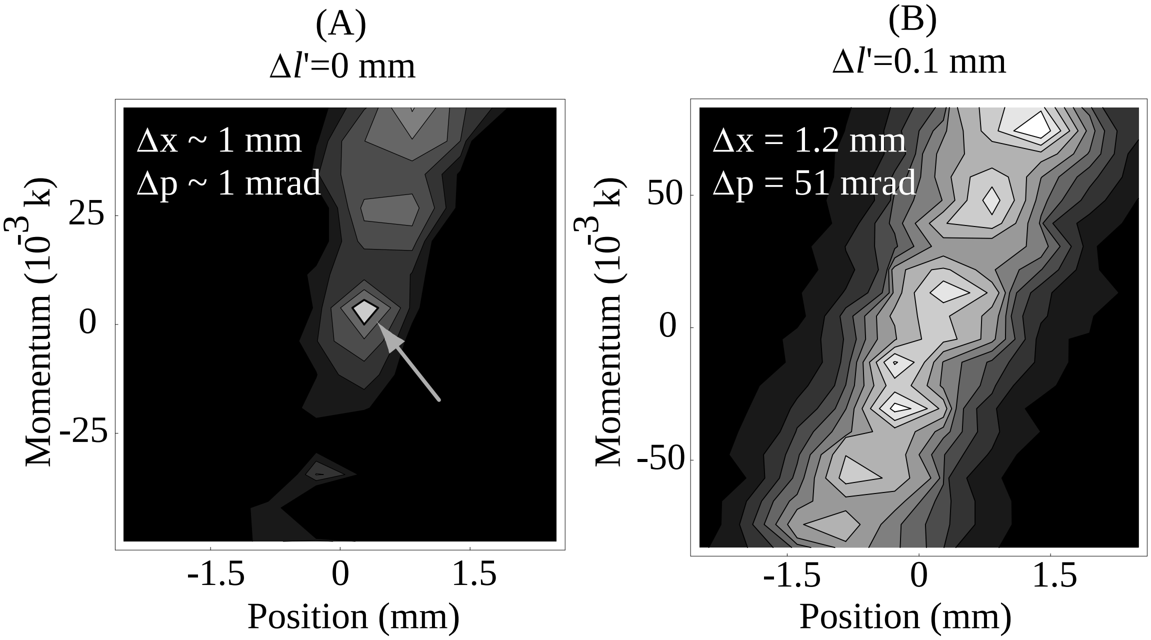

Figure 1.4: Measured optical phase space distributions in position, x, and momentum, p, for fixed path lengths relative to the ballistic light. (A) zero path delay (B) a path delay of 0.1 mm. Concentration $\rho = 1.5 \times 10^7/\mathrm{cm}^3$.

source and sample. Figure 1.4(A) shows the distribution when the signal and LO paths are matched to within the coherence length of the source. This distribution is dominated by ballistic light that is localized at zero transverse position and momentum. For clarity, it is indicated by an arrow. When a path delay of 0.1 mm is introduced in the LO path, the measured distribution becomes dominated by low-order scattered light as shown in Fig. 1.4(B). Although the scattered light is spread out in position and momentum compared to the ballistic light, it remains relatively narrow in momentum compared to the diffuse light measured at longer path delays. This light may still be useful for imaging applications. Fig. 1.4 demonstrates that our system can measure the position and momentum distribution of light with a chosen path length within a turbid sample. The example shown here is explored in more detail in section 7.2.3.

In summary, our system offers several advantages for studying light propagation in turbid media. First, by measuring the mean square heterodyne beat, our detected signal can be related to the Wigner distribution of the field of interest. This places our measurements on a firm theoretical footing, as the Wigner distribution rigorously incorporates the phase and intensity information of an optical field. Second, the heterodyne method is an extremely sensitive and selective detection scheme. It offers high dynamic range, allowing sub-femtowatt signals to be detected. It possesses high angular and position resolution as governed by the form of the local oscillator. Heterodyne detection also offers high longitudinal resolution when implemented with a broadband low-coherence source. The ability to select the phase space parameters of the detected light permits detailed study of its coherence properties. Finally, optical phase space measurements can selectively detect both ballistic and scattered light. Thus, our method can be used to obtain the maximum information about the light field emerging from a multiple scattering medium. This knowledge can be used to improve understanding and enhance imaging for a variety of current biological imaging studies and applications.

1.3 Overview of Thesis

The remainder of this thesis is organized as follows. In Chapter 2, an overview of past light scattering studies and light scattering theories is presented. This provides perspective on the current understanding of light propagation in scattering media and to see how this work can contribute to that understanding. A cursory overview of current optical medical imaging methods is included in this chapter as well. Chapter 3 presents a discussion of Wigner distributions and their properties. As illustrative examples of these properties, measured optical phase space contour plots are presented for gaussian beams from a coherent source in various configurations. An example of deconvolution of an optical phase space distribution to recover the true Wigner distribution is also shown in Chapter 3.

The heterodyne method for measuring smoothed Wigner phase space distributions as contour maps is presented in Chapter 4. The heterodyne method can be used to measure smoothed Wigner phase space distributions for a optical fields from a variety of light sources. Chapter 5 outlines a method for characterizing the coherence properties of a given light source using optical phase space distributions. The characterization method is then used to measure the coherence properties of the light sources used in the experiments. This serves not only as a needed reference but also to demonstrate the utility of the method in characterizing optical fields.

The first of three turbid media studies is presented in Chapter 6. This study examines the measured optical phase space distributions obtained for light from a coherent source that has been transmitted through a turbid medium. The data are analyzed using approximate solutions to the transport equation for the Wigner distribution in a turbid medium. Physical insights on the theoretical model used to analyze the data are discussed in the final section of this chapter. Chapter 7 presents a turbid media study of the optical phase space distributions for low-coherence light that has been transmitted through a multiple scattering medium. Although, no detailed theoretical model has been developed to interpret the data at present, trends which are evident in the data are presented. The discussion section of this chapter relates this study to current medical imaging methods.

The third and final turbid media study, presented in Chapter 8, examines the optical phase space distributions for light from a low-coherence source that has been backscattered from a turbid medium. The data are analyzed using a model that examines the field propagation under the assumption of isotropic scattering. The theoretical model is cast in the form of a Wigner distribution for comparison to the data. The results are discussed in terms of the propagation of optical coherence in a multiply scattering medium. Chapter 9 concludes this thesis with a summary of this work and discusses its potential application to current biomedical imaging techniques.

Chapter 2

Background

To assess the present status of light scattering studies, I began by surveying current techniques used in biological imaging. Along the way, I uncovered various experimental techniques used in light scattering experiments ranging from short pulse studies to coherence techniques to diffusion wave spectroscopy. I also studied a variety of theoretical treatments, such as the Mie solution for an electromagnetic field scattered by a dielectric sphere. While new advances in understanding are still being made today, some properties of light scattering have been known for over a century.

I begin this chapter with a brief historical perspective on the scientific study of light scattering. Any topic with over a hundred years of history would take volumes to fully explore; therefore, this perspective only covers the beginnings of light scattering studies. Included in this section is a bibliography of reference books that are suitable places for beginning literature searches. These references are the well-known guidebooks for the field of light scattering. The second section presents different theoretical approaches that have been used to explain light scattering. It begins with scattering from a single particle, and includes multiple scattering from the radiative transport and diffusion approximation viewpoints. Finally, I conclude the chapter by discussing a variety of experimental methods that are currently in use to employ light in biological imaging applications.

2.1 Beginnings

The earliest inquiries into the scattering of light were conducted in an attempt to explain the color of the sky. The first scientific study of light scattering is attributed to Tyndall in 1869 [22], although thinkers such as DaVinci (ca. 1500) and Alhazen of Basra (ca. 1000) suggested that the blue sky was due to the “reflection” of light [23]. Tyndall observed a bluish color in the light scattered from particles smaller than the wavelength of the incident light. This phenomenon was explained by Rayleigh in 1881 who showed that the scattering of light by small particles is inversely proportional to the fourth power of the wavelength. The preferential scattering of short wavelengths accounts for the blue color of the sky although such an explanation may not satisfy the curiosity of a child: “Why is the sky blue?”

A significant theoretical advance in understanding light scattering was finding the solution for the distribution of light scattered by a sphere, known as the “Mie solution.” This theory gives the exact solution for the scattering of electromagnetic radiation by a dielectric sphere as presented in Mie’s 1908 paper. The mathematics of this theory are straightforward yet cumbersome. However, with the modern aid of the computer and readily available programs, the Mie solution can easily be calculated [24].

Although the history of the application of light scattering is too broad to summarize completely, several reference books present overviews on the subject from different perspectives. Among those I have found helpful are *Light Scattering by Small Particles* by H. C. van de Hulst [25], *Wave Propagation and Scattering in Random Media*, Vols. I, II by A. Ishimaru [26] and *Absorption and Scattering of Light by Small Particles* by C. F. Bohren and D. R. Huffman [24].

Light Scattering by Small Particles by H. C. van de Hulst is an early reference on light scattering originally published in 1957 [25]. In addition to presenting theoretical treatment of the scattering of light by a variety of particle types and sizes, it outlines some of the earliest applications of light scattering in the fields of chemistry, physics, meteorology and astronomy. As this text dates from before the advent of the laser, the light scattering applications it presents make use of white light filtered by wavelength or polarization and hence have limited applicability to modern light scattering studies using lasers. However, it is useful for appreciation of historical perspective and for its theoretical treatments of single scattering for a large number of different types of particles.

Wave Propagation and Scattering in Random Media, Vols. I, II by A. Ishimaru is based on a set of lecture notes from a graduate engineering course in wave propagation in random media published in 1978 [26]. It covers single and multiple scattering theory, presenting several perspectives on how to treat theoretically the transport of waves in random media. While few specific applications are actually detailed, the text is intended for engineers and thus it presents theoretical treatments for a wide variety of experimentally useful configurations. Of particular use as a reference is Chapter 3, which presents scattering characteristics for several multiple scattering media, including biological materials.

Lastly, *Absorption and Scattering of Light by Small Particles* by C. F. Bohren and D. R. Huffman [24], is a more modern text, published in 1983. It presents the usual theories on single scattering as an introduction to the properties of light scattering by bulk matter. The experimental detail of this last text makes it particularly useful to an experimentalist. It contains several Fortran computer programs for calculating Mie solutions, results for angular scattering experiments and a discussion of applications of light scattering, including scattering by biological materials.

2.2 Theoretical Background

2.2.1 Single Scattering

When a wave is incident on a single particle, the incident power is scattered into all directions with varying scattering amplitudes $f(\theta)$. The distribution of these amplitudes by angle is known as the differential cross section $d\sigma/d\Omega$. The scattering amplitude is related to the differential cross section by $d\sigma/d\Omega = |f(\theta)|^2$. Integrating this distribution over all angles yields the scattering cross section σ_S. The scattering cross section approximates the total cross section σ_T when absorption is negligible, the case which is focused on in this work. The albedo of a scattering medium is defined as the scattering cross section divided by the total cross section. Thus, this condition can be specified by the albedo of the particles approaching unity.

An interesting property of cross sections is that it approaches twice the geometric cross section σ_g when the particle size is much greater than a wavelength. This is known as the extinction paradox [25]. This seeming paradox can be explained by identifying the fluxes of energy involved in the scattering process. All energy falling on the object is scattered from the incident wave, giving a cross section equal to σ_g, the geometric area of the object. In addition, there will be diffraction at the edges of the shadow cast by the object. The light that forms this diffraction pattern is also removed from the incident flux, again accounting for a cross section equal to σ_g. Thus the actual cross section is roughly twice the geometrical cross section.

The exact scattering and differential cross sections can be calculated using the Mie solution. With the aid of a Fortran computer program from Bohren and Huffman [24] which is well known in the light scattering field, the exact scattering solution of a dielectric sphere can be calculated by specifying the index of refraction n relative to the background medium, and size of the sphere a, as well as the wavelength of incident light λ. The calculated Mie solutions presented in Chapter 5 show that the total cross section can be slightly more or less than twice the geometrical cross section for particles large compared to the wavelength of incident light.

The Mie solution provides good numerical results for angular scattering profiles. However, several useful approximations can be employed under certain conditions when an analytic form of the differential cross section is needed. When the scatterer size is much smaller than the wavelength of incident light, the scattering is known as Rayleigh scattering. In this approximation, the field inside the sphere is assumed to be constant and uniform. The angular scattering dependence in this approximation resembles an electric dipole oriented in the direction of the incident field and the amplitude has the familiar λ^{-4} dependence. Another case that has an approximate solution is when the relative dielectric constant $\epsilon_r = (n_2/n_1)^2$ of the scatterer is close to unity, indicating that the index of the object n_2 is nearly the same as the index of the background material n_1. This is called Rayleigh-Debye or Born approximation scattering and is valid for large or small scatterers provided $(\epsilon_r - 1)\ ka \ll 1$, where k is an optical wavenumber. In this situation, the field inside the scatterer is approximated by the incident field, allowing for calculation of the scattered field for several geometries of scatterers.

A third approximate solution is the WKB (Wentzel-Kramers-Brillouin) interior wave number technique, valid for $(\epsilon_r - 1) < 1$ and $(\epsilon_r - 1)\ ka \gg 1$. In this case, the field inside of a large scatterer is approximated by a field that has propagated through it according to the change of index of refraction at the interface between the particle and its surroundings. Also, for $(\epsilon_r - 1) < 1$, there is no change of angle at the interface and the interior wave travels at the same angle as the incident wave. In this approximation, the total cross section can be found using the forward scattering theorem or optical theorem and is given by

$$\sigma_T = \frac{4\pi}{k}\,\mathrm{Im}[f(\theta = 0)]. \tag{2.1}$$

Lastly, I note that this approximation is not accurate for small particles and the Rayleigh or Born solution should be used [26].

2.2.2 Radiative Transport Theory

Radiative transport theory is based on phenomenological observations and makes use of a heuristic quantity known as the specific intensity. This quantity is the average power flux density at a given position within a unit solid angle in a given direction $\hat{s}$. The specific intensity is often identified as the Fourier transform of the mutual coherence function although since it is a heuristic quantity, the relation has never been rigorously shown.

The transport characteristics of the specific intensity are governed by the equation of transfer, a differential equation analogous Boltzmann's equation in the kinetic theory of gases. The equation of transfer is given as [26]

$$\frac{dI(\mathbf{r},\hat{\mathbf{s}})}{ds} = -\rho\sigma_T I(\mathbf{r},\hat{\mathbf{s}}) + \frac{\rho\sigma_T}{4\pi}\int_{4\pi} p(\hat{\mathbf{s}},\hat{\mathbf{s}}')I(\mathbf{r},\hat{\mathbf{s}}')d\Omega', \tag{2.2}$$

where $I(\mathbf{r},\hat{\mathbf{s}})$ is the specific intensity at position $\mathbf{r}$ moving in the direction of unit vector $\hat{\mathbf{s}}$. In this equation, the left hand side represents the change in specific intensity over a volume element ds, while the right hand side represents the effects of scattering. The first term on the right hand side is negative, indicating a loss of specific intensity in element ds due to scattering. The loss arises from the number of particles within the unit volume, specified by the density ρ, each removing specific intensity via its total extinction coefficient σ_T. The second term is positive and thus represents additions to the specific intensity due to scattering. In this term, intensity is scattered into the direction $\hat{\mathbf{s}}$ from $\hat{\mathbf{s}}'$ by the phase function $p(\hat{\mathbf{s}},\hat{\mathbf{s}}')$. The phase function is simply the differential cross section $d\sigma/d\Omega$ normalized by the total cross section σ_T; its name has its origins in astronomy where it refers to lunar phases. The phase function does not relate to the phase of a wave [26]. The contributions are summed over all possible incident directions $\hat{\mathbf{s}}'$ via the integral over the 4π solid angle indicated by the variable Ω'. The integral is weighted by the number of particles ρ in the volume element and the cross section each subtends σ_T.

There are no known exact analytical solutions to the equation of transfer. However, there are useful approximate solutions in special cases. If the particles are large, the equation of transfer (Eq. 2.2), can be approximated by a parabolic differential equation that can be solved through Fourier transform methods. This approximation is often referred to as the small angle approximation [27]. If the particles are small compared to a wavelength or the particles are sufficiently dense, the specific intensity becomes isotropic and the diffusion approximation can be used as discussed in the next section.

2.2.3 Diffusion Approximation

In situations where there are high densities of scatterers, much greater than 1% volume fraction, the equation of transfer (Eq. 2.2) can be approximated by a diffusion equation. By assuming that the scattering has become nearly isotropic such that the angular dependence of the scattering is nearly constant, the specific intensity can be approximated as [26]

$$I_d(\mathbf{r}, \hat{\mathbf{s}}) = U_d(\mathbf{r}) + \frac{3}{4\pi}\mathbf{F}_d(\mathbf{r}) \cdot \hat{\mathbf{s}}, \tag{2.3}$$

where U_d represents the average diffuse intensity and $\mathbf{F}_d(\mathbf{r}) \cdot \hat{\mathbf{s}}$ represents the diffuse flux in the direction $\hat{\mathbf{s}}$. Modelling light transport by using Equation 2.3 is known as the diffusion approximation. Using this approximation, a diffusion equation can be derived from the equation of transfer. The fundamental steady state diffusion equation takes the form [26]

$$\nabla^2 U_d(\mathbf{r}) - 3\rho\sigma_{tr}\rho\sigma_a U_d(\mathbf{r}) = -\frac{3}{4\pi}\rho\sigma_{tr}E(\mathbf{r}) + \frac{3}{4\pi}\nabla \cdot \hat{\mathbf{s}}E(\mathbf{r}). \tag{2.4}$$

Here $E(\mathbf{r})$ represents the angle integrated source function, ρ is the density of scatterers, σ_a is the absorprtion cross section and σ_{tr} represents the transport cross section.

The transport cross section accounts for the anisotropy of the scattering and is related to the total cross section by:

$$\sigma_{tr} = \sigma_T(1 - g), \tag{2.5}$$

where g is the average of the cosine of the scattering angle.

The average diffuse intensity U_d can be completely described using Eq. 2.4 by including suitable boundary conditions. The diffuse flux $\mathbf{F}_d(\mathbf{r})$ can be found from U_d using conservation of power arguments, enabling calculation of the specific intensity. The diffusion approximation has been employed to solve a number of light transport problems. For example, a current biomedical imaging technique employing diffuse photon density waves uses the diffusion approximation to model the propagation of light in thick turbid media [9]. This method is discussed further in section 2.4.2.

2.3 Recent Developments

2.3.1 Enhanced Backscatter

In 1984 a new coherent effect of light scattering by a random medium was observed by Kuga and Ishimaru [28]. In this effect, the intensity backscattered from a dense distribution of scatterers is seen to have a sharp peak in the retroreflected direction. The backscattered peak is found to be twice as large as that predicted by transport theory and thus it is called enhanced backscatter. Enhanced backscattering is not predicted by radiative transport theory, which deals with intensities. Instead, analysis of the problem using optical fields shows that the effect arises from the interference of coherent time-reversed paths. An example of time-reversed paths is shown in Figure 2.1.

Coherent effects had been predicted previously, but only small effects had been observed experimentally [29, 30]. The clear interference effect observed by Kuga

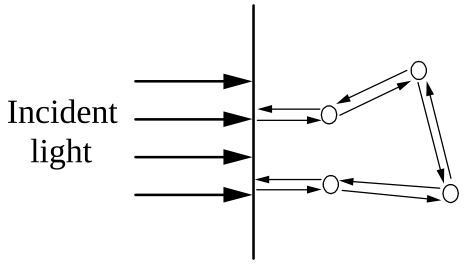

Figure 2.1: Enhanced backscattering through time reversed paths.

and Ishimaru sparked renewed interest in the subject. A recent review article in *Progress in Optics* Vol. XXIX [31] discusses the theoretical understanding of enhanced backscattering in optics. It presents theories of the origin, shape, and magnitude of the backscattering peak and discusses related effects. For example, the enhanced backscattering effect has been linked to the weak localization of light in a random medium [32,33].

More recent studies of enhanced backscattering have explored various characteristics of the effect. Using ultrafast pulses, temporal and angular profiles of enhanced backscattering have been measured [34,35] and the effects of finite coherence length have been examined [36]. Of particular interest is a recent theoretical discussion of the effect of partial spatial coherence on enhanced backscatter [37] which is used in conjunction with an earlier theoretical work [38] to analyze the experimental backscattering data in section 8.2.

2.4 Current Studies for Biomedical Applications

There are several methods actively being developed for medial imaging applications. In this section, I will present brief discussions of three of the most promising techniques. These include time domain methods which employ short light pulses, the use of amplitude modulated light in frequency domain methods, and optical coherence tomography (OCT) which exploits the coherence properties of broadband light.

2.4.1 Time Domain Methods

One avenue currently being explored for biological applications employs short laser pulses to measure either the reflected or transmitted intensity for different propagation times in turbid media. In these experiments a laser pulse, typically of subpicosecond to tens of picoseconds pulse duration (10^{-13}- 10^{-11} s), is incident on a multiply scattering sample. The transmitted intensity is recorded using a streak camera yielding a time resolved record. In a multiple scattering medium, the scattered light takes longer to traverse the medium than unscattered light. Thus, this method can be used to isolate the ballistic light from multiply scattered light. The time resolved method for studying turbid media was first initiated by the research group of R. R. Alfano at the Institute for Ultrafast Spectroscopy and Lasers at the City College of New York. The earliest experiments using this method sought to simply confirm previous theories on pulse propagation in random media [39] or note the properties of tissues [40].

Further experiments using time resolved methods focused on imaging objects within turbid media. One experiment [41] uses a time of flight method to examine only the photons which are unscattered or weakly scattered. In this technique, the early arriving photons are selectively detected using a triggered streak camera. Another experiment uses a triggered streak camera to measure time-resolved fluorescence to image objects embedded in a turbid medium [42]. Using other means of time gating leads to improvements in resolution and signal-to-noise. For example, experiments using an optical shutter known as an ultrafast Kerr gate result in submillimeter resolution [4] and 100 dB dynamic range [43] for imaging applications.

Efforts to implement time-resolved imaging methods in clinical applications has driven scientific inquiry into more practical areas. Recent studies have centered around resolution enhancements [44, 45], studies of inhomogeneity contrasts [46–48], and image reconstruction algorithms [49–51]. Currently, time resolved methods are beginning to be employed clinically. Their application to the characterization of normal and cancerous breast tissues shows the potential to provide much more information than even x-ray (conventional) mammography provides [52, 53].

2.4.2 Frequency Domain Methods

Methods such as time gating seek to extract weakly scattered or unscattered photons from the total intensity. However, with thick turbid media a vanishingly small number of these photons are detectable. Thus, a second area which has substantial interest for potential application to biological applications employs diffusing photons [9]. Photons are termed diffuse if they have undergone enough scattering so that their direction of propagation has become randomized. Imaging applications employ diffuse light in the form of diffuse photon density waves which are travelling waves of energy density. These waves are produced by introducing amplitude modulated light into a multiple scattering medium and thus are referred to as frequency domain methods [54].

As the potential use for biomedical imaging applications of diffuse photon density waves became apparent, scientific studies examined their basic wavelike properties. For example, diffuse photon density waves were seen to undergo refraction at a boundary [54], to undergo scattering and wavelength transduction [55], and to produce interference patterns [56]. Such fundamental investigations gave rise to more directed studies of particular configurations for imaging applications. These included investigations of their properties as the frequency of the amplitude modulation was varied [57], and in the presence of absorbing and reflecting objects [58]. Other studies presented schemes on how to localize objects using diffuse photon density waves [59].

The first experimental images of inhomogeneities embedded in turbid media based on frequency domain methods were published in 1995 by the research group of Arjun Yodh at the University of Pennsylvania [60].

As the technology matured, studies began to turn toward clinical implementations. At a recent conference where I presented my work, Advances in Optical Imaging and Photon Migration, held March 8-11, 1998, in Orlando, Florida many sessions were devoted to the fundamental and clinical studies of diffusive photon optical imaging. Several results were presented that employed diffuse photon density waves for non-invasive characterization of breast tumors [61–63]. These studies were capable of locating tumors as small as 1 cm in diameter but more importantly were able to characterize the chemical processes occurring within the diseased tissue.

2.4.3 Coherence Methods

Perhaps the most promising biomedical imaging method currently being developed is Optical Coherence Tomography (OCT). In this method, the coherence properties of a broadband light source are exploited to select the time of flight of detected photons. In this respect it is similar to time resolved methods; however, OCT is implemented with continuous wave broadband sources thus eliminating the need for the costly and complex generation of ultrashort pulses.

The OCT technique is an extension of previous work done with low-coherence reflectometer systems specialized to allow high-speed, continuous motion longitudinal scanning and a transverse scanning mechanism. The term OCT was popularized in the publications by the research group of James G. Fujimoto at the Massachusetts Institute of Technology, a group responsible for much of the pioneering research in OCT. The method is based on a Michelson interferometer which uses a low coherence source and fiber optics to deliver the beam. The reflected light from a sample placed in one arm of the interferometer is recombined with the reflections from a reference mirror. Interference is observed only between the coherent components of these two reflections. Thus, when using a source with a low coherence length, the interference signal arises only from light that has travelled the same optical path in the tissue as the optical path specified by the reference arm [64]. The envelope of the interference pattern is recorded with high dynamic range by scanning the reference mirror at a fixed velocity and demodulating the photocurrent at the corresponding Doppler shifted frequency [65].

The method is particularly useful when combined with confocal microscopy to obtain high resolution images. The combination, known as Optical Coherence Microscopy (OCM), employs a high numerical aperture objective to focus the light to a tight focal spot. This improves the transverse resolution of the imaging system allowing individual cells to be imaged compared to OCT, which only resolves histological tissue layers [7, 66].

As a mature technology, OCT has been used to study a variety of tissue characteristics. It has been used to measure the index of refraction of various human tissues [67], to image the beating heart of an African frog [68], to study internal organs using a catheter-endoscope [69, 70], and for retinal imaging [71].

2.5 Optical Phase Space Distributions

The biomedical imaging techniques discussed above all rely on position based intensity measurements to learn about the light field emerging from a biological sample. These methods neglect the potentially useful information contained in the momentum distribution of the light. By measuring the joint position and momentum distribution of the light field, optical phase space distributions obtain the maximum information about the light field of interest.

In addition, optical phase space distributions are related to the Wigner distribution of the light field. This is important because rigorous transport equations can be derived for the Wigner distribution from the underlying wave equation. While light transport is usually explained using heuristic treatments like those discussed in this chapter, studies based on Wigner distributions can be treated rigorously. The next chapter presents Wigner distributions and their properties to illustrate their importance to light scattering studies.

Chapter 3

Wigner Distributions and their properties

The Wigner distribution is a wave-mechanical phase space distribution that is applicable to the study of the propagation of light in turbid media. At first glance, the Wigner distribution appears to behave simply as a classical phase space distribution in position and momentum. However, the Wigner distribution contains information about the wave nature of the optical field that it describes. This relationship allows rigorous derivation of transport equations for the Wigner distribution based on the underlying wave equation. The details of this derivation are presented in this chapter. As an introduction to Wigner distributions, I present a discussion of their properties and then demonstrate their characteristics using measured optical phase space distributions as an illustrative example.

3.1 Wigner Distributions

The Wigner distribution is a wave-mechanical phase space distribution function that is applicable to coherence tomography. It is defined by (Eq.1.2)

$$W(x,p) = \int \frac{d\epsilon}{2\pi} \exp(i\epsilon p)\langle \mathcal{E}^*(x+\epsilon/2)\mathcal{E}(x-\epsilon/2)\rangle. \tag{3.1}$$

This is the definition of the Wigner distribution for the wave field $\mathcal{E}$. Here x indicates position, p indicates momentum, and $\langle ... \rangle$ indicates a statistical average. It is easy to show that $\int dp\, W(x,p) = \langle |\mathcal{E}(x)|^2 \rangle$, the position distribution of the intensity, and $\int dx\, W(x,p) = \langle |\mathcal{E}(p)|^2 \rangle$, the corresponding momentum distribution. The Wigner distribution plays a role closely analogous to a classical phase space distribution in that it is a real function containing position and momentum information about the wave field. This analogy breaks down when one considers that the Wigner distribution can have negative values.

Wigner distributions are particularly useful for theoretical modeling of light propagation in turbid media because they bridge the gap between the wave and particle natures of light. In free space, the Wigner distribution appears to propagate in straight lines as though it obeys geometrical ray optics. However, the Wigner distribution is Fourier transform related to the two-point coherence function so it also contains information about the spatial coherence of the wave field. Thus, its free space propagation properly accounts for diffraction. As an initial illustration of this dual nature, I present the propagation of the Wigner distribution through a distance d in free space by Fresnel diffraction and Fourier optics.

3.1.1 Propagation in free space

In Fourier optics, the propagation of an optical field in free space is regarded as a linear dispersive spatial filter. Thus, for propagation over a distance d, the amplitude of the field in the plane $z = d$ is written as the convolution of the linear transfer function h with the field amplitude in the plane $z = 0$ [72] and is given by

$$E(x_d, z = d) = \int h(x_d, z = d; x_o, z = 0) E(x_o, z = 0) dx_o. \tag{3.2}$$

Here only one transverse spatial dimension is included but parallel arguments for a second transverse dimension y_d can easily be included. The transfer function h can be determined directly from the wave equation using Green's function methods. However, in the case where the region of interest about the z axis is small compared to the distance d, a paraxial approximation to this transfer function can greatly simplify the mathematics. In the paraxial case the transfer function is given by [72]

$$h(x_d, z = d; x_o, z = 0) \simeq \sqrt{\frac{k}{2\pi i d}} \exp\left(ikr_{od}\right), \tag{3.3}$$

where k is the optical wavevector and r_{od} is the distance between the point x_o and the point x_d. I note that the sign conventions used here are for a field propagating as $e^{-i\omega t}$ but this analysis also could be done for a field propagating as $e^{+i\omega t}$ as is done in Goodman [72]. The transfer function can be further simplified by using the *Fresnel approximation*. Here the distance r_{od}, which is defined as:

$$r_{od} = d\sqrt{1 + \left(\frac{x_o - x_d}{d}\right)^2}, \tag{3.4}$$

is assumed to be approximated adequately by the binomial expansion as:

$$r_{od} \simeq d\left[1 + \frac{1}{2}\left(\frac{x_o - x_d}{d}\right)^2\right]. \tag{3.5}$$

This allows the transfer function to be written as:

$$h(x_d, z = d; x_o, z = 0) \simeq \sqrt{\frac{k}{2\pi i d}} \exp\left\{i\frac{k}{2d}\left[(x_o - x_d)^2\right]\right\}, \tag{3.6}$$

multiplied by a phase, $\exp(ikd)$. This phase is important when considering the overall phase of the field but I will neglect it here as I am only tracing the effects of propagation on the *transverse* Wigner distribution. Using Eq. 3.6, one can relate the field amplitude in the plane $z = d$ to that in the plane $z = 0$:

$$E(x_d, z = d) = \sqrt{\frac{k}{2\pi i d}} \int dx_o \exp\left[i\frac{k}{2d}(x_o - x_d)^2\right] E(x_o, z = 0). \tag{3.7}$$

Equation 3.7 can be used to find the transverse Wigner distribution in the plane $z = d$, in terms of the transverse Wigner distribution in the plane $z = 0$:

$$W(x_d, p_d, z = d) = \int \frac{d\epsilon}{2\pi} \exp(i\epsilon p)\langle E^*(x_d + \epsilon/2, z = d)E(x_d - \epsilon/2, z = d)\rangle. \tag{3.8}$$

Substituting the expression for the field amplitude in the plane $z = d$ from Eq. 3.7

yields:

$$\begin{aligned} W(x_d, p_d, z=d) &= \int \frac{d\epsilon}{2\pi} \exp(i\epsilon p) \\ &\times \sqrt{\frac{-k}{2\pi i d}} \int dx_o \exp\left[-i\frac{k}{2d}\left(x_o - x_d - \epsilon/2\right)^2\right] E^*(x_o, z=0) \\ &\times \sqrt{\frac{k}{2\pi i d}} \int dx'_o \exp\left[+i\frac{k}{2d}\left(x'_o - x_d + \epsilon/2\right)^2\right] E(x'_o, z=0). \end{aligned} \tag{3.9}$$

This expression can be simplified to give:

$$\begin{aligned} W(x_d, p_d, z=d) &= \int \frac{d\epsilon}{2\pi} \exp(i\epsilon p) \int dx_o \int dx'_o \frac{k}{2\pi d} \\ &\times \exp\left[-i\frac{k}{2d}\left(x_o^2 - 2x_o x_d - \epsilon(x_o - x_d)\right)\right] E^*(x_o, z=0) \\ &\times \exp\left[+i\frac{k}{2d}\left(x_o'^2 - 2x'_o x_d + \epsilon(x'_o - x_d)\right)\right] E(x'_o, z=0). \end{aligned} \tag{3.10}$$

The integration over ϵ will yield a delta function as

$$\int \frac{d\epsilon}{2\pi} \exp(i\epsilon p) \exp\left[i\frac{k}{2d}\epsilon(x_o + x'_o - 2x_d)\right] = \delta\left(p + \frac{k}{2d}(x_o + x'_o - 2x_d)\right). \tag{3.11}$$

The resulting expression is

$$\begin{aligned} W(x_d, p_d, z=d) &= \tfrac{k}{2\pi d} \int dx_o \int dx'_o \delta\left[p + \frac{k}{d}\left(\frac{x_o + x'_o}{2} - x_d\right)\right] \\ &\times \exp\left[-i\frac{k}{2d}\left(x_o^2 - 2x_o x_d\right)\right] E^*(x_o, z=0) \\ &\times \exp\left[+i\frac{k}{2d}\left(x_o'^2 - 2x'_o x_d\right)\right] E(x'_o, z=0). \end{aligned} \tag{3.12}$$

This expression is more tractable when the following variable transformations are made:

$$\begin{aligned} x_o &= x + \eta/2 \\ x'_o &= x - \eta/2 \end{aligned} \tag{3.13}$$

The Jacobian of this transformation is 1 so it amounts to a simple substitution. With some simplification, Eq. 3.12 can now be written as

$$\begin{aligned} W(x_d, p_d, z=d) &= \frac{k}{2\pi d} \int dx \int d\eta \frac{k}{2\pi d} \delta\left(p + \frac{k}{d}x - \frac{k}{d}x_d\right) \\ &\times \exp\left[-i\frac{k}{d}\eta\left(x - x_d\right)\right] E^*(x + \eta/2, z=0) E(x - \eta/2, z=0). \end{aligned} \tag{3.14}$$

Using the delta function, the x integration can be easily carried out to yield

$$\begin{aligned} W(x_d, p_d, z = d) \;&=\; \int \frac{d\eta}{2\pi} \exp(i\eta p) \\ &\langle E^*(x_d - \frac{d}{k} p + \eta/2, z = 0) E(x_d - \frac{d}{k} p - \eta/2, z = 0)\rangle. \end{aligned} \tag{3.15}$$

The right hand side of Eq. 3.15 can be identified as the Wigner distribution of the field amplitude in the plane $z = 0$ with the spatial variable transformed to $x_d - (d/k)\ p$. Thus the output distribution W' can be written in terms of the input distribution W for the propagation over a distance d as:

$$W'(x_d, p_d, z = d) = W(x_d - \frac{d}{k} p_d, p_d, z = 0) = W(x_o, p_o, z = 0). \tag{3.16}$$

This relation shows that the transverse Wigner distribution in the plane $z = d$ can be written as the same transverse Wigner distribution in the plane $z = 0$ with the spatial argument, x_o, replaced by $x_d - (d/k)\ p$. Alternatively, the Wigner distribution in the plane $z = 0$ ($W(x, p)$) can be viewed as changing its spatial arguments to become $W'(x + (d/k)\ p, p)$ as it propagates to the plane $z = d$. This alternative relation for propagating a Wigner distribution forward can be written as:

$$W(x_o, p_o, z = 0) \Rightarrow W'(x_o + \frac{d}{k} p_o, p_o, z = d) = W'(x_d, p_d, z = d). \tag{3.17}$$

This is an extremely useful means of propagating an optical field. While it appears to propagate via straight line motion akin to ray optics, the Wigner distribution properly accounts for the wave nature of light also. As Eq. 3.16 was derived using Fresnel diffraction, clearly the Wigner distribution includes diffraction effects in its propagation.

3.1.2 Propagation through a lens

For propagation through a lens it can also be shown with Fourier optics that the Wigner distribution is transformed simply through a translation of its arguments. In

Fourier optics, a lens is treated as a phase transformer. The field amplitude after a lens E' can be related to the input field amplitude E by:

$$E'(x) = t(x)E(x). \tag{3.18}$$

Here t represents the thickness function of the lens and serves to introduce a spatially varying phase to the field amplitude. For a lens of focal length f, the thickness function is given in the paraxial approximation by [72]

$$t(x) = \exp\left[ikn\Delta\right] \exp\left[-i\frac{k}{2f}\,x^2\right], \tag{3.19}$$

where k is the optical wavevector, n is the index of refraction of the lens material and Δ is the thickness at the lens center.

The transverse Wigner distribution for the field that has passed through a lens of focal length f can be found by inserting Eq. 3.18 into Eq. 3.1. This gives the Wigner distribution in terms of the input field $E(x)$

$$W(x,p) = \int \frac{d\epsilon}{2\pi} \exp(i\epsilon p)\langle t^*(x+\epsilon/2)E^*(x+\epsilon/2)t(x-\epsilon/2)E(x-\epsilon/2)\rangle. \tag{3.20}$$

Inserting the expression for the thickness function (Eq. 3.19) and simplifying yields

$$W(x,p) = \int \frac{d\epsilon}{2\pi} \exp(i\epsilon p) \exp\left(i\epsilon\frac{k}{f}\,x\right)\langle E^*(x+\epsilon/2)E(x-\epsilon/2)\rangle. \tag{3.21}$$

The right hand side of this equation can be identified as the Wigner distribution of the input field amplitude with the momentum argument shifted to $p + (k/f)\; x$. The Wigner distribution emerging from the lens W' can thus be written as:

$$W'(x,p) = W(x, p + \frac{k}{f}x), \tag{3.22}$$

where W is the Wigner distribution entering the lens. While these results appear to be identical to propagation via ray optics, the Wigner distribution does properly take into account wave effects as this result was obtained by examining the phase of the field. Again, the alternative view could be taken that the Wigner distribution at the lens input $W(x,p)$ is transformed by the lens to become $W'(x, p-(k/f)\ x)$ at the output. This relationship can be written as

$$W(x,p) \Rightarrow W'(x, p - \frac{k}{f}x). \tag{3.23}$$

Using the two simple propagation laws derived in this section: Eq. 3.16 and Eq. 3.22, the Wigner distribution can simply and quickly be traced through any optical system consisting of lenses spaced over arbitrary distances. This approach offers an advantage over using ray optics in that it properly includes all the wave effects as the field propagates. The utility of these laws will be demonstrated in tracing the effects of the imaging systems presented in sections 4.1.1 and 4.1.4.

3.2 Examples of smoothed Wigner distributions

As a demonstration of the characteristics of Wigner distributions, I have measured optical phase space distributions for Gaussian beams with different radii of curvature as well as for a source consisting of two mutually coherent gaussian beams [73]. Optical phase space distributions are a form of smoothed Wigner distributions where the optical (signal) beam of interest is smoothed by convolution with a window of finite resolution. In the case of the heterodyne method, the signal beam is smoothed by the local oscillator (LO) with spatial resolution given by the spatial extent of the LO and momentum resolution given by its diffraction angle. This relationship is derived using Fourier optics in section 4.1.1.

In principle, a smoothed Wigner distribution can be obtained using pinholes, one near the source to determine the position and a second pinhole, widely separated from the first, to determine the momentum. In such a case, the Wigner function of the transmitted light is smoothed by convolution with the Wigner function for the two separated pinholes. For the heterodyne method, the Wigner function for the local oscillator is Gaussian in momentum and position, yielding a minimum uncertainty product. However, the position and momentum resolution cannot be varied independently in either case. The smoothed Wigner distribution is therefore coarse grained and contains less information about the phase and amplitude of the field than the true Wigner distribution. The true Wigner distribution can be determined experimentally by Fourier transforming the two-point coherence function [74], as measured either by shearing interferometry [75], or through tomographic inversion of intensity measurements made in a number of planes [76]. These arrangements offer an advatage in that the position and momentum resolution can be independently controlled but can be difficult to implement experimentally. In cases of practical interest such as the light transmitted through biological materials, the smoothed Wigner distributions obtained by the heterodyne method have sufficient resolution to provide substantial sensitivity to both the coherence and intensity of the transmitted field.

The first example I present to illustrate the properties of Wigner distributions is the elementary case of a Gaussian beam from a coherent source. This is followed by the case of two spatially separated mutually coherent co-propagating beams, an example which nicely illustrates how the smoothed Wigner distribution is sensitive to the coherence properties of the detected light. Finally, as a demonstration of recovery of the true Wigner distribution, I show using Fourier analysis that a measured smoothed Wigner distribution can be deconvoluted to obtain the true Wigner distribution within the limits imposed by the noise present in the measurement.

3.2.1 Measured Smoothed Wigner Distributions for Gaussian Beams

A Gaussian beam has a slowly varying field of the form $\mathcal{E}(x) \propto \exp\left(-x^2/(2w^2) + ikx^2/(2R)\right)$. The corresponding normalized Wigner distribution is given by inserting this field into Equation 3.1

$$W_G(x,p) = \frac{1}{\pi} \exp\left(-\frac{x^2}{w^2}\right) \exp\left[-w^2(p - \frac{kx}{R})^2\right] \tag{3.24}$$

where w is the 1/e intensity width, R is the wavefront radius of curvature and the distribution has been normalized to unity. To illustrate the phase space characteristics of such a distribution, I present measured smoothed Wigner distributions for Gaussian beams with varying radii of curvature. In the examples shown in Figures 3.2-3.4 the signal field is gaussian so $W_S(x,p)$, the corresponding Wigner distribution, takes the form of Eq. 3.24. The Wigner distribution of the signal beam is convoluted with that of the LO beam to yield optical phase space distributions. This relationship is derived rigorously in section 4.1.1. The LO beam is chosen also to be gaussian, positioned so that its waist overlaps with the signal field of interest. Then $W_{LO}(x,p) = W_G(x,p)$ is given by Eq. 3.24 with $w = 380$ μm and $R = \infty$:

$$W_G(x,p) = \frac{1}{\pi} \exp\left(-\frac{x^2}{w^2}\right) \exp\left[-w^2 p^2\right]. \tag{3.25}$$

The signal beam waist and radius of curvature are determined by inserting a lens in the signal path. This focuses the input beam to a waist $w_S = 35$ μm at a distance L behind the signal input plane where the optical phase space distribution is measured. This arrangement is shown in Figure 3.1.

Figure 3.2 shows measured optical phase space contours obtained by scanning the LO center position and center momentum as indicated on the axes of the plot. The momentum is given in units of the optical wave vector p_c/k and thus can be interpreted as the angle relative to the axis of propagation in milliradians. For the

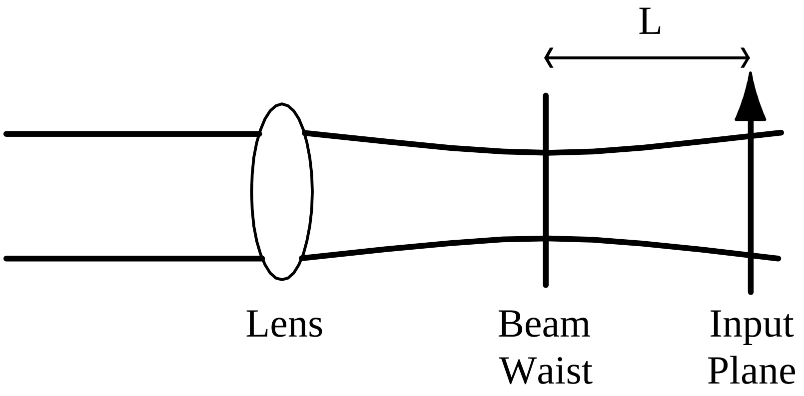

Figure 3.1: Illustration of the distance between the beam waist and input plane.

case where the waist of the signal beam is in the detection plane $(L = 0)$, the optical phase space ellipse has its principal axes oriented vertically and horizontally as in Fig. 3.2. The disparate sizes of the LO and signal beams in this example causes the position width of the distribution to be dominated by the LO width and the momentum width to be dominated by the signal beam. The phase space contours are seen to rotate as the distance L in Fig. 3.1 is changed. The phase space ellipse rotates clockwise (counterclockwise) for $L > 0$ $(L < 0)$ indicating positive (negative) curvature. Figure 3.3 shows the optical phase space distribution for $L = 5$ cm. This distribution is for a diverging beam with a positive radius of curvature, $R > 0$ at the detection plane. The rotation of the phase space ellipse is a simple consequence of the correlation between the momentum and the position for a beam with curvature, as shown in Eq. 3.24. As one would expect for a diverging beam, the mean momentum shifts to the right $(p > 0)$ for the right side of the beam $(x > 0)$. Figure 3.4 shows the distribution for $L = -5$ cm, which corresponds to a converging beam with a negative radius of curvature, $R < 0$. These results clearly demonstrate how the measured optical phase space distributions are sensitive to the spatially varying phase of the field.

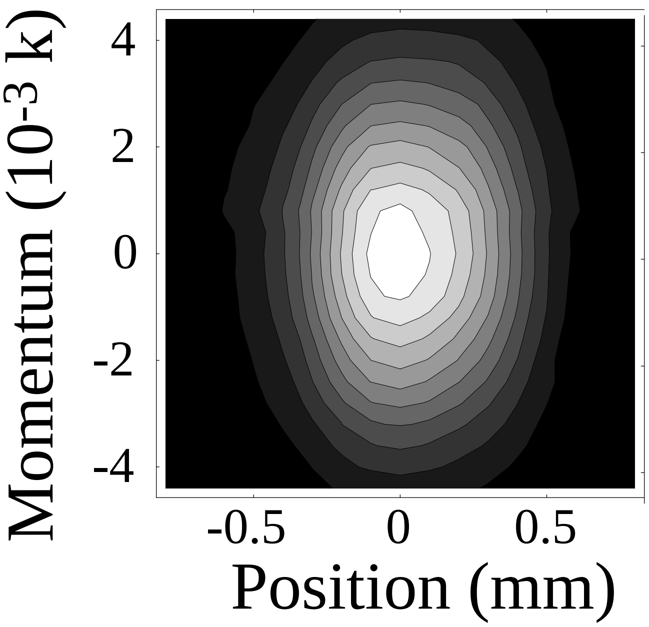

Figure 3.2: Measured smoothed Wigner phase space contours for a Gaussian beam at its beam waist.

Another instructive example of optical phase space contours is the case of two mutually coherent, spatially separated Gaussian beams. The two parallel propagating beams are generated using an interferometer which allows variable spatial separation. A simplified schematic of this interferometer is shown in Figure 3.5. In this arrangement, the output beamsplitter is rotated an angle θ away from 45°, creating two diverging beams. The beams are transformed by a cylindrical lens with its back focus at the face of the output beamsplitter. The result is two parallel propagating focused beams, spatially separated by a distance d, in the detection plane of the imaging system. Here the detection plane is indicated by the lens, L2 (this lens is labelled consistently with the scheme presented in Chapter 4 - Figure 4.1). The Wigner distribution for two focused Gaussian beams separated by a distance d is given by

$$W_S(x,p) = W_G(x-d/2,p) + W_G(x+d/2,p) + 2W_G(x,p)\cos(d\,p+\varphi), \qquad (3.26)$$

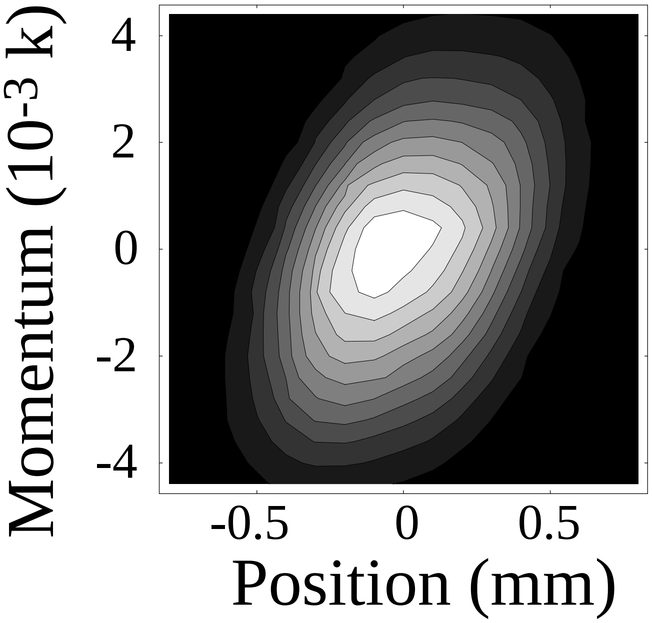

Figure 3.3: Measured smoothed Wigner phase space contours for a diverging Gaussian beam. The radius of curvature is positive here ($R > 0$).

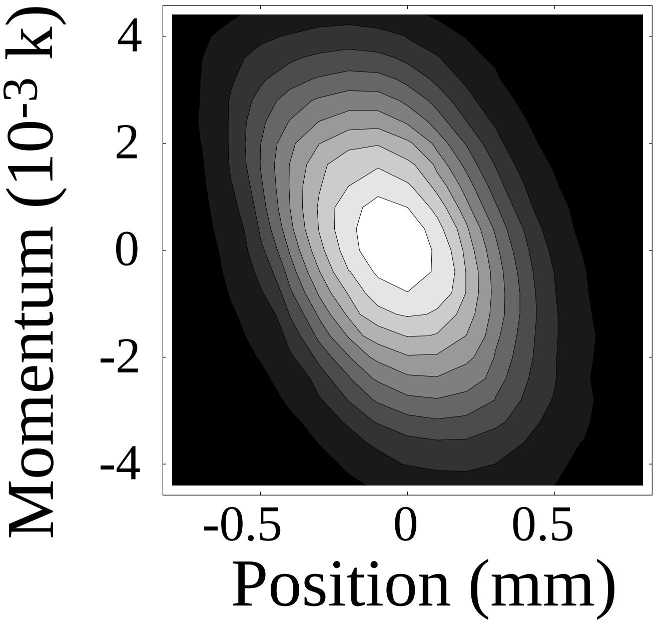

Figure 3.4: Measured smoothed Wigner phase space contours for a converging Gaussian beam. The radius of curvature is negative ($R < 0$).

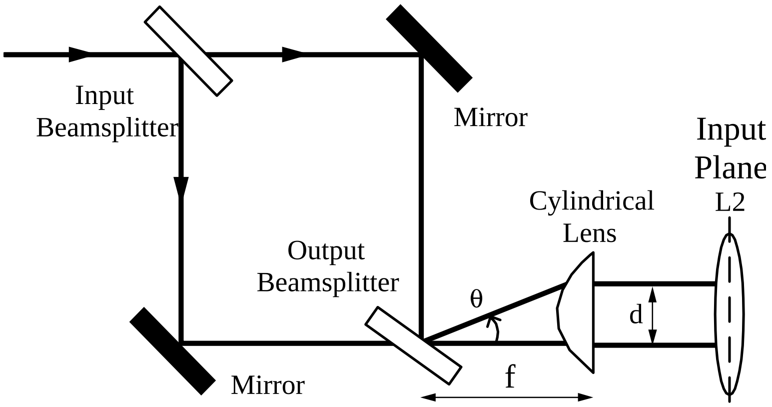

Figure 3.5: Interferometer for generation of two parallel beams spatially separated by a distance d. The output beamsplitter is rotated away from 45° by an angle θ.

where W_G denotes the Wigner distribution for either Gaussian beam at its waist as given by Eq. 3.25. A particularly interesting feature of this distribution is that the cosine term is dominant at $x = 0$ and negative values are obtained as p is varied for a spatial separation d larger than the beam diameter.

Figure 3.6 shows the measured optical phase space contours for two input beams separated by $d = 1$ mm and of 1/e intensity radii of 110 μm. In the central region, the intensity oscillates with nearly 100 percent modulation but remains positive definite as it must [77]. The two-peaked position profile for $p = 0$ is shown in Figure 3.7(A) along with the oscillating momentum profile for $x = 0$ midway between the two intensity peaks in Figure 3.7(B). The solid curve shows the theoretical fit to the momentum distribution with a signal beam 1/e width of 103 μm, which is consistent with diode array measurements within 10 percent.

3.2.2 Deconvolution of Smoothed Wigner Distributions

The measured smoothed Wigner distributions are positive definite as they must be [77]; however, as noted in the introduction to this chapter, the Wigner distribution

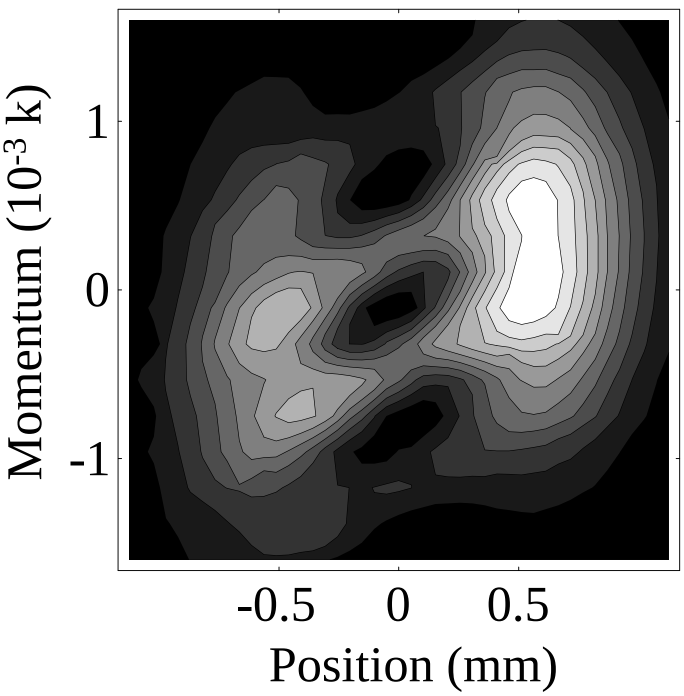

Figure 3.6: Measured smoothed Wigner phase space contours for two spatially separated mutually coherent beams.

itself can be negative. The detected smoothed Wigner distributions are actually convolutions of the Wigner distribution of the signal beam with that of the LO beam. This relationship is derived in detail in Chapter 4 (Eq. 4.20). In principle, one can recover the true Wigner distribution of the signal beam through deconvolution using Fourier transform methods if one knows the form of the Wigner distribution of the LO beam.

The Fourier transform of convolution of two signals is equal to the product of the Fourier transforms of each signal. For two signals $f(t)$ and $g(t)$, we can write

$$\Im\left[f(t) * g\right] = \tilde{f}(\omega)\tilde{g}(\omega), \tag{3.27}$$

where $\Im$ indicates Fourier transformation, $*$ indicates convolution, and $\tilde{f}(\omega)$ $(\tilde{g}(\omega))$ denotes the Fourier transform of $f(t)$ $(g(t))$. The original signal $f(t)$ can be recovered

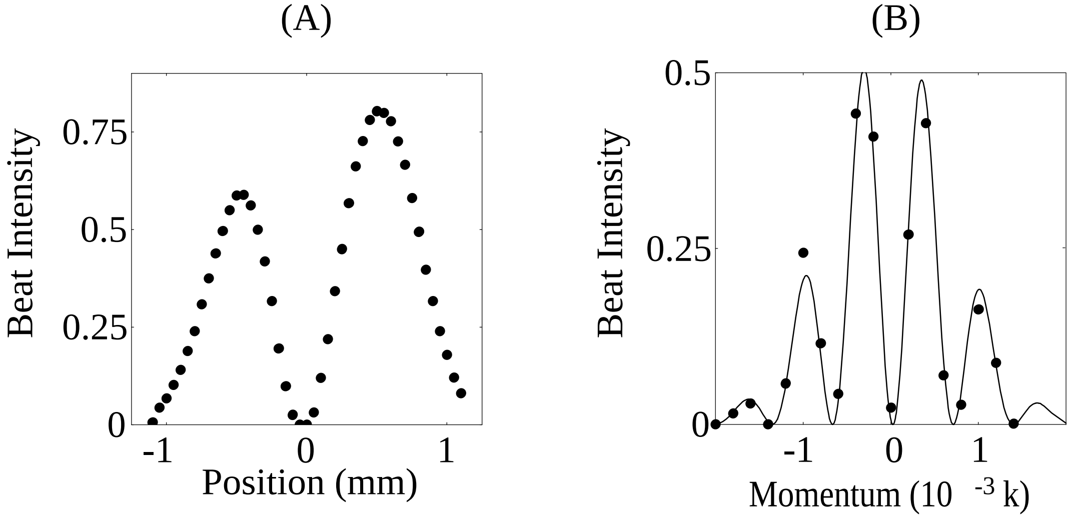

Figure 3.7: Position and momentum profiles for two mutually coherent spatially separated beams. (A) position profile for momentum $p = 0$, (B) momentum profile at position $x = 0$. Dotted curves, data; solid curve, theory.

by Fourier transforming the convoluted signal, dividing by the Fourier transform of the window function $g(t)$ and then inverse Fourier transforming back. This can be written as:

$$f(t) = \Im^{-1}\left[\frac{\Im\left[f(t) * g\right]}{\tilde{g}(\omega)}\right]. \tag{3.28}$$

As an illustration of how this may be done for smoothed Wigner distributions, let us consider once again the case of two mutually coherent spatially separated gaussian beams. This case is particularly interesting because the true Wigner distribution for this beam configuration has negative values. Figure 3.8 shows a measured smoothed Wigner phase space contour for two spatially separated beams. This distribution differs from that shown in Figure 3.6 in that it has improved resolution and signal-to-noise which will improve the deconvolution process. The reduction in noise was accomplished by averaging each point for a longer interval than normal (10 sec vs. 3 sec) which reduces the effects of transient noise introduced as the LO center position

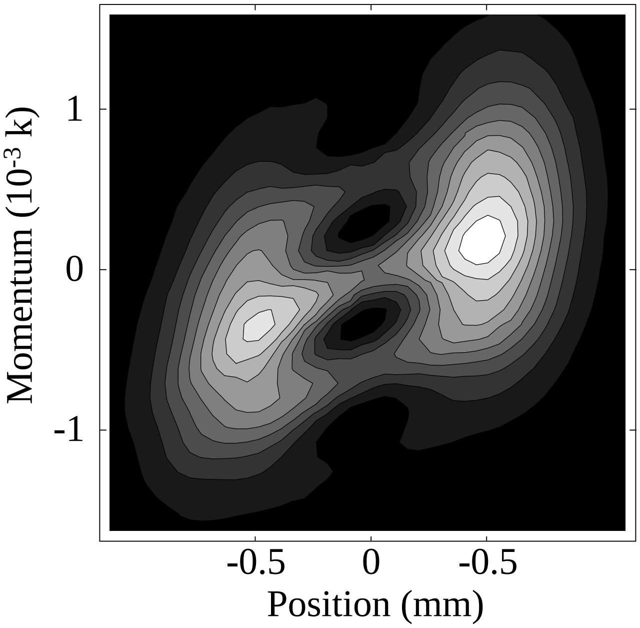

Figure 3.8: Measured smoothed Wigner phase space distribution for two spatially separated beams with improved resolution and signal-to-noise.

and momentum are scanned. In this case we wish to recover the negative Wigner distribution that exists in the region of the signal distribution between the two beams. The smoothed Wigner distribution remains positive here due to the spatial width of the LO beam which causes it to always overlap with both spatially separated beams. In order to see a negative distribution, we must deconvolve the two distributions in position for each profile in momentum. No deconvolution is necessary in momentum because the resolution is already adequate to resolve the fringe at $x = 0$.

We begin the deconvolution process by Fourier transforming the position distribution for each of n measured momentum values:

$$\Im\left[W_{LO}(x, p = p_n) * W_S\right] = \tilde{W}_{LO}(k, p = p_n)\tilde{W}_S(k, p = p_n), \tag{3.29}$$

where x is Fourier transformed into the spatial frequency k. The resulting distribution must then be divided by the Fourier transform of the LO Wigner distribution for each particular momentum value. The form of the LO Wigner distribution is Gaussian in both position and momentum, therefore Fourier transforming the position distribution yields a function that is Gaussian in the spatial wavevector k. This property causes problems in the deconvolution operation as dividing by a Gaussian distribution causes the high spatial wavevectors to be weighted more heavily than the small ones. Thus, high spatial frequency noise degrades the signal when one Fourier transforms the signal back to position space. To overcome this difficulty, a small positive valued constant ϵ is added to the Fourier transform of the LO Wigner distribution which effectively sets the spatial resolution that is recovered. The deconvolved signal Wigner distribution for the momentum component p_n is then given by

$$W_S(x, p = p_n) = \Im^{-1}\left[\frac{\Im\left[W_{LO}(x, p = p_n) * W_S\right]}{\tilde{W}_{LO}(k, p = p_n) + \epsilon}\right]. \tag{3.30}$$

To illustrate the effectiveness of this method, Figure 3.9 shows the momentum profile for $x = 0$ of the smoothed Wigner distribution shown in Figure 3.8 (dotted line) and the recovered Wigner distribution of the signal beam $W_S(x = 0, p)$ (dashed line). The positive constant ϵ used for this deconvolution was set to be $1/e$, effectively setting the spatial resolution to be the $1/e$ spatial width of the LO beam. Reducing this constant, in an effort to improve resolution, introduces noise to the deconvolution process and degrades the recovered distribution.

3.3 Transport equation for the Wigner distribution in free space

In free space, Wigner distributions obey a simple propagation law: The convective derivative is zero. This follows from the wave equation in the slowly varying amplitude approximation. The rigorous connection between the Wigner distribution and the wave equation allows turbid media studies employing the Wigner distribution to be

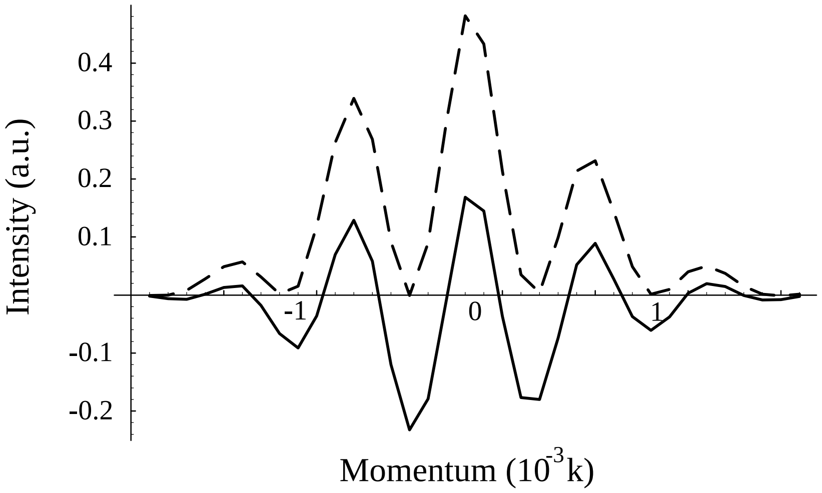

Figure 3.9: Deconvolution of smoothed Wigner distribution of two mutually coherent spatially separated beams. The dashed line is the original smoothed Wigner distribution and the solid line is the momentum profile of the recovered true Wigner distribution for a position halfway in between the two beams.

placed on a firm theoretical footing. As discussed previously, this offers advantages over heuristic treatments which correctly identify the transport of photons as particles but neglect their wave nature. In this section I will derive the transport equation for the Wigner distribution in free space from the wave equation.

I begin with the scalar wave equation for the electric field $E(\vec{x}, t)$

$$\vec{\nabla}_{\vec{x}}^2 E(\vec{x}, t) - \frac{1}{c^2}\frac{\partial^2}{\partial t^2}E(\vec{x}, t) = -\mu_o \frac{\partial^2}{\partial t^2}P(\vec{x}, t). \tag{3.31}$$

In a multiple scattering medium the polarization $P(\vec{x}, t)$ can vary in time and space but it is zero in free space. Thus, the wave equation is written as

$$\vec{\nabla}_{\vec{x}}^2 E(\vec{x}, t) - \frac{1}{c^2}\frac{\partial^2}{\partial t^2}E(\vec{x}, t) = 0. \tag{3.32}$$

Next, I make the approximation that the electric field can be separated into a narrowband frequency and a slowly varying amplitude which I can write as

$$E(\vec{x}, t) = \mathcal{E}(\vec{x}, t)e^{-i\omega t}. \tag{3.33}$$

In this approximate form, ω is the center frequency and $\mathcal{E}$ is the slowly varying field amplitude. Because $\mathcal{E}$ is assumed to vary slowly, its second derivative in time can be taken as zero. Using the slowly varying field approximation, Eq. 3.33 can be inserted into the wave equation (Eq. 3.32) to yield

$$\vec{\nabla}^2_{\vec{x}}\mathcal{E}(\vec{x},t) + \frac{\omega^2}{c^2}\mathcal{E}(\vec{x},t) + \frac{1}{c^2}(2i\omega)\frac{\partial \mathcal{E}(\vec{x},t)}{\partial t} = 0. \tag{3.34}$$

Arranging this into another form and defining $\omega^2/c^2 \equiv k^2$, the time derivative of $\mathcal{E}$ can be written as

$$\frac{\partial \mathcal{E}(\vec{x},t)}{\partial t} = \frac{ic^2}{2\omega}\left(\vec{\nabla}^2_{\vec{x}} + k^2\right)\mathcal{E}(\vec{x},t), \tag{3.35}$$

the wave equation for the slowly varying field amplitude $\mathcal{E}$.

To find the evolution equation for the Wigner distribution I begin by taking the total time derivative of the three dimensional Wigner distribution. Analogous to Eq. 1.2, the three dimensional Wigner distribution is defined by

$$W(\vec{x},\vec{p},t) = \int \frac{d^3\vec{\epsilon}}{(2\pi)^3}\,\exp(i\vec{\epsilon}\cdot\vec{p})\,\mathcal{E}^*(\vec{x}+\vec{\epsilon}/2\,,t)\mathcal{E}(\vec{x}-\vec{\epsilon}/2\,,t), \tag{3.36}$$

where $\vec{x}$ denotes position and $\vec{p}$ is a wavevector (momentum) and the statistical average has been suppressed. Taking its time derivative yields:

$$\begin{aligned}\frac{\partial W(\vec{x},\vec{p},t)}{\partial t} &= \int \frac{d^3\vec{\epsilon}}{(2\pi)^3}\,\exp(i\vec{\epsilon}\cdot\vec{p}) \\ &\times \left(\frac{\partial\,\mathcal{E}^*(\vec{x}+\vec{\epsilon}/2\,,t)}{\partial t}\mathcal{E}(\vec{x}-\vec{\epsilon}/2\,,t) + \mathcal{E}^*(\vec{x}+\vec{\epsilon}/2\,,t)\frac{\partial\mathcal{E}}{\partial t}(\vec{x}-\vec{\epsilon}/2\,,t)\right).\end{aligned} \tag{3.37}$$

The expression for the time derivative of $\mathcal{E}$ (Eq. 3.35) can be inserted into this expression to obtain:

$$\begin{aligned}\frac{\partial W(\vec{x},\vec{p},t)}{\partial t} &= \int \frac{d^3\vec{\epsilon}}{(2\pi)^3}\,\exp(i\vec{\epsilon}\cdot\vec{p})\left(\frac{-ic^2}{2\omega}\right) \\ &\times[\left(\vec{\nabla}^2_{\vec{x}+\vec{\epsilon}/2} + k^2\right)\mathcal{E}^*(\vec{x}+\vec{\epsilon}/2,t)\mathcal{E}(\vec{x}-\vec{\epsilon}/2\,,t) \\ &-\mathcal{E}^*(\vec{x}+\vec{\epsilon}/2\,,t)\left(\vec{\nabla}^2_{\vec{x}-\vec{\epsilon}/2} + k^2\right)\mathcal{E}(\vec{x}-\vec{\epsilon}/2,t)],\end{aligned} \tag{3.38}$$

which reduces to:

$$\begin{aligned}\frac{\partial W(\vec{x},\vec{p},t)}{\partial t} &= \int \frac{d^3\vec{\epsilon}}{(2\pi)^3}\,\exp(i\vec{\epsilon}\cdot\vec{p})\left(\frac{-ic^2}{2\omega}\right) \\ &\times[\left(\vec{\nabla}^2_{\vec{x}+\vec{\epsilon}/2}\mathcal{E}^*(\vec{x}+\vec{\epsilon}/2,t)\right)\mathcal{E}(\vec{x}-\vec{\epsilon}/2\,,t) \\ &-\mathcal{E}^*(\vec{x}+\vec{\epsilon}/2\,,t)\left(\vec{\nabla}^2_{\vec{x}-\vec{\epsilon}/2}\mathcal{E}(\vec{x}-\vec{\epsilon}/2,t)\right)].\end{aligned} \tag{3.39}$$

The term in brackets can be rewritten as the divergence of a current:

$$\begin{aligned}&[\left(\vec{\nabla}^2_{\vec{x}+\vec{\epsilon}/2}\mathcal{E}^*(\vec{x}+\vec{\epsilon}/2,t)\right)\mathcal{E}(\vec{x}-\vec{\epsilon}/2\,,t)-\mathcal{E}^*(\vec{x}+\vec{\epsilon}/2\,,t)\left(\vec{\nabla}^2_{\vec{x}-\vec{\epsilon}/2}\mathcal{E}(\vec{x}-\vec{\epsilon}/2,t)\right)] \\ =\;& \vec{\nabla}_{\vec{x}}\cdot[(\vec{\nabla}_{\vec{x}}\mathcal{E}^*(\vec{x}+\vec{\epsilon}/2,t))\mathcal{E}(\vec{x}-\vec{\epsilon}/2\,,t)-\mathcal{E}^*(\vec{x}+\vec{\epsilon}/2\,,t)\vec{\nabla}_{\vec{x}}\mathcal{E}(\vec{x}-\vec{\epsilon}/2,t)],\end{aligned} \tag{3.40}$$

where $\vec{\epsilon}$ is taken to be a constant so that $\vec{\nabla}_{\vec{x}\pm\vec{\epsilon}/2}=\vec{\nabla}_{\vec{x}}$. Using this expression, the time derivative of W (Eq. 3.39) can be written as

$$\begin{aligned}\frac{\partial W(\vec{x},\vec{p},t)}{\partial t} &= \left(\frac{-ic^2}{2\omega}\right)\vec{\nabla}_{\vec{x}}\cdot\int\frac{d^3\vec{\epsilon}}{(2\pi)^3}\,\exp(i\vec{\epsilon}\cdot\vec{p}) \\ &\times\;[(\vec{\nabla}_{\vec{x}}\mathcal{E}^*(\vec{x}+\vec{\epsilon}/2,t))\mathcal{E}(\vec{x}-\vec{\epsilon}/2\,,t)-\mathcal{E}^*(\vec{x}+\vec{\epsilon}/2\,,t)\vec{\nabla}_{\vec{x}}\mathcal{E}(\vec{x}-\vec{\epsilon}/2,t)].\end{aligned} \tag{3.41}$$

This can be further simplified by making the following substitutions:

$$\vec{\nabla}_{\vec{x}}\mathcal{E}(\vec{x}-\vec{\epsilon}/2,t) = -2\vec{\nabla}_{\vec{\epsilon}}\mathcal{E}(\vec{x}-\vec{\epsilon}/2,t) \tag{3.42a}$$

$$\vec{\nabla}_{\vec{x}}\mathcal{E}^*(\vec{x}+\vec{\epsilon}/2,t) = 2\vec{\nabla}_{\vec{\epsilon}}\mathcal{E}^*(\vec{x}+\vec{\epsilon}/2,t). \tag{3.42b}$$

Using Eq.3.42a and 3.42b, the time derivative of W (Eq. 3.41) now becomes

$$\begin{aligned}\frac{\partial W(\vec{x},\vec{p},t)}{\partial t} &= \left(\frac{-ic^2}{\omega}\right)\vec{\nabla}_{\vec{x}}\cdot\int\frac{d^3\vec{\epsilon}}{(2\pi)^3}\,\exp(i\vec{\epsilon}\cdot\vec{p}) \\ &\times[(\vec{\nabla}_{\vec{\epsilon}}\mathcal{E}^*(\vec{x}+\vec{\epsilon}/2,t))\mathcal{E}(\vec{x}-\vec{\epsilon}/2\,,t)+\mathcal{E}^*(\vec{x}+\vec{\epsilon}/2\,,t)\vec{\nabla}_{\vec{\epsilon}}\mathcal{E}(\vec{x}-\vec{\epsilon}/2,t)],\end{aligned} \tag{3.43}$$

which can be rewritten as

$$\frac{\partial W(\vec{x},\vec{p},t)}{\partial t} = \left(\frac{-ic^2}{\omega}\right)\vec{\nabla}_{\vec{x}}\cdot\int\frac{d^3\vec{\epsilon}}{(2\pi)^3}\,\exp(i\vec{\epsilon}\cdot\vec{p})\vec{\nabla}_{\vec{\epsilon}}(\mathcal{E}^*(\vec{x}+\vec{\epsilon}/2,t)\mathcal{E}(\vec{x}-\vec{\epsilon}/2\,,t)). \tag{3.44}$$

The integral can be carried out via integration by parts subject to the boundary condition that $\mathcal{E}(\vec{x} \pm \vec{\epsilon}/2\,,t)$ goes to zero as $\vec{\epsilon}$ goes to infinity. The result of this integration yields

$$\frac{\partial W(\vec{x},\vec{p},t)}{\partial t} = \left(\frac{-ic^2}{\omega}\right) \vec{\nabla}_{\vec{x}}\cdot(-i\vec{p}) \int \frac{d^3\vec{\epsilon}}{(2\pi)^3} \exp(i\vec{\epsilon}\cdot\vec{p})\mathcal{E}^*(\vec{x}+\vec{\epsilon}/2,t)\mathcal{E}(\vec{x}-\vec{\epsilon}/2\,,t). \tag{3.45}$$

By employing the definition of the three dimensional Wigner distribution (Eq. 3.36) and simplifying, this becomes

$$\frac{\partial W(\vec{x},\vec{p},t)}{\partial t} = \frac{-c^2}{\omega}\vec{p}\cdot \vec{\nabla}_{\vec{x}} W(\vec{x},\vec{p},t). \tag{3.46}$$

This can be further simplified by using the relation $\omega = ck$, where the wavevector $k = |\vec{p}|$. Equation 3.46 now can be written as

$$\frac{\partial W(\vec{x},\vec{p},t)}{\partial t} = -c\,\hat{p}\cdot \vec{\nabla}_{\vec{x}} W(\vec{x},\vec{p},t). \tag{3.47}$$

Using the fact that $c\hat{p}$ is simply the velocity, the expression for the evolution of the Wigner distribution in free space can be written as

$$\frac{\partial W(\vec{x},\vec{p},t)}{\partial t} + \vec{\mathrm{v}}\cdot \vec{\nabla}_{\vec{x}} W(\vec{x},\vec{p},t) = 0. \tag{3.48}$$

This expression shows that the convective derivative of W is equal to zero for free space propagation. It gives the straight line propagation of the arguments as discussed above. This transport equation can be interpreted as the conservation of the total phase space density in free space.

3.4 Summary

This chapter has illustrated the basic properties and utility of the Wigner distribution. The examples of measured smoothed Wigner distributions shown here were obtained using the heterodyne imaging system presented in the next chapter. In addition, the next chapter derives in detail the relationship between the Wigner distributions and optical phase space distributions. This link is important as it allows light scattering studies based on optical phase space distributions to be treated using the language of Wigner distributions as will be shown in later chapters.

Chapter 4

Experimental Setup

In this chapter, I will describe a simple optical heterodyne technique that we have developed for directly measuring smoothed Wigner phase space distributions as optical phase space contour plots with high dynamic range. The experimental scheme presented is initially implemented for a coherent light source and further modified for a low-coherence-length light source. Particular aspects of each configuration are discussed. The smoothed Wigner distributions obtained with this setup are always positive definite [77] but the true Wigner distribution of the signal field can be recovered through deconvolution within the resolution imposed by the noise in the system as shown in section 3.2.2.

The first section of this chapter provides an overview of the scheme of the heterodyne imaging system. Included in this section is a discussion that relates the detected signal to the Wigner distributions for the signal and local oscillator (LO) fields. Also included are the corrections needed to use a low coherence source, a brief discussion on the consequences of using a thick imaging lens, and the modifications made to the system to examine light backscattered from a turbid sample. This section is concluded with a description of the motion control system used to scan the various elements that dictate the phase space detection parameters. The second section of the chapter presents the detection apparatus used in the heterodyne imaging system. Included in this section are descriptions of the various components used to convert the optical signals to the recorded electronic voltages. I begin the description of the experimental setup by describing the heterodyne imaging system.

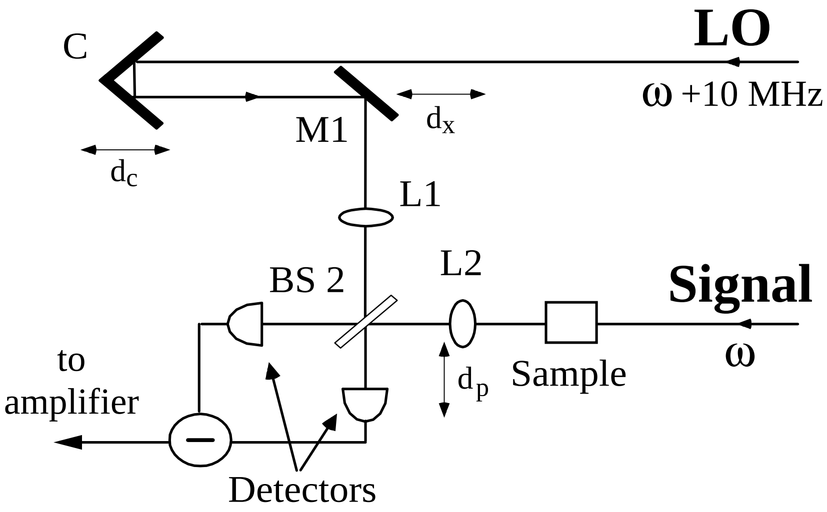

Figure 4.1: Scheme of heterodyne imaging system for measuring optical phase space distributions.

4.1 Heterodyne imaging system

The imaging scheme of the heterodyne experiments shown in Fig. 4.1 employs either a coherent or a low-coherence-source. The beam from the source is split into a local oscillator (LO) and a signal beam which is input to the sample. The relative frequency between the LO and the signal beam are determined by acousto-optic modulators that differ in drive frequency by 10 MHz. The signal beam is mixed with the LO at a 50-50 beam splitter (BS2). The two outputs from the beamsplitter are monitored using photodiode detectors. Technical noise is suppressed by employing a standard balanced detection system [78]. In such a configuration, the photodiodes are connected so as to subtract their photocurrents. As the heterodyne signal undergoes a 180° phase shift upon reflection by the beam splitter, the beat signals from the two outputs of the beamsplitter add together.

The beat signal at 10 MHz is amplified then measured with an analog spectrum analyzer. The spectrum analyzer measures the root mean square of the electronic signal. This signal consists of the sums of squares of voltages arising from the heterodyne beat signal and noise present in the detection system

$$V_{RMS} = \sqrt{V_B^2 + V_{Noise}^2}. \tag{4.1}$$

An important feature of the experiments is that the analog output of the spectrum analyzer, which is proportional to V_{RMS}, is squared using a low noise multiplier [79]. The multiplier output is fed to a lock-in amplifier that subtracts the mean square signal and noise voltages with the signal beam on and off [80]. In this way, the mean square electronic noise and LO shot noise are subtracted in real time, and the lock-in output is directly proportional to the *mean square* beat amplitude $|V_B|^2$. In the next section, I will show that the mean square beat signal is directly proportional to the overlap of the Wigner phase space distributions for the local oscillator and signal fields at the input lenses L1 and L2 [73].

4.1.1 Measurement of Smoothed Wigner Distributions

The beat amplitude V_B is determined in the paraxial ray approximation by the spatial overlap of the local oscillator (LO) and signal (S) fields in the plane of the detector, $z = z_D$ [81–84] and is given by

$$V_B = \int dx' \mathcal{E}_{LO}^*(x', z_D)\mathcal{E}_S(x', z_D), \tag{4.2}$$

where x' denotes the transverse position in the detector plane with the corresponding y integration suppressed. In this expression, $\mathcal{E}$ is the field amplitude with the band center frequency phase factor removed. The LO center position can be varied by scanning the mirror M1 (Fig. 4.1). When M1 is translated off-axis a distance d_x, the LO field has its spatial argument shifted to give

$$V_B(d_x) = \int dx' \mathcal{E}_{LO}^*(x' - d_x, z_D)\mathcal{E}_S(x', z_D). \tag{4.3}$$

In order to keep the LO beam physically on the detector while d_x is varied, the detector plane is located in the focal planes of the input achromatic lenses, L1 and L2.

Using Fourier optics, the fields in the detector plane can be related to the fields in the source planes ($z = 0$) of lenses L1 and L2, which have equal focal lengths $f = 6$ cm. After passing through their respective lens, the LO and signal fields each acquire a spatially varying phase as given by Eq.'s 3.18 and 3.19

$$\begin{aligned} \mathcal{E}'_{LO}(x - d_x, z &= 0) = \exp\left[-i\frac{k}{2f}x^2\right]\mathcal{E}_{LO}(x - d_x, z = 0), && (4.4a) \\ \mathcal{E}'_S(x, z &= 0) = \exp\left[-i\frac{k}{2f}x^2\right]\mathcal{E}_S(x, z = 0). && (4.4b) \end{aligned}$$

When the input lens L2 (Fig. 4.1) is translated off axis by a distance d_p, the spatially varying phase acquired by the signal field (Eq. 4.4b) is altered and the field emerging from lens L2 becomes:

$$\mathcal{E}'_S(x, z = 0) = \exp\left[-i\frac{k}{2f}(x - d_p)^2\right]\mathcal{E}_S(x, z = 0). \tag{4.5}$$

The fields in the planes of the detectors can now be calculated using Equation 3.7 to propagate the fields a distance $d = f$. The fields in the detector plane are

$$\begin{aligned} \mathcal{E}_{LO}(x' - d_x, z_D) &= \sqrt{\frac{k}{2\pi i f}}\int dx \exp\left[i\frac{k}{2f}(x - x')^2\right] && (4.6a) \\ &\times \exp\left[-i\frac{k}{2f}x^2\right]\mathcal{E}_{LO}(x, z = 0), \\ \mathcal{E}_S(x', z_D) &= \sqrt{\frac{k}{2\pi i f}}\int dx \exp\left[i\frac{k}{2f}(x - x')^2\right] && (4.6b) \\ &\times \exp\left[-i\frac{k}{2f}(x - d_p)^2\right]\mathcal{E}_S(x, z = 0). \end{aligned}$$

The quadratic phases that depend on x^2 cancel in these expressions because the detector plane is in the focal plane of the lenses, L1 and L2. Canceling these terms in Eq.'s 4.6a and 4.6b yields

$$\begin{aligned}\mathcal{E}_{LO}(x'-d_x,z_D) &= \sqrt{\frac{k}{2\pi i f}}\exp\left[-i\frac{k}{2f}\,x'^2\right] \qquad (4.7a)\\ &\times \int dx\exp\left[i\frac{k}{2f}xx'\right]\mathcal{E}_{LO}(x,z=0),\\ \mathcal{E}_S(x',z_D) &= \sqrt{\frac{k}{2\pi i f}}\exp\left[-i\frac{k}{2f}\,(x'^2-d_p^2)\right] \qquad (4.7b)\\ &\times \int dx\exp\left[i\frac{k}{2f}x(x'-d_p)\right]\mathcal{E}_S(x,z=0).\end{aligned}$$

Inserting these expressions into Eq. 4.3, the quadratic phases in x' cancel, leaving:

$$\begin{aligned}V_B(d_x,d_p) &= \frac{k}{2\pi f}\exp\left[i\frac{k}{2f}d_p^2\right]\int dx'\int dx_1\exp\left[-i\frac{k}{f}x_1x'\right]\mathcal{E}^*_{LO}(x_1,z=0)\\ &\times \int dx_2\exp\left[i\frac{k}{f}x_2(x'-d_p)\right]\mathcal{E}_S(x_2,z=0). \qquad (4.8)\end{aligned}$$

Carrying out the integration over x' yields a delta function as

$$\int dx'\exp\left[-i\frac{k}{f}x'(x_1-x_2)\right] = 2\pi\delta(x_1-x_2). \qquad (4.9)$$

Thus, equation 4.8 can now be written as

$$\begin{aligned}V_B(d_x,d_p) &= \frac{k}{f}\exp\left[i\frac{k}{2f}d_p^2\right]\int dx_2\exp\left[-i\frac{k}{f}(x_2d_p)\right]\mathcal{E}_S(x_2,z=0) \qquad (4.10)\\ &\times \int dx_1\mathcal{E}^*_{LO}(x_1-d_x,z=0)\delta(x_1-x_2).\end{aligned}$$

The integration over x_1 can now be carried out simply to yield:

$$\begin{aligned}V_B(d_x,d_p) &= \frac{k}{f}\exp\left[i\frac{k}{2f}d_p^2\right]\int dx_2\exp\left[-i\frac{k}{f}(x_2d_p)\right] \qquad (4.11)\\ &\times \; \mathcal{E}^*_{LO}(x_2-d_x,z=0)\,\mathcal{E}_S(x_2,z=0).\end{aligned}$$

Rearranging this expression and taking its magnitude squared, yields the mean square beat amplitude for a narrowband field

$$|V_B(d_x,d_p)|^2 \propto \left|\int dx\,\mathcal{E}^*_{LO}(x-d_x,z=0)\,\mathcal{E}_S(x,z=0)\,\exp(-ik\frac{d_p}{f}x)\right|^2. \qquad (4.12)$$

Here x replaces x_2 and denotes position in the source plane. The effects of lens thickness on the location of the source plane are discussed in section 4.1.3. For simplicity, the corresponding y integrals are suppressed as is the statistical average. For a coherent source, it is reasonable to assume that the Rayleigh and coherence lengths of the LO and signal fields are large compared to d_x, so that the translation of M1 simply shifts the center of the input LO field without significantly altering the LO optical path length prior to L1. When this is not the case, a translating corner cube (C in Fig. 4.1) can be added to the LO arm to compensate for path length changes arising from translating M1. The phase factor due to the translation of L2 is neglected in Equation 4.12 but the additional phase requires the use of additional path length compensation when a low coherence source is used, the specific corrections are detailed in the next section (4.1.2).

The mean square heterodyne beat signal as given by Equation 4.12 easily can be shown to be the convolution of the Wigner distribution of the signal field with that of the LO. I begin by explicitly writing out the magnitude squared of the detected signal

$$\begin{aligned} |V_B(d_x,d_p)|^2 \;\propto\; & \int dx\, \mathcal{E}^*_{LO}(x-d_x,z=0)\, \mathcal{E}_S(x,z=0)\, \exp(-ik\frac{d_p}{f}x) \\ \times\; & \int dx'\, \mathcal{E}_{LO}(x'-d_x,z=0)\, \mathcal{E}^*_S(x',z=0)\, \exp(+ik\frac{d_p}{f}x'). \end{aligned} \tag{4.13}$$

The following variable transformations are made:

$$\begin{aligned} x &= x_o + \eta/2, \\ x' &= x_o - \eta/2. \end{aligned} \tag{4.14}$$

The Jacobian of this transformation is 1 so it amounts to a simple substitution. The beat signal can be written in terms of these variables as

$$\begin{aligned} |V_B(d_x,d_p)|^2 \;\propto\; & \int dx_o \int d\eta\, \mathcal{E}^*_{LO}(x_o+\eta/2-d_x)\, \mathcal{E}_{LO}(x_o-\eta/2-d_x) \\ \times\; & \mathcal{E}^*_S(x_o-\eta/2)\, \mathcal{E}_S(x_o+\eta/2)\, \exp(-ik\frac{d_p}{f}\eta). \end{aligned} \tag{4.15}$$

For simplicity, the notation that the LO and signal fields are in the source plane ($z = 0$) has been dropped. Recalling the definition of the Wigner distribution (Eq.1.2),

$$W(x,p) = \int \frac{d\epsilon}{2\pi} \exp(i\epsilon p) \langle \mathcal{E}^*(x+\epsilon/2)\mathcal{E}(x-\epsilon/2)\rangle, \tag{4.16}$$

from Chapter 1, I note that it is the Fourier transform of the two point coherence function. Thus the inverse transform is given by

$$\mathcal{E}^*(x+\epsilon/2)\mathcal{E}(x-\epsilon/2) = \int dp \exp(-i\epsilon p) W(x,p). \tag{4.17}$$

Using this definition to replace the signal fields in Eq. 4.15, the beat signal becomes

$$\begin{aligned} |V_B(d_x,d_p)|^2 \;\; &\propto \;\; \int dx_o \int d\eta \, \mathcal{E}^*_{LO}(x_o+\eta/2-d_x)\, \mathcal{E}_{LO}(x_o-\eta/2-d_x) \qquad (4.18) \\ &\times \int dp \exp(-i\eta p) W_S(x,p) \exp(-ik\frac{d_p}{f}\eta). \end{aligned}$$

Again using the definition of the Wigner distribution (Eq. 4.16), the LO Wigner distribution can be written as

$$\begin{aligned} W_{LO}(x-d_x, p+k\frac{d_p}{f}) \;\; &= \;\; \int \frac{d\eta}{2\pi} \exp\left[i\eta(p+k\frac{d_p}{f})\right] \qquad (4.19) \\ &\times \;\; \mathcal{E}^*_{LO}(x_o+\eta/2-d_x)\, \mathcal{E}_{LO}(x_o-\eta/2-d_x). \end{aligned}$$

Using this expression for the Wigner distribution of the LO in Eq. 4.18, the mean square heterodyne beat signal (Eq. 4.12) can now be rewritten (again suppressing the y integration) as

$$|V_B(d_x,d_p)|^2 \propto \int dx\, dp\, W_{LO}(x-d_x, p+\frac{k}{f}d_p)\, W_S(x,p), \tag{4.20}$$

where $W_S(x,p)$ is the Wigner distribution of the signal field in the plane of L2 ($z = 0$), given by Eq. 4.16, and $W_{LO}(x,p)$ is the LO Wigner distribution in the plane of L1.

Equation 4.20 shows that the mean square beat signal is the convolution integral of the LO and signal field Wigner phase space distributions. Hence, the optical phase space distributions measured in the experiments are smoothed Wigner distributions [77]. Scanning the positions of M1 by d_x and L2 by d_p using stepper translators yields an optical phase space contour map of W_S with resolution limited in position by the LO diameter and in momentum by the LO diffraction angle. This method permits position measurement over a range ±1 cm, and momentum measurement over a range ±300 mrad. Including both transverse dimensions (x and y) the mean square beat signal S can be rewritten as

$$S(d_x\hat{x}, d_p\hat{x}) = \int d^2\vec{x}_\perp\, d^2\vec{p}_\perp\, W_{LO}(\vec{x}_\perp - d_x\hat{x}, \vec{p}_\perp + \frac{k}{f}d_p\hat{x})\, W_S(\vec{x}_\perp, \vec{p}_\perp). \tag{4.21}$$

Here, the subscript $\perp$ denotes the direction perpendicular to the propagation axis. The transverse Wigner distribution at the exit of the sample ($z = L$) is given in terms of the three dimensional Wigner distribution by

$$W_S(\vec{x}_\perp, \vec{p}_\perp) = \int dp_z\, W_S(z = L, \vec{x}_\perp, \vec{p}). \tag{4.22}$$

Recalling Eq. 3.36, the three dimensional Wigner distribution is defined by

$$W(\vec{x}, \vec{p}, t) = \int \frac{d^3\vec{\epsilon}}{(2\pi)^3}\, \exp(i\vec{\epsilon}\cdot\vec{p})\, \mathcal{E}^*(\vec{x} + \vec{\epsilon}/2\,, t)\mathcal{E}(\vec{x} - \vec{\epsilon}/2\,, t), \tag{4.23}$$

where $\vec{x}$ denotes position and $\vec{p}$ is a wavevector (momentum).

The transverse Wigner distributions that appear in Eq. 4.20 have an important property. Since, the transverse momentum $\vec{p}_\perp$ is conserved in propagation between media of different indices of refraction, the transverse Wigner distribution does not change in propagating between the sample and the air. This is a consequence of the boundary condition that yields Snell's law: the momentum in the plane of the interface is conserved although the magnitude of the total momentum vector changes. Hence, the angles of incidence and refraction must be different. The change in angle must be included when analyzing Wigner distributions which have propagated from inside the sample cell to air before being detected.

4.1.2 Corrections for Low Coherence Source

When a low-coherence source is used in the heterodyne imaging system, the LO and signal optical paths must be equal to within the coherence length of the source. In order to equalize the path lengths, a corner cube (C in Fig. 4.1) is included to allow the LO path length to be varied relative to that of the signal beam. Moving the corner cube by a distance d_c, changes the LO path length by $\Delta l = 2d_c$.

As described in the previous section, when an optical phase space distribution is measured, the position and effective momentum of the LO are scanned by moving optical elements. Moving these elements introduces small changes in the relative path lengths of the two beams. These path length changes are compensated by adjusting the LO path length to keep the difference between the two beam paths at a constant fixed value, $\Delta l'$.

To calculate the corrections needed for using a low coherence length source, the arguments used in the previous section must be modified to include the broad range of frequencies that are present. This is accomplished by expressing the light field as a sum over its Fourier components $\omega_k = ck/n_o$

$$\mathbf{E}(\mathbf{x},t) = \int d\omega_k \mathcal{E}_k(\mathbf{x}_\perp, z) e^{-i\omega_k(t-z/c)} \tag{4.24}$$

where the $\mathcal{E}_k$'s are the slowly varying amplitude of the frequency component ω_k. It is assumed that the $\mathcal{E}_k$'s are delta-correlated such that $\langle \mathcal{E}_k^* \mathcal{E}_{k'} \rangle$ is only nonzero for $\omega_k = \omega_{k'}$. The heterodyne beat can be written using this definition of the field as

$$\begin{aligned} V_B &= \int dx' \, \mathbf{E}_{LO}^*(x', z_D) \, \mathbf{E}_S(x', z_D) && \text{(4.25a)} \\ &= \int dx' \int d\omega_k \mathcal{E}_{k_{LO}}^*(x, z_D) e^{i\omega_k(t-z/c-\Delta l/c)} && \text{(4.25b)} \\ &\times \int d\omega_k' \mathcal{E}_{k_S'}(x, z_D) e^{-i\omega_k'(t-z/c)}, \end{aligned}$$

where x', is in the plane of the detector $z = z_D$. In this expression, the corresponding y integration has been suppressed as well as the statistical average. The correlation of the $\mathcal{E}_k$'s allows the double integral over LO and signal beam frequencies to be reduced to a single integral. Once this correlation is assumed the common phase factors can be eliminated, leaving only $e^{-i\omega_k \Delta l/c}$, the phase factor due to the variable delay introduced in the LO path. Thus the expression for the heterodyne beat in the plane of the detectors is

$$V_B = \int dx' \int d\omega_k \mathcal{E}^*_{k_{LO}}(x, z_D) \mathcal{E}_{k_S}(x, z_D) e^{-i\omega_k \Delta l/c}. \tag{4.26}$$

Similar to the derivation in the previous section, the fields in the plane of the detectors can be related to the field in the source plane ($z = 0$) of the input lenses, L1 and L2 (Figure 4.1), by using Fourier optics methods. The resulting expression differs from Eq. 4.12 only in that the phase factors now can no longer be neglected. The mean square beat amplitude using light from a low coherence source is thus:

$$\begin{aligned} |V_B(d_x, d_p, \Delta l)|^2 \;\; &\propto \;\; |\int dx' \int d\omega_k \mathcal{E}^*_{k_{LO}}(x' + d_x, z = 0) e^{-i\omega_k \Delta l/c}\, \mathcal{E}_{k_S}(x', z = 0) \\ &\times \exp(-ik \frac{d_p^2}{2f_o}) \exp(ik \frac{d_p}{f_o} x')|^2. \end{aligned} \tag{4.27}$$

In this expression there are two additional phase factors that are direct consequences of moving lens L2. Each of these phase factors has a physical interpretation (Figure 4.2). The first term, $\exp(-ik\, d_p^2 \,/\, 2f_o)$ represents the phase acquired by the signal beam as it propagates an additional path length relative to the LO from lens L2 to the detector. In Figure 4.2(A) we see that when L2 is moved a distance d_p and the detected signal field remains on axis ($x = 0$), the detected light travels along path $\overline{BD}$ where D represents the position of the detector. Light traveling along $\overline{BF}$ has travelled a distance f_o, as will any light propagating from the plane of a lens to its focal point. The difference between paths $\overline{BD}$ and $\overline{BF}$ is simply $f_o(1 - \cos\theta) \approx f_o\theta^2/2$.

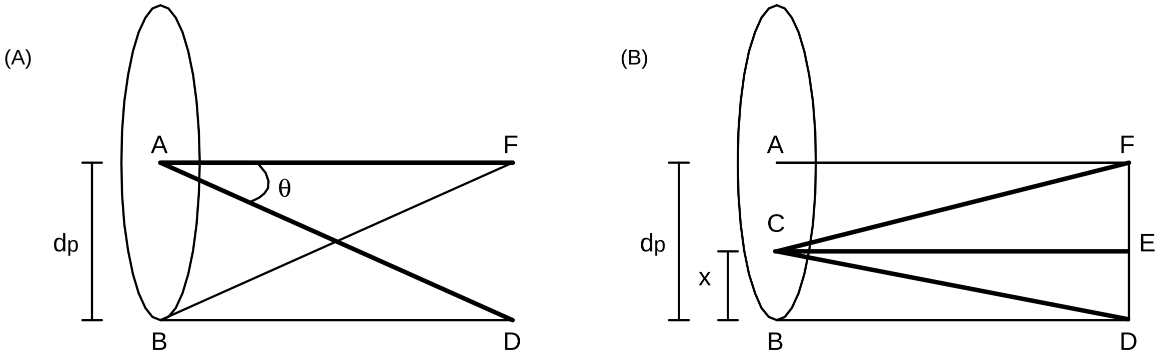

Figure 4.2: Physical meaning of correction terms: (A) Term 1: $d_p^2/\ 2f_o$ (B) Term 2: xd_p/f_o.

Since the LO path length is also f_o (L1 is not translated), the detected light ($\overline{BD}$) has travelled a distance $\theta^2 f_o/2 = d_p^2/\ 2f_o$ less than the LO, effectively increasing the LO path.

The second term, $\exp(ikd_p x/f_o)$, represents the change in distance travelled by off axis light ($x \neq 0$) when lens L2 is moved a distance d_p. In Figure 4.2(B), the light is detected along $\overline{CD}$ and path $\overline{CF}$ is of length f_o. Using the Pythagorian theorem, the length $\overline{CD} = f_o\sqrt{(1 - d_p^2/f_o^2 + 2xd_p/f_o^2)}$ which can be approximated as $\overline{CD} \approx f_o - d_p^2/2f_o + xd_p/f_o$. Thus the path length difference between the LO path $\overline{CF} = f_o$ and the signal path $\overline{CD}$, is $d_p^2/2f_o - xd_p/f_o$. These factors are both included as corrections to keep the path difference between the two beams constant when optical phase space measurements are made. In turbid media studies, the signal beam undergoes multiple scatterings before being detected, causing it to be much broader in both position and momentum than the LO beam. In this case the position of the LO, d_x, can be substituted into the correction term and the effective path difference between the beams is given by:

$$\Delta l' = \Delta l + \frac{d_p^2}{2f_o} - \frac{d_x d_p}{f_o}. \tag{4.28}$$

This is the quantity that must be kept constant to ensure that the path length difference between the LO and signal beams remains fixed as optical phase space measurements are made in turbid media studies. This correction term must be modified slightly when the LO and signal beams are of comparable diameters as is the case in the beam characterization studies presented in Chapter 5. The modification depends on the specific form of the $\mathcal{E}_k$'s and simply introduces a scaling factor to the last term in equation 4.28.

The heterodyne beat signal can now be written in terms of the overlap between the complex amplitude of the signal field and that of an effective LO field:

$$|V_B(d_x, d_p, \Delta l')|^2 \propto |\int dx' \int d\omega_k \mathcal{E}'^{*}_{k_{LO}}(x' + d_x, \Delta l', d_p)\, \mathcal{E}_{k_S}(x', z = 0)|^2. \tag{4.29}$$

In this expression, the complex amplitude of the effective LO field is defined as

$$\begin{aligned} \mathcal{E}'^{*}_{k_{LO}}(x' + d_x, \Delta l', d_p) &= \mathcal{E}^{*}_{k_{LO}}(x' + d_x, z = 0) e^{-i\omega_k \Delta l/c} \\ &\times \exp(-ik\frac{d_p^2}{2f_o}) \exp(ik\frac{d_p}{f_o}x'), \end{aligned} \tag{4.30}$$

where $\mathcal{E}_{k_{LO}}$ is the complex amplitude of the frequency component of the LO field, $\omega_k = ck_{LO}$ as defined by Eq. 4.24. The effective LO field specifies the transverse profile of the LO field and includes all the phase factors introduced by the shifts d_x, d_p, and $\Delta l'$. Starting with Eq. 4.29 an expression for the heterodyne beat can now be given as the overlap of two wigner distributions:

$$\begin{aligned} |V_B(d_x, d_p, \Delta l')|^2 &= \int d\omega_k \int dx \int dp\, W_S(x, z_o, \omega_k) \\ &\times W'_{LO}(x + d_x, z_o + \Delta l'; p + k\frac{d_p}{f_o}, \omega_k). \end{aligned} \tag{4.31}$$

Here W'_{LO} is the Wigner distribution of the frequncy component of the effective LO field, ω_k and W_S is that of the signal field. This form is useful because the Wigner distribution for the signal field emerging from a turbid medium can be calculated in many practical situations. However, using the Wigner distribution for the signal field to calculate the detected signal can be problematic when using a low coherence source. This is due to the fact that to calculate the Wigner distribution for a given field (Eq. 4.16), the field must be correlated with itself. A heterodyne beat, on the otherhand, is truly a correlation between the LO and signal fields. Thus, in order to rigorously incorporate the effect of an LO path delay $\Delta l'$, the optical phase space distribution must be calculated using fields as in Equation 4.29.

4.1.3 Thick Achromatic Lenses

The achromatic lenses used for imaging in the heterodyne scheme (L1, L2 in Fig. 4.1) are thick lenses. The Melles Griot catalog specifies the thickness of the 01 LAO 079 Achromats as 12.5 mm at their centers. Thus the detection plane cannot be assumed to be at the center as if it were a thin lens. Instead, one must use the principal plane to determine the detection plane. When using a thick lens, the object and image distances are measured from the front and back principal planes respectively, H and H' respectively [85].

Figure 4.3 shows that although a turbid sample can be placed extremely close to the imaging lens, the transmitted light still propagates a distance d from the sample to the front principal plane. Although this distance is small, it must still be accounted for in theoretical treatments. Typical sample cell to lens distances are 1-2 mm. For the lenses used in my experiments, the distance between the input face of the lens and the front principal plane is specified as 1.6 mm. Thus, the total distance d between the lens and sample is 1-2 mm in air plus 1.6 mm in glass.

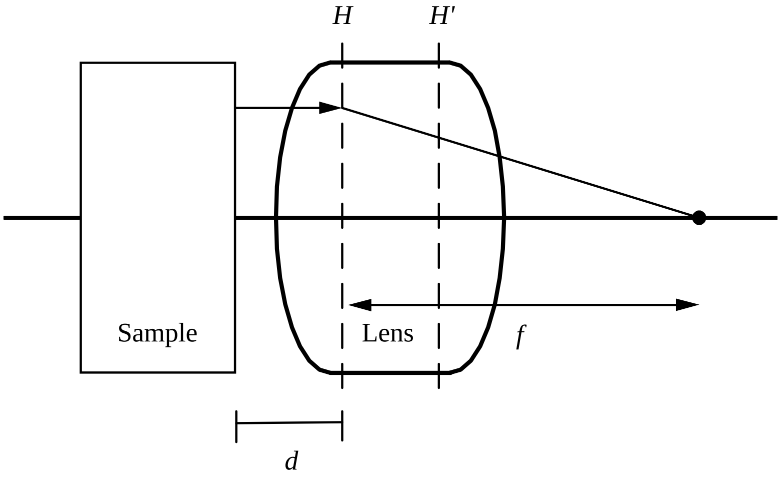

Figure 4.3: Front and back principal planes for a thick lens H and H'. It is assumed that a single refraction occurs in the front principal plane for rays travelling left to right. Also indicated are the effective focal length of the lens f and the distance d between the sample and the front principal plane.

4.1.4 Modifications for Backscattering Experiments

The imaging system presented in Fig. 4.1 is configured to measure the light transmitted through a turbid sample. However, a problem that is also the subject of scattering studies is the distribution of light backscattered from a multiple scattering medium. To study backscattered light, the imaging system must be reconfigured. Fig. 4.4 shows that inserting a beamsplitter between the input lens L2 and the sample permits the detection of light backscattered by a turbid medium. The input beam is rerouted to enter the appropriate port of the beamsplitter.

One problem with this configuration is that the distance between the sample and input lens has increased greatly from the transmission measurement configuration. The propagation over this distance causes the Wigner distribution to be altered. As equation 3.17 shows, when a Wigner distribution propagates, its spatial argument is translated by an amount that depends on it momentum argument. Thus, the Wigner

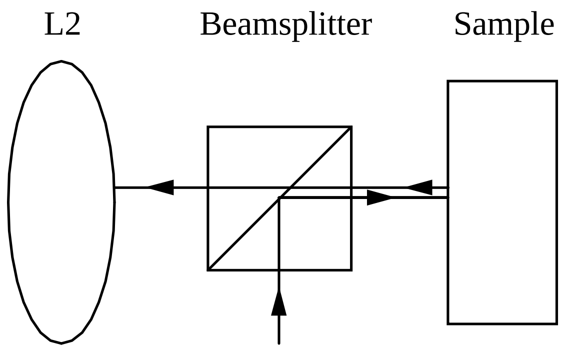

Figure 4.4: Modifications for measurement of light backscattered from a turbid sample. Lens L2 is the input lens of the heterodyne imaging system (Fig. 4.1). The arrows indicate the beam path.

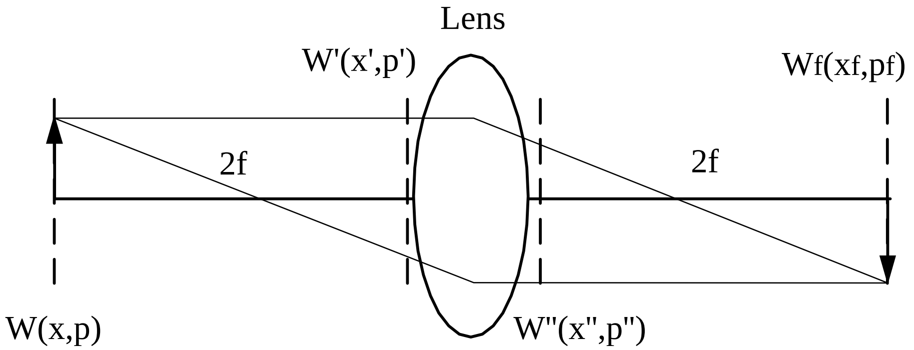

Figure 4.5: The Wigner distribution in an image plane: the position distribution in the image plane replicates that in the object plane, but the momentum distribution is altered.

distribution in the plane of L2 is not identical to that which emerged from the sample. In order to reproduce the original Wigner distribution in the plane of the input lens, a simple imaging system is used.

A single lens can produce an image of a spatial light distribution. For example, an object a distance $2f$ from a lens of focal length f will create a spatial image a distance $2f$ past that lens. However, a Wigner distribution is not reproduced in the same way. Figure 4.5 shows the propagation of a Wigner distribution for this arrangement. A

Wigner distribution $W(x,p)$ that propagates a distance $2f$ will have its x arguments changed to $x+(2f/k)p$ as shown by Eq. 3.17. Thus the Wigner distribution in the plane just before the lens is

$$W'(x',p',z=2f)=W(x+\frac{2f}{k}p,p,z=2f). \tag{4.32}$$

This equation shows that for free space propagation the final Wigner distribution retains the same form as the initial distribution. However, the position in the final plane, x', is simply related to the position and momentum in the initial plane.

The effect of passing through the lens can be calculated using Eq. 3.23. The Wigner distribution after the lens is related to the initial distribution through another simple translation of its arguments. When it passes through the lens of focal length f, the momenta are changed by $p \to p-(k/f)x$, yielding

$$\begin{aligned} W''(x'',p'') &= W(x+\frac{2f}{k}(p-\frac{k}{f}x),p-\frac{k}{f}x) \\ &= W(-x+\frac{2f}{k}p,p-\frac{k}{f}x). \end{aligned} \tag{4.33}$$

Subsequent propagation over an additional distance $2f$ yields the Wigner distribution in the image plane in terms of the input distribution. Again using Eq. 3.17, the final distribution in the image plane is

$$\begin{aligned} W_f(x_f,p_f) &= W(x+\frac{2f}{k}p+\frac{2f}{k}(p-\frac{k}{f}(x+\frac{2f}{k}p),p-\frac{k}{f}(x+\frac{2f}{k}p)) \\ &= W(-x,-p-\frac{k}{f}x). \end{aligned} \tag{4.34}$$

Thus, while a single lens will reproduce the spatial distribution as an inverted image, the momentum distribution will not be replicated correctly.

An imaging system that reproduces both the position and momentum of a Wigner distribution is pictured in Fig. 4.6. Here we see that the Wigner distribution in the object plane, $W_0(x,p)$ is transformed to

$$W_1(x_1,p_1)=W(x+\frac{f}{k}p,p) \tag{4.35}$$

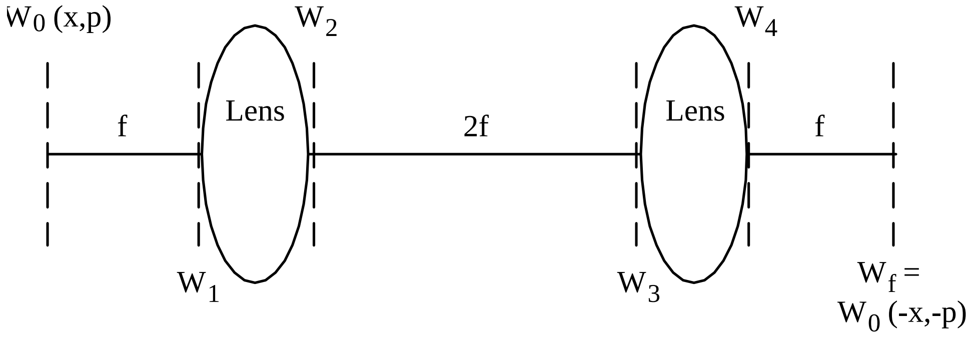

Figure 4.6: Wigner distribution imaging system. The Wigner distribution in the source plane is replicated with arguments negated in the image plane.

after propagation over a distance f. The first lens alters the momentum distribution, yielding:

$$\begin{aligned} W_2(x_2, p_2) &= W(x + \frac{f}{k}(p - \frac{k}{f}x), p - \frac{k}{f}x) \\ &= W(\frac{f}{k}p, p - \frac{k}{f}x) \end{aligned} \tag{4.36}$$

at its output. The subsequent propagation over a distance $2f$ results in a Wigner distribution of

$$\begin{aligned} W_3(x_3, p_3) &= W(\frac{f}{k}p, p - \frac{k}{f}(x + \frac{2f}{k}p)) \\ &= W(\frac{f}{k}p, -p - \frac{k}{f}x). \end{aligned} \tag{4.37}$$

The second lens changes the momentum arguments, yielding at its output face:

$$\begin{aligned} W_4(x_4, p_4) &= W(\frac{f}{k}(p - \frac{k}{f}x), -(p - \frac{k}{f}x) - \frac{k}{f}x) \\ &= W(-x + \frac{f}{k}p, -p). \end{aligned} \tag{4.38}$$

Finally, propagation over the remaining distance f, restores the position argument:

$$\begin{aligned} W_f(x_f, p_f) &= W(-(x + \frac{f}{k}p) + \frac{f}{k}p, -p) \\ &= W(-x, -p), \end{aligned} \tag{4.39}$$

thus reproducing the original Wigner distribution with its arguments inverted. By inserting this lens combination between the input lens L2 and the beamsplitter in Figure 4.4, the Wigner distribution at the output face of the sample is imaged at the input lens of the heterodyne imaging system.

4.1.5 Motion Control System

The measurement of optical phase space distributions is accomplished by translation of optical elements. The variables d_x, d_p, and d_c respectively indicate the positions of a mirror, lens and retroreflector (Figure 4.1). These elements are all mounted on translation stages driven by computer controlled linear actuators. The motion control system is based on the MotionMaster 2000 (MM2000) system from Newport Research Corporation (NRC). The MM2000 is an advanced motion controller card that plugs directly into a PC. The main board supports up to four "piggy-back" plug-in modules each of which controls one axis of motion via a stepping or DC servo motor. In our system the MM2000 is configured to control three axes of motion using DC motors. Each motor controls an 850F Series Linear Actuator also from NRC which provides the linear translation needed for the experiments.

The MM2000 system can be controlled using Labview software from National Instruments with drivers downloaded from the world wide web (http://www.natinst.com). This software permits a high level of motion control using commands issued with a PC. The command set includes directives to change the distance, direction, speed and acceleration of each move. The commands are sent from the controller card to a Universal Interface Box (UIB) from NRC. The UIB directs commands to each axis of motion and supplies power to the motors.

The 850F Series Linear Actuators are long travel, high resolution linear actuators. They are capable of two inches of total travel with 0.05 μm resolution. The software directs the motion by commanding the actuators to move a given number of 0.05 μm steps, so they effectively act as stepper motors. The resolution is accomplished with a precision-rolled leadscrew combined with a high ratio gearbox. The actuators incorporate a manual actuation knob for coarse adjustment with the motor power off. Care must be taken not to manually adjust the actuator position with the power applied or damage will result to the gearhead. The simplest method to ensure that the motor is unpowered is to unplug the cable from the UIB before manually adjusting the position.

The actuators typically have approximately 15 μm of backlash. That is, upon changing the direction of motion, the motor must spool for approximately 300 steps before motion resumes. Using the backlash compensation feature of the controller software, the bidirectional repeatability is better than 1 μm. Travelling in one direction, the overall accuracy of the motors is better than 0.1 percent of the total travel. The high precision, repeatability and accuracy of the motion control system is essential for our experiments, particularly when using a source with a coherence length of only a few microns.

4.2 Detection Apparatus

The detection system is a sensitive detection method used in measuring optical quantum noise previously in our laboratories [86]. Figure 4.7 shows a schematic which traces the signal from the point it is detected by the photodiodes, D1 and D2, through the transimpedece amplifier to the spectrum analyzer. The signal is then squared using a low noise multiplier and finally fed to a lock-in amplifier. This section will discuss each of these components in detail. The final analysis in this section will trace the heterodyne beat signal giving the lock-in amplifier reading V_{LI} in terms of the power of the heterodyne beat P_B.

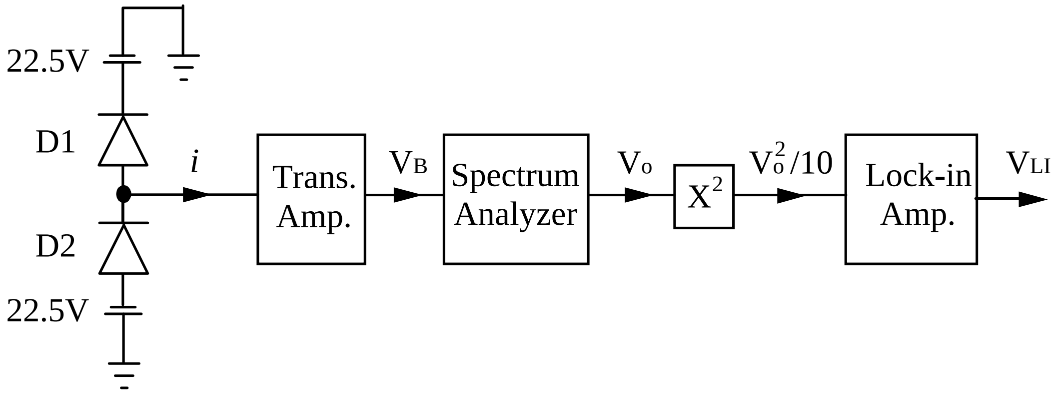

Figure 4.7: Block diagram illustrating the signal flow through the components of the detection apparatus.

4.2.1 Photodetectors

The optical signal is converted to a photocurrent by two EG&G FFD-040B photodiodes connected so that their outputs subtract (Fig. 4.7). These diodes were originally chosen for their small capacitance (1.8 pF) and are each reverse-biased by 22.5V batteries to increase their response time. As shown in Figure 4.8, the diodes have been mounted in an aluminum fitting which positions each diode directly at the output of the cube beamsplitter (BS2 in Fig.4.8) used to mix the LO and signal beams. This allows the use of input lenses (L1, L2 in Fig. 4.8) with short focal lengths and therefore large numerical apertures. The aluminum mount has been directly attached to the circuit board that contains the amplification electronics. The photocurrent is converted to a voltage by a CLC425 wide bandwidth operational amplifier configured as a transimpedance amplifier.

4.2.2 Transimpedence Amplifier

The CLC425 transimpedance circuit (Figure 4.9) for this experiment was designed to maximize its response at 10 MHz (the frequency of the heterodyne beat signal)

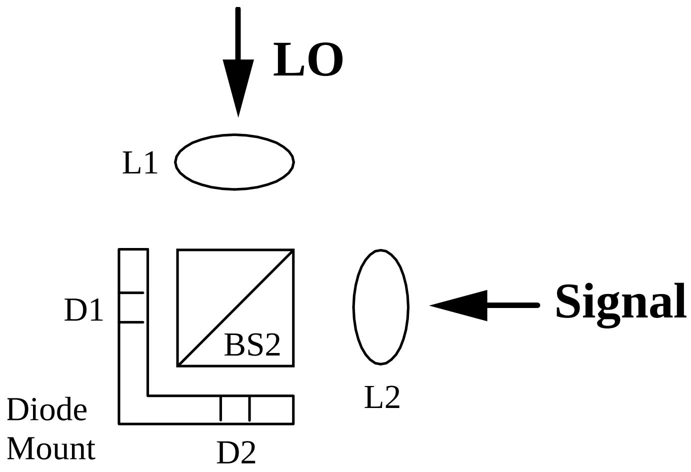

Figure 4.8: Schematic of diode mount positioning relative to optical elements of the heterodyne imaging scheme (Fig. 4.1).

yet remain stable. The 2.3 pF capacitor in this circuit stabilizes it by cancelling the pole caused by the photodetector capacitance at the input. However, it also causes the amplifier response to roll off at higher frequencies. In order to utilize the lowest possible capacitor and thus increase the amplifier bandwidth, a 50 ohm resistor is needed in series at the output, (Figure 4.9). The resistor further stabilizes the circuit by isolating the output from any capacitive loading that is introduced when monitoring the output with either an oscilloscope or spectrum analyzer. The increased stability permits a small capacitor to be used in the feedback path thus widening the bandwidth of the amplifier. Figure 4.10 shows the frequency response of the modified amplifier when the 2.3 pF capacitor is used in the feedback path. This response curve was obtained by measuring the shot noise level at each frequency and comparing it with predicted values. The amplifier rolloff at 10 MHz for the modified configuration is 0.722 times that of its zero frequency response as indicated.

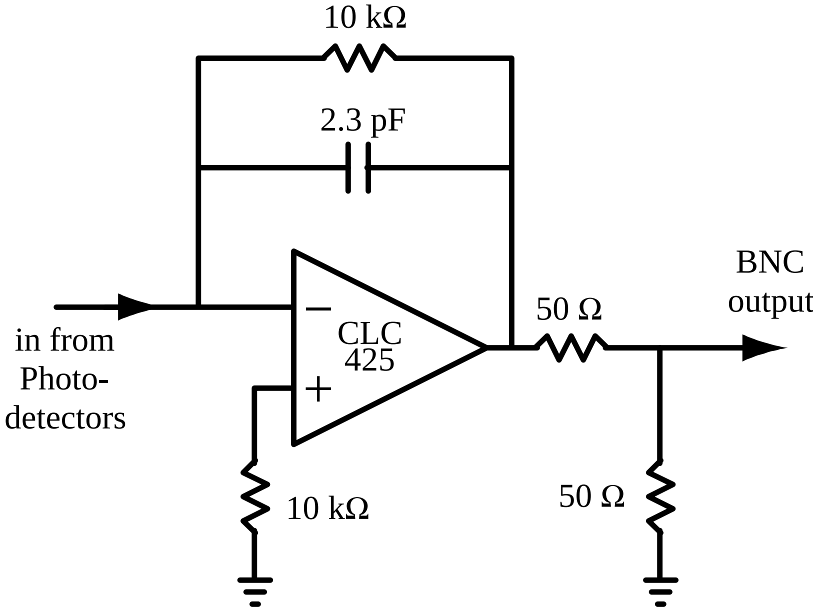

Figure 4.9: Schematic of transimpedence amplifier.

4.2.3 Spectrum Analyzer

The amplifier output is fed to a spectrum analyzer, Hewlett Packard model # ESA-L1500A. Although the final output on the display of the instrument is digital, the spectrum analyzer is itself analog and can be configured to include an analog video output (option A4J). This is an essential component of the analyzer as we rely on squaring the analog output to yield a signal that measures smoothed Wigner distributions and to allow us to subtract electronic noise in real time. An unfortunate drawback of this analog video output is that it is specified as uncalibrated. This means that the signal at the video output is proportional to the input signal but that the proportionality varies depending on the reference level set on the front panel. The change in scaling must be measured and accounted for every time the spectrum analyzer amplitude scale is changed.

A second feature of the spectrum analyzer which is not ideal for our purposes is

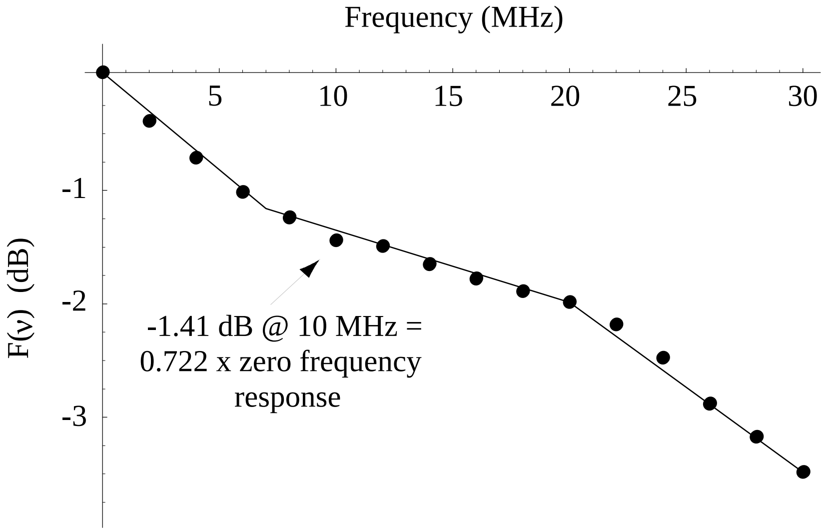

Figure 4.10: Frequency response F(ν) of transimpedence amplifer, normalized to zero frequency response F(0).

its automatic alignment. The unit is designed to perform automatic frequency and amplitude alignments with every scan and make small adjustments to the display data using digital processing. These small adjustments account for the difference between the analog video output and the true readings given on the unit's display screen. The auto-alignment feature causes the analog video output to be blanked occasionally during refresh so it must be disabled when the analog output is being continually monitored. As a result, the unit must be manually aligned using the "align now all" feature before measurements are made. According to the spectrum analyzer reference manual, once the unit is at a stable temperature for ninety minutes, it will meet noise and accuracy specifications if the "align now all" routine is run every hour.

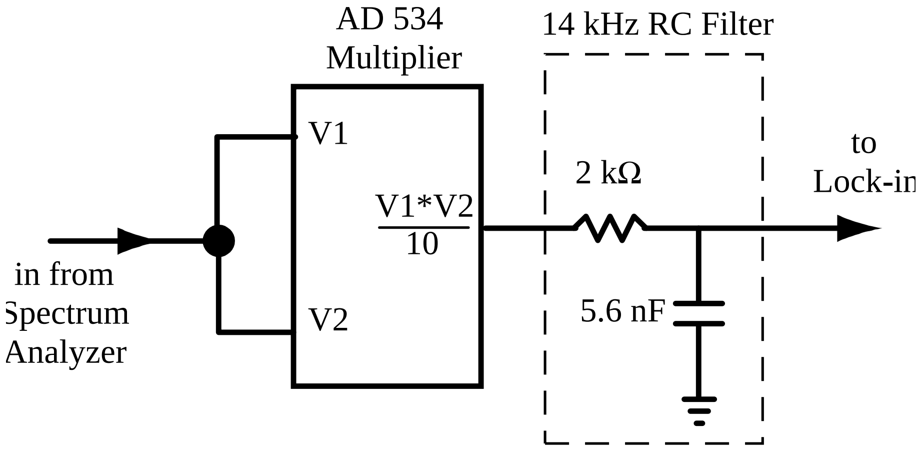

Figure 4.11: Squarer ciruit employing a low noise multiplier.

4.2.4 Lock-in Amplifier

The analog video output is squared using a low noise multiplier (Analog Devices AD534) in a circuit designed previously in our laboratories [86]. The circuit (Fig. 4.11) feeds the signal from the spectrum analyzer into both inputs of the multiplier. The multiplier thus produces a signal proportional to the square of its input. The output of the squarer is filtered before being sent to a lock-in amplifier, EG&G Princeton Applied Research Model 124A which was loaned to us by Dr. Henry Everitt. The lock-in is referenced to an electronic square wave signal at 483 Hz which is also used to chop the signal beam via the acousto-optic modulator. Thus the 14kHz low pass RC filter between the multiplier and lock-in amplifier (Fig. 4.11) allows the chopped signal at 483 Hz to pass with 0.99 efficiency but still removes any noise present at higher frequencies.

4.2.5 Detected signal

To calculate the lock-in input voltage due to an optical heterodyne beat signal at the detectors, we must trace the signal through our detection apparatus (Fig. 4.7).

Initially, we must calculate the power of the heterodyne beat signal, P_B for a given signal beam and LO powers, P_S and P_{LO}, respectively. Using simple phasors for the LO (E_{LO}) and signal field (E_S), we can write the signal as:

$$|E_{LO} + E_S|^2 = |E_{LO}|^2 + |E_S|^2 + \langle E_{LO} E_S^* \rangle + c.c. \tag{4.40}$$

$$\begin{aligned} \langle E_{LO} E_S^* \rangle + c.c. &= \left\langle \sqrt{P_{LO}}\, e^{i(\omega+\delta)t} \sqrt{P_S}\, e^{-i\omega t} \right\rangle + c.c \\ &= 2\sqrt{P_{LO} P_S} \cos(\delta t) \\ &= P_B \cos(\delta t)\,. \end{aligned} \tag{4.41}$$

Here ω is the optical frequency, δ is the 10 MHz difference frequency and *c.c.* denotes a complex conjugate. I have defined the power of the heterodyne beat signal, $P_B = 2\sqrt{P_{LO} P_S}$. Equation 4.41 only accounts for the interference between the LO and signal beams as their DC components are subtracted off using the balanced detector arrangement.

The heterodyne beat power P_B incident on the detector generates a photocurrent

$$i = \eta_D P_B$$

where η_D is the responsivity of the photodiodes. At the wavelength of a helium neon laser beam ($\lambda = 633$ nm) the responsivity was experimentally found to be 0.32 A/W, while for the low-coherence-length sources ($\lambda \approx 850$ nm) the responsivity was found to be 0.54 A/W. The transimpedance amplifier produces an output of $\mathrm{F}(\nu)\ \mathrm{R}\ i$ where $\mathrm{R} = 10\ \mathrm{k}\Omega$ is the feedback resistance and $\mathrm{F}(\nu) = 0.722$ is the frequency response of the amplifier (Figure 4.10). Finally an efficiency η_{het} must be included to account for wavefront alignment. Typically, for two identical helium neon laser beams the heterodyne efficiency was greater than 0.90. For broadband sources or two beams of different diameters, it is much more difficult to achieve good wavefront alignment and this figure was usually in the range of 0.40 to 0.60. The output of the transimpedance amplifier is thus given by:

$$V_B = \eta_D \times P_B \times R \times \mathrm{F}(\nu) \times \eta_{het}. \tag{4.42}$$

This is the amplitude of the heterodyne beat signal as measured with an oscilloscope. The spectrum analyzer divides this voltage by 2 due to its 50 Ω input impedance in parallel with the 50 Ω resistor at the output of the transimpedance amplifier (Fig. 4.9) and again by $\sqrt{2}$ because it measures the root-mean-square of the sinusoidal heterodyne beat. Thus on the spectrum analyzer, the voltage of the beat signal is read as $V_{SA} = V_B/(2\sqrt{2})$. By setting the spectrum analyzer to a frequency span of zero, the beat signal can be monitored using the analog video output. The output of the spectrum analyzer divides the signal voltage by the voltage for the full scale deflection, also called the reference level, V_{ref}, to yield a signal as a scaled voltage from 0 to 1V. As mentioned previously, the analog video output is uncalibrated so a scale factor η_{sa} must be included. Thus the signal at the output is:

$$V_o = \frac{\eta_{sa} V_{SA}}{V_{ref}} = \frac{\eta_{sa} V_B}{V_{ref} \cdot 2\sqrt{2}} = \frac{\eta_{sa} \times 2\sqrt{P_{LO} P_S} \times \eta_D \times F(\nu) \times R \times \eta_{het}}{V_{ref} \cdot 2\sqrt{2}} \tag{4.43}$$

The scale factor η_{sa} is determined by dividing the signal voltage by the reference level as measured via the spectrum analyzer's GPIB interface and comparing it to the video output. This scale factor will remain constant as long as the amplitude scale is unchanged. The output signal is fed to the low noise multiplier which is configured to give the input signal squared and divided by 10V. The signal which is fed to the lock-in is given by $V_{LI} = V_o^2/10V$. The resulting signal depends linearly on the power of the signal beam P_S as well as on the power of the LO beam P_{LO}. The analog output of the lock-in is monitored by our laboratory computer using an analog to digital converter input. By incorporating all of the above mentioned scale factors, our recorded signal is then proportional to the magnitude of the beat note squared, $|V_B|^2$.

The heterodyne method presented in this chapter is suitable for measuring the optical phase space distributions for a variety of light fields. The following chapter presents a method for coherence characterization of an arbitrary light source based on optical phase space distributions.

Chapter 5

Beam Characterization using Optical Phase Space Distributions

The heterodyne technique for measuring optical phase space distributions can be implemented using light from a variety of sources. The experimental data presented in Chapter 6 are obtained by employing light generated by both coherent and low coherence length sources. The coherence properties of these sources vary widely, ranging from the coherent helium neon laser to the low coherence length superluminescent diode. The character of the source used in a light scattering study will influence the measurements that are made. Therefore, knowledge of the coherence properties of an input light source is a necessary reference in studies exploring the propagation of optical coherence in multiple scattering media. In this chapter, I present a means of beam characterization using measurements of optical phase space distributions. This is followed by characterizations of the sources I have used in light scattering studies. I begin with a discussion of coherence and the mathematical model used to describe the coherence properties of our light sources.

5.1 Coherence Properties

There have been three types of light sources I have employed to study light scattering. They can be classified by their coherence properties. The first source I used was a helium-neon laser beam. Light from a helium-neon laser is nearly completely coherent both longitudinally and transversely.

Longitudinal or temporal coherence refers to the coherence of a beam along its axis of propagation. It is often characterized by a coherence length, the largest path length difference which can be introduced between two beams for which interference fringes can still be observed. It is well known that the coherence length is inversely proportional to the bandwidth of the light used [87]. Transverse or spatial coherence describes the coherence of a beam perpendicular to its axis of propagation. It can be characterized by a tranverse coherence length, the largest lateral shear between two beams which still produces interference fringes.

The remaining two sources I have used are broadband light sources known as superluminescent diodes (SLD). These sources are characterized by a large bandwidth and thus low longitudinal coherence. However, they do not suffer from poor spatial coherence as do other broadband sources, such as LED's. The first type of SLD's I used were commercially available sources purchased from the Anritsu Corporation of Japan. These are fairly broadband sources with good spatial coherence characteristics but produce relatively low output power, limiting their usefulness. This aspect was improved in the other sources used in my experiments which were novel high-power, extended bandwidth SLD's supplied to us by the Sarnoff Corporation of Princeton, NJ. The extended bandwidth of these sources corresponds to an extremely short longitudinal coherence length, a property which is very useful for selecting photon path lengths in light scattering studies. However, the very low coherence length and increased power also come with a cost of decreased spatial coherence.

5.1.1 Gaussian Schell-Model Source

Both longitudinal and spatial coherence refer to the correlation between two fields. Mathematically, one can specify these correlations using the cross-spectral density, defined here for a frequency component ω,

$$\mathcal{W}(x, x', \omega) = \langle \mathbf{E}^* (x, \omega) \, \mathbf{E} (x', \omega) \rangle \, . \tag{5.1}$$

A reaonable model to use for our purposes is the beam generated by a Schell-model source. This type of source is capable of generating a narrow angle beam despite being only partially coherent. The cross-spectral density for this model is given by Mandel and Wolf [87] as:

$$\mathcal{W}(x,x',\omega) \propto \exp\left[-\frac{x^2+x'^2}{4a^2}\right]\exp\left[-\frac{(x-x')^2}{2\sigma^2}\right]\exp\left[\frac{ik}{2R}(x^2-x'^2)\right]. \tag{5.2}$$

In this model, $2a$ is the intensity width of the beam, σ is the transverse coherence length, k is the optical wavevector and R is the radius of curvature of the wavefront. In this model, it is assumed that the beam is relatively well collimated and near its beam waist, which describes the case of interest. The first two terms in this model are Gaussian distributions, one is a function of the sums of x^2 and x'^2 and the other of the difference between x and x'. For this reason, the model is known as a Gaussian Schell-model. The final term accounts for the spatially varying phase due to the wavefront curvature.

To apply this model to our method of optical phase space measurement, I recall Equation 4.27:

$$\begin{aligned} |V_B|^2 \;\; &\propto \;\; |\int dx \int d\omega_k \left\langle \mathcal{E}^*_{k_{LO}}(x+d_x,z=0)\,\mathcal{E}_{k_S}(x,z=0)\right\rangle \\ &\times e^{-i\omega_k \Delta l/c}\exp(-ik\frac{d_p^2}{2f_o})\exp(ik\frac{d_p}{f_o}x)|^2, \end{aligned} \tag{5.3}$$

where d_x is the spatial shift of the LO, d_p/f_o is the momentum shift of the LO, Δl is the change in path length between the LO and signal beams and f_o is the focal length of the imaging lenses. This expression for the detected beat signal depends on the integral of cross-spectral densities over frequency components, ω_k's. The frequency distribution is taken to be Gaussian, of width $\Delta\omega_k$ and centered about ω_o. Inserting the frequency distribution and the Gaussian Schell-model for the cross spectral densities into Eq. 5.3, the detected beat signal can be rewritten as,

$$\begin{aligned} |V_B|^2 \;\; \propto \;\; & |\int dx \int d\omega_k \times e^{-i\omega_k \Delta l/c} \exp(-ik\frac{d_p^2}{2f_o}) \exp(ik\frac{d_p}{f_o}x) \\ & \times \exp\left[-\frac{x^2+(x+d_x)^2}{4a^2}\right] \exp\left[-\frac{(d_x)^2}{2\sigma^2}\right] \\ & \times \exp\left[\frac{iK}{2R}(x^2-(x+d_x)^2)\right] \exp\left[-\left(\frac{\omega_k-\omega_o}{\Delta\omega_k}\right)^2\right] |^2. \end{aligned} \tag{5.4}$$

The spatial (x) integral can be performed, which leaves:

$$\begin{aligned} |V_B|^2 \;\; \propto \;\; & |\exp\left[-d_x^2(\frac{1}{8a^2}+\frac{1}{2\sigma^2})\right] \int d\omega_k \exp\left[-\frac{k^2a^2}{2}\left(\frac{d_p}{f_o}-\frac{d_x}{R}\right)^2\right] \\ & \times e^{-i\omega_k \Delta l/c} \exp(-ik\frac{d_p^2}{2f_o}) \exp(ik\frac{d_p}{2f_o}d_x) \exp\left[-\left(\frac{\omega_k-\omega_o}{\Delta\omega_k}\right)^2\right] |^2. \end{aligned} \tag{5.5}$$

Realizing that the Gaussian frequency distribution will cause $\omega_k \approx \omega_o$, I set $k = k_o$ (as $\omega_k = ck$) in this expression.This allows the integral over frequencies to be performed as a Fourier transform. The result is a simple expression for the mean square beat signal:

$$|V_B|^2 \propto \exp\left[-d_x^2(\frac{1}{4a^2}+\frac{1}{\sigma^2})\right] \exp\left[-k_o^2a^2\left(\frac{d_p}{f_o}-\frac{d_x}{R}\right)^2\right] \exp\left[-\frac{(\Delta k \Delta l')^2}{2}\right]. \tag{5.6}$$

Here, I have set $\Delta l' = \Delta l + \frac{d_p^2}{2f_o} - \frac{d_x d_p}{2f_o}$ which is the path difference between the LO and signal beams as defined in section 4.1.2 (Eq. 4.28). Additionally, in this expression the dependence on the the frequency bandwidth, $\Delta\omega_k$, has been replaced by a spread of wavevectors, $\Delta k = \Delta\omega_k/c$. Equation 5.6 gives the heterodyne beat signal as a function of the scanned variables: d_p, d_x and $\Delta l'$, and depends only on the bandwidth of the source and the beam parameters specified in Eq. 5.2: a, σ, and R.

1) Helium-Neon Laser
Meles Griot #05 LHP 141
Min. Power Output: 4mW Tem00 CW
Mode Spacing 438 MHz
Wavelength: 632.8 nm

2) Anritsu SLD's
Anritsu # SD1S101C, serial nos. C1246, C1178
Test power output: 1.5 mW
Current for 1.5 mW: 83mA, 69mA
FWHM Bandwidth: 12.3 nm, 16.3 nm
Center Wavelength: 851 nm, 852 nm

3) Sarnoff SLD's
David Sarnoff Research Center #CD 1247 - VFS, diode ID nos. A2, A10
Test conditions operating current: 728mA, 640mA
Power Output after columnation lens: 28 mW
FWHM bandwidth: 44 nm
Center Wavelength: 832 nm

Table 5.1: Source manufacturer specifications.

5.2 Source Characterizations

The method of coherence characterization uses optical phase space measurements to determine the properties of a light source [88]. Scanning the phase space parameters of the detected heterodyne beat signal allows the determination of the parameters of the Gaussian Schell-model source as well as the longitudinal coherence length using one set of measurements. The method of determining these source characteristics from the phase space measurements is presented in the next section using the coherent, helium-neon source as an example. The method is then applied to both the Anritsu and Sarnoff SLD's. Their properties are presented in the subsequent sections. The specifications of the light sources used in my experiments as given by the manufacturers are listed in Table 5.1.

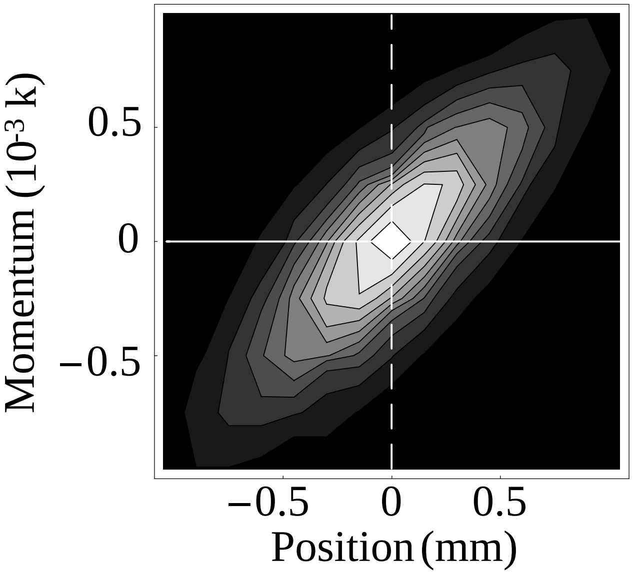

Figure 5.1: Low resolution phase space contour plot for a single mode He-Ne laser beam. Each position step is 150 μm and each momentum step is 0.25 mrad.

5.2.1 Method of Coherence Characterization using coherent light: Helium-Neon source

Figure 5.1 shows measured optical phase space contours, $|V_B(d_x, d_p)|^2$, for the single-mode He-Ne laser beam obtained by scanning d_x and d_p with the path difference between the LO and signal, $\Delta l'$, held at zero. As discussed in section 3.2.1, the orientation of the ellipse indicates that the beam is diverging, i.e. it has a positive radius of curvature, $R > 0$. Plotting the transverse momentum distribution for $d_x = 0$, the dotted veritcal line in Figure 5.1, yields a Gaussian distribution with a 1/e momentum width $p_{1/e}/k_o = (d_p/f_o)_{1/e} = 0.375$ mrad. Setting $d_x = 0$ and $\Delta l' = 0$ in Eq. 5.6, the heterodyne beat intensity drops to $1/e$, for

$$d_p = \frac{f_o}{k_o a} \equiv (d_p)_{1/e} \,. \tag{5.7}$$

The intensity width, $2a$, can now be determined by

$$2a = \frac{2f_o}{k_o \left(d_p\right)_{1/e}} = \frac{2}{k_o p_{1/e}}. \tag{5.8}$$

In the case of the He-Ne laser beam, this yields an intensity width of 0.54 mm, which agrees with measurements of the beam profile made with a diode array. Similarly, by plotting the position distribution for zero transverse momentum ($d_p = 0$), as shown by the solid horizontal line in Figure 5.1, a Gaussian distribution is again seen. Here the 1/e width, $(d_x)_{1/e} = 0.37$ mm. This is smaller than the intensity $1/e$ width due to the curvature of the LO and signal beam wavefronts.

The effect of wavefront curvature can be seen in the pictorial representation in Figure 5.2. This cartoon shows the effects of scanning d_x and d_p on the overlap of LO and signal beam wavefronts. In this illustration, the wavefronts are represented by two identical rectangles of finite thickness and their overlap as the gray shaded area. Fig. 5.2(A), shows the decrease in wavefront overlap when a shear $\Delta x = d_x$ is introduced between the two beams. Fig. 5.2(B) shows that for curved wavefronts, the overlap is decreased for an identical shear.

The radius of curvature of the wavefront R can be determined from the position distribution at zero transverse momentum ($d_p = 0$). As shown by Equation 5.6, for $d_p = 0$, the beat intensity drops to $1/e$ for

$$d_x = \left(\frac{1}{4a^2} + \frac{1}{\sigma^2} + \frac{k_o^2 a^2}{R^2}\right)^{-1/2} \equiv \left(d_x\right)_{1/e}. \tag{5.9}$$

Since we have previously determined the parameter a from the $p_{1/e}$ width, the $(d_x)_{1/e}$ width depends only on σ, the transverse coherence width and R the wavefront radius of curvature. For the case of the He-Ne laser beam, the wavefront is completely spatially coherent so that $\sigma \gg 2a$. This allows R to be determined by

$$R = k_o a \left(\frac{1}{\left(d_x\right)_{1/e}^2} - \frac{1}{4a^2}\right)^{-1/2}. \tag{5.10}$$

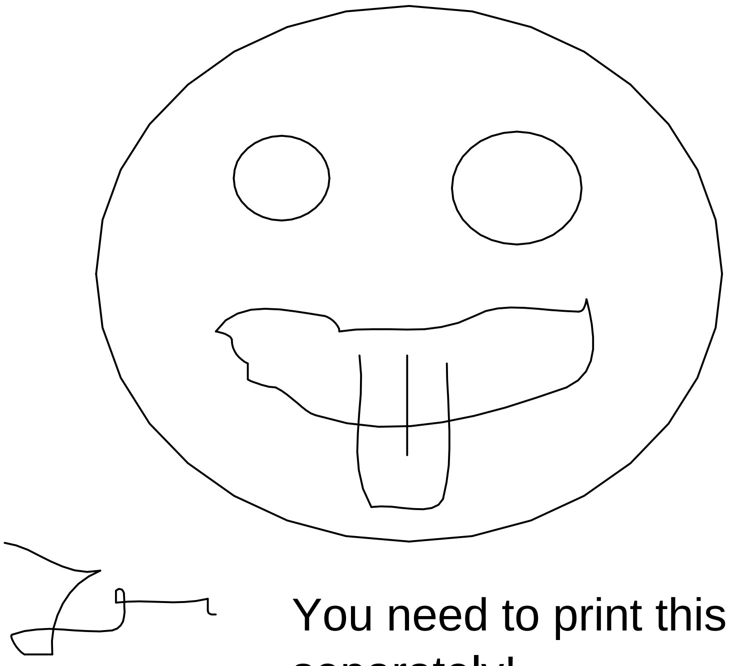

You need to print this on separately!

Figure 5.2: Pictorial interpretation of the overlap of two identical wavefronts when a shear or relative angle is introduced between them.

From the He-Ne laser beam data shown in Figure 5.1, R is found to be 1.36 m.

For beams which have only partial spatial coherence, the assumption that $\sigma \gg 2a$ is not valid. The effects of a transverse coherence length σ, smaller than the beam diameter, $2a$ are shown in Fig. 5.2(C). In this cartoon, the graded area represents the coherent area and the shaded area shows that for the same shear Δx, the overlap is decreased compared to the fully spatially coherent wavefronts shown in Fig. 5.2(A). For such a case, the transverse coherence width, σ, must be determined before R can be found. Recalling Eq. 5.6,

$$|V_B|^2 \propto \exp\left[-d_x^2(\frac{1}{4a^2}+\frac{1}{\sigma^2})\right]\exp\left[-k_o^2a^2\left(\frac{d_p}{f_o}-\frac{d_x}{R}\right)^2\right]\exp\left[-\frac{(\Delta k\Delta l')^2}{2}\right], \quad (5.11)$$

I note that by integrating $|V_B|^2$ over all momentum displacements (d_p), I can remove the dependence on the wavefront curvature (R). This yields a signal

$$\overline{|V_B|^2} \propto \exp\left[-d_x^2(\frac{1}{4a^2}+\frac{1}{\sigma^2})\right], \quad (5.12)$$

for $\Delta l' = 0$. This momentum-integrated signal now depends only on a and σ. This can be realized from the experimental data by summing all of the d_p values in the optical phase space distribution for each position d_x. This will yield a gaussian distribution with a $1/e$ width of

$$\overline{(d_x)}_{1/e} = \left(\frac{1}{4a^2}+\frac{1}{\sigma^2}\right)^{-1/2}. \quad (5.13)$$

This allows determination of σ provided that a is already known. Once σ has been found, it can be inserted into Eq. 5.8 to find the wavefront radius of curvature, R. Because $\sigma \gg 2a$ for the He-Ne laser beam, the momentum-integrated signal did not yield a value for $\overline{(d_x)}_{1/e}$ significantly different than the spatial width $2a$, as expected for a spatially coherent beam.

To complete the characterization of the coherence, the longitudinal coherence length is also needed. The coherence length is conventionally defined as the range of path length differences between two beams for which an interference pattern is observed at an intensity greater that half the maximum intensity. It is related to the source charcteristics by

$$l_c = \frac{2\ln 2}{\pi}\frac{\lambda_o^2}{\Delta\lambda_{FWHM}}. \tag{5.14}$$

where λ_o is the center wavelength of the source and $\Delta\lambda_{FWHM}$ is the full width at half maximum of the source wavelength distribution. In our method, according to Eq. 5.6 the beat intensity drops to $1/e$ for

$$\Delta l' = \frac{\sqrt{2}}{\Delta k} \equiv \Delta l_B, \tag{5.15}$$

where Δk is the $1/e$ width of the wavevector distribution. Since $k = 2\pi/\lambda$, the wavevector distribution is related to the wavelength distribution as

$$\Delta k = 2\pi\frac{\Delta\lambda_{1/e}}{\lambda_o^2} = \frac{\pi}{\sqrt{\ln 2}}\frac{\Delta\lambda_{FWHM}}{\lambda_o^2}. \tag{5.16}$$

Using Eq.'s 5.14 and 5.16, the parameter our method measures is related to the coherence length as

$$\Delta l_B = \frac{l_c}{\sqrt{2\ln 2}} \equiv \frac{\sqrt{2\ln 2}}{\pi}\frac{\lambda_o^2}{\Delta\lambda_{FWHM}}. \tag{5.17}$$

For the He-Ne beam, Table 5.1 lists the center wavelength as $\lambda_o = 632.8$ nm and the Melles-Griot catalog specifies the laser linewidth approximately as $\Delta\nu \sim 1$ MHz. Using the fundamental relation $c = \nu\lambda$, the linewidth can be related to the wavelength spread as

$$\Delta\nu = c\frac{\Delta\lambda}{\lambda_o^2} \tag{5.18}$$

Thus the He-Ne beam has a wavelength bandwidth of $\Delta\lambda \sim 10^{-6}$ nm which corresponds to a coherence length of $l_c > 100$ m. This coherence length is obviously too long for our method to measure as $\Delta l'$ can be scanned 2" at most. However, for sources with coherence lengths of a few microns, our method is very useful as shown in the SLD characteristics in the next section .

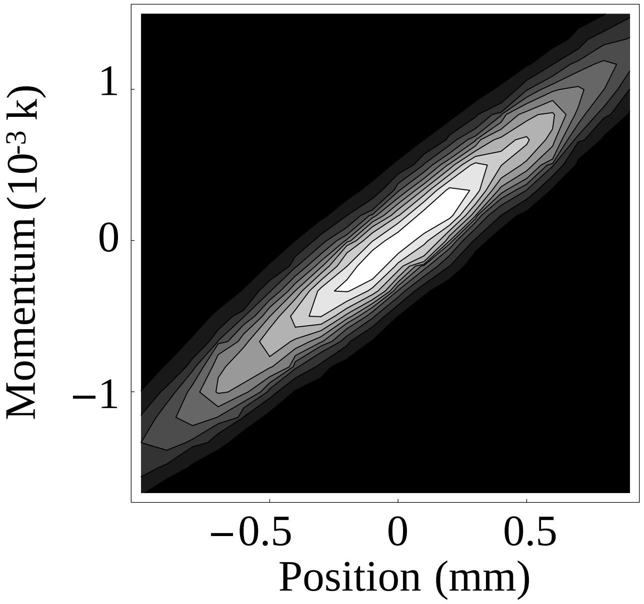

Figure 5.3: Measured optical phase space distribution for Anritsu SLD beam.

5.2.2 Low Coherence Source: Anritsu SLD

Figure 5.3 shows the measured optical phase space contours, $|V_B(d_x, d_p)|^2$ for a typical beam generated by an Anritsu superluminescent diode (SLD) after collumation and beam-shaping. As with the optical phase space contours for the He-Ne beam, the data in Fig. 5.3 is obtained by scanning d_x and d_p while keeping the difference between the LO and signal path lengths, $\Delta l'$, at zero. The Anritsu SLD's typically have a bandwidth of $\Delta\lambda_{FWHM}$ =10-16 nm and a center wavelength of $\lambda_o = 852$ nm. The data presented in Fig. 5.3 were taken for a power output of 1.5 mW produced by a driving current of 85 mA.

Proceeding with the coherence characterization as before, the momentum distribution at zero transverse position ($d_x = 0$) is seen to be gaussian with a $1/e$ width $p_{1/e}/k_o = (d_p/f_o)_{1/e} = 0.32$ mrad. Substituting this value into Equation 5.8 the intensity width is found to be $2a = 0.85$ mm. For zero transverse momentum, the position

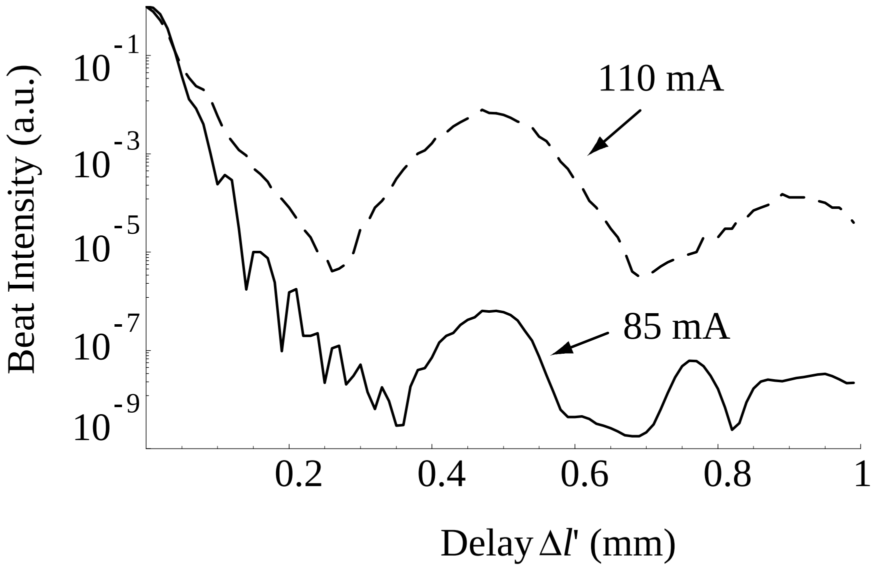

Figure 5.4: Mean-square heterodyne signal plotted as a function of effective path delay $\Delta l'$ for the Anritsu SLD at two different driving currents. The power output at 85 mA is 1.5 mW and at 110 mA is almost 4 mW.

distribution has a gaussian $1/e$ width $(d_x)_{1/e} = 0.24$ mm, signifigantly smaller than the calculated spatial $1/e$ width, $2a$, of 0.85 mm. This is because the beam from the SLD not only has a curved wavefront, but also possesses a finite transverse coherence width, σ. As illustrated in Fig. 5.2, both of these effects will diminish the wavefront overlap which contributes to the heterodyne beat.

To determine the transverse coherence width, σ, the data are summed over d_p for each value of d_x. This results in a gaussian with a $1/e$ width $\overline{(d_x)}_{1/e} = 0.83$ mm. Using $2a = 0.85$ mm and Eq. 5.13, we find that $\sigma = 4$ mm. Since the $1/e$ transverse coherence width is approximately 5 times larger than the $1/e$ spatial width, the output of the Anritsu SLD is deemed to be spatially coherent. Lastly, I note that since σ and $2a$ are known, the $1/e$ width of the position distribution can be used to deduce that the radius of beam curvature R is 0.78 m by using Eq. 5.10.

The longitudinal coherence characteristics of the Anristu SLD are examined by holding d_p and d_x constant and scanning $\Delta l'$. The beat intensity drops to $1/e$ for $\Delta l'$ = 26.4 μm = Δl_B. By Eq. 5.17, the corresponding coherence length is l_c = 31.1 μm. This agrees with the coherence length found by inserting the center wavelength (λ_o = 852 nm) and bandwidth ($\Delta\lambda_{FWHM}$ = 10.3 nm), as measured with a monochrometer, into Equation 5.14. The measured bandwidth is slightly less than the 12.3 nm specified by the manufacturer as some bandwidth is lost due to aperaturing in collumation and beam shaping. These measurements were made at an output power of 1.5 mW which corresponds to a driving current of 85 mA. Although increasing the driving current results in increased power, the longitudinal coherence characteristics began to degrade for currents greater than 85 mA.

To examine this degradation, $\Delta l'$ scans were taken at two different driving currents over a range of 1 mm. As shown in Fig. 5.4, the scans for driving currents of 85 mA and 110 mA are markedly different. At 85 mA, secondary peaks appear which are 6 orders of magnitude lower than the primary peak at zero path delay. These peaks indicate coherence between LO and signal beams for nonzero path differences. At 110 mA, the secondary peaks become only a factor of 100 smaller than the primary peak, and repeat every 0.45 mm. This periodicity suggests that the secondary peaks arise from multiple reflections within the diode package. The secondary peaks are extremely undesirable for imaging applications based on detecting heterodyne signals because they degrade the longitudinal resolution of the measurement. The secondary peaks seen here are eliminated for the novel high power, extended bandwidth SLD's from the Sarnoff Corporation which are characterized in the next section.

5.2.3 Low Coherence Source: Sarnoff SLD

The optical phase space contour plot for a typical beam coming from a high power, extended bandwidth Sarnoff SLD is shown in Figure 5.5. As with the previous contour

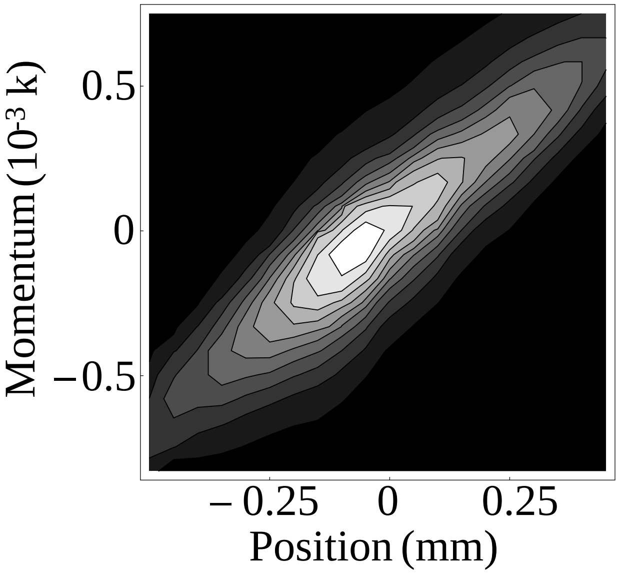

Figure 5.5: Measured optical phase space distribution for Sarnoff SLD beam.

plots, the data are obtained by scanning d_x and d_p while holding $\Delta l'$ fixed at zero. These SLD's have bandwidths of 40-50 nm, a center wavelength of 830 nm and can produce 50-100 mW with adequate heat sinking. The data shown are obtained for a driving current of 640 mA, producing an output power of 28 mW. These are the test conditions specified by the manufacturer.

To begin the coherence characterization of the Sarnoff SLD beam, the momentum distribution at zero transverse position ($d_x = 0$) is plotted. Its distribution is gaussian with a $1/e$ width $p_{1/e}/k_o = (d_p/f_o)_{1/e} = 0.27$ mrad. Using this value in Equation 5.8, the intensity width of the beam is found to be $2a = 0.98$ mm. The position distribution at zero transverse momentum ($d_p = 0$) is found to be gaussian with a $1/e$ width of $(d_x)_{1/e} = 0.24$ mm, which for the same reason as the Anritsu SLD is signifigantly smaller than the calculated spatial $1/e$ width, $2a$, of 0.98 mm. This is due to the curved wavefront and finite transverse coherence width, σ, of the beam from the Sarnoff SLD. Both of these characteristics serve to diminish the wavefront

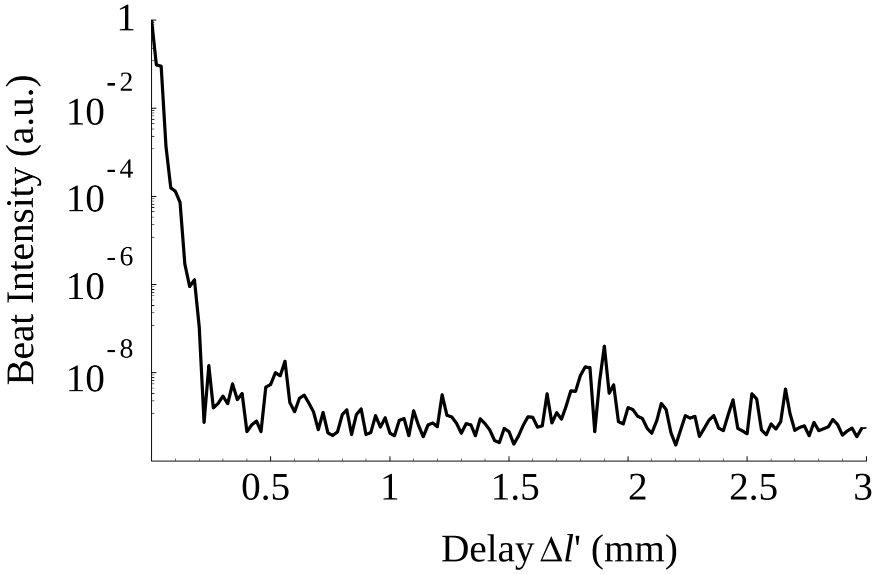

Figure 5.6: Mean-square heterodyne signal plotted as a function of effective path delay $\Delta l'$ for the Sarnoff SLD

overlap, as illustrated in Fig. 5.2.

The transverse coherence width, σ, is determined by summing the data over d_p for each value of d_x. The resulting distribution is gaussian with a $1/e$ width $\overline{(d_x)}_{1/e} = 0.37$ mm. Using this value and the intensity width $2a = 0.98$ mm in Eq. 5.13, σ is found to be 0.4 mm. The radius of curvature, R, is found to be 0.61 m using Eq. 5.10. For the Sarnoff SLD, the transverse coherence width is only 40% of the spatial beam width. Thus it is concluded that this source does not have a fully spatially coherent output.

The longitudinal coherence of the Sarnoff SLD is characterized by scanning $\Delta l'$, the path difference between the LO and signal beams, while d_x and d_p are held fixed at zero. Figure 5.6 shows the data from a scan of path delays from 0 to 3 mm. The bandwidth for the SLD was measured at the source to be $\Delta\lambda_{FWHM} = 44$ nm with a center wavelength $\lambda_o = 832$ nm using a monochrometer. For these spectral characteristics, the coherence length is calcluated using Eq. 5.17 to be $l_c = 7\ \mu$m, which corresponds to an expected $1/e$ width of $\Delta l_B = 5.9\ \mu$m. From the data in Fig. 5.6 however, the beat intensity is seen to drop to $1/e$ for $\Delta l' = 7.4\ \mu\text{m} = \Delta l_B$. This is signifigantly longer than the expected $1/e$ width as the optics used did not have enough bandwidth for this source. As with the phase space contour plot, the longitudinal coherence characteristics of this SLD were determined using an output power of 28 mW produced by a driving current of 640 mA.

Figure 5.6 shows that secondary peaks in the longitudinal coherence scan for the Sarnoff SLD are a factor of 10^8 smaller than the primary peak. This is an improvement over the longitudinal coherence characteristics of the Anritsu diode operating at both high and low powers. While the Sarnoff SLD offers extremely high power and improved longitudinal coherence characteristics, it suffers from decreased spatial coherence which make it less useful for certain imaging applications. For example, optical coherence tomography relies on a tightly focused beam to achieve high spatial resolution. For spatially incoherent beams such as that generated by the Sarnoff SLD, tight focusing cannot be achieved. If the spatially coherent portion of the beam from the Sarnoff SLD is selected by setting an aperature at 40% of the beam diameter, the output power is decreased to 4.5 mW. While this power is still greater than that produced by the Anritsu SLD, the decreased spatial coherence of the Sarnoff SLD does hinder its utility.

To summarize, Table 5.2 lists the coherence characterization results for the three types of sources used in my experiments. The parameters listed in this table correspond to those used in the Gaussian Schell-model (Eq. 5.6) and also includes the output power, wavelength distribution and coherence length (Eq. 5.14) for each source.

Source:	He-Ne laser beam	Anritsu SLD	Sarnoff SLD
Output Power:	4 mW	1.5 mW @85mA	28 mW @640mA
Beam width, $2a$:	0.54 mm	0.85 mm	0.98 mm
Transverse coherence length, σ:	∞	4 mm	0.4 mm
Radius of wavefront curvature, R:	1.36 m	0.78 m	0.61 m
Center wavelength, λ_o:	632.8 nm	852 nm	832 nm
FWHM bandwidth, $\Delta\lambda_{FWHM}$:	$<10^{-6}$ nm	10.3 nm	44 nm
Coherence length, l_c:	>100 m	31.1 μm	7 μm

Table 5.2: Summary of source coherence characteristics.

Chapter 6

Multiple diffractive scattering in transmission

This chapter presents a study of measured optical phase space distributions for light from a coherent source which has been transmitted through a turbid medium. The transmitted momentum distributions exhibit three components, a ballistic peak, a narrow pedestal and a broad background. The narrow pedestal is found to decay more slowly than the ballistic peak as the concentration of scatterers is increased. This behavior is explained with a simple theory that includes multiple diffractive scattering but treats large angle scattering as a loss.

The first section of this chapter begins by presenting a brief review of the experimental setup as configured for this transmission study. The basic characteristics of the turbid media used as scattering samples are presented in this section as well. The second section of this chapter presents the experimental data for the study. Initially, optical phase space contour plots are presented for a narrow collimated He-Ne beam transmitted through turbid media for various concentrations of scatterers. This data contains interesting features in its momentum distribution which are investigated further using a large diameter input beam. The large beam prevents the input beam size from limiting the detected angular (momentum) scattering characteristics. The data obtained using the large diameter He-Ne beam are also included in this section. The data are analyzed using a theoretical model derived from the transport equation for the Wigner distribution. The model is derived in detail in section 6.3. Finally, the chapter concludes with a discussion of the physical interpretation of the theoretical model.

6.1 Experimental Setup

6.1.1 Heterodyne detection scheme for a coherent source

Figure 6.1 shows the experimental scheme as configured to measure the light from a coherent source transmitted through a turbid sample. In this scheme, the signal beam at frequency ω is incident on a scattering sample. The light emerging from the sample is mixed with a strong local oscillator (LO) at frequency $\omega + 10$ MHz at a beamsplitter (BS2), resulting in a heterodyne beat signal. The beat signal is detected using photodiodes configured in a balanced detection arrangement As shown in detail in section 4.1.1, by squaring the detected beat signal, the overlap of the Wigner distributions for the LO and signal fields is measured. In addition, scanning mirror M1 and lens L2 allows the effective center position and momentum of the LO to be varied respectively. Thus the optical phase space distribution of the signal field is mapped out as a function of LO position and momentum. The detected signal is given in terms of the Wigner distributions of the LO and signal fields by Eq. 4.21 as

$$S(d_x\hat{x}, d_p\hat{x}) = \int d^2\vec{x}_\perp \, d^2\vec{p}_\perp \, W_{LO}(\vec{x}_\perp - d_x\hat{x}, \vec{p}_\perp + \frac{k}{f} d_p\hat{x}) \, W_S(\vec{x}_\perp, \vec{p}_\perp). \tag{6.1}$$

In this expression, d_x is the shift of mirror M1, d_p is the shift of lens L2 and f is the focal length of lenses L1 and L2.

6.1.2 Turbid medium

To learn how to interpret the optical phase space distribution of light emerging from a turbid sample, scatterers with known characteristics are needed. Biological samples can have particles of various sizes and optical properties which make them difficult to model as scatterers. Thus they would make a poor choice for an initial study such as this. We chose a turbid medium consisting of latex microspheres ($n = 1.59$)

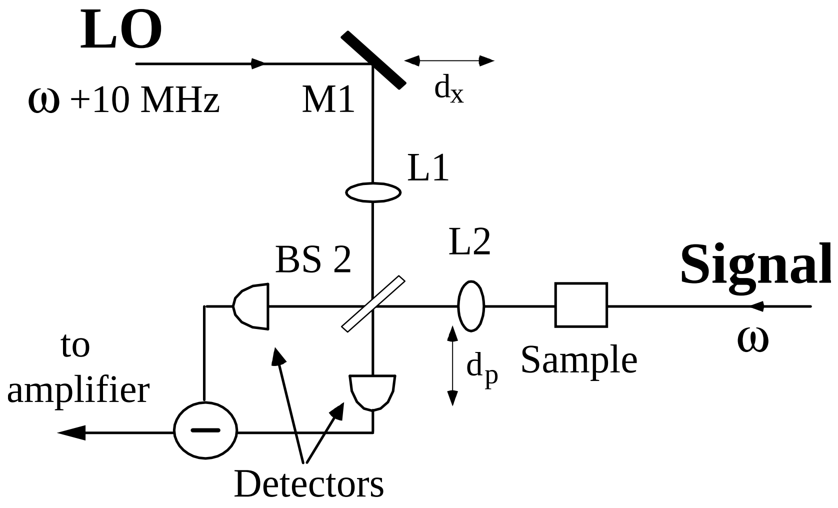

Figure 6.1: Experimental scheme for transmission experiments.

in a water/glycerol mixture. Monodisperse size distributions of latex microspheres are available in a variety of particle sizes and concentrations from companies such as Polysciences, Inc of Warrington, PA and Duke Scientific Corp. of Palo Alto, CA. The scattering characteristics of these particles can easily be modelled using the Mie solution [24] provided their size and index of refraction are known.

The particles are suspended in a mixture of 75% water and 25% glycerol. This mixture is chosen to produce neutral buoyancy for the microspheres. The index of refraction of the mixture is found to be 1.36 by passing a He-Ne laser beam through a triangular container similar to an equilateral triangular prism. By noting the angular deviation caused by adding the mixture, the index of refraction is measured to within 0.3% of published values for this mixture at this wavelength. This index of refraction of the medium results in a relative refractive index of 1.17 for the latex microspheres compared to the medium. Data were taken for varying concentrations of spheres in water/glycerol in a precision 1” diameter cylindrical cell of optical path length $L = 10$ mm.

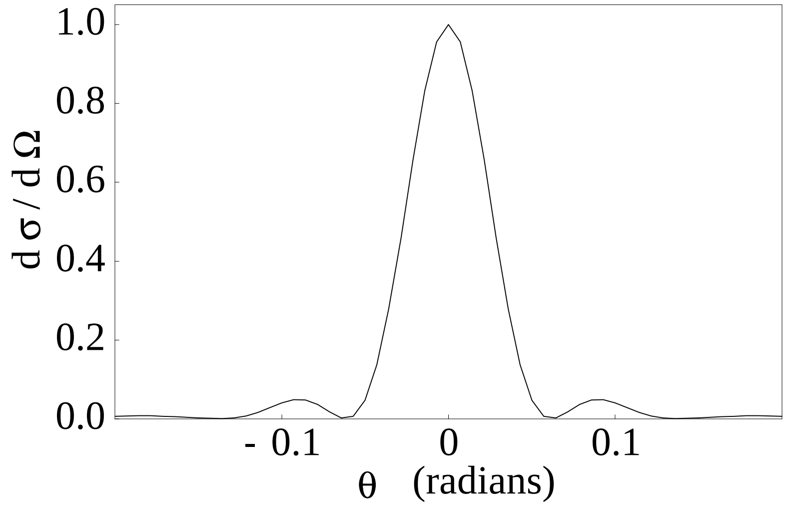

Figure 6.2: Mie differential cross section for scattering from 11.4 μm diameter polystyrene spheres with parameters $n_{rel} = 1.17$, $n_o = 1.36$, and $\lambda_{air} = 633$ nm.

Large spheres are specifically selected for the transmission studies to give highly forward peaked scattering . The scattering characteristics are determined using the Mie solution for scattering of light by a dielectric sphere [24] for each size particle and wavelength of light used. In the coherent source experiments (section 6.2), the wavelength of the He-Ne beam in air is $\lambda_{air} = 632.8$ nm and the spheres used have a radii of 5.7 micrometers. The Mie solution for these parameters gives a total scattering cross section σ_s that is 1.98 times the geometrical cross section, i.e., $\sigma_S = 202\,\mu\text{m}^2$. It is assumed that there is no absorption. The theoretical angular distribution (differential cross section) is shown in Fig. 6.2. The peak amplitude has been normalized to 1. The angles are the transverse momenta given in units of the photon wavevector, k_o, in vacuum. These angles have been multiplied by 1.36 to account for the propagation from the water/glycerol mixture into air where they are detected. The differential scattering cross section shows a central diffractive peak that is nominally gaussian. Its half width at 1/e is 31.6 mrad which corresponds to a width of 23.2 mrad in the medium. This distribution is highly peaked in the forward direction with a low amplitude broad background that is not visible here. This characteristic is implied by the average of the cosine of the scattering angle, which for these spheres is found to be $\langle \cos\theta \rangle = 0.92$.

6.2 Experimental Data

6.2.1 Measured phase space distributions

Initially, we have measured the optical phase space distribution for transmission of a narrow, collimated gaussian beam through a turbid medium of 5.7 μm radius polystyrene sphere in a 25% glycerol/75% water mixture. Fig. 6.3 shows a measured phase space contour plot (log scale) for a 0.5 mm diameter input beam to the sample. Here, the concentration of spheres is $\rho = 2 \times 10^6/\text{cm}^3$, and the ballistic contribution is attenuated by $\exp(-4)$. The ballistic light appears as a narrow island in the center of the contour plot. A narrow pedestal appears around the ballistic contribution. Both the pedestal and the broad large angle scattering contribution exhibit a correlation between momentum and position as expected for a diverging localized source. This divergence corresponds to a wavefront curvature of 2.1 cm, approximately the distance between the input face of the sample and the input plane of lens L2 (see Fig. 6.1), where the signal Wigner distribution is sampled. Fig. 6.4 shows the phase-space contours at higher concentration, $\rho = 6 \times 10^6/\text{cm}^3$, where the ballistic attenuation is $\exp(-12)$. In this case, the momentum and position distributions broaden. (Note the increased horizontal and vertical scales). The correlation between position and momentum indicates a wavefront curvature of 1.5 cm, corresponding to a source located near the center of the cell. At higher concentrations the source position appears to move toward the sample output face.

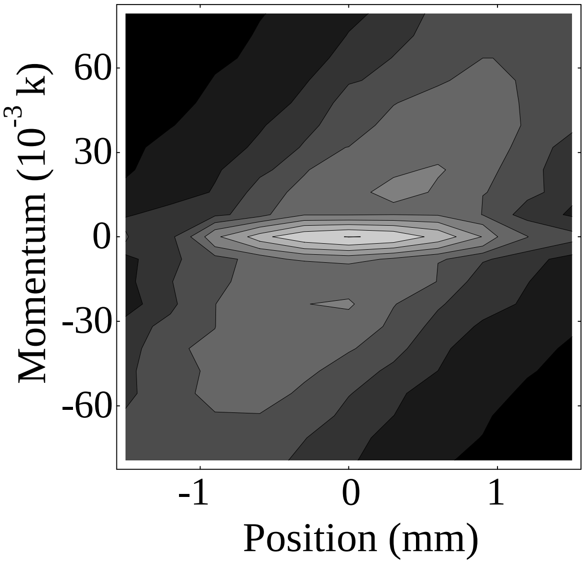

Figure 6.3: Measured optical phase space distribution (log scale) for light transmitted through a turbid medium for $\rho = 2 \times 10^6/\text{cm}^3$ (ballistic attenuation: $\exp(-4)$). The central island is the ballistic contribution.

6.2.2 Momentum distributions of diffractive pedestal

To explore in detail the shape and amplitude of the pedestal shown in Fig. 6.3, we have measured the optical phase space distributions for transmission of a large diameter input beam through the sample ($a = 3.8$ mm half width at 1/e intensity). In this case, the LO beam is small in diameter ($a_o = 0.38$ mm) compared to the input beam, so that the output Wigner distribution is nearly independent of position x over the LO diameter. Further, the momentum width of the local oscillator is small compared to the width of the momentum distribution of the scattered light. In this case, the measured mean square heterodyne beat signal $S(d_x = 0, \frac{k}{f}d_p)$ (Eq. 6.1), determines approximately the true transmitted Wigner distribution of the scattered light, $W_S(x = 0, p = \frac{k}{f}d_p)$, excluding the ballistic contribution that is sharply peaked in the forward scattering direction.

For fixed LO position $d_x = 0$, plots of $S(d_x = 0, \frac{k}{f}d_p) = W_S(x = 0, p = \frac{k}{f}d_p)$,

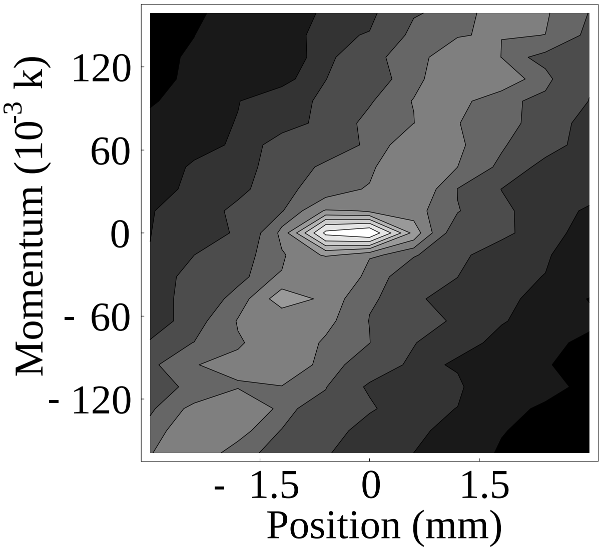

Figure 6.4: Measured optical phase space distribution (log scale) for light transmitted through a turbid medium for $\rho = 6 \times 10^6/\text{cm}^3$ (ballistic attenuation $\exp(-12)$). The central island is the ballistic contribution.

are shown for various concentrations of 5.7 μm radius spheres ranging from $\rho = 0.4 \times 10^6/\text{cm}^3$ to $\rho = 6 \times 10^6/\text{cm}^3$. In general, the scattering distribution is seen to have three components: a ballistic peak, a central narrow pedestal and a broad background. The ballistic contribution is not shown, as it is orders of magnitude larger than the narrow pedestal and the broad background. The half width at 1/e intensity of the ballistic peak is 0.4 mrad, which is much narrower than the widths of the scattered light distributions. At low concentrations, the scattered light data shows a diffractive peak, Fig. 6.5, that agrees with the Mie solution. As the concentration is increased, Fig. 6.6, the diffractive peak is seen to broaden and attenuate while the broad background becomes more prominent, until in Fig. 6.7 the diffuse background becomes comparable to the diffractive component. Here, the ballistic component is still a factor of 10 larger than the pedestal, and is not shown.

The experimental angular distributions, $W_S(x = 0, p = \frac{k}{f} d_p)$, are fit to two com-

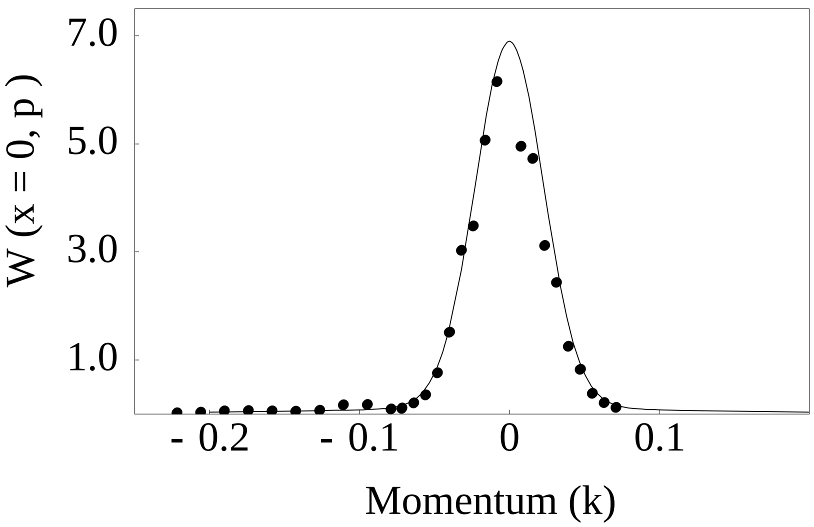

Figure 6.5: Measured optical phase space distribution $\simeq W(x = 0, p)$ for $\rho = 0.4 \times 10^6/\mathrm{cm}^3$ (linear scale, ballistic contribution: $\exp(-0.8)$, not shown). The theoretical prediction is shown as a solid curve. Vertical scale is 10^{-5} of the signal with no scatterers present.

ponent curves (solid lines) consisting of a narrow central pedestal and a broad diffuse background. As discussed above, the ballistic contribution is ignored, as it is localized near the origin. The central pedestal in the two component curve arises from multiple diffractive scattering. The shape of this component (normalized to 1 at $p = 0$) is determined using the theory described in detail in section 6.3.3. The amplitude of this component is left as a free parameter and is later compared to the predicted value. The broad background, which is not of interest here, is modeled as a Gaussian distribution in p with an undetermined amplitude.

Fig. 6.5 shows the angular scattering distribution $W_S(x = 0, p = \frac{k}{f} d_p)$ for a scatterer concentration of $\rho = 0.4 \times 10^6/\mathrm{cm}^3$ (vertical scale is 10^{-5} of the signal with zero scatterers present). The transverse momentum p is given in units of the optical wavevector in air k_o. The position x is in mm. This figure shows data points which are taken for angles $\theta = p/k$ in the range from -225 to +75 mrad. However, the fitted

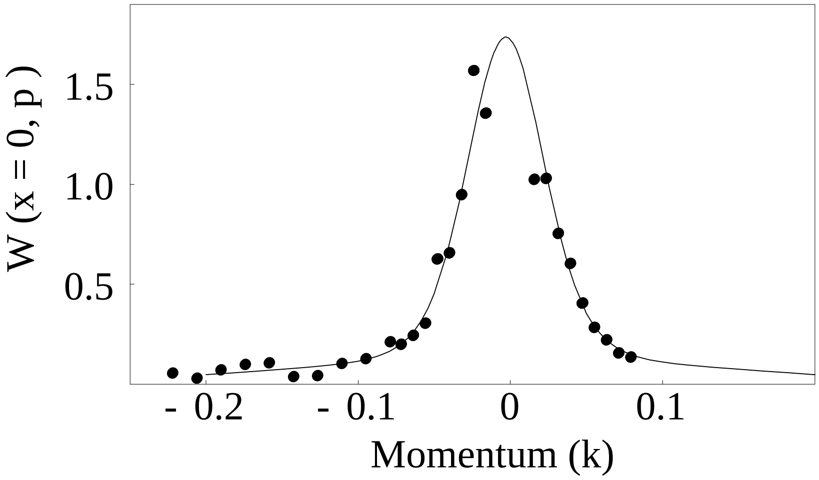

Figure 6.6: Measured optical phase space distribution $\simeq W(x = 0, p)$ for $\rho = 2 \times 10^6/\text{cm}^3$ (linear scale, ballistic contribution: exp(−4), not shown). The theoretical prediction is shown as a solid curve. Vertical scale is 10^{-5} of the signal with no scatterers present.

curves (solid line) are done for the data outside ±30 mrad, as interference with the gaussian tail of the ballistic light distribution causes these points to be unreliable. The ballistic peak is attenuated at this concentration by exp(−0.8) and is not shown in this figure as it is orders of magnitude larger than the scattered light.

Fig. 6.6 shows the angular scattering distribution at a higher concentration, $\rho = 2 \times 10^6/\text{cm}^3$ (vertical scale is 10^{-5} of the signal with zero scatterers present). Here we can see the broad diffuse background become significant while the central pedestal has broadened slightly. The ballistic light at this concentration has been attenuated by exp(−4) and again is not shown here as it is orders of magnitude larger than the scattered intensity.

In Fig. 6.7, the angular scattering distribution is shown for a scatterer concentration $\rho = 6 \times 10^6/\text{cm}^3$ (vertical scale is 10^{-7} of the signal with zero scatterers present). In this plot, we see the broad background has become comparable in magnitude to the central pedestal. At this concentration the ballistic light has been attenuated by

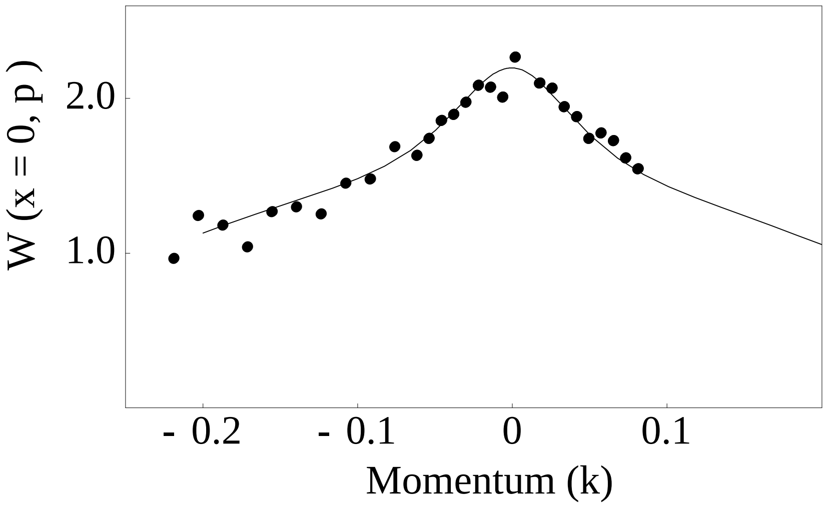

Figure 6.7: Measured optical phase space distribution $\simeq W(x = 0, p)$ for $\rho = 6 \times 10^6/\text{cm}^3$ (linear scale, ballistic contribution: $\exp(-12)$, not shown). The solid curve shows the theoretical prediction. Vertical scale is 10^{-7} of the signal with no scatterers present.

$\exp(-12)$, an order of magnitude larger than the scattered light, so again it is not shown.

To explore how the amplitude of the central pedestal varies with concentration, the maximum amplitudes for each of the fitted curves are shown in Fig. 6.8 as a function of scatterer concentration (Table A.2). These are compared to the predicted amplitude (solid line) with no free parameters as given by Equation 6.52. For comparison, the amplitude of the ballistic peak as a function of scatterer concentration is shown in Fig. 6.9. Over most of the range of scatterer concentrations, the amplitude of the central pedestal, Fig. 6.8, is found to decay exponentially with an attenuation coefficient that is 65% of that found for the ballistic.

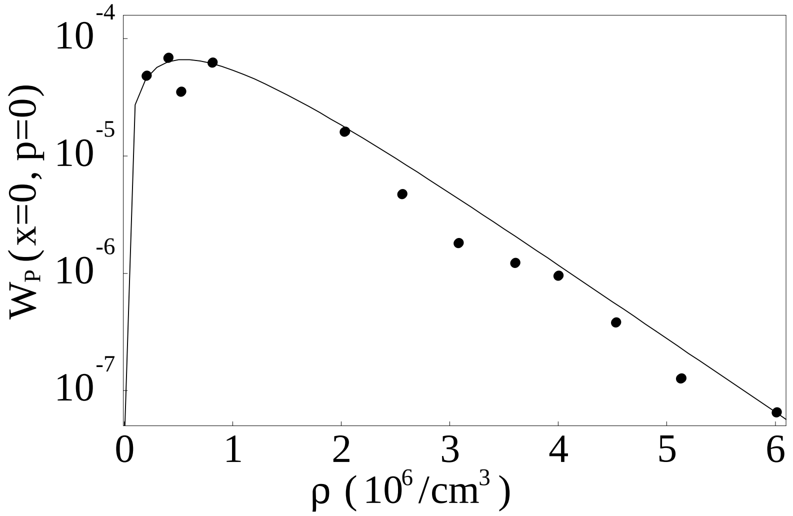

Figure 6.8: Amplitude of the narrow pedestal arising from multiple diffractive scattering as a function of scatterer concentration ρ. The solid curve shows the prediction with no free parameters. Note that the amplitude of the pedestal decays with an extinction coefficient that is 0.65 of the ballistic extinction coefficient of Fig. 6.9.

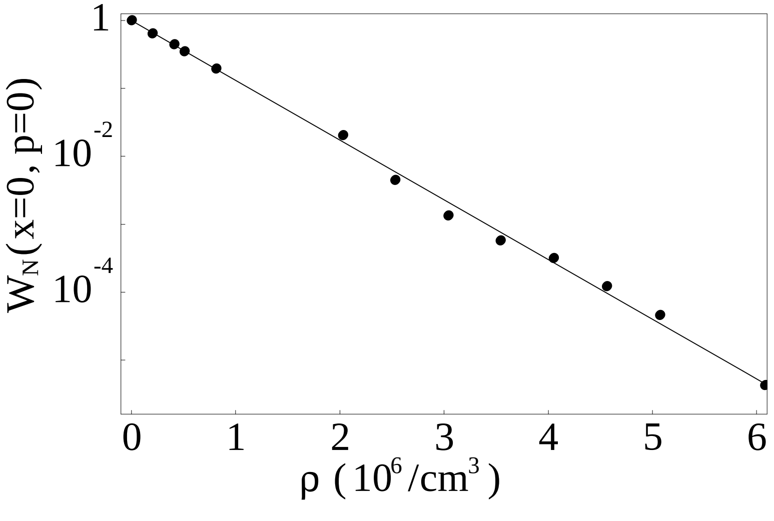

Figure 6.9: Amplitude of the ballistic component as a function of scatterer conectration ρ. The solid line shows the prediction for exponential decay with the extinction coefficient determined from the total scattering cross section.

6.3 Theory

In this section, a theoretical model is developed to explain the data shown in section 6.2.2. The theoretical treatment begins by considering the evolution equation of the Wigner distribution in a multiple scattering medium. The treatment employs a Green's function approach to predict the transmitted optical phase space distribution in terms of the input distribution. As an initial demonstration of its utility, the Green's function approach is used to predict the Wigner distribution transmitted through a turbid medium in the limit of a highly scattering sample such as Intralipid solution (Fig. 1.1). This limit allows an approximate form of the scattering kernel to be used. The model is used to explain the experimental data for transmission of a coherent source through Intralipid solutions of varying concentration shown in Figure 1.1.

The Green's function is also used to predict the output momentum distribution for the transmission of a large diameter coherent input beam through a sample of large diameter spheres, as is the case for the data in section 6.2.2. These two criteria are important as they allow certain approximations to be made in the theoretical treatment. The large diameter of the spheres results in sharply forward peaked scattering. This allows the scattering kernel to be modeled as a narrow gaussian distribution corresponding to the diffractive component of the scattering. Thus the transport can be viewed in this treatment as multiple diffractive scattering. In addition, the input beam is assumed large in diameter compared to the LO beam, so that the system exhibits approximate translation invariance across the output face of the sample [89]. These conditions are approximately satisfied in the experiments.

6.3.1 Transport equation for the Wigner distribution in a scattering medium

In general, the transport equation for the Wigner distribution can be somewhat complicated, exhibiting nonlocal scattering [13, 90]. However, when the Wigner distribution varies slowly in its spatial argument compared to an optical wavelength, the transport equation is approximately local and is identical in structure to the usual radiative transport equation for the specific intensity [13,90]. As a first approximation, this equation is used to model the data.

The evolution equation for the Wigner distribution can be divided into two parts:

$$\frac{\partial W(\vec{x},\vec{p},t)}{\partial t} = \left(\frac{dW}{dt}\right)_{FREE} + \left(\frac{dW}{dt}\right)_{SCATT.}. \tag{6.2}$$

In this expression one component accounts for the free space evolution and one component accounts for the evolution due to scattering. The free space evolution of the Wigner distribution was derived in section 3.3. Recalling Eq. 3.48, the free space evolution is given by

$$\frac{\partial W(\vec{x},\vec{p},t)}{\partial t} + \vec{\mathrm{v}} \cdot \vec{\nabla}_{\vec{x}} W(\vec{x},\vec{p},t) = 0. \tag{6.3}$$

The velocity given in the above expression is related to the momentum by

$$\vec{\mathrm{v}} = \frac{c^2}{n_o^2 \omega}\vec{p}. \tag{6.4}$$

Here, c/n_o is the velocity in the medium and ω is the optical frequency. Thus the free evolution term in Eq. 6.2 is given as

$$\left(\frac{dW}{dt}\right)_{FREE} = -\frac{c^2}{n_o^2 \omega}\vec{p} \cdot \vec{\nabla}_{\vec{x}} W(\vec{x},\vec{p},t) \tag{6.5}$$

Provided that the Wigner function is slowly varying compared to an optical wavelength, the scattering term can be modelled as a collistion integral, which can be written as [91]:

$$\left(\frac{dW}{dt}\right)_{SCATT.} = -\frac{c}{n_o}\mu_T(\vec{p})W(\vec{x},\vec{p},t) + \int d^3\vec{p}\,'K(\vec{p},\vec{p}\,')W(\vec{x},\vec{p},t). \tag{6.6}$$

In this expression, $\mu_T(\vec{p})$ is the total scattering coefficient. It is the sum of the scattering and absorption coefficients,

$$\mu_T = \mu_s + \mu_a \tag{6.7}$$

and can be related to the total cross section $\sigma_T(\vec{p})$ by

$$\mu_T(\vec{p}) = \rho\sigma_T(\vec{p}), \tag{6.8}$$

where ρ is the density of scatterers. $K(\vec{p},\vec{p}\,')$ is the scattering kernel, it is related to the differential scattering cross section $d\sigma/d\Omega$ by

$$K(\vec{p},\vec{p}\,') = \rho\frac{c^2}{n_o^2\omega}\delta\left(\frac{\vec{p}^2 - \vec{p}\,'^2}{2}\right)\frac{d\sigma}{d\Omega}. \tag{6.9}$$

An energy conserving delta function is included so that the kernel describes elastic scattering. Note that

$$\int d^3\vec{p}\,'K(\vec{p},\vec{p}\,') = \frac{c}{n_o}\rho\sigma_S(\vec{p}) = \frac{c}{n_o}\mu_S(\vec{p}). \tag{6.10}$$

The origin of the two terms in Eq. 6.6 can be understood heuristically. The first term represents the loss of phase space density of momentum $\vec{p}$ due to collisions with the particles in the unit volume (ρ) at position $\vec{x}$, each subtending a total cross section σ_T. The second term represents the arrival of phase space density due to collisions changing the momentum to $\vec{p}$ from all other momenta $\vec{p}\,'$.

Using these results, the approximate transport equation is given by

$$\begin{aligned}\frac{\partial W(\vec{x},\vec{p},t)}{\partial t} + \frac{c^2}{n_o^2\omega}\vec{p}\cdot\vec{\nabla}_{\vec{x}}W(\vec{x},\vec{p},t) &= -\frac{c}{n_o}\mu_T(\vec{p})W(\vec{x},\vec{p},t) \\ &+ \int d^3\vec{p}\,'K(\vec{p},\vec{p}\,')W(\vec{x},\vec{p},t).\end{aligned} \tag{6.11}$$

This equation is analogous to the transport equation used in phenomenological radiative transport theory [26]. The two equations have the same structure when the Wigner distribution is assumed to vary slowly over the scale of an optical wavelength. Physically, this criteria implies that the scattering is local, i.e. the position $\vec{x}$ does not change during the scattering process. Provided that this key assumption is met, Equation 6.11 can be used to correctly model the propagation of light in multiply scattering media in many situations.

6.3.2 Transmission via Green's function approach

Green's functions for the transport equation (Eq. 6.11) are easily obtained by Fourier transform methods [26] with the approximations that the total scattering rate is independent of momentum and the kernel is a function of $\vec{p}-\vec{p}'$ only. For a time-independent solution, the Green's function, G_p satisfies

$$\begin{aligned}\left(\frac{c\vec{p}}{n_o k}\cdot\vec{\nabla}_x+\frac{c}{n_o}\mu_T\right)G_p(\vec{x},\vec{x}\,';\vec{p},\vec{p}') &- \int d^3\vec{p}\,''K(\vec{p}-\vec{p}')\,G_p(\vec{x},\vec{x}\,';\vec{p}\,'',\vec{p}') \\ &= \delta(\vec{x}-\vec{x}\,')\delta(\vec{p}-\vec{p}'). \qquad (6.12)\end{aligned}$$

The solution to this equation is given by [91]

$$\begin{aligned}G_p(\vec{x},\vec{x}\,';\vec{p},\vec{p}') &= \int\frac{d^3\vec{q}}{(2\pi)^3}\int\frac{d^3\vec{r}}{(2\pi)^3}\exp\left(i\vec{q}\cdot(\vec{x}-\vec{x}\,')+i\vec{r}\cdot(\vec{p}-\vec{p}')\right) \qquad (6.13)\\ &\times\ \frac{n_o}{c}\int_0^\infty dl\ \exp(-il\vec{q}\cdot\vec{p}'/k)\,exp\left[-\int_0^l dl'\,\tilde{\mu}(\vec{r}+\vec{q}l'/k)\right],\end{aligned}$$

where $k=n_o\omega/c$ is the magnitude of the optical wavevector. Here,

$$\frac{c}{n_o}\tilde{\mu}(\vec{r})\equiv\frac{c}{n_o}\mu_T-\tilde{K}(\vec{r}), \qquad (6.14)$$

and

$$\tilde{K}(\vec{r})=\int d^3\Delta\vec{p}\,\exp(-i\vec{r}\cdot\Delta\vec{p})\,K(\Delta\vec{p}). \qquad (6.15)$$

The Green's function can be viewed as a transfer function which propagates the Wigner distribution within the scattering medium. Thus, the Wigner distribution at the output face of the scattering sample ($z = L$) can be calculated in terms of the input distribution. The relation is given by:

$$W_S(L, \vec{x}_\perp; \vec{p}) = \int d^2\vec{x}\,'_\perp \int d^3\vec{p}\,' \frac{p'_z}{k} G_p(\vec{x}_\perp, L, \vec{x}\,', z_o; \vec{p}, \vec{p}\,') W_S(z_o, \vec{x}\,'_\perp; \vec{p}\,'). \tag{6.16}$$

This method can be used to find the output distribution in a variety of situations when an explicit form of the Green's function can be realized. Finding an analytic form of the Green's function can be difficult as the l and l' integrals in Eq. 6.13 can only be performed numerically when the exact form of the scattering kernel is inserted into $\tilde{\mu}(\vec{r})$. Instead, approximate forms of the scattering kernel are often used to find an approximate Green's function. Useful forms of the Green's function can be found by considering the limiting cases of scattering kernels which are either very broad in momentum or very narrow in momentum compared to the momentum distribution of the Wigner distribution of interest.

For a collimated Gaussian beam, the corresponding Wigner distribution is narrow in momentum. For an input distribution which is narrow in momentum, such that $\vec{p}\,' \simeq k\hat{z}$, the corresponding Fourier transform variable, $\vec{r}$, becomes large. In the limiting case of $\vec{r} \to \infty$, corresponding to an infinitely narrow input momentum distribution, $\tilde{K}(\vec{r})$ goes to zero. Eq. 6.14 then shows that

$$\frac{c}{n_o}\tilde{\mu}(\vec{r}) = \frac{c}{n_o}\mu_T. \tag{6.17}$$

Physically, this makes sense as the ballistic light, which is narrow in momentum, will decay with the maximum attenuation coefficient μ_T.

In the opposite limit of a Wigner distribution that is very broad in momentum (narrow in the conjugate variable $\vec{r}$) compared to the scattering kernel, the kernel can be expanded in powers of $\vec{r}$. Assuming the kernel is a symmetric function of $\vec{r}$, the scattering kernel can be written as

$$\tilde{\mu}(\vec{r}) = \mu_T - \tilde{K}(\vec{r}) = \mu_a + \mu_T \frac{\overline{\theta^2}}{6} k^2 \vec{r}^{\,2}, \tag{6.18}$$

where

$$\overline{\theta^2} = 2\overline{(1 - \cos\theta)}, \tag{6.19}$$

which reduces to the mean square scattering angle for small angle scattering. Eq. 6.18 arises in the limit of a highly scattering sample.

The two limiting cases discussed above can be applied to explain the propagation of bimodal Wigner distributions containing both broad and narrow features. Two component distributions are common in transmission through a medium containing scatterers comparable in size to a wavelength. In such a case, the ballistic light, representing one component is narrow in momentum compared to the scattering kernel while the incoherent background, representing the second component, is broad compared to the scattering kernel. The transmitted distribution can be found by treating the overall transmitted Wigner distribution as the sum of a broad and a narrow component. Each transmitted component can then be found using Eq. 6.16, by inserting the approximate kernels given by Eq.'s 6.17 and 6.18 for the kernel in the respective Green's function for the narrow and broad components.

The approach of using a two component distribution can be used to explain the distribution transmitted through a scattering medium of length L containing particles comparable to the size of the wavelength of incident light. In such a situation, the measured heterodyne beat $S(d_x\hat{x}, d_p\hat{x})$ for $d_x = 0, d_p = 0$ is divided into a narrow component, S_N, representing the ballistic light and S_B representing the incoherent background. The overall signal is found to scale with concentration as [91]

$$\begin{aligned} \frac{S(0,0,\mu_T)}{S(0,0,0)} &= S_N + S_B \qquad (6.20) \\ &= \exp(-\mu_T L) + \sqrt{\frac{2}{\pi}} \frac{72\exp(-\mu_a L)}{(\mu_s \overline{\theta^2} L)^{5/2}(kL)^2}. \end{aligned}$$

In this expression, the measured beat intensity is normalized to the beat intensity for no scatterers present. The mean square scattering angle $\overline{\theta^2}$ is defined in Eq. 6.19 and the total attenuation coefficient is related to the scattering and absorption coefficients by Eq. 6.7. The scattering and absorption coefficients depend on the concentration of scatterers ρ by

$$\mu_s = \rho\sigma_s \qquad (6.21a)$$

$$\mu_a = \rho\sigma_a. \qquad (6.21b)$$

This model was found to agree with the data (Fig. 1.1) for transmission through varying concentrations of Intralipid solution [14].

6.3.3 Multiple diffractive scattering

The experimental data for transmission of a large diameter beam through a sample of large scatterers is seen to have three components: a ballistic peak, a central narrow pedestal and a broad background (section 6.2.2). The following model describes the evolution of the central narrow pedestal which is identified as arising from multiple diffractive scattering.

For Mie scattering from large diameter (11.4 μm) spheres, the differential scattering cross section, Fig. 6.2, exhibits a large diffractive scattering component that is forward peaked. In addition, there is a component that scatters broadly into 4π solid angle. This corresponds approximately to the geometric (classical) scattering cross section. According to the Mie differential scattering cross section, approximately

65% of the total scattering cross section arises from the broad part and 35% from the diffractive part. In this case, the kernel can be modeled as having two distinct components, denoted as K_N and K_B respectively, where N denotes the narrow diffractive kernel and B the broad kernel:

$$K(\vec{p},\vec{p}') = K_N(\vec{p},\vec{p}') + K_B(\vec{p},\vec{p}'). \tag{6.22}$$

It is convenient to divide the Wigner phase space distribution into the three components seen in the experimental data:

$$W = W_{BALL} + W_P + W_B. \tag{6.23}$$

Here, W_{BALL} denotes the narrow contribution arising from purely ballistic propagation of the input phase space distribution with attenuation at the total loss rate. W_P denotes the phase space distribution of the narrow pedestal that arises from diffractive scattering. W_B denotes a broad background contribution arising from large angle scattering. An evolution equation can be derived for each of these components. The derivation is closely related to those employed in previous studies of small angle scattering [92].

For a time independent distribution, the evolution equation (Eq. 6.11) takes the form

$$\frac{c^2}{n_o^2\omega}\vec{p}\cdot\vec{\nabla}_{\vec{x}}W(\vec{x},\vec{p}) = -\frac{c}{n_o}\mu_T(\vec{p})W(\vec{x},\vec{p}) + \int d^3\vec{p}'K(\vec{p},\vec{p}')W(\vec{x},\vec{p}). \tag{6.24}$$

The evolution equations for the three components are derived by inserting Eq.'s 6.22 and 6.23 into this expression and identifying the terms which contribute to each component.

The ballistic contribution has a very narrow momentum distribution compared to the width of both K_N and K_B. Hence, the integral term in Eq. 6.24 can be neglected in its propagation and W_{BALL} obeys the equation

$$\frac{c\vec{p}}{n_o k} \cdot \vec{\nabla}_{\vec{x}}\, W_{BALL}(\vec{x}, \vec{p}) = -\frac{c}{n_o}\mu_T\, W_{BALL}(\vec{x}, \vec{p}). \tag{6.25}$$

Using Eq.s 6.22, 6.23, and 6.25 in Eq. 6.24 yields an equation for the narrow pedestal arising from small angle scattering:

$$\begin{aligned} \frac{c\vec{p}}{n_o k} \cdot \vec{\nabla}_{\vec{x}}\, W_P(\vec{x}, \vec{p}) &= -\frac{c}{n_o}\mu_T\, W_P(\vec{x}, \vec{p}) + \int d^3\vec{p}\,' K_N(\vec{p}, \vec{p}\,')\, W_P(\vec{x}, \vec{p}) \\ &+ \int d^3\vec{p}\,' K_N(\vec{p}, \vec{p}\,')\, W_{BALL}(\vec{x}, \vec{p}\,'). \end{aligned} \tag{6.26}$$

The last term on the right hand side in Eq. 6.26 arises from small angle scattering of the ballistic phase space distribution. It acts as the source for the pedestal. The first integral term on the right hand side describes multiple scattering of the phase space distribution of the pedestal. This equation can be straightforwardly solved by Green's function methods as shown below.

Similarly, the broad phase space component obeys the equation

$$\begin{aligned} \frac{c\vec{p}}{n_o k} \cdot \vec{\nabla}_{\vec{x}}\, W_B(\vec{x}, \vec{p}) &= -\frac{c}{n_o}\mu_T\, W_B(\vec{x}, \vec{p}) + \int d^3\vec{p}\,' \left[K_N(\vec{p}, \vec{p}\,') \;+\; K_B(\vec{p}, \vec{p}\,')\right] W_B(\vec{x}, \vec{p}\,') \\ &+ \int d^3\vec{p}\,'\, K_B(\vec{p}, \vec{p}\,')\, [W_{BALL}(\vec{x}, \vec{p}\,') \;+\; W_P(\vec{x}, \vec{p}\,')]. \end{aligned} \tag{6.27}$$

The first integral term on the right hand side of Eq. 6.27 contains the large angle scattering kernel that causes multiple scattering of the broad phase space distribution. The narrow kernel causes scattering within W_B and does not cause attenuation of W_B. In this case, the decay rate of W_B is approximately $(c/n_o)\mu_T - \int d^3\vec{p}\,' K(\vec{p}, \vec{p}\,')$. Large angle scattering of the ballistic and narrow pedestal distributions acts as the source for the broad component of the phase space distribution. The sum of Eq.'s 6.25, 6.26, and 6.27 reproduces Eq. 6.24 with the two component kernel. Eq. 6.27 will not be needed, as the phase space distribution for the narrow pedestal, W_P is of interest here.

The phase space distribution for the ballistic component obtained by solving Eq. 6.25 is given by

$$W_{BALL}(z,\vec{x}_\perp;\vec{p}) \simeq \exp(-\mu_T z)\, W^0_{BALL}(z=0,\vec{x}_\perp - \frac{z}{k}\vec{p}_\perp;\vec{p}). \tag{6.28}$$

Here, we have assumed that the input beam is a collimated gaussian laser beam with a half width at 1/e intensity a and that $p_z \simeq k$ and $v_z \simeq c/n_o$. The input distribution just inside the medium at $z=0$ is given by

$$W^0_{BALL}(z=0,\vec{x}_\perp;\vec{p}) \simeq \delta(p_z-k)\frac{1}{\pi^2}\exp\left(-\frac{x^2+y^2}{a^2} - a^2(p_x^2+p_y^2)\right). \tag{6.29}$$

Note that W^0_{BALL} is normalized so that $\int d^2\vec{x}_\perp d^3\vec{p}\, W^0_{BALL}(\vec{x},\vec{p}) = 1$. The total extinction coefficient $\mu_T = \rho\sigma_T$ in Eq. 6.28 arises from the total scattering cross section and absorption.

The distribution for the diffractive pedestal, W_P is readily found using a Green's function method to solve Eq. 6.26 With Eq. 6.28 for the ballistic component, the source term for the phase space distribution of the narrow pedestal in Eq. 6.26 is given by

$$S(\vec{x},\vec{p}) = \int d^3\vec{p}'\, K_N(\vec{p},\vec{p}')\, W_{BALL}(\vec{x},\vec{p}'). \tag{6.30}$$

The phase space distribution for the narrow pedestal of Eq. 6.26 is given by

$$W_P(\vec{x},\vec{p}) = \int d^3\vec{x}' d^3\vec{p}'\, G_p(\vec{x},\vec{x}\,';\vec{p},\vec{p}')\, S(\vec{x}\,',\vec{p}'). \tag{6.31}$$

Where the Green's function (Eq. 6.13) takes the general form

$$\begin{aligned} G_p(\vec{x},\vec{x}\,';\vec{p},\vec{p}') &= \int \frac{d^3\vec{q}}{(2\pi)^3}\int \frac{d^3\vec{r}}{(2\pi)^3}\exp\left(i\vec{q}\cdot(\vec{x}-\vec{x}\,') + i\vec{r}\cdot(\vec{p}-\vec{p}\,')\right) \\ &\times \frac{n_o}{c}\int_0^\infty dl\, \exp(-il\vec{q}\cdot\vec{p}\,'/k)\, exp\left[-\int_0^l dl'\, \tilde{\mu}(\vec{r}+\vec{q}l'/k)\right], \end{aligned} \tag{6.32}$$

In order to obtain an explicit form of the Green's function for the pedestal G_p an expression for the scattering kernel is needed. The diffractive component of the Mie scattering solution is approximately gaussian in shape, and yields a differential cross section of the form

$$|f(\vec{p},\vec{p}\,')|^2 = \frac{d\sigma}{d\Omega} = \frac{\sigma_N}{\pi\theta_o^2}\exp\left[-\frac{(\Delta\vec{p}_\perp)^2}{\theta_o^2 p^2}\right]. \tag{6.33}$$

Here, σ_N is the cross section for diffractive scattering. θ_o is the scattering diffraction angle, of order $\theta_o \simeq 2/(ka_S)$, where a_S is the radius of the scatterer and $p = k = n_o\omega/c$ is the wavevector in the medium. The scattering angle is $\theta = |\Delta\vec{p}_\perp|/p$ where $\Delta\vec{p}_\perp = \vec{p}_\perp - \vec{p}\,'_\perp$ is the momentum change transverse to the ẑ direction. The differential cross section is normalized so that

$$\int d\Omega \frac{d\sigma}{d\Omega} \simeq \int_0^\infty 2\pi\theta\, d\theta \frac{\sigma_N}{\pi\theta_o^2}\, exp\left[-\frac{\theta^2}{\theta_o^2}\right] = \sigma_N.$$

Using Eq. 6.33, the collision kernel (Eq. 6.9) can be simplified for small angle scattering. With $\delta(\vec{p}^{\,2}/2 - \vec{p}\,'^{\,2}/2) = \delta(p - p')/k \simeq \delta(p_z - p'_z)/k$, the collision kernel K_N takes the approximate form:

$$K_N(\vec{p},\vec{p}\,') \simeq K_N(\vec{p}-\vec{p}\,') = \frac{c}{n_o}\mu_N\,\delta(p_z - p'_z)\,\frac{1}{\pi\theta_o^2 k^2}\exp\left[-\frac{(\Delta\vec{p}_\perp)^2}{\theta_o^2 p^2}\right] \tag{6.34}$$

where $\mu_N = \rho\sigma_N$ is the attenuation coefficient for diffractive scattering. The diffractive kernel is normalized so that

$$\int d^3\Delta\vec{p}\, K_N(\Delta\vec{p}) = \frac{c}{n_o}\mu_N. \tag{6.35}$$

With this approximate kernel, the Green's function, Eq. 6.13, is determined using $\tilde{\mu}(\vec{r})$, Eq. 6.14. In this case, $\tilde{\mu}(\vec{r})$ is independent of r_z, so that

$$\tilde{\mu}(\vec{r}_\perp) = \mu_T - \mu_N\exp\left[-\frac{\theta_o^2 k^2}{4}(r_x^2 + r_y^2)\right] \equiv \mu_T - \tilde{K}'(\vec{r}_\perp). \tag{6.36}$$

The source for the narrow pedestal, $S(\vec{x},\vec{p})$, Eq. 6.30, is

$$S(\vec{x},\vec{p}) = \frac{c}{n_o}\mu_N\,\frac{\exp(-\mu_T z)}{\pi a^2}\exp\left[-\frac{x^2+y^2}{a^2}\right]\frac{\delta(p_z - k)}{\pi\theta_o^2 k^2}\exp\left[-\frac{p_x^2+p_y^2}{\theta_o^2 k^2}\right]. \tag{6.37}$$

Here, we have assumed that the input field 1/e radius, a, is sufficiently large that the diffraction angle of the input field $2/(ka)$, satisfies $2/(ka) << \theta_o$, as is the case in our experiments. Note that the source is nonzero only in the medium, so that $0 \leq z \leq L$, where $z = L$ is the output face of the sample.

The phase space distribution for the pedestal, W_P is now easily determined from Eq. 6.31. Since $\tilde{\mu}(\vec{r}_\perp)$ (Eq. 6.14) is independent of r_z, the r_z and q_z integrals in the Green's function (Eq. 6.13) are readily carried out and yield delta functions, $\delta(p_z - p_z')$ and $\delta[l - (z - z')k/p_z']$. With the source function, Eq. 6.37, $p_z' = k$ so that $l = z - z' = L - z'$ for $z = L$. Using Eq.s 6.15 and 6.36 for $\tilde{K}'(\vec{r}_\perp)$, it is straightforward to obtain

$$\begin{aligned} W_P(L, \vec{x}_\perp; \vec{p}) \;&=\; \delta(p_z - k)\, \exp(-\mu_T L) \\ &\times \int \frac{d^2\vec{q}_\perp}{(2\pi)^2}\, \exp(i\vec{q}_\perp \cdot \vec{x}_\perp) \int \frac{d^2\vec{r}_\perp}{(2\pi)^2}\, \exp\left(i\vec{r}_\perp \cdot \vec{p}_\perp - a_\perp^2 \vec{q}^{\,2}/4\right) \\ &\times \int_0^L dz'\, \tilde{K}'[\vec{r}_\perp + (L - z')\vec{q}_\perp/k]\, \exp\left[\int_0^{L-z'} dl'\, \tilde{K}'(\vec{r}_\perp + \vec{q}_\perp l'/k)\right] \end{aligned} \tag{6.38}$$

The z' integral in Eq. 6.38 is just

$$\exp\left[\int_0^L dl'\, \tilde{K}'(\vec{r}_\perp + \vec{q}_\perp l'/k)\right] - 1.$$

Hence, the phase space density, W_P, is given by

$$\begin{aligned} W_P(L, \vec{x}_\perp; \vec{p}) \;&=\; \delta(p_z - k)\, \exp(-\mu_T L) \int \frac{d^2\vec{q}_\perp}{(2\pi)^2}\, \exp\left(i\vec{q}_\perp \cdot \vec{x}_\perp - a_\perp^2 \vec{q}^{\,2}/4\right) \\ &\times \int \frac{d^2\vec{r}_\perp}{(2\pi)^2}\, \exp(i\vec{r}_\perp \cdot \vec{p}_\perp) \left\{\exp\left[\int_0^L dl'\, \tilde{K}'(\vec{r}_\perp + \vec{q}_\perp l'/k)\right] - 1\right\}. \end{aligned} \tag{6.39}$$

As shown in Equation 6.1 the heterodyne signal measures the convolution of transverse Wigner phase space distributions. For the phase space distribution of the pedestal, the transverse distribution at the detection plane $W_P(L, \vec{x}_\perp, \vec{p}_\perp)$ is given by

$$W_P(L, \vec{x}_\perp; \vec{p}) = \delta(p_z - k)\, W_P(L, \vec{x}_\perp, \vec{p}_\perp). \tag{6.40}$$

To check the normalization of $W_P(L, \vec{x}_\perp, \vec{p}_\perp)$, note that integrating Eq. 6.39 over $\vec{x}_\perp$ and $\vec{p}_\perp$ yields delta functions in $\vec{q}_\perp$ and $\vec{r}_\perp$. Using $\tilde{K}'(0) = \mu_N$ which follows from Eq. 6.14, one then obtains

$$\begin{aligned} \int d^2\vec{x}_\perp \int d^2\vec{p}_\perp \, W(L, \vec{x}_\perp, \vec{p}_\perp) &= \exp(-\mu_T L)\, (\exp(\mu_N L) - 1) \\ &= \exp(-\mu_B L) - \exp(-\mu_T L). \end{aligned} \tag{6.41}$$

Here, $\mu_B \equiv \mu_T - \mu_N$ is the attenuation coefficient arising from large angle scattering and absorption, i.e., the minimum attenuation rate for the pedestal phase space distribution. This attenuation rate occurs when the pedestal is broad in transverse momentum compared to the diffractive kernel, but narrow compared to the large angle scattering kernel. In this case, large angle collisions and absorption are effective in attenuating W_P but diffractive collisions are ineffective, as they cause scattering *within* the distribution. The source of the pedestal is just the diffractive scattering probability $\mu_N dz'$ times the intensity of the ballistic component, $\exp(-\mu_T z')$. The pedestal contribution decays as $\exp[-\mu_B(L - z')]$. Hence, one expects an integrated output intensity given by

$$\int_0^L dz' \mu_N \, \exp(-\mu_T L) \, \exp[-\mu_B(L - z')] = \exp(-\mu_B L) - \exp(-\mu_T L), \tag{6.42}$$

in agreement with Eq. 6.41.

When the input field 1/e radius a is sufficiently large that $a/L >> \theta_o$, Eq. 6.39 can be further simplified. Note that $q_\perp \simeq 1/a$ and l' is at most L in the argument of $\tilde{K}'$. Then the maximum value of $q_\perp l'/k$ is $L/(ka)$. The maximum value of $r_\perp$ is of order $2/(k\theta_o)$, since $\tilde{K}' \rightarrow 0$ if $\vec{r}_\perp > 2/(k\theta_o)$. If $a/L >> \theta_o$, the $\vec{q}_\perp$ dependence in the argument of $\tilde{K}'$ can be neglected and the $\vec{q}_\perp$ integral performed to obtain a gaussian spatial distribution identical to that of the input field. This is consistent with the assumption of a being large enough to achieve approximate translation invariance.

The phase space distribution for the pedestal then takes the simple form

$$\begin{aligned} W_P(L,\vec{x}_\perp,\vec{p}_\perp) &= \frac{\exp(-\vec{x}_\perp^{\,2}/a^2)}{\pi a^2}\exp(-\mu_T L) \qquad (6.43)\\ &\times\int\frac{d^2\vec{r}_\perp}{(2\pi)^2}\exp(i\vec{r}_\perp\cdot\vec{p}_\perp)\left\{\exp\left[\mu_N L\,\exp\left(-\frac{\theta_o^2k^2\vec{r}_\perp^{\,2}}{4}\right)\right]-1\right\}. \end{aligned}$$

In the limit that $\mu_N L >> 1$, the gaussian in the exponent appearing in Eq. 6.43 can be expanded to lowest order in $\vec{r}_\perp^2$ to give a gaussian function of $r_\perp$ for which the 1/e width is of order $2(\theta_o k\sqrt{\mu_N L})^{-1}$. In this limit, multiple diffractive scattering causes momentum diffusion. As long as $(a/L)^2 >> \mu_N L(\theta_o k/2)^2$, i.e.e, the mean square width of the momentum distribution for $\mu_N L$ scatterings is smaller than the mean square angular aperture of the illuminated volume, the approximations used to obtain Eq. 6.43 remain valid.

The $\vec{r}_\perp$ integral in Eq. 6.43 can be simplified by introducing the dimensionless variable $\vec{\eta}_\perp \equiv \theta_o k\vec{r}_\perp/2$ Using $\vec{\eta}_\perp\cdot\vec{p}_\perp = \eta_\perp p_\perp\cos\phi$ and $d_\perp^2\vec{\eta} = \eta_\perp d\eta_\perp d\phi$, we have η

$$\int_0^{2\pi}\frac{d\phi}{2\pi}\exp\left(i\frac{2p_\perp}{\theta_o k}\eta_\perp\cos\phi\right) = J_0\left(\eta_\perp\frac{2p_\perp}{\theta_o k}\right).$$

Then, the transverse Wigner distribution for the pedestal is given by

$$\begin{aligned} W_P(L,x_\perp,p_\perp) &= \frac{\exp(-x_\perp^2/a^2)}{\pi^2\theta_o^2k^2a^2}\exp(-\mu_T L) \qquad (6.44)\\ &\times\int_0^\infty d\eta_\perp\,2\eta_\perp\,J_0\left(\eta_\perp\frac{2p_\perp}{\theta_o k}\right)\left\{\exp\left[\mu_N L\,\exp(-\eta_\perp^2)\right]-1\right\}. \end{aligned}$$

Here, the transverse position is $x_\perp = \sqrt{x^2+y^2}$ and similarly for the transverse momentum $p_\perp$. The normalization of Eq. 6.44 is identical to that of Eq. 6.41, as is readily shown using

$$\int d^2\vec{p}_\perp\,J_0\left(\eta_\perp\frac{2p_\perp}{\theta_o k}\right) = \frac{\pi}{2}\theta_o^2k^2\frac{\delta(\eta_\perp)}{\eta_\perp}.$$

For the 11.4 μm spheres, the scattering diffraction angle obtained from the Mie solution is $\theta_o = 23.2$ mrad. The extinction coefficient $\mu_N = 0.35\,\mu_S$ arises from diffractive scattering only, where $\mu_S = \rho\sigma_S$ is the extinction coefficient corresponding to the total scattering cross section, i.e., the ballistic extinction coefficient excluding absorption.

Recalling Eq. 6.1, the expression for the measured mean square beat signal when a coherent source is used is given in terms of the transverse Wigner distributions for the LO and signal fields as

$$S(d_x\hat{x}, d_p\hat{x}) = \int d^2_\perp\vec{x}\, d^2_\perp\vec{p}\, W_{LO}(\vec{x}_\perp - d_x\hat{x}, \vec{p}_\perp + \frac{k}{f}d_p\hat{x})\, W_S(\vec{x}_\perp, \vec{p}_\perp). \tag{6.45}$$

With the LO displaced in position and momentum along the $\hat{x}$ axis only, the transverse Wigner distribution for the LO field is given by

$$\begin{aligned} W_{LO}(\vec{x}_\perp - d_x\hat{x}, \vec{p}_\perp - d_p\frac{k}{f_o}\hat{x}) \quad &= \quad \frac{1}{\pi^2}\exp\left[-\frac{(x-d_x)^2 + y^2}{a_o^2}\right] \\ &\quad \times \exp\left[-a_o^2\left((p_x - d_p\frac{k}{f_o})^2 + p_y^2\right)\right]. \end{aligned} \tag{6.46}$$

The measurements in this specific case are carried out using an LO half width at 1/e intensity a_o that is small compared to the spatial extent of the signal field, so that $a_o << a$. Further, the diffraction angle of the LO is small compared to the scattering diffraction angle, $2/(ka_o) << \theta_o$. Thus, the Wigner distribution of the LO is sharply peaked both in position and momentum compared to that of the scattered signal field. Since the LO Wigner distribution of Eq. 6.46 is normalized to unity, the mean square beat signal for the pedestal can be evaluated using Eq. 6.45 with Eq. 6.46 given by the approximation

$$W_{LO}(\vec{x}_\perp - d_x\hat{x}, \vec{p}_\perp - d_p\frac{k}{f_o}\hat{x}) \simeq \delta(x - d_x)\,\delta(y)\,\delta(p_x - d_p\frac{k}{f_o})\,\delta(p_y). \tag{6.47}$$

Hence, we obtain

$$S_P(x_M, p_M) = W_P(L, x = d_x, y = 0; p_x = d_p\frac{k}{f_o}, p_y = 0), \tag{6.48}$$

where we take $p_\perp = \sqrt{p_x^2 + p_y^2} = |d_p k/f_o|$ in the transverse Wigner distribution for the pedestal, W_P.

As a reference level, the ballistic contribution to the mean square beat signal is determined by using Eq. 's 6.28, 6.29, and 6.46 in Eq. 6.45:

$$S_{BALL}(x_M, p_M) = \frac{a_o^2}{\pi^2 a^2} \exp\left[-a_o^2 p_M^2 - \frac{x_M^2}{a^2}\right] \exp(-\mu_T L). \tag{6.49}$$

Diffraction of the input beam is negligible in the experiments and is therefore not included in Eq. 6.49.

The experimental data in section 6.2.2 show measured smoothed Wigner phase space distributions that are plotted as the mean square beat signal divided by the maximum ballistic mean square beat signal (for zero concentration at $x = p = 0$). The latter is given by

$$S_{MBALL} = \eta_{het}^2 \frac{a_o^2}{\pi^2 a^2}, \tag{6.50}$$

where η_{het} is the heterodyne efficiency for detection of the ballistic light. In the experiments, $a/a_o = 10$ and the heterodyne efficiency is found to be 0.4, due to difficulty in matching wavefront curvatures for beams of such disparate diameters. For the pedestal, only scattered light that is mode matched to the LO is detected. Thus, the heterodyne efficiency for detection of the scattered light is unity.

With Eq. 6.44 and Eq. 6.48, the smoothed Wigner distribution for the pedestal and the diffuse background normalized to S_{MBALL} is given by

$$\frac{S(x_M = 0, p_M)}{S_{MBALL}} = A(\rho)\, F_P(p_\perp, \rho) \;+\; B \exp\left(-p_\perp^2/(\Delta p_B)^2\right) \tag{6.51}$$

Here, B is the amplitude and Δp_B is the width of the broad background component that is fit to the data. $A(\rho)$ is the magnitude of the pedestal mean square beat signal normalized to S_{MBALL}:

$$A(\rho) = \frac{\exp(-\mu_T L)}{\eta_{Het}^2 \theta_o^2 k^2 a_o^2} \int_0^\infty d\eta_\perp\, 2\eta_\perp \left\{\exp\left[\mu_N L \exp(-\eta_\perp^2)\right] - 1\right\}. \tag{6.52}$$

$F_P(p_\perp)$ is the shape of the pedestal normalized to 1 at $p_\perp = 0$:

$$F_P(p_\perp) = \frac{W_P(x_\perp = 0, p_\perp)}{W_P(x_\perp = 0, p_\perp = 0)}, \tag{6.53}$$

where $W_P(x_\perp, p_\perp)$ is given by Eq. 6.44. This theoretical result was found to agree very well with the data presented in section 6.2.2 as discussed below.

6.4 Discussion

Eq. 6.44 describes the Wigner phase space distribution, $W_P(x_\perp, p_\perp)$ for a pedestal that arises from multiple diffractive scattering. This pedestal has a much broader momentum distribution than the Wigner distribution for the ballistically transmitted field from which it arises.

Eq. 6.44 has a simple physical interpretation. $W_P(x_\perp, p_\perp)$ can be expanded as a power series in $\mu_N L$ that explicitly displays the distributions for various numbers of multiple scatterings:

$$\begin{aligned} W_P(L, x_\perp, p_\perp) &= \frac{\exp(-x_\perp^2/a^2)}{\pi a^2} \exp(-(\mu_T - \mu_N)L) \\ &\times \sum_{n=1}^{\infty} \exp(-\mu_N L) \frac{(\mu_N L)^n}{n!} \frac{\exp[-p_\perp^2/(n\theta_o^2 k^2)]}{\pi n \theta_o^2 k^2}. \end{aligned} \tag{6.54}$$

Note that $x_\perp = \sqrt{x^2 + y^2}$ and similarly for $p_\perp$. For each term, there is a normalized gaussian momentum distribution of width $\theta_o k \sqrt{n}$ in the x and y directions. This describes a random walk distribution for n momentum changes of magnitude $\theta_o k$. $\exp(-\mu_N L)(\mu_N L)^n/n!$ is a Poisson distribution describing the probability of n scatterings, with $\bar{n} = \mu_N L$ the mean number of scattering events. With $\exp(-\mu_N L)$ incorporated into the probability of n scatterings, the pedestal decays as $\exp[-(\mu_T - \mu_N)L]$. The factor $\mu_B = \mu_T - \mu_N$ is just the extinction coefficient arising from large angle scattering (and absorption).

Note that the missing $n = 0$ term in Eq. 6.54 that is nonzero for $\mu_N L = 0$ represents the ballistic contribution that was treated separately in determining the mean square beat signals of Eq. 6.1. Separation of these contributions is convenient since the momentum distribution of the ballistically transmitted light is narrow compared to that of the local oscillator (LO) beam while the momentum distribution for W_P is broad compared to that of the LO for the conditions of the experiment..

For $\mu_N L >> 1$, W_P is approximately a single gaussian distribution. In this case, we can approximate

$$\exp[\mu_N L \, \exp(-\eta_\perp^2)] - 1 \simeq \exp[\mu_N L(1 - \eta_\perp^2)].$$

Here, $\mu_N L >> 1$ assures that $\eta_\perp^2 << 1$ over the dominant region of integration. In this limit, the Wigner distribution for the pedestal is given by

$$W_P(L, x_\perp, p_\perp) = \frac{\exp - x^2/a^2}{\pi a^2} \, \exp(-(\mu_T - \mu_N)L) \, \frac{\exp[-p^2/(\mu_N L \theta_o^2 k^2)]}{\pi \mu_N L \theta_o^2 k^2} \tag{6.55}$$

Eq. 6.55 describes a momentum distribution for a random walk with $\bar{n} = \mu_N L$ steps of size $\theta_o k$. This result arises because the width $\sqrt{\bar{n}}$ of the Poisson distribution of Eq. 6.54 is small compared to $\bar{n}$ for $\bar{n} >> 1$. Hence, the term in Eq. 6.54 with $n = \bar{n}$ dominates, yielding Eq. 6.55. Neglecting absorption, the pedestal decays as $\mu_T - \mu_N = \mu_B$, the extinction coefficient arising from large angle scattering, as described above. Note that Eq.'s 6.54 and 6.55 are valid only for small angle scattering. Further, the input beam half width at 1/e intensity, a, must be large enough so that $\theta_o \sqrt{\mu_N L} << a/L$. Hence, there is negligible expansion of the input beam.

Theoretical Wigner phase space distributions $S(x = 0, p)$ have been fit to the data of Fig.'s 6.5 - 6.7 using Eq. 6.51. The fits are shown as smooth curves. The broad background is fit using the phenomenological constants B and Δp_B and is not of interest here. However, the shape of the narrow pedestal is obtained from the Eq. 6.53 using the experimentally determined parameters: LO half width at 1/e $a_o = 0.38$ mm, half width at 1/e for the input beam to the sample $a = 3.8$ mm, and cell length $L = 1$ cm. The index of refraction of the background medium is $n_o = 1.36$. The optical wavevector in the medium is $k = n_o k_o$ where $k_o = 2\pi/\lambda_o$ is the wavevector in the air, with $\lambda_o = 0.63\,\mu$m the HeNe laser wavelength. The heterodyne efficiency defined in Eq. 6.50 is $\eta_{het} = 0.4$. From the Mie solution, Fig. 6.2, we find that the half width at 1/e of the central diffractive peak in the medium is $\theta_o = 23.2$ mrad. The total scattering cross section, $\sigma_S = 202\,\mu\text{m}^2$. The diffractive cross section σ_N is estimated from the area under the diffractive peak (for $0 \leq \theta \leq 0.1$ rad) to be $0.35\,\sigma_S$, while the remaining classical scattering cross section, obtained by integrating the differential cross section from $\theta = 0.1$ to π rad is found to be $0.65\,\sigma_S$. The density ρ of scatterers is determined from the known volume fraction of the polystyrene spheres. Initially, the amplitude of the narrow pedestal $A(\rho)$ is taken to be a free parameter that yields the best fits to the data. The figures show that very good fits are obtained.

Fig. 6.8 shows the amplitude $A(\rho)$ obtained from the fits as a function of scatterer concentration, ρ. Also shown is the prediction, based on Eq. 6.52. The prediction for the amplitude of the pedestal that arises from multiple diffractive scattering is found to be in very good agreement with the data using no free parameters.

For comparison, the decay of the ballistic signal with scatterer concentration is shown in Fig. 6.9. The ballistic signal decays exponentially according to $\exp(-\mu_S L)$, where $\mu_S = \rho\sigma_S$ as expected. By contrast, the pedestal arising from near forward diffractive scattering decays much more slowly, as shown in Fig. 6.8. For concentrations beyond the maximum amplitude, this signal decays approximately exponentially with an attenuation coefficient, $\mu_B = 0.65\mu_S$.

It is not difficult to understand why the diffractive pedestal decays more slowly than the ballistic signal. Diffractive momentum changes tend to scatter photons within the momentum distribution of the diffractive pedestal. Only large momentum changes are effective in scattering photons outside the momentum distribution of the pedestal. Hence, the pedestal decays with the attenuation coefficient μ_B that arises from the large angle scattering cross section. By contrast, both small and large angle momentum changes are effective in scattering photons out of the very narrow momentum distribution of the ballistic light. Hence, the ballistic distribution must decay with the extinction coefficient corresponding to the total scattering cross section, μ_S.

Chapter 7

Low order scattering in transmission

This chapter presents a transmission study of optical phase space distributions using a low coherence length light source to generate the input beam to the turbid sample. Use of a low coherence length source in the heterodyne scheme permits selection of photon path lengths within the medium, effectively giving timing resolution. This capability is exploited to separate ballistic and low order scattered light from multiply scattered diffuse light.

The first section of this chapter begins by describing the configuration of the heterodyne scheme for use of a low coherence source. The section also includes the specific parameters of the turbid medium used in this study. The next section presents measured optical phase space distributions for low coherence light transmitted through a turbid medium. The data are presented for various concentrations of scatterers, different input beam diameters and as a function of the photon path length within the medium. Although no detailed theory has been developed to fully explain this data, certain trends in the data are identified. A discussion of these trends is presented in the final section of this chapter.

7.1 Experimental Setup

7.1.1 Heterodyne detection scheme for a low coherence source

The experimental scheme configured for transmission experiments using a low coherence source is shown in Figure 7.1. In this arrangement, the low coherence length signal beam at center frequency ω is incident on a scattering sample. The light transmitted through the sample is mixed with a strong local oscillator LO at center

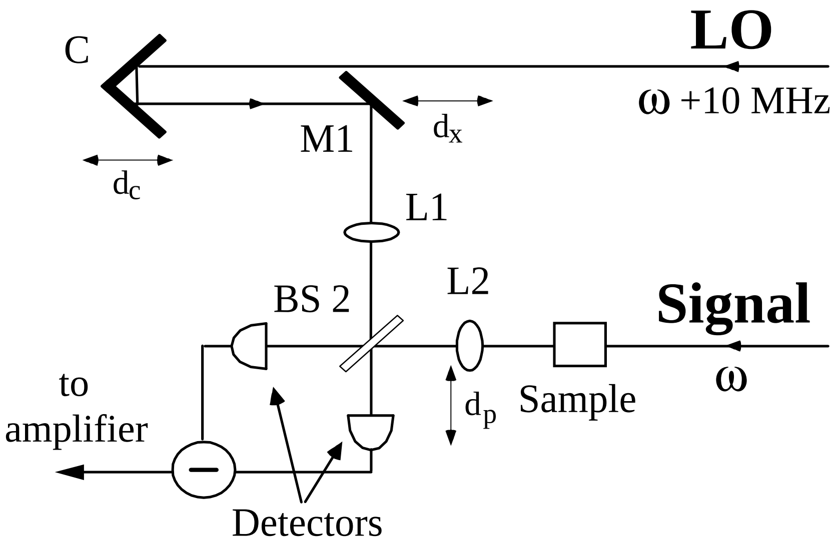

Figure 7.1: Experimental scheme configured for transmission experiments using a low coherence source.

frequency $\omega + 10$ MHz at beamsplitter BS2. A heterodyne beat signal is produced when the optical path lengths of the LO beam and the light emerging from the sample are matched to within the coherence length of the source. The LO path length can be varied by moving retroreflector, C, by a distance d_c. This permits selective detection of the light transmitted through the sample by its path length within the medium. In addition, scanning mirror M1 by a distance d_x and lens L2 by a distance d_p, allows the effective center position and momentum of the LO to be varied respectively. Thus the optical phase space distribution of the signal field is mapped out as a function of LO position and momentum for a given path length. Scanning mirror M1 and lens L2 also introduces changes in optical path lengths. These changes must be compensated for in order to keep the relative path difference between the LO and signal paths constant. The path difference between the two paths is given by Eq.

4.28 as

$$\Delta l' = \Delta l + \frac{d_p^2}{2f_o} - \frac{d_x d_p}{f_o}, \tag{7.1}$$

where $\Delta l = 2d_c$ and f_o is the focal length of the imaging lenses L1 and L2. The mathematical derivation and physical origin of these two correction terms is given in section 4.1.2.

The measured mean square heterodyne beat signal can be given in terms of the overlap of the Wigner distribution of the signal field and that of an effective LO field

$$\begin{aligned} |V_B(d_x, d_p, \Delta l')|^2 &= \int d\omega_k \int dx \int dp \, \langle W_S(x, z_o, \omega_k) \\ &\quad \times W'_{LO}(x + d_x, z_o + \Delta l'; p + d_p k/f_o, \omega_k)\rangle \, . \end{aligned} \tag{7.2}$$

In this expression, $W_S(x, z_o, \omega_k)$ is the Wigner distribution for the frequency component ω_k of the signal field specified in the input plane, i.e. in the principal plane of lens L2 as discussed in section 4.1.3. The Wigner distribution for the effective LO field is also specified in the input plane (principal plane of lens L1) but includes the shifts d_x, d_p, and $\Delta l'$ which allow the center position, momentum and path delay of the LO beam to be varied. The amplitude of the effective LO field is given in Eq. 4.30 as

$$\begin{aligned} \mathcal{E}'^{\,*}_{k_{LO}}(x' + d_x, \Delta l', d_p) &= \mathcal{E}^*_{k_{LO}}(x' + d_x, z = 0)e^{-i\omega_k \Delta l/c} \\ &\times \; \exp(-ik\frac{d_p^2}{2f_o}) \exp(ik\frac{d_p}{f_o}x'). \end{aligned} \tag{7.3}$$

As discussed in section 4.1.2, in order to rigorously calculate heterodyne beat signals for low coherence light, the beat signal given in terms of fields is needed. The expression is given in Eq. 4.27 as

$$\begin{aligned} |V_B(d_x, d_p, \Delta l)|^2 \;\propto\; &\left| \int dx' \int d\omega_k \mathcal{E}^*_{k_{LO}}(x' + d_x, z = 0)e^{-i\omega_k \Delta l/c} \, \mathcal{E}_{k_S}(x', z = 0) \right. \\ &\left. \times \exp(-ik\frac{d_p^2}{2f_o}) \exp(ik\frac{d_p}{f_o}x') \right|^2 . \end{aligned} \tag{7.4}$$

This can be simplified by using the definition of the effective LO field (Eq. 7.3) to yield

$$|V_B(d_x, d_p, \Delta l')|^2 \propto \left| \int dx' \int d\omega_k \mathcal{E}'^{*}_{k_{LO}}(x' + d_x, \Delta l', d_p)\, \mathcal{E}_{k_S}(x', z = 0) \right|^2 \tag{7.5}$$

as given in Eq. 4.29.

7.1.2 Turbid medium

For the low coherence source transmission experiments, slightly smaller spheres (radius = 4.9 μm) are used than those in the coherent source experiments. This is simply due to variations in the sizes available from the manufacturers which were found to vary up to 10%. The latex microspheres ($n = 1.59$) are suspended in a mixture of 25% glycerol and 75% water which provides neutral buoyancy. As discussed in section 6.1.2, the mixture was found to have an index of ($n = 1.36$). Thus the index of the spheres relative to the background medium is given by $n = 1.17$. In addition, the parameters of the experiment also changed as the low coherence length SLD's have different wavelengths than the HeNe laser beam. The characteristics of the two low coherence sources were discussed in detail in sections 5.2.2 and 5.2.3. Table 5.2 gives a center wavelength of $\lambda_{air} = 832$ nm, for the Sarnoff SLD and $\lambda_{air} = 852$ nm for the Anritsu SLD. As the source and sphere characteristics varied significantly from those in the coherent source experiments, it was necessary to calculate angular scattering characteristics for the new parameters. Although the center wavelength of the Anritsu and Sarnoff SLD's varied by 20 nm, the scattering characteristics were found to be very similar at both wavelengths. The scattering cross section $\sigma_s$was found to be 2.42 times the geometrical cross section, i.e., $\sigma_S = 181\,\mu\text{m}^2$ for an incident wavelength $\lambda_{air} = 852$ nm (for the Anritsu SLD). The scattering cross section is found to be slightly smaller for an incident wavelength of $\lambda_{air} = 832$ nm (for the Sarnoff SLD) but is still $\sigma_S = 181\,\mu\text{m}^2$ to three significant digits. The theoretical

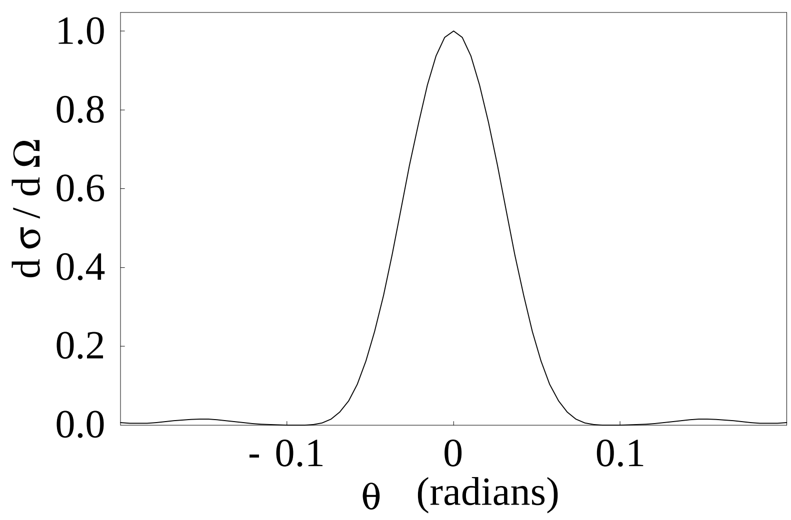

Figure 7.2: Mie differential cross section for scattering from 9.8 μm diameter polystyrene spheres with parameters $n_{rel} = 1.17$, $n_o = 1.36$, and $\lambda_{air} = 852$ nm.

angular distribution (differential cross section) for these spheres is shown in Fig. 7.2.

The angular distribution shown here is very similar to those shown in Fig. 6.2 with slight changes due to the longer wavelength (in this figure $\lambda_{air} = 852$ nm was used). Again, the angles shown in this plot have been multiplied by 1.36 to account for the propagation from the water/glycerol mixture into air where the light is detected. The central peak again is seen to be nominally gaussian. Its half width at $1/e$ is 53.9 mrad which corresponds to a width of 39.6 mrad in the medium. For $\lambda_{air} = 832$ nm, the average of the cosine of the scattering angle was found to be $\langle \cos\theta \rangle = 0.93$ and for $\lambda_{air} = 832$ nm, it was found to be $\langle \cos\theta \rangle = 0.91$. However, the variation is simply due to rounding errors. Both of these values are close to the mean cosine of the scattering angle found for the coherent source. This figure is significant as it indicates that for any of the sources used, the large spheres are highly forward scattering.

7.2 Transmission Data

Measurement of optical phase space distributions with a low coherence source permits selection of the optical path length in the medium for the detected light by changing the LO path outside the medium. Hence, phase space distributions can be obtained for zero path delay to study ballistic propagation and for nonzero path delay to study low order and multiple scattering contributions. In this section data are presented using two low coherence sources. Initially, a superluminescent diode (SLD) from Anritsu was used to perform transmission experiments. Subsequent experiments used an extended bandwidth, high power superluminescent diode from Sarnoff. The characteristics of each of these sources is discussed in detail in Chapter 5 and their properties are summarized in Table 5.2.

7.2.1 Momentum distributions for low order scattering

Initial studies with the Anritsu SLD employed a large diameter ($1/e$ width = 3.1 mm) beam to the turbid sample for comparison to the coherent source data shown in section 6.2.2. The input beam is approximately ten times as large as the LO beam ($1/e$ width = 0.31 mm). The coherence length of this source ($l_c = 31.1.\mu$m from Table 5.2) corresponds to a longitudinal resolution of $\Delta l_B = 26.4$ μm using Eq. 5.17. In this arrangement, the phase space distribution of the field transmitted through a weakly scattering sample of 4.9 μm radius polystyrene spheres at a density of $\rho = 1.5 \times 10^6/\text{cm}^3$ is measured. The ballistic light is attenuated by a factor of $\exp(-2.7)$ at this concentration. Fig. 7.3 shows momentum (angular) scans as a function of path delay $\Delta l'$ with the LO centered at transverse position $d_x = 0$. It shows a two peak structure in the momentum distributions, with the two peaks moving out to larger angles for increasing path delay. A momentum scan is shown

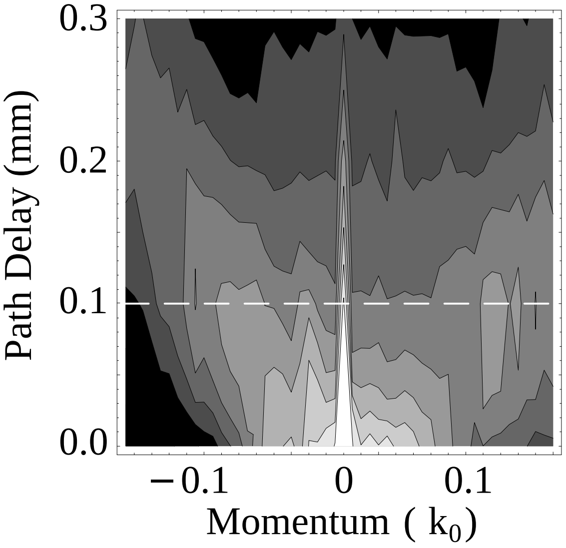

Figure 7.3: Momentum distribution as a function of the path delay between LO and Signal beams (Log scale).

for a path delay $\Delta l' = 0.1$ mm, Fig. 7.4, which corresponds to the slice indicated by the dotted line in Fig. 7.3. The theoretical fit to the data shown in Fig. 7.4, given by Eq. 7.42, is described in more detail in section 7.3.1.

7.2.2 Momentum distributions for thicker samples

Propagation of low coherence light through thicker turbid samples ($\rho = 1.15 \times 10^7/\text{cm}^3$) for the large diameter input beam yields interesting results. At this concentration, the ballistic light is attenuated by a factor of $\exp(-20.6)$. The scattered light has a gaussian angular distribution which increases in width with increasing path delay. Figures 7.5 - 7.7 show typical angular distributions for the scattered light at various LO path delays. For zero LO path delay ($\Delta l' = 0$), Fig. 7.5, the ballistic light can be seen as the point that lies well above the gaussian curve. Increasing the LO path delay results in the gaussian distribution for the momenta of scattered light increasing in width. Fig. 7.6, shows the angular distribution for a LO path delay

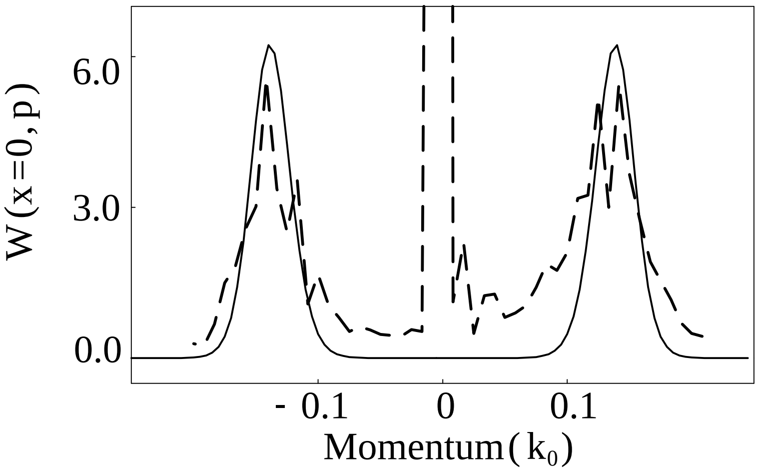

Figure 7.4: Momentum distribution for a 0.1 mm LO path delay relative to signal beam. [Indicated by dotted line in Fig. 7.3]. Dashed line-data; solid line-theory. Vertical scale is 10^{-7} of the signal with no scatterers present.

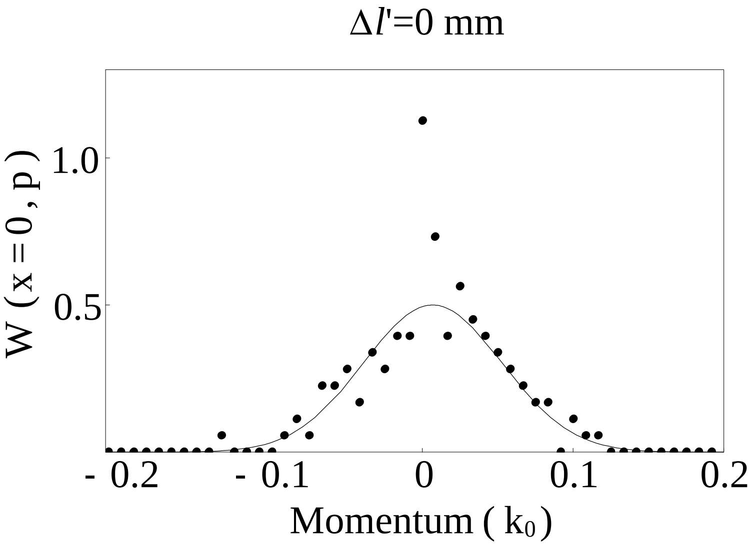

Figure 7.5: Momentum (angular) distribution of scattered light for a path delay $\Delta l' = 0$ mm. Vertical scale is 10^{-9} of the signal with no scatterers present.

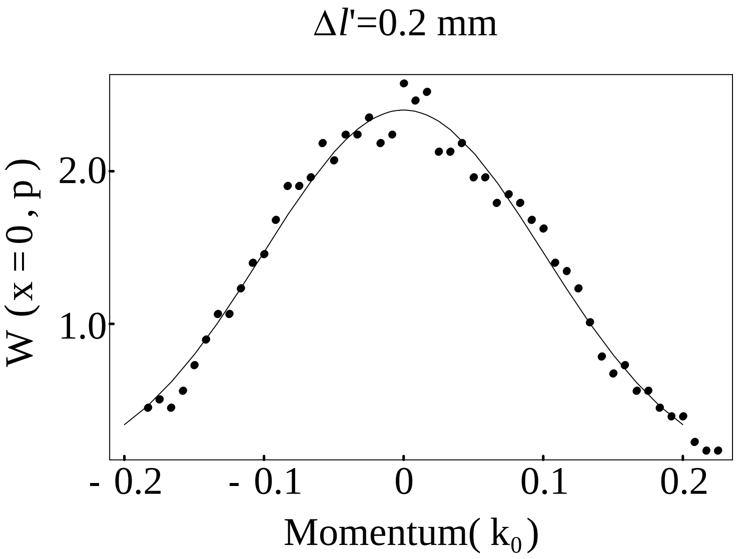

Figure 7.6: Momentum (angular) distribution of scattered light for a path delay $\Delta l' = 0.2$ mm. Vertical scale is 10^{-9} of the signal with no scatterers present.

$\Delta l' = 0.2$ mm and Fig. 7.7 shows the angular distribution for $\Delta l' = 0.4$ mm. An interesting trend becomes evident when one examines the 1/e width of the gaussian distribution as a function of path delay. Fig. 7.8 shows that this width increases linearly with path delay until approximately 300 mrad which represents the maximum angular aperture of our system (Table A.3). In this data, a five-fold increase in the width of the momentum distribution is observed when the optical path length in the medium is increased from 1 cm to 1.06 cm, representing only a 6% increase in path length. As of the time this thesis was written no theory has been developed to explain the transition from ballistic propagation or single scattering to this linear growth regime nor the subsequent transition to the diffusion regime.

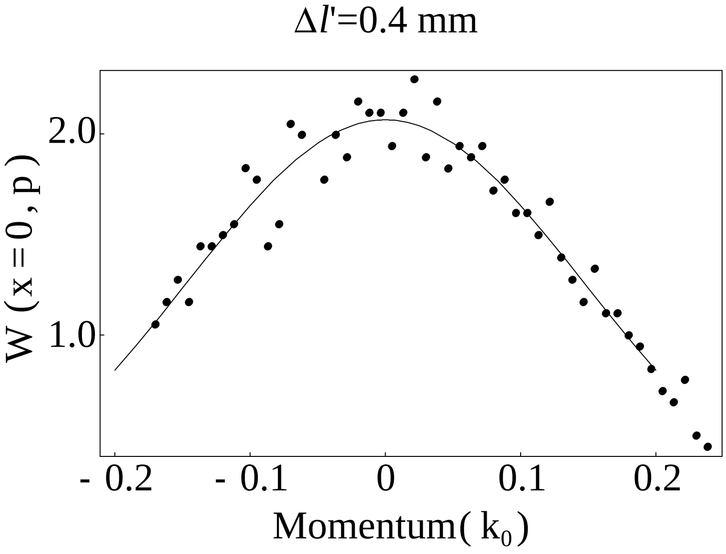

Figure 7.7: Momentum (angular) distribution of scattered light for a path delay $\Delta l' = 0.4$ mm. Vertical scale is 10^{-9} of the signal with no scatterers present.

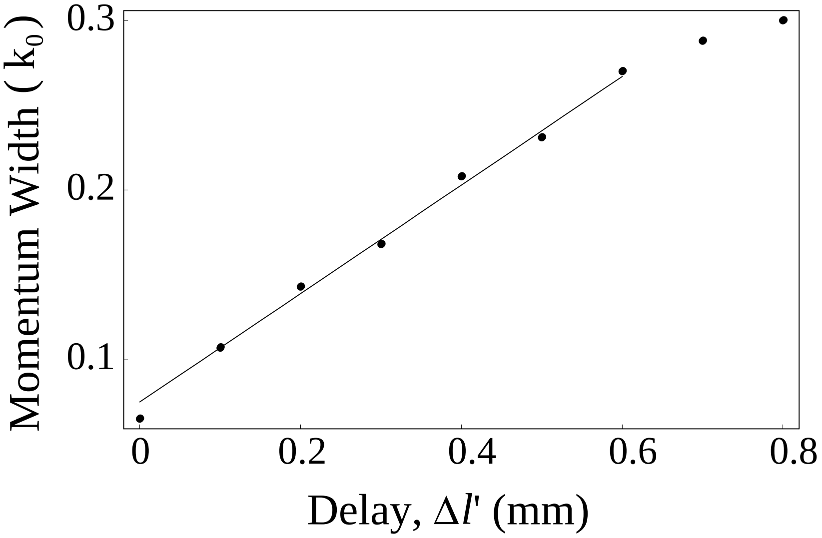

Figure 7.8: Width (half width at $1/e$) of the gaussian distribution of the scattered light as a function of path delay $\Delta l'$.

7.2.3 Time-resolved optical phase space distributions for thin samples

To complete the transmission studies, optical phase space measurements are made for a narrow collimated low coherence length beam transmitted through turbid samples of 4.9 μm radius spheres of various concentrations. In these experiments the high power Sarnoff SLD is used as a light source. The Sarnoff SLD has an extended bandwidth which results in a extremely low coherence length, $l_c = 7\mu$m. This corresponds to a longitudinal resolution of $\Delta l_B = 5.9$ μm by Eq. 5.17. However, as discussed in section 5.2.3, the bandwidth of the optical elements used in the heterodyne imaging system limit the longitudinal resolution to $\Delta l_B = 7.4$ μm. Here the Sarnoff SLD is used to produce signal and LO beams of the same size ($1/e$ width = 0.98 mm). The data in this section consist of longitudinal scans of the LO path delay for zero transverse momentum and position ($x = 0$, $p = 0$) and optical phase space contour plots in position and momentum taken for different LO path delays ($\Delta l'$).

At low concentrations of scatterers, ($\rho = 1 \times 10^6/\text{cm}^3$ to $4 \times 10^6/\text{cm}^3$) the phase space distributions are dominated by ballistic light. These concentrations correspond to ballistic attenuations of $\exp(-1.8)$ to $\exp(-7.2)$ respectively. To characterize the behavior of the transmitted light in this regime, I will use the optical phase space distributions obtained for $\rho = 1.9 \times 10^6/\text{cm}^3$ as an example. Figure 7.9 shows a longitudinal scan as the LO path is lengthened relative to the signal path from 0 to 1 mm for a sample at this concentration (solid line) . This scan is very similar to that for no scatterers but scaled by the overall ballistic attenuation of $\exp(-3.5)$. For comparison, the dashed line in Figure 7.9 shows a scan with the sample cell removed and scaled by this factor. There are noticeable differences between the two scans. First, the scan with the scattering sample present has an increased amplitude for delays of 0.1 to 0.5 mm compared to the scan with the sample removed. This is due

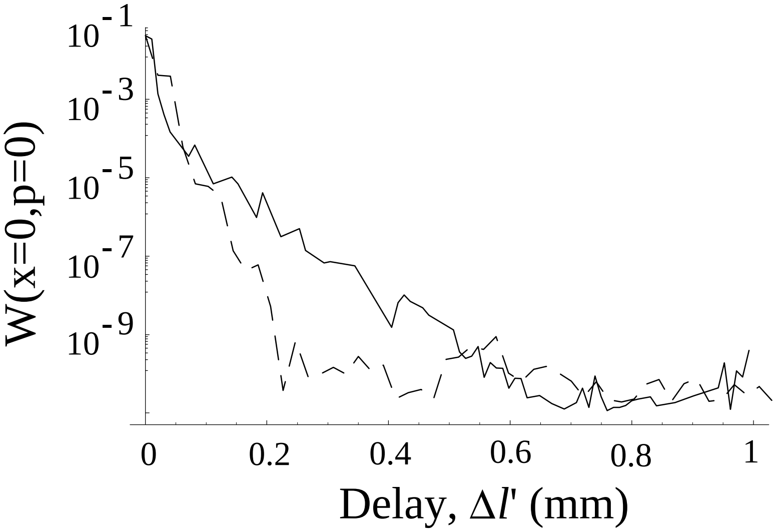

Figure 7.9: Measured optical phase space density at $x = 0$, $p = 0$ as a function of LO path delay. Solid line: $\rho = 1.9 \times 10^6/\text{cm}^3$; dashed line - no sample (ballistic attenuation - $\exp(-3.5)$).

to dispersion introduced by the glass walls of the cell and the background medium of the sample. Phase space measurements in position and momentum confirm that with the scatterers present, the signal at this range of delays is due to ballistic light (shown in the data in Figure 7.11). Second, there are ripples in this scan due to vibrations which arise when the LO path length is scanned. These have been eliminated in the presented data through averaging. The ripples can be avoided by using a slower velocity setting for the translator which controls the LO path delay. However, slowing the velocity causes the longitudinal scans to take much longer. This is unacceptable for collecting turbid media transmission data because long scans permit drifts in optical power.

Figures 7.10-7.12 show optical phase space contour plots for transmission through a scattering sample of concentration $\rho = 1.9 \times 10^6/\text{cm}^3$ for various LO path delays. As with the longitudinal scan, the optical phase space contours for low concentration

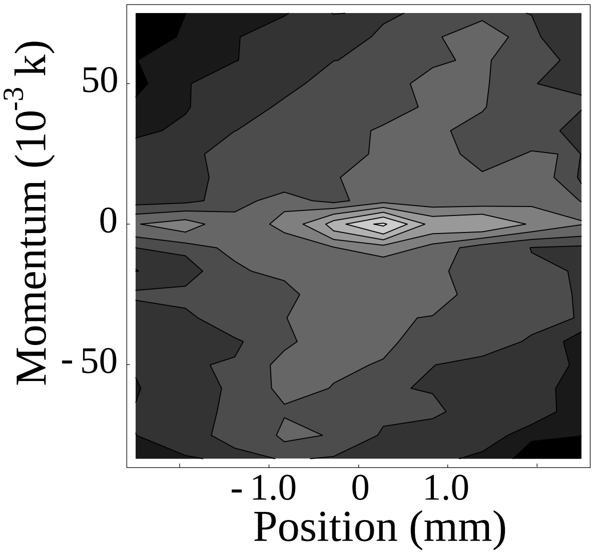

Figure 7.10: Measured optical phase space distribution (x,p) at zero LO path delay ($\Delta l' = 0$) for scatterer concentration $\rho = 1.9 \times 10^6/\text{cm}^3$. (Log scale; ballistic attenuation - $\exp(-3.5)$)

samples are dominated by ballistic light. Figure 7.10 shows the measured optical phase space distribution for equal LO and signal path lengths ($\Delta l' = 0$) on a log scale. The ballistic light is represented by the narrow island at zero transverse momentum. The grey area which surrounds it represents scattered light. The plot uses a log scale because the scattered light is several orders of magnitude lower than the ballistic light. Scattered light is seen in this plot as the increase in path length due to scattering can still be smaller than the coherence length of the source. Therefore even though the LO and signal paths are equal, scattered light is still seen.

As the LO path length is increased, the ballistic light continues to dominate the transmitted phase space distribution. Figure 7.11 shows the measured optical phase space contours for $\Delta l' = 0.2$ mm on a log scale. Again, the ballistic light is shown as the narrow island at zero transverse momentum. The scattered light, represented by the grey area surrounding the ballistic, has grown in position and momentum bur

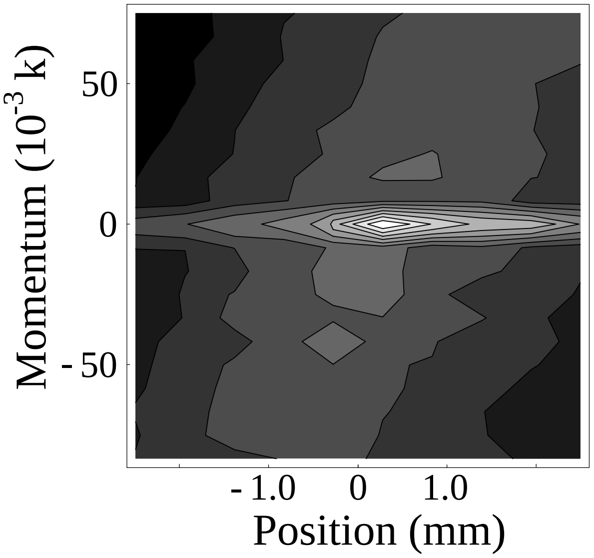

Figure 7.11: Measured optical phase space distribution (x,p) for LO path delay $\Delta l' = 0.2$ mm for scatterer concentration $\rho = 1.9 \times 10^6/\mathrm{cm}^3$. (Log scale; ballistic attenuation - $\exp(-3.5)$)

remains orders of magnitude smaller than the ballistic light. It is clear from this plot that the signal at $x = 0$, $p = 0$ is due to ballistic light by the characteristic shape in phase space.

The phase space distribution for the scattered light continues to grow in position and momentum as the LO path length is increased until a remarkable feature emerges at $\Delta l' = 0.6$ mm. Figure 7.12 shows the measured optical phase space distribution for $\rho = 1.9 \times 10^6/\mathrm{cm}^3$ at this path delay. In this contour plot, the ballistic light, represented by the white diamond in the center of the plot, is still dominant. However, the scattered light has split into a two peak distribution, each peak centered at zero transverse momentum and ±2.5 mm in position. The distribution appears to be diverging from these two points. As the path delay is increased further, the centers of the two peaks remain at zero transverse momentum but move further off axis, i.e., away from zero position. The two peak distribution finally fades into the

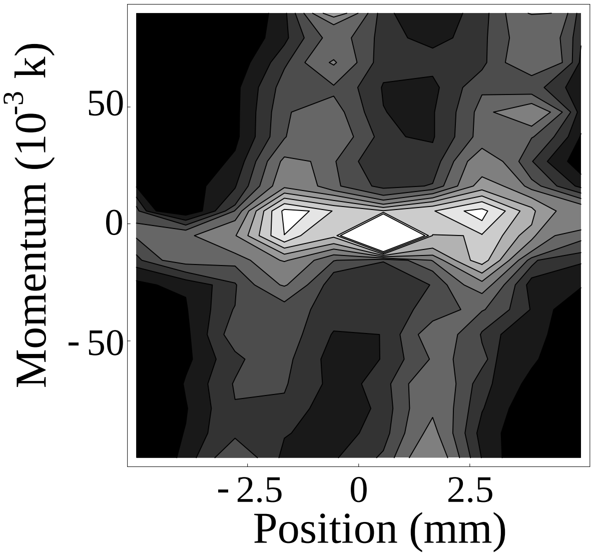

Figure 7.12: Measured optical phase space distribution (x,p) for LO path delay $\Delta l' = 0.6$ mm for scatterer concentration $\rho = 1.9 \times 10^6/\text{cm}^3$. (Log scale; ballistic attenuation - $\exp(-3.5)$)

background at a path delay of 1 mm. For higher concentrations, the two peaks in position consistently appear for path delays between 0.5 and 1.0 mm. These peaks are discernible at concentrations of up to $\rho = 7.5 \times 10^6/\text{cm}^3$, over the same range of path delays. At the time of this writing, no detailed theory has been devised to explain this phenomenon but it is believed to be similar in origin to the two peak distribution shown in section 6.2.2.

At intermediate concentrations, $\rho = 5 \times 10^6/\text{cm}^3$ to $1.5 \times 10^7/\text{cm}^3$, the ballistic and scattered light emerging from the turbid sample are of comparable magnitude. This can be seen in the measured optical phase space density for $x = 0$ and $p = 0$ as the LO path is increased. Fig. 7.13 shows a scan of $\Delta l'$ for a concentration of $\rho = 1.2 \times 10^7/\text{cm}^3$. At this concentration, the ballistic light has been attenuated by $\exp(-21.6)$. It is represented in this plot by the sharp peak at zero path delay and the scattered light is shown as the tail that extends for increasing LO path delays. This

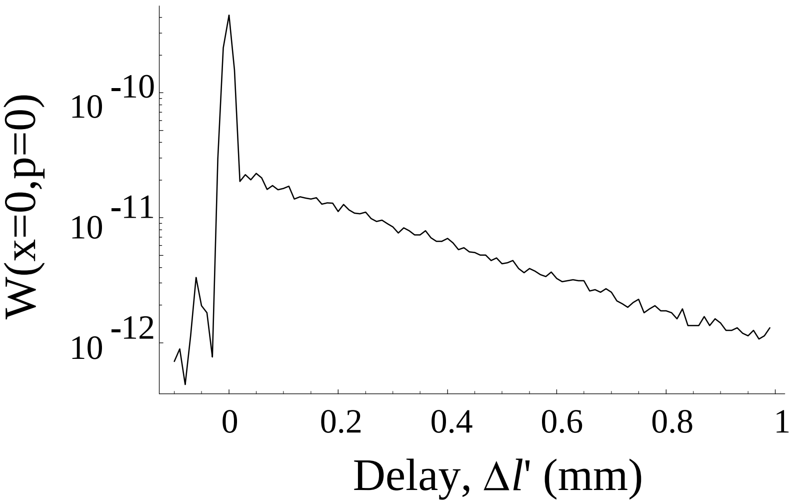

Figure 7.13: Measured optical phase space density for $x = 0$, $p = 0$ as a function of LO path delay $\Delta l'$ for $\rho = 1.2 \times 10^7/\text{cm}^3$ (ballistic attenuation - $\exp(-21.6)$).

is confirmed in the optical phase space measurements in position and momentum. Figure 7.14 shows the measured phase space distribution for $\Delta l' = 0$ on a log scale. The ballistic light is seen as the small island at zero position and zero transverse momentum. It is identified by its characteristic shape. In this plot, it appears smaller in position compared to the ballistic light at lower concentrations (Fig.'s 7.10 and 7.11). This is due to the lower amplitude, off-axis tails of the ballistic light becoming overwhelmed by the scattered light, shown as the gray bands extending in position and momentum.

For this intermediate concentration, the scattered light becomes dominant at increased LO path lengths (as shown in the LO path delay scan in Fig. 7.13). This transition is seen in the phase space contour plots. Fig. 7.15 shows the measured optical phase space distribution for an LO path delay, $\Delta l' = 20$ μm. In this contour plot, there is no ballistic component and only scattered light is seen. This distribution is displayed on a linear scale as the scattered light only varies over one order of

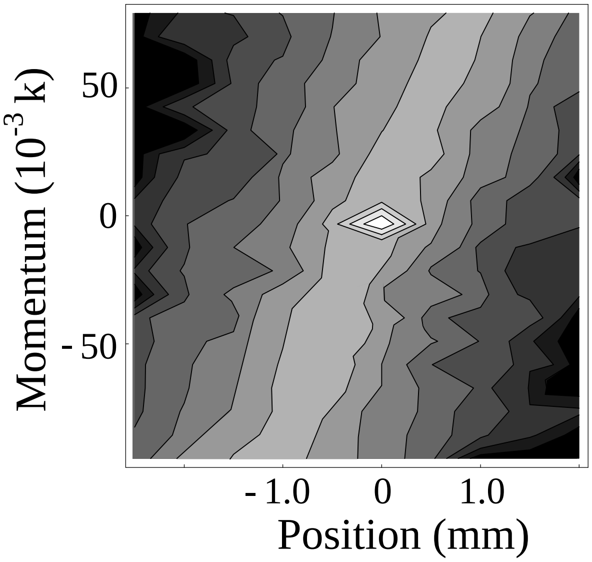

Figure 7.14: Measured optical phase space distribution (x,p) for LO path delay $\Delta l' = 0$ for scatterer concentration $\rho = 1.2 \times 10^7/\text{cm}^3$. (Log scale; ballistic attenuation - $\exp(-21.6)$)

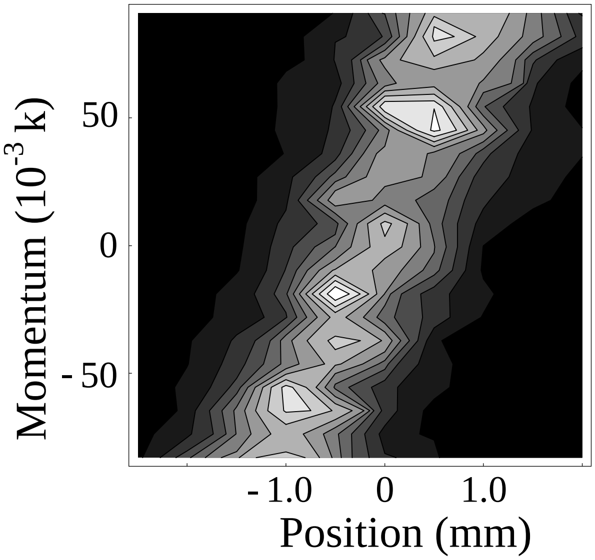

Figure 7.15: Measured optical phase space distribution (x,p) for LO path delay $\Delta l' = 0.02$ mm for scatterer concentration $\rho = 1.2 \times 10^7/\text{cm}^3$ (Linear scale; ballistic attenuation - $\exp(-21.6)$).

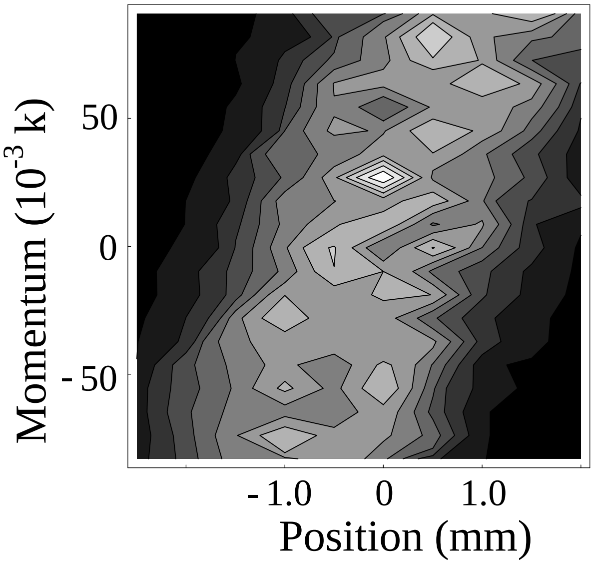

Figure 7.16: Measured optical phase space distribution (x,p) for LO path delay $\Delta l' = 0.2$ mm for scatterer concentration $\rho = 1.2 \times 10^7/\text{cm}^3$ (Linear scale; ballistic attenuation - $\exp(-21.6)$).

magnitude. The lighter spots seen here are due to variations in the measured beat intensity which become more obvious on the linear scale. Unlike the distributions obtained for lower concentrations, no two peak structure emerges for longer LO path delays. Instead, the scattered light is seen to grow broader in both position and momentum. As an example, Figure 7.16 shows measured optical phase space contours for the same concentration with an LO path delay, $\Delta l' = 0.2$ mm on a linear scale.

For the optical phase space distributions at this intermediate concentration ($\rho = 1.2 \times 10^7/\text{cm}^3$), the position width at zero transverse momentum is a gaussian distribution for all LO path lengths. The fitted width of the position distribution versus LO path delay is plotted in Figure 7.17 (Table A.4). The 1/e width of this distribution is seen to grow as

$$\Delta x_{1/e}(\text{mm}) \propto 0.55\sqrt{1 + 0.034 \times \Delta l'(\mu\text{m})}. \tag{7.6}$$

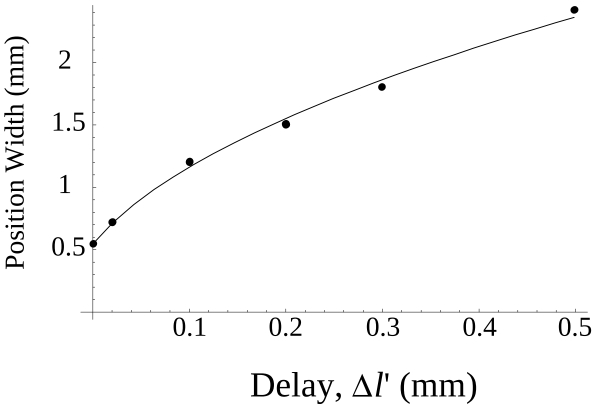

Figure 7.17: Width of the position distribution at zero transverse momentum versus LO path delay for $\rho = 1.2 \times 10^7/\mathrm{cm}^3$ (ballisticattenuation$-\exp(-21.6)$). Solid line - emprical fit to data.

where $\Delta l'$ is the LO path delay, as usual. This relation was found by using a least-squares fit to the data and is shown as the solid line in Fig. 7.17. The momentum distribution at zero position is not fitted as easily. The angular distribution appears to be a flattened gaussian distribution. As an example of this type of distribution, Figure 7.18 shows the measured momentum distribution at zero position for this concentration with an LO path delay, $\Delta l' = 0.2$ mm.

7.2.4 Time-resolved optical phase space distributions for low order scattering in thick samples

At high concentrations of scatterers ($\rho \geq 1.5 \times 10^7/\mathrm{cm}^3$), the magnitude of the scattered intensity transmitted through the sample becomes greater than that for the ballistic light. Fig. 7.19 shows a scan of the measured optical phase space density for $x = 0$ and $p = 0$ as the LO path length is increased for $\rho = 1.5 \times 10^7/\mathrm{cm}^3$. In this plot, the ballistic light, indicated by the arrow at zero LO path delay, is still present but has a peak magnitude lower than the peak magnitude of the scattered light. The ballistic light has been attenuated by a factor of $\exp(-27.2)$ for this concentration.

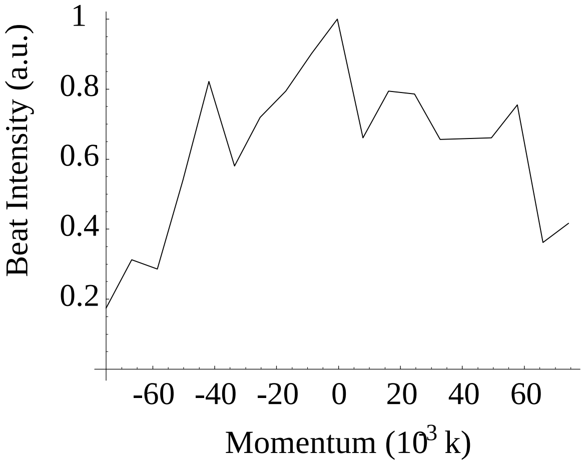

Figure 7.18: Momentum distribution at zero position for $\Delta l' = 0.2$ mm and $\rho = 1.2 \times 10^7/\mathrm{cm}^3$ (ballistic attenuation - $\exp(-21.6)$).

While the thickness of this sample begins to test the limits of ballistic imaging, it is possible to probe denser samples by making use of low-order scattered light. Figures 7.20 and 7.21 show measured optical phase space distributions for two different path delays using this concentration. When the LO and signal paths are matched to within the coherence length of the source ($\Delta l' = 0$), the distribution is dominated by the ballistic light, indicated by the arrow in Fig. 7.20. For an LO path delay of $\Delta l' = 0.1$ mm, the scattered light dominates the contour plot (Fig. 7.21). What is most notable about this phase space distribution is that it is still fairly narrow in momentum indicating that it may still be useful for imaging applications.

The spatial width of the distributions for high concentrations is found to grow in a similar manner as those for intermediate concentrations. Figure 7.22 shows the fitted 1/e width of the position distributions at zero transverse momentum for varying LO path delays (Table A.5). The solid line shows a curve fitted to these spatial widths, it is given by

$$\Delta x_{1/e}(\mathrm{mm}) \propto 0.55\sqrt{1 + 0.022 \times \Delta l'(\mu\mathrm{m})}. \tag{7.7}$$

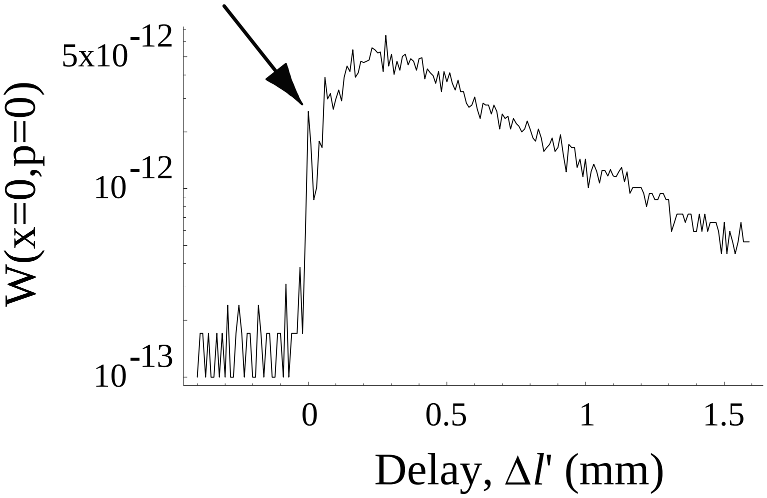

Figure 7.19: Measured optical phase space density for $x = 0$, $p = 0$ as a function of LO path delay $\Delta l'$ for $\rho = 1.5 \times 10^7/\mathrm{cm}^3$ (ballistic attenuation - $\exp(-27.2)$).

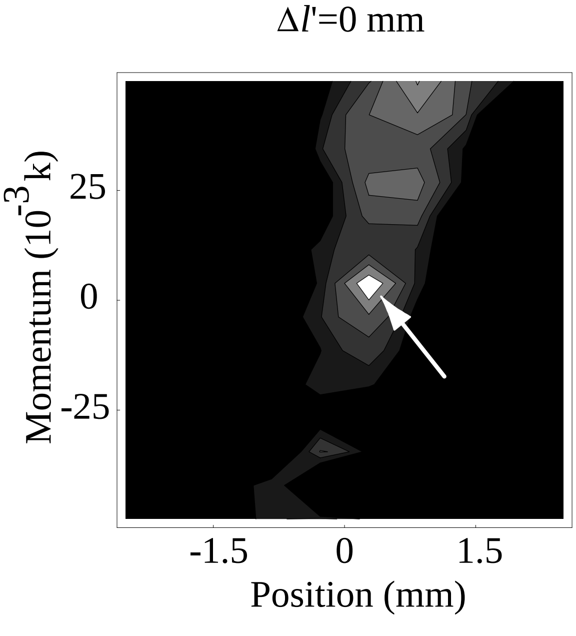

Figure 7.20: Measured optical phase space distribution (x,p) for LO path delay $\Delta l' = 0$ for scatterer concentration $\rho = 1.5 \times 10^7/\mathrm{cm}^3$ (Linear Scale; ballistic attenuation - $\exp(-27.2)$).

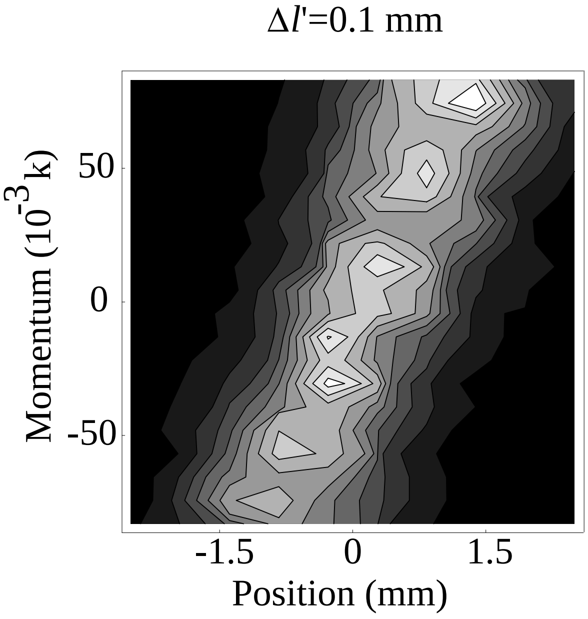

Figure 7.21: Measured optical phase space distribution (x,p) for LO path delay $\Delta l' = 0.1$ mm, for scatterer concentration $\rho = 1.5 \times 10^7/\text{cm}^3$ (Linear scale).

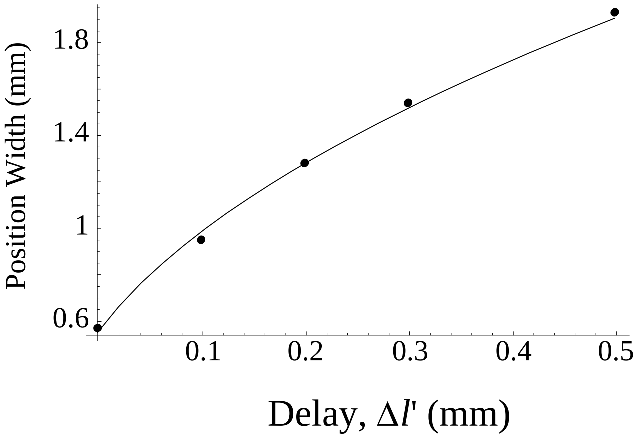

Figure 7.22: Width of the position distribution at zero transverse momentum versus LO path delay for $\rho = 1.5 \times 10^7/\text{cm}^3$(ballistic attenuation$-\exp(-27.2)$). Solid line - curve fit to data.

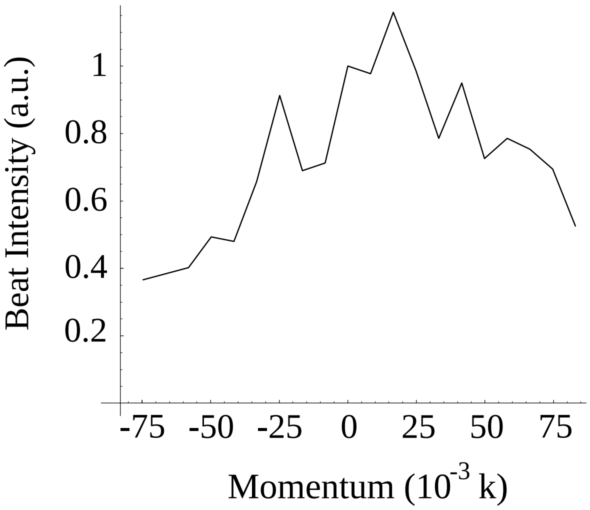

Figure 7.23: Momentum distribution at zero position for $\Delta l' = 0.1$ mm and $\rho = 1.5 \times 10^7/\text{cm}^3$ (ballistic attenuation - $\exp(-27.2)$).

Again, the trend of the momentum distributions is not easily identified. At these high concentrations, the transverse momentum distributions at zero position appear to be nominally gaussian. As an example of this type of distributions, Figure 7.23 shows the momentum distribution at zero position for a path delay of $\Delta l' = 0.1$ mm at this concentration. Fitting the data with a gaussian distribution, the least squares fit is minimized for a gaussian with a width of approximately 50 mrad. Further theoretical analysis is needed to correctly model the change in width of the angular distributions.

At higher concentrations, the ballistic light is completely overwhelmed and cannot be discerned in either the path delay scans nor contour plots. However, by introducing a small delay into the LO path, narrow momentum distributions can still be measured at these high concentrations. Fig. 7.24 shows a scan of the measured optical phase space density for $x = 0$ and $p = 0$ as the LO path length is increased for $\rho = 1.8 \times 10^7/\text{cm}^3$. This concentration corresponds to a ballistic attenaution of $\exp(-32.6)$,

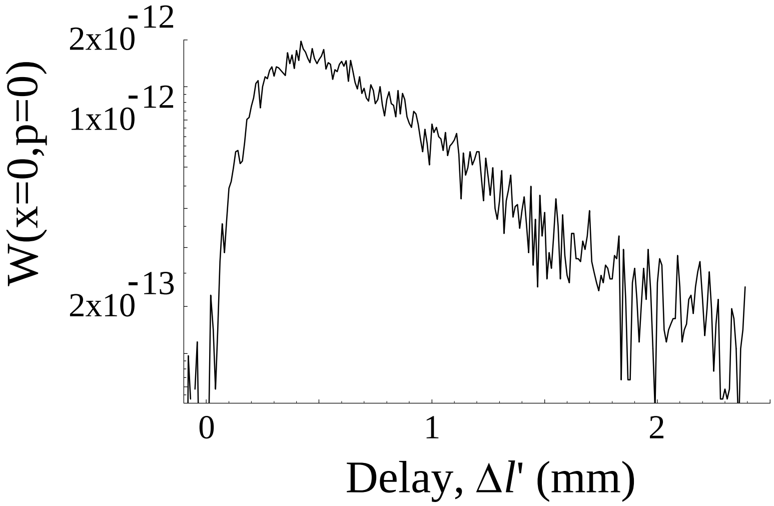

Figure 7.24: Measured optical phase space density for $x = 0$, $p = 0$ as a function of LO path delay $\Delta l'$ for $\rho = 1.8 \times 10^7/\text{cm}^3$ (ballistic attenuation - $\exp(-32.6)$).

however the zero intensity at zero path delay indiates that no measureable ballistic light is transmitted. In spite of this fact, optical phase space distributions can still be measured which have narrow momentum profiles by introducing small path delays in the LO path. Figures 7.25, 7.26 and 7.27 show measured optical phase space distributions for three different path delays using this concentration. No contour plot is presented for zero LO path delay as there is no measureable phase space density at that path delay.

Figure 7.25 shows the measured optical phase space distribution for an LO path delay of $\Delta l' = 0.05$ mm. In this figure the scattered light is fairly narrow in momentum, indicating that it retains information about the scattering medium. Figure 7.26 shows the distribution transmitted through the same sample for a slightly longer delay of $\Delta l' = 0.10$ mm. This distribution has grown in both position and momentum compared to the distribution shown in Fig. 7.26. Finally, Figure 7.27 shows the distribution for an LO path delay of $\Delta l' = 0.30$ mm. This distribution is substantially

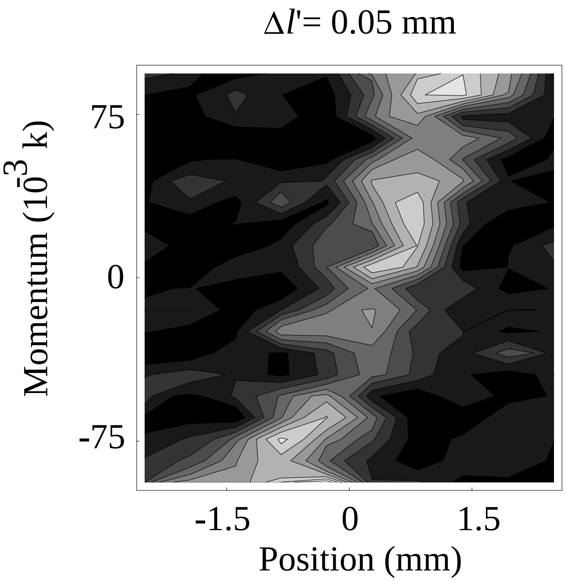

Figure 7.25: Measured optical phase space distribution (x,p) for LO path delay $\Delta l' = 0.05$ mm, for scatterer concentration $\rho = 1.8 \times 10^7/\text{cm}^3$ (Linear Scale; ballistic attenuation - $\exp(-32.6)$).

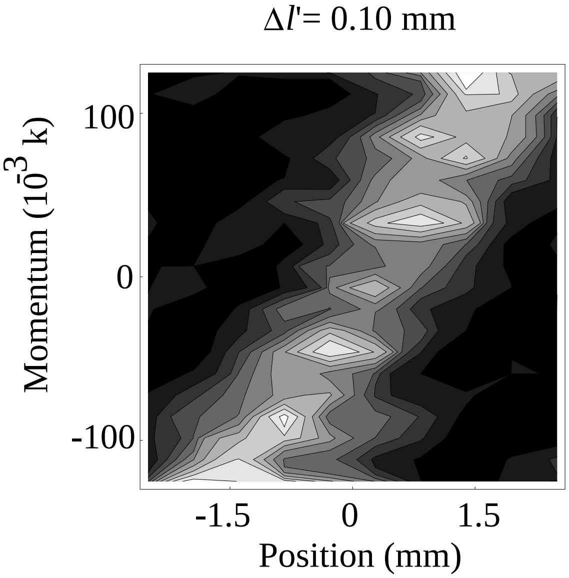

Figure 7.26: Measured optical phase space distribution (x,p) for LO path delay $\Delta l' = 0.10$ mm, for scatterer concentration $\rho = 1.8 \times 10^7/\text{cm}^3$ (Linear Scale; ballistic attenuation - $\exp(-32.6)$).

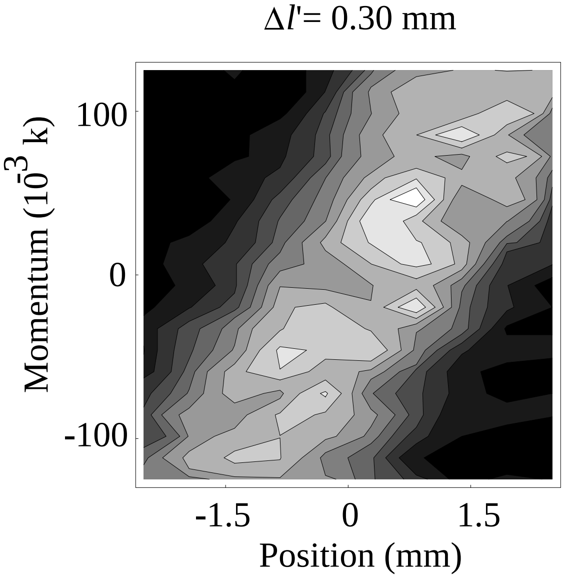

Figure 7.27: Measured optical phase space distribution (x,p) for LO path delay $\Delta l' = 0.30$ mm, for scatterer concentration $\rho = 1.8 \times 10^7/\text{cm}^3$ (Linear Scale; ballistic attenuation - $\exp(-32.6)$).

broader in position and momentum than the distributions at shorter path delays.

Examining the momentum width of these distributions does not yield a clear trend in the growth. Figure 7.28 (Table A.6) shows the width of the momentum distribution at zero position for increasing LO path delay. This plot shows that for a small LO path delay, the momentum width remains small but increases for larger LO path delays. It is difficult to identify a trend in this data as the fits to the individual momentum curves tend to not be very good. These fits may be improved by increasing the averaging time during data collection to reduce noise. The width of the spatial distribution at zero transverse momentum for this concentration is shown in Figure 7.29 (Table A.7) for various LO path delays. The solid line shows a curve fitted to these spatial widths, it is given by

$$\Delta x_{1/e}(\text{mm}) \propto 0.75\sqrt{1 + 0.013 \times (\Delta l'(\mu\text{m}) - 62)}. \tag{7.8}$$

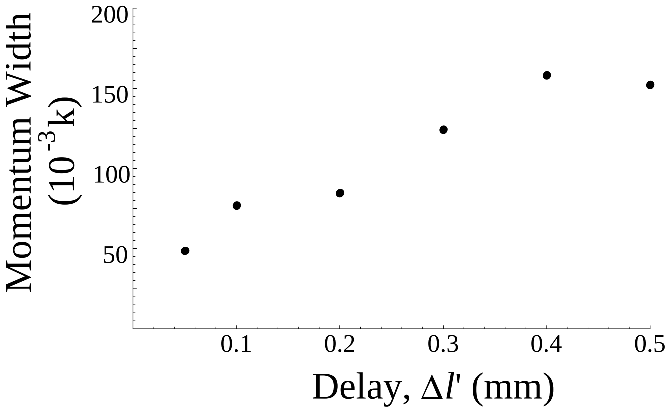

Figure 7.28: Width of the momentum distribution at zero position versus LO path delay for $\rho = 1.8 \times 10^7/\text{cm}^3$ (ballistic attenuation– exp(−32.6)).

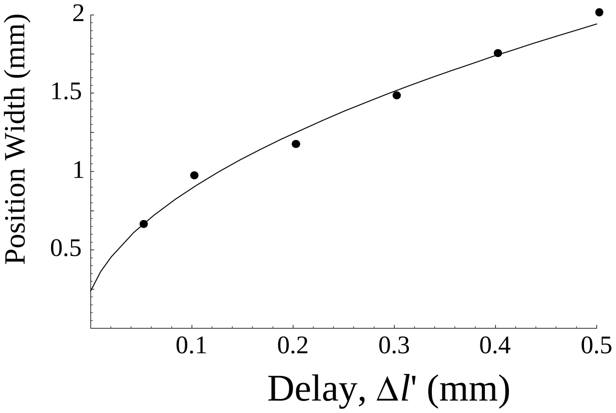

Figure 7.29: Width of the position distribution at zero transverse momentum versus LO path delay for $\rho = 1.8 \times 10^7/\text{cm}^3$ (ballistic attenuation– exp(−32.6)).

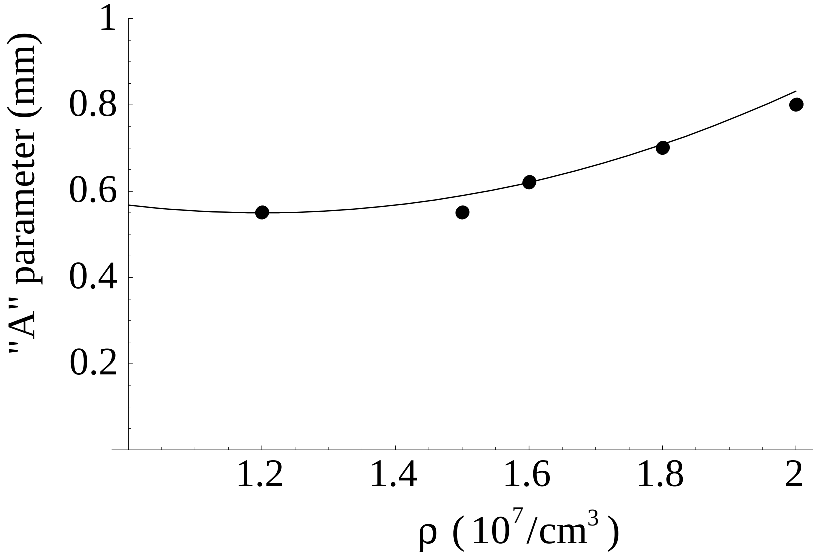

Figure 7.30: Scaling of the position width model "A" parameter (Eq. 7.9) with concentration. Solid line - empirical fit to data.

7.2.5 Position width trend

Analysis of the increase in width of the spatial distribution with increasing LO path delay for various concentrations of scatterers leads to the following empirical result:

$$\Delta x_{1/e}(\text{mm}) \propto A\sqrt{1 + B \times (\Delta l'(\mu\text{m}) - C)}. \tag{7.9}$$

The trends of the A, B, and C parameters were identified by plotting the values obtained by fitting a curve of the form of Eq. 7.9 to the data at each concentration. Examining the trend in the A parameter as a function of concentration of 4.9 micron spheres (Fig. 7.30, Table A.8), the parameter was found to scale with concentration as:

$$A = 0.55 + 0.44(1.2 - c)^2, 1.2 \leq c \leq 2.0 \tag{7.10}$$

where c is the concentration in units of 10^7 scatterers per cm^3. This function is plotted as a solid line in Figure 7.30. The values of the B parameter, obtained by fitting the

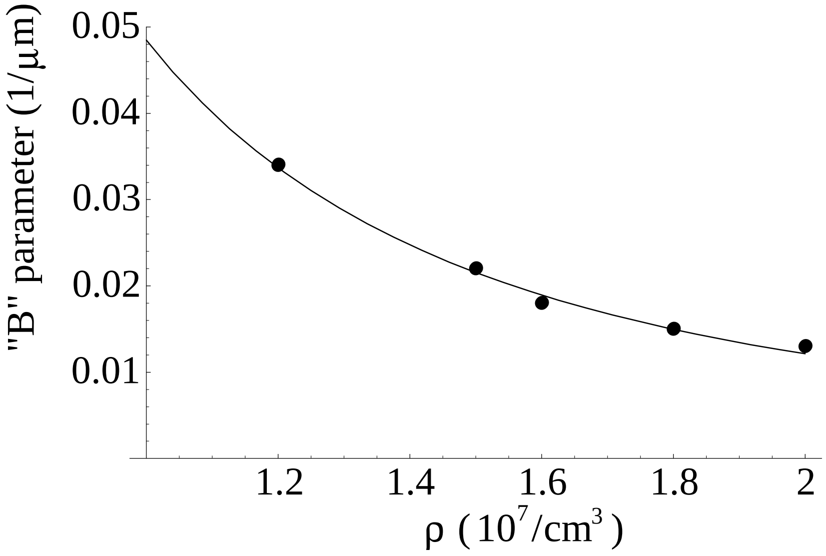

Figure 7.31: Scaling of the position width model "B" parameter (Eq. 7.9) with concentration. Solid line - empirical fit to data.

data to the model (Eq. 7.9) at various concentrations, is shown in Figure 7.31 (Table A.9). In this figure, the solid line represents an empirical model for the B parameter. It was found to scale as

$$B = \frac{0.049}{c^2}\,\mu\text{m}^{-1}, 1.2 \leq c \leq 2.0 \tag{7.11}$$

where again the concentration c is in units of 10^7 scatterers per cm^3. Finally, the C parameter in Eq. 7.9 accounts for the fact that although $\Delta l'$ is measured relative to the ballistic light, at concentrations greater than $1.2 \times 10^7/\text{cm}^3$ phase space distributions are not observed until longer delays are introduced in the LO path. This offset of $\Delta l'$ was found to scale roughly as

$$C = 262\,\mu\text{m}(c - 1.2)^2,\ 1.2 \leq c \leq 2.0 \tag{7.12}$$

where c is again concentration in units of 10^7 scatterers per cm^3. This relation is shown as a solid in the plot for the fitted C parameter as a function of scatterer

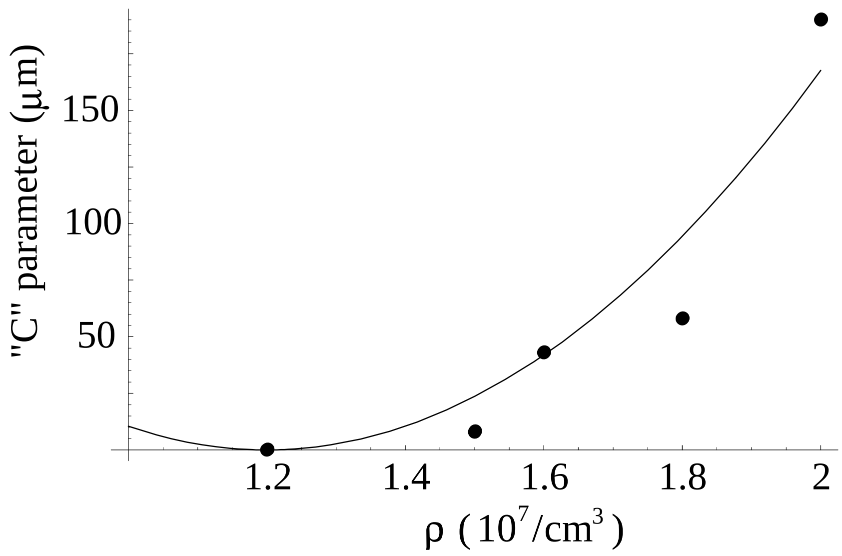

Figure 7.32: Scaling of the position width model "*C*" parameter (Eq. 7.9) with concentration. Solid line - empirical fit to data.

concentration in Figure 7.32 (Table A.10). At the time this thesis was written, no model has been devised to explain these trends.

7.3 Theory

Although no detailed theory has been developed to fully model the propagation of low coherence length light in a multiple scattering medium, the two peak distribution seen in the data in section 7.2.1 can be understood by using perturbation theory to devise a model. In this treatment, single scattering is treated as a perturbation to the free space propagation of the Wigner distribution.

7.3.1 Wigner distribution for weak scattering of low coherence light

For a large diameter, low coherence length beam incident on a weakly scattering medium, a two peak structure is seen in the angular distribution of the transmitted distribution (section 7.2.1). The two peak distribution can be modeled by treating the scattering as a first order perturbation to the free space propagation. In this case the Green's function for the free space evolution equation is needed. Recalling Eq. 6.5, the unperturbed Wigner distribution evolves in free space according to

$$\left(\frac{\partial}{\partial t}+\frac{c^2}{n_o^2\omega}\vec{p}\cdot\vec{\nabla}_{\vec{x}}\right)W^o(\vec{x},\vec{p},t)=0. \tag{7.13}$$

Thus the Green's function for this evolution will obey

$$\left(\frac{\partial}{\partial t}+\frac{c^2}{n_o^2\omega}\vec{p}\cdot\vec{\nabla}_{\vec{x}}\right)G_w(\vec{x},\vec{x}\,';\vec{p},\vec{p}\,';t,t')=\delta(\vec{x}-\vec{x}\,')\delta(\vec{p}-\vec{p}\,'). \tag{7.14}$$

The solution to this equation is found using Fourier methods [26] and is given by [91]

$$G_w(\vec{x},\vec{x}\,';\vec{p},\vec{p}\,';t,t')=\delta\left[\vec{x}-\vec{x}\,'-\frac{c^2}{n_o^2\omega}\vec{p}(t-t')\right]\delta(\vec{p}-\vec{p}')\Theta(t-t'), \tag{7.15}$$

where the step function in time, $\Theta(t-t')$, ensures that causality is maintained. Equation 7.15 can be interpreted as reproducing the apparent straight line motion of the Wigner distribution. As illustrated in section 3.1.1, the Wigner distribution appears to travel in straight lines yet properly takes into the wave nature of the field.

Treating the scattering as a first order perturbation to the free space evolution, the distribution resulting from a single scattering is given by

$$\begin{aligned} W'(\vec{x},\vec{p},t) &= \int d^3\vec{x}\,'\int d^3\vec{p}\,'G_w(\vec{x},\vec{x}\,';\vec{p},\vec{p}\,';t,t') \\ &\quad\times\int d^3\vec{p}\,''K(\vec{p}\,',\vec{p}\,'')W^o(\vec{x}\,',\vec{p}\,',t'). \end{aligned} \tag{7.16}$$

Here $K(\vec{p}\,',\vec{p}\,'')$ is the scattering kernel as defined in Eq. 6.9. It is related to the differential cross section $d\sigma/d\Omega$. Inserting the Green's function (Eq. 7.15) into this expression, the distribution takes the form

$$\begin{aligned} W'(\vec{x},\vec{p},t) &= \int\frac{dz'}{|v_z|}\int d^3\vec{p}\,'K(\vec{p},\vec{p}\,') \\ &\quad\times W^o(\vec{x}_\perp-\frac{\vec{p}_\perp}{p_z}(z-z'),z',\vec{p}\,',t-\frac{z-z'}{v_z}), \end{aligned} \tag{7.17}$$

where v_z is the velocity in the $\hat{z}$ direction and is given by

$$v_z = \frac{c}{n_o}\frac{p_z}{k}. \tag{7.18}$$

The expression for the scattered distribution (Eq. 7.17) can be further simplified by assuming that the input distribution is sharply peaked about the $\hat{z}$ direction compared to the width of the scattering kernel, $K(\vec{p},\vec{p}\,')$. Under this assumption of an input beam which is narrow in momentum, the distribution for the scattered light becomes

$$W'(\vec{x},\vec{p},t) = K(\vec{p},k\hat{z})\int\frac{dz'}{|v_z|}\int d^3\vec{p}\,'W^o(\vec{x}_\perp - \frac{\vec{p}_\perp}{p_z}(z-z'),z',\vec{p}\,',t-\frac{z-z'}{v_z}). \tag{7.19}$$

7.3.2 Heterodyne beat signal

To model the two peak distribution seen in the experimental data, the Wigner distribution of the scattered field must be convoluted with that of the effective LO field. An effective LO field (Eq. 7.3) is used to include the additional phases acquired by the LO field due to propagation through the imaging system. The mean square heterodyne beat signal is then given by (Eq. 7.2)

$$\begin{aligned} S_B(d_x,d_p,\Delta l') &= \int d^2\vec{x}_\perp\,d^2\vec{p}_\perp \qquad (7.20)\\ &\quad \left\langle W'_{LO}(\vec{x}_\perp - d_x\,\hat{x},L+\Delta l',\vec{p}_\perp - \frac{k}{f_o}d_p\,\hat{x},t)\,W'(\vec{x}_\perp,L;\vec{p}_\perp,t)\right\rangle, \end{aligned}$$

where W'_{LO} is the Wigner distribution of the effective LO field. The path length difference between the LO and signal fields is included as $\Delta l'$ as defined in Eq. 7.1. The Wigner distributions in Eq. 7.20 are transverse Wigner distribution thus to use the distribution in Eq. 7.19, it must be integrated over p_z

$$W'(\vec{x},\vec{p}_\perp,t) = \int dp_z W'(\vec{x},\vec{p},t)\,. \tag{7.21}$$

Inserting the distribution for the first order scattered field (Eq. 7.19) into Eq. 7.20, the expression for the heterodyne beat signal can be written as

$$\begin{aligned} S_B(d_x,d_p,\Delta l') &= \int d^2\vec{x}_\perp\, d^2\vec{p}_\perp \int dp_z K(\vec{p},k\hat{z}) \int \frac{dz'}{|v_z|} \\ &\quad \Big\langle W'_{LO}(\vec{x}_\perp - d_x\,\hat{x}, L+\Delta l', \vec{p}_\perp - \frac{k}{f_o} d_p\,\hat{x}, t) \\ &\quad \int d^3\vec{p}\,' W^o(\vec{x}_\perp - \frac{\vec{p}_\perp}{p_z}(L-z'), z', \vec{p}\,', t - \frac{L-z'}{v_z}) \Big\rangle . \end{aligned} \tag{7.22}$$

This expression gives the heterodyne beat in terms of the Wigner distribution for the effective LO field, W'_{LO}, and that of the input signal field, W^o. However, as discussed in section 4.1.2, in order to rigorously calculate heterodyne beat signals for low coherence light, the beat signal given in terms of fields is needed. Conversion of Eq.7.22 into an expression involving the overlaps of fields can be simplified by realizing that integrating the Wigner distribution over all momenta yields the position distribution:

$$\int d^3\vec{p}\,' W^o(\vec{x}\,'_\perp, \vec{p}\,', t') = \left| E_S(\vec{x}\,'_\perp, t') \right|^2 , \tag{7.23}$$

as discussed in Chapter 3.

Using the definition of the Wigner distribution Eq. 3.1 and Eq. 7.23, Eq. 7.22 can be written as the overlap of the signal field and effective LO field

$$\begin{aligned} S_B(d_x,d_p,\Delta l') &= \int d^2\vec{x}_\perp\, d^3\vec{p}\, K(\vec{p},k\hat{z}) \int \frac{dz'}{|v_z|} \int \frac{d^2\vec{\epsilon}_\perp}{(2\pi)^2} \exp\left(i\vec{\epsilon}_\perp\cdot\vec{p}_\perp\right) \\ &\quad \Big\langle E'^*_{LO}(\vec{x}_\perp + \vec{\epsilon}_\perp/2, L+\Delta l', t) \\ &\times \quad E'_{LO}(\vec{x}_\perp - \vec{\epsilon}_\perp/2, L+\Delta l', t) \\ &\times \quad E^*_S(\vec{x}_\perp - \frac{\vec{p}_\perp}{p_z}(L-z'), t - \frac{L-z'}{v_z}) \\ &\times \quad E_S(\vec{x}_\perp - \frac{\vec{p}_\perp}{p_z}(L-z'), t - \frac{L-z'}{v_z}) \Big\rangle . \end{aligned} \tag{7.24}$$

In this expression, the effective LO field is defined as

$$E'^*_{LO}(\vec{x}_\perp, L+\Delta l', t) = \int d\omega_k \mathcal{E}'^*_{k_{LO}}(\vec{x}_\perp - d_x\hat{x}, \Delta l', d_p) e^{i\omega_k t} e^{-i\omega_k L/c} \tag{7.25}$$

where $\mathcal{E}'^{*}_{k_{LO}}$ is the slowly varying complex amplitude of the frequency component, $\omega_k = ck_{LO}$, of the effective LO field, as defined in Eq. 7.3:

$$\begin{aligned} \mathcal{E}'^{*}_{k_{LO}}(\vec{x}_\perp - d_x\hat{x}, \Delta l', d_p) &= \mathcal{E}^{*}_{k_{LO}}(\vec{x}_\perp - d_x\hat{x}, z=0)e^{-i\omega_k \Delta l/c} \\ &\times \exp(-ik\frac{d_p^2}{2f_o})\exp(ik\frac{d_p\hat{x}}{f_o}\cdot\vec{x}_\perp). \end{aligned} \tag{7.26}$$

Similarly, the signal field can also be decomposed into its Fourier components:

$$E_S(\vec{x}_\perp, L, t) = \int d\omega_k \mathcal{E}_{k_S}(\vec{x}_\perp, z=0)e^{i\omega_k t}e^{-i\omega_k L/c}. \tag{7.27}$$

The bracketed term in Eq. 7.24 can be simplified by realizing that the LO and signal fields must be correlated not with themselves but with each other in order to produce the heterodyne beat signal. Thus the bracketed term can be rewritten as

$$\begin{aligned} &\left\langle\left\langle E'^{*}_{LO}(\vec{x}_\perp + \vec{\epsilon}_\perp/2, L+\Delta l', t)\ E_S(\vec{x}_\perp - \frac{\vec{p}_\perp}{p_z}(L-z'), t - \frac{L-z'}{v_z})\right\rangle\right. \\ &\times \left.\left\langle E^{*}_S(\vec{x}_\perp - \frac{\vec{p}_\perp}{p_z}(L-z'), t - \frac{L-z'}{v_z})E'_{LO}(\vec{x}_\perp - \vec{\epsilon}_\perp/2, L+\Delta l', t)\right\rangle\right\rangle. \end{aligned} \tag{7.28}$$

The derivation is made easier by examining one pair of correlated fields at a time. By expanding each of the fields in terms of their Fourier components as in Eq. 7.25 and 7.27, the first bracketed term in Eq. 7.28 can be rewritten as

$$\begin{aligned} V_B(z', \vec{\epsilon}_\perp) &\equiv \left\langle E'^{*}_{LO}(\vec{x}_\perp + \vec{\epsilon}_\perp/2, L+\Delta l', t)\ E_S(\vec{x}_\perp - \frac{\vec{p}_\perp}{p_z}(L-z'), t - \frac{L-z'}{v_z})\right\rangle \\ &= \int d\omega_k \left\langle \mathcal{E}^{*}_{k_{LO}}(\vec{x}_\perp + \vec{\epsilon}_\perp/2 - d_x\hat{x}, z=0)\mathcal{E}_{k_S}(\vec{x}_\perp - \frac{\vec{p}_\perp}{p_z}(L-z'), z=0\right\rangle \\ &\quad \times \exp(-ik\frac{d_p^2}{2f_o})\exp\left[ik\frac{d_p\hat{x}}{f_o}\cdot(\vec{x}_\perp + \vec{\epsilon}_\perp/2)\right] \\ &\quad \times \exp(-ik\Delta l)\exp\left[-i\omega_k(\frac{L-z'}{c} - \frac{L-z'}{v_z})\right], \end{aligned} \tag{7.29}$$

by using Eq. 7.26 and exploiting the fact that k_{LO} will be equal to k_S. As discussed in section 4.1.2 it is assumed that the $\mathcal{E}_k$'s are delta-correlated such that $\langle \mathcal{E}^{*}_k \mathcal{E}_{k'} \rangle$ is only nonzero for $\omega_k = \omega_{k'}$. The specific form for the bracketed term in Eq. 7.29, $\langle \mathcal{E}_k^* \mathcal{E}_k \rangle$, can be simply written as

$$\left\langle \mathcal{E}_{k_{LO}}^*(\vec{x}_\perp, z=0)\mathcal{E}_{k_S}(\vec{x}'_\perp, z=0)\right\rangle = |\mathcal{E}_o|^2 \exp\left(-\frac{(k-k_o)^2}{\Delta k^2}\right)\exp\left(-\frac{\vec{x}_\perp^{\,2}}{2a^2}\right). \quad (7.30)$$

This expression is a simplified form of the Gaussian Schell model given in Eq. 5.2. It has been simplified by setting $\vec{x}'_\perp$ to zero by assuming that the large diameter input beam provides approximate translational invariance for the signal beam. The bandwidth and center wavevector of the source are given by Δk and k_o, respectively. Using Eq. 7.30, the expression for $V_B(z', \vec{\epsilon}_\perp)$ (Eq. 7.29) can be rewritten as

$$\begin{aligned} V_B(z', \vec{\epsilon}_\perp) &= |\mathcal{E}_o|^2 \exp\left(-\frac{(\vec{x}_\perp + \vec{\epsilon}_\perp/2 - d_x\hat{x})^2}{2a^2}\right)\frac{1}{\Delta k\sqrt{\pi}} \qquad (7.31)\\ &\times \int dk \exp\left(-\frac{(k-k_o)^2}{\Delta k^2}\right)\exp\left[ik\frac{d_p\hat{x}}{f_o}\cdot(\vec{x}_\perp + \vec{\epsilon}_\perp/2 - d_x\hat{x})\right]\\ &\times \exp(-ik\Delta l')\exp\left[-ik(L-z')(\frac{c}{v_z}-1)\right], \end{aligned}$$

where all terms involving the frequency ω have been converted to terms involving the wavevector k and $\Delta l'$ has been substituted by employing Eq. 7.1. A similar expression can be derived for the second bracketed term in Eq. 7.28:

$$\begin{aligned} V_B^*(z', \vec{\epsilon}_\perp) &= |\mathcal{E}_o|^2 \exp\left(-\frac{(\vec{x}_\perp - \vec{\epsilon}_\perp/2 - d_x\hat{x})^2}{2a^2}\right)\frac{1}{\Delta k\sqrt{\pi}} \qquad (7.32)\\ &\times \int dk \exp\left(-\frac{(k-k_o)^2}{\Delta k^2}\right)\exp\left[-ik\frac{d_p\hat{x}}{f_o}\cdot(\vec{x}_\perp - \vec{\epsilon}_\perp/2 - d_x\hat{x})\right]\\ &\times \exp(-ik\Delta l)\exp\left[ik(L-z')(\frac{c}{v_z}-1)\right]. \end{aligned}$$

The derivation can be simplified further by introducing the variable $\Delta k_S = k - k_o$ in the expressions for $V_B(z', \vec{\epsilon}_\perp)$ and $V_B^*(z', \vec{\epsilon}_\perp)$. In addition, simply translating $\vec{x}_\perp$ to $\vec{x}_\perp + d_x\hat{x}$ removes all d_x dependence, as expected for the case of a translationally invariant signal (Eq. 7.30). Inserting Eq.'s 7.31 and 7.32 into Eq. 7.24 yields:

$$
\begin{aligned}
S_B(d_p,\Delta l') &= \int d^2\vec{x}_\perp\, d^3\vec{p}\, K(\vec{p},k\hat{z}) \int \frac{dz'}{|v_z|} \int \frac{d^2\vec{\epsilon}_\perp}{(2\pi)^2} \exp\left(i\vec{\epsilon}_\perp\cdot\vec{p}_\perp\right) |\mathcal{E}_o|^4\, \frac{1}{\Delta k^2\pi} \\
&\times \exp\left(-\frac{(\vec{x}_\perp-\vec{\epsilon}_\perp/2)^2}{2a^2}\right) \exp\left(-\frac{(\vec{x}_\perp+\vec{\epsilon}_\perp/2)^2}{2a^2}\right) \exp\left(i\frac{k_o}{f_o}d_p\hat{x}\cdot\vec{\epsilon}_\perp\right) \\
&\times \left|\int d\Delta k_S \exp(-i\frac{\Delta k_S}{f_o}d_p\hat{x}\cdot\vec{x}_\perp)\exp\left(-\frac{(\Delta k_S)^2}{\Delta k^2}\right)\right. \\
&\times \left.\exp\left[i\Delta k_S(\Delta l'-(L-z')(\frac{c}{v_z}-1)\right]\right|^2. \qquad (7.33)
\end{aligned}
$$

In this expression, the $\exp\left(\pm i\frac{\Delta k_S}{f_o}d_p\hat{x}\cdot\vec{\epsilon}_\perp\right)$ term under each Δk_S integral has been dropped. This is important because it allows the two integrals over Δk_S to be written as the magnitude squared of one integral. It is a reasonable approximation to make as $\vec{\epsilon}_\perp$ will remain small due to the narrow size of the LO beam. The $\vec{\epsilon}_\perp$ integral in Eq. 7.33 can now be performed directly to yield

$$
\begin{aligned}
S_B(d_p,\Delta l') &= |\mathcal{E}_o|^4\,\frac{1}{\Delta k^2\pi}\int d^3\vec{p}\,K(\vec{p},k\hat{z})\int\frac{dz'}{|v_z|}\int d^2\vec{x}_\perp \qquad (7.34)\\
&\times\exp\left(-\frac{\vec{x}_\perp^2}{a^2}\right)\exp\left(-a^2(\vec{p}_\perp+\frac{k_o}{f_o}d_p\hat{x})^2\right)\\
&\times\left|\int d\Delta k_S\exp(-i\frac{\Delta k_S}{f_o}d_p\hat{x}\cdot\vec{x}_\perp)\exp\left(-\frac{(\Delta k_S)^2}{\Delta k^2}\right)\right.\\
&\times\left.\exp\left[i\Delta k_S(\Delta l'-(L-z')(\frac{c}{v_z}-1)\right]\right|^2.
\end{aligned}
$$

For a small enough LO beam, it is also a reasonable approximation to assume that the integral over $\vec{x}_\perp$ will force $\vec{x}_\perp \simeq 0$ such that

$$
\begin{aligned}
S_B(d_p,\Delta l') &\simeq |\mathcal{E}_o|^4\,\frac{1}{\Delta k^2\pi}\int d^3\vec{p}\,K(\vec{p},k\hat{z})\int\frac{dz'}{|v_z|}\exp\left(-a^2(\vec{p}_\perp+\frac{k_o}{f_o}d_p\hat{x})^2\right) \qquad (7.35)\\
&\times\left|\int d\Delta k_S\exp\left(-\frac{(\Delta k_S)^2}{\Delta k^2}\right)\exp\left[i\Delta k_S(\Delta l'-(L-z')(\frac{c}{v_z}-1)\right]\right|^2.
\end{aligned}
$$

In addition, because the LO beam is narrower in momentum than the kernel, K, the integral over transverse momenta, $\vec{p}_\perp$will force $\vec{p}_\perp \simeq \frac{k_o}{f_o}d_p\hat{x}$. The integral over p_z

can also be done approximately using the energy conserving delta function in the scattering kernel which demands that the length of the momentum vector remains constant. The kernel can then be replaced by the elastic scattering differential cross section as a function of the scattering angle in the medium θ_1. Thus Eq. 7.35 can be rewritten as

$$\begin{aligned} S_B(d_p, \Delta l') &\propto \frac{d\sigma}{d\Omega}(\theta_1) \int dz' \\ &\times \left| \int d\Delta k_S \exp\left(-\frac{(\Delta k_S)^2}{\Delta k^2} \right) \exp\left[i\Delta k_S(\Delta l' - (L - z')(\frac{c}{v_z} - 1) \right] \right|^2 . \end{aligned} \tag{7.36}$$

This expression can be simplified further by converting the scattering angle in the medium, θ_1, to the detected angle in air, $\theta = \frac{k_o}{f_o} d_p = \theta_1 n_o$, where $n_o = 1.36$ is the index of refraction of the background medium. The ratio c/v_z can be related to this angle as $v_z = c\cos(\theta_1)$. The expression in the exponential under the integral can then be replaced using

$$(\frac{c}{v_z} - 1) \simeq \frac{1}{2}\theta_1^2 = \frac{1}{2}\frac{\theta^2}{n_o^2}, \tag{7.37}$$

to give

$$\begin{aligned} S_B(\theta &= \frac{k_o}{f_o} d_p, \Delta l') \propto \frac{d\sigma}{d\Omega}(\theta/n_o) \int dz' \\ &\times| \left| \int d\Delta k_S \exp\left(-\frac{(\Delta k_S)^2}{\Delta k^2} \right) \exp\left[i\Delta k_S \left(\Delta l' - \frac{\theta^2}{2n_o^2}(L - z') \right) \right] \right|^2 . \end{aligned} \tag{7.38}$$

The integral over Δk_S in Eq. 7.38 can easily be performed to yield

$$\begin{aligned} S_B(\theta &= \frac{k_o}{f_o} d_p, \Delta l') \propto \frac{d\sigma}{d\Omega}(\theta/n_o) \int dz' \\ &\times \exp\left[-\frac{\Delta k^2}{2} \left(\Delta l' - \frac{\theta^2}{2n_o^2}(L - z') \right)^2 \right] . \end{aligned} \tag{7.39}$$

This expression can be put in a more useful form by making some substitutions. Using Eq. 5.15, the spread of wavevectors Δk can be replaced by the $1/e$ width of the heterodyne signal Δl_B

$$\Delta k = \frac{\sqrt{2}}{\Delta l_B}. \tag{7.40}$$

Here Δl_B is defined as (Eq. 5.17)

$$\Delta l_B = \frac{l_c}{\sqrt{2\ln 2}} = \frac{\sqrt{2\ln 2}}{\pi}\frac{\lambda_o^2}{\Delta\lambda_{FWHM}}, \tag{7.41}$$

where l_c is the coherence length of the source as given by Eq. 5.14. The center wavelength of the source λ_o and full width at half maximum of the source bandwidth, $\Delta\lambda_{FWHM}$, for the Anritsu SLD are listed in Table 5.2. Finally, the integral over z' in Eq. 7.39 is limited to positions within the medium so it runs from 0 to n_oL. It is convenient to change this expression so that it contains an integral over the unitless variable $u = \frac{1}{n_o}\left(1 - z'/L\right)$. The resulting expression is then given as

$$S(\theta = d_p/f, \Delta l') \propto \frac{d\sigma}{d\Omega}(\theta/n_o)\int_0^1 du\, \exp\left(-\frac{(\Delta l' - \frac{L\theta^2}{2n_o}u)^2}{\Delta l_B^2}\right). \tag{7.42}$$

This expression is integrated numerically to obtain the theoretical model shown in Figure 7.4.

7.4 Discussion

The data shown in sections 7.2.1 and 7.2.3 are classified by the relative density of scatterers in the sample. The transmitted optical phase space distributions show different characteristics for each scattering regime. This section discusses the results obtained for transmission through weakly and strongly scattering samples and relates them to current biomedical optical imaging techniques.

7.4.1 Weak Scattering of a Low Coherence Source

For low concentrations of scatterers, the optical phase space distributions are dominated by ballistic light. However, the ability of the heterodyne method to selectively detect light with specific phase space parameters enables scattered light to be discerned from the ballistic. The scattered light is seen to form a two peak structure in momentum for the large diameter input beam and a two peak structure in position for the small diameter beam.

In the case of a large diameter input beam, the two peak structure in momentum (Fig. 7.4) is easily shown to arise from single scattering. When the LO path length is increased by $\Delta l'$, only light scattered in the medium through a nonzero angle θ_1 traverses an optical path with an increase equal to that of the LO:

$$n_o(L - z_s)\left(\frac{1}{\cos\theta_1} - 1\right) = \Delta l'. \tag{7.43}$$

Here, L is the location of the output plane of the medium, n_o is the index of refraction in the medium, and z_s is one possible plane in which the scattering occurs. By symmetry, positive or negative angles produce equal path lengths in the medium, yielding a two peak structure. For the small diameter beam, a two peak structure is also seen but in position instead of momentum. This two peak structure in position is more difficult to explain as it appears at much longer path delays than the two momentum peaks seen in the large diameter beam data. The longer path delay makes it seem unlikely that the two peaks in position arise from single scattering. Hence perturbation theory does not predict the structure seen in the data. At present, no theory has yet been developed which includes scattering of low coherence light to all orders.

7.4.2 Strong Scattering of a Low Coherence Source

At high concentrations of scatterers, the ballistic light is strongly attenuated so the possibility of using it for biological imaging becomes impractical. However, low ordered scattered light still retains information about its history and as shown in Chapter 6, light that has undergone multiple diffractive scatterings survives longer than ballistic light. By accepting photons that have a path length in the medium only marginally longer than the ballistic light, narrow momentum distributions can be recovered. The majority of these photons have undergone fewer scatterings than the background diffuse intensity and still retain information about the scattering medium.

7.4.3 Relation to Optical Coherence Tomography

The heterodyne method for measuring optical phase space distributions using low coherence light is related to the medical imaging technique known as optical coherence tomography (OCT) discussed in section 2.4.3. Both techniques rely on interferometry using a low coherence source to probe multiple scattering samples. OCT is based on a Michelson interferometer with a sample placed in one arm and a moveable mirror placed in the other. An interference signal is produced when the paths of the two arms are matched to within the coherence length of the source. Thus OCT achieves a similar timing resolution to the heterodyne method by exploiting the low coherence length of the source. However, the heterodyne method is capable of measuring both the position and momentum distribution of a light field whereas OCT only measures the position dependent intensity. Thus, measurement of optical phase space distributions recovers more information about the sample than OCT. Obtaining the additional information comes at a price. While OCT can measure a sample quickly enough for clinical applications, the heterodyne technique takes a much longer time to measure the full phase space distribution. Thus the method of heterodyne detection to measure optical phase space distributions will not replace OCT as a clinical method but instead can be used to understand and perhaps expand the limitations of OCT. In this way, measurement of optical phase space distributions can be used to enhance the images obtained with OCT.

Certain applied problems which have been observed in OCT can be explained using the results obtained using the heterodyne method. The coherent source transmission experiments in Chapter 6 show that multiple diffractive scattering in the forward direction can produce a narrow pedestal that decays more slowly than the ballistically transmitted component. At high concentrations of scatterers, if the diffractive pedestal is comparable to the ballistic component, it can modify the apparent intensity of a probe beam compared to that expected for exponential attenuation of ballistic light. This is consistent with the anomalous probe intensity observed by Yadlowsky et al., in OCT [20]. As large structures tend to produce more forward scattering than small ones, this effect serves to exaggerate finer structures over broad ones in OCT images.

Another issue in OCT which has received attention is the role that speckle plays in forming OCT images [21]. OCT imaging relies on the coherent addition of light which has been scattered only once by the sample. The image is corrupted by light which has undergone multiple scattering yet returns with the same path length as the singly scattered light. Both types of scattering are simultaneously detected using OCT since the received light is integrated over a broad range of angles using a lens with a large numerical aperature. By selecting a narrow angle for the detected light, as in the heterodyne method, the multiply scattered light can be selectively suppressed. In addition, it is possible that by making several narrow angle measurements at once, the speckle due to multiple scattering can be subtracted leaving only the desired signal arising from single scattering. While optical phase space distributions have shown the ability to isolate low order scattered light, further work is needed to relate it to the applied problem of speckle present in OCT.

Finally, I note that the method for characterizing the coherence of a source presented in Chapter 5, can be applied to determine the usefulness of a source for OCT.

For example, the Sarnoff SLD used in these experiments has an extremely low coherence length and high power yet lacks the spatial coherence need to form a tight focus. OCT relies on a tightly focused beam using a large numerical aperature lens to achieve high spatial resolution. Thus the advantage gained by an increase in power using this source may be offset by a loss of spatial resolution due to its decreased spatial coherence.

Chapter 8

Time-resolved optical phase space distributions for enhanced backscattering

This chapter presents a study of optical phase space distributions for light that has been backscattered by a turbid sample. The low coherence length Anritsu SLD is employed to measure backscattered light for various photon path lengths within the turbid media. Solutions of 0.5 μm diameter polystyrene spheres in a glycerol/water mixture are used as scattering samples because of their broad angular scattering distributions. Their nearly isotropic scattering and a high concentration permit many possible time reversed paths. As described in section 2.3.1, time reversed paths give rise to an increased intensity in the direction antiparallel to the incident light. This effect is known as enhanced backscattering.

The chapter begins by presenting the heterodyne system configured to measure light backscattered by a turbid sample. The first section also describes the specific turbid medium used in the backscattering experiments. The next section presents measured optical phase space distributions of backscattered light for various photon path lengths within the medium and compares them to theoretical distributions. Trends in the width and height of the enhanced backscattering peak are identified and compared to predicted values. The theoretical model used to obtain the predicted values is presented in the following section. The model is derived using the propagation of fields but is cast in the form of a Wigner distribution for comparison to the data. Finally, the last section discusses the results in terms of the propagation of coherence within the turbid medium.

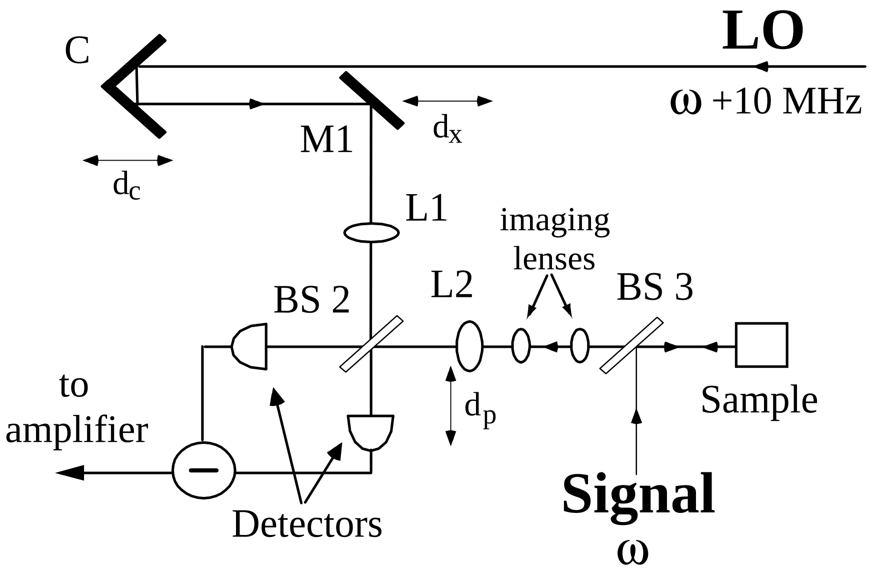

Figure 8.1: Experimental scheme configured for backscattering experiments using a low coherence source.

8.1 Experimental Setup

8.1.1 Heterodyne detection scheme configured for backscattering experiments

Figure 8.1 shows the heterodyne detection scheme as configured to measure low coherence length light that has been backscattered by a turbid medium. In this arrangement, the low coherence length signal beam at center frequency ω is directed to the turbid sample by beamsplitter BS3. The light scattered by the sample in the reverse direction passes through BS3 to lens L2 through the imaging lens system described below. The light from the signal beam is mixed at beamsplitter BS2 with the strong local oscillator at frequency $\omega + 10$ MHz. A heterodyne beat signal is produced for LO and signal paths which are matched to within the coherence length of the source. The path length of the LO can be varied by moving retroreflector C by a distance d_c. In addition, by varying the position of mirror M1 and lens L2, the effective center position and momentum of the LO are scanned. This allows the optical phase space distribution of the light backscattered from the sample to be mapped out in position and momentum for various path lengths within the medium.

As discussed in section 7.1.1, scanning mirror M1 and lens L2 also introduces changes in the optical path lengths. These changes must be compensated in order to keep the relative path difference between the LO and signal paths constant. The path difference between the two paths is given by Eq. 4.28 as

$$\Delta l' = \Delta l - \frac{d_p^2}{2f_o} + \frac{d_x d_p}{f_o}, \tag{8.1}$$

where $\Delta l = 2d_c$ and f_o is the focal length of the imaging lenses L1 and L2. The mathematical derivation and physical origin of these two correction terms is given in section 4.1.2.

The expression for the mean square heterodyne beat signal, as derived in section 4.1.2 is given by Eq. 4.27 as

$$\begin{aligned} |V_B(d_x, d_p, \Delta l)|^2 \quad \propto \quad & \left| \int dx' \int d\omega_k \mathcal{E}^*_{k_{LO}}(x' + d_x, z = 0) e^{-i\omega_k \Delta l/c}\, \mathcal{E}_{k_S}(x', z = 0) \right. \\ & \left. \times \exp(-ik\frac{d_p^2}{2f_o}) \exp(ik\frac{d_p}{f_o}x') \right|^2 . \end{aligned} \tag{8.2}$$

It is useful to define an effective LO field; its amplitude is given in Eq. 4.30 as

$$\begin{aligned} \mathcal{E}'^*_{k_{LO}}(x' + d_x, \Delta l', d_p) \quad &= \quad \mathcal{E}^*_{k_{LO}}(x' + d_x, z = 0) e^{-i\omega_k \Delta l/c} \\ &\times \quad \exp(-ik\frac{d_p^2}{2f_o}) \exp(ik\frac{d_p}{f_o}x'). \end{aligned} \tag{8.3}$$

This allows the mean square heterodyne beat signal to be written in terms of the overlap of the Wigner distribution of the signal field and that of the effective LO field

$$\begin{aligned} |V_B(d_x, d_p, \Delta l')|^2 \quad &= \quad \int d\omega_k \int dx \int dp\, W_S(x, z_o, \omega_k) \\ & \times W'_{LO}(x + d_x, z_o + \Delta l'; p + k\frac{d_p}{f_o}, \omega_k). \end{aligned} \tag{8.4}$$

In this expression, $W_S(x, z_o, \omega_k)$ is the Wigner distribution for the frequency component ω_k of the signal field specified in the input plane, i.e. in the principal plane of lens L2 as discussed in section 4.1.3. The Wigner distribution for the effective LO field is also specified in the input plane (principal plane of lens L1) but includes the shifts d_x, d_p, and $\Delta l'$ which allow the center position, momentum and path delay of the LO beam to be varied.

One particular problem with the configuration shown in Figure 8.1 is that the field emerging from the sample must propagate a considerable distance before reaching the input plane of the imaging system (principal plane of lens L2). As discussed in section 3.1.1, free space propagation alters the Wigner distribution of the field. Thus the detected signal does not map out the Wigner distribution emerging from the sample but rather measures a distribution which has had its position distribution altered according to Eq. 3.16 as

$$W'(x_d, p_d, z = d) = W(x_d - \frac{d}{k} p_d, p_d, z = 0) = W(x_o, p_o, z = 0), \tag{8.5}$$

In this expression the propagation is through a distance d. In order to reproduce the Wigner distribution of the light emerging from the sample in the plane of lens L2, an imaging system consisting of two lenses is inserted between beamsplitter BS3 and lens L2 as shown in Figure 8.2. As discussed in section 4.1.4, a two lens system is needed because one lens will not correctly reproduce the Wigner distribution on its own. The lenses used in the imaging system are equal focal length achromats separated by a distance of twice their focal lengths. Section 4.1.4 describes in detail how this two lens system reproduces a Wigner distribution while a single lens cannot.

8.1.2 Turbid Medium

Small spheres were specifically selected for the backscattering experiments to generate nearly isotropic scattering. For these experiments, latex microspheres ($n = 1.59$)

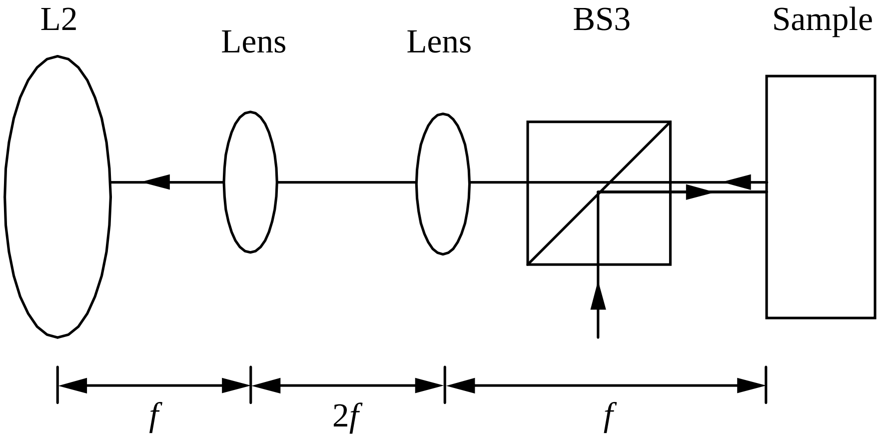

Figure 8.2: Two lens system for imaging Wigner distributions as installed in the backscattering configuration of the heterodyne scheme (Fig. 8.1). Note: distances are not to scale.

with a diameter of 0.5 μm are used. They are suspended in a mixture of 25% glycerol and 75% water which provides neutral buoyancy. As discussed in section 6.1.2, the mixture was found to have an index of ($n = 1.36$). Thus the index of the spheres relative to the background medium is given by $n = 1.17$. The source used in the backscattering experiments is the Anritsu SLD ($\lambda_{air} = 852$ nm), its properties are presented in Table 5.2. The scattering properties of the small spheres were found to only vary slightly over the bandwidth of this source so it is sufficient to calculate the theoretical scattering distribution at one wavelength. Using the Mie solution, the scattering cross section was found to be $\sigma_S = 0.063\,\mu\text{m}^2$, which is 0.32 times the geometrical cross section. The theoretical angular distribution is shown in Fig. 8.3. The angles in the plot again have been multiplied by 1.36 to account for the propagation of light from the background medium to air where it is detected. The distribution appears gaussian; however, as the particles here are smaller than a wavelength, the scattering distribution is now quite broad compared to the distribution of the larger spheres used in the transmission experiments. The

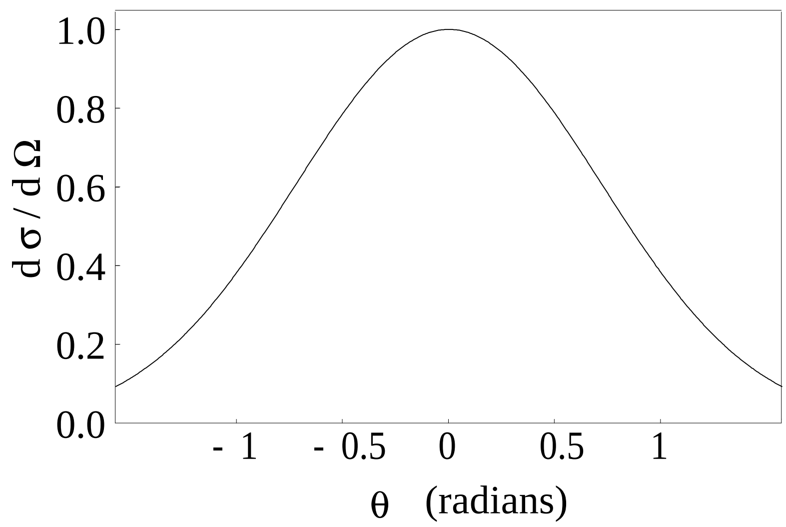

Figure 8.3: Mie differential cross section for scattering from 0.5 μm diameter polystyrene spheres with parameters $n_{rel} = 1.17$, $n_o = 1.36$, and $\lambda_{air} = 852$ nm.

half width at $1/e$ is 1.14 *radians* which corresponds to a width in air of 0.84 radians. The average of the cosine of the scattering angle for these spheres is $\langle \cos\theta \rangle = 0.74$, again indicating that the small spheres tend to scatter light over broader angles than the larger spheres.

8.2 Experimental Data

This section presents measured optical phase space contours for light backscattered from an extremely thick sample of 0.5 micron spheres. The broadband Anritsu SLD is used as the light source. As described in section 8.1.1, the low coherence length of this source ($l_c = 31.1.\mu$m from Table 5.2) can be exploited in a heterodyne scheme to selectively detect specific photon paths within the scattering medium. This enables the enhanced backscattering effect to be examined for various the photon path lengths. The data shows that with increasing photon path length, the enhanced backscattering peak narrows and becomes less prominent. These data are compared

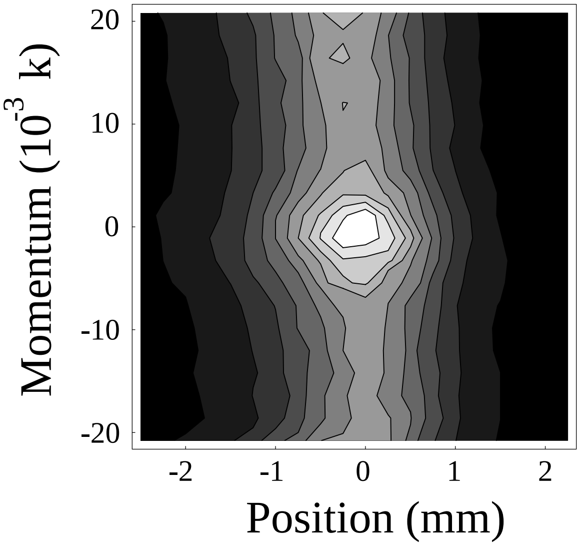

Figure 8.4: Measured optical phase space contours for backscattered light. $\Delta l' = 0.2$ mm, $\rho = 1.1 \times 10^{12}/\text{cm}^3$ (Linear scale).

to theoretical predictions using a model presented in section 8.3.

8.2.1 Optical phase space distributions for enhanced backscattering

Figure 8.4 shows typical measured optical phase space contours for light backscattered from a turbid sample. The concentration of spheres here is $\rho = 1.1 \times 10^{12}/\text{cm}^3$. This concentration would correspond to a ballistic attenuation of $\exp(-724)$ in a transmission experiment. The scattering mean free path for this concentration is $l = 13.8\ \mu$m while the transport mean free path is found to be

$$l^* = \frac{l}{(1 - \langle \cos\theta \rangle)} = 53.1\mu\text{m}. \tag{8.6}$$

To obtain the data in this plot, the LO path was delayed by 0.2 mm compared to light directly reflected from the input face of the sample, i.e. the detected light had a path length of 0.2 mm$/n_o$ = 0.2 mm/1.36 $\approx$ 0.15 mm within the medium. Two distinct features are observed here. The bright spot localized at zero transverse momentum

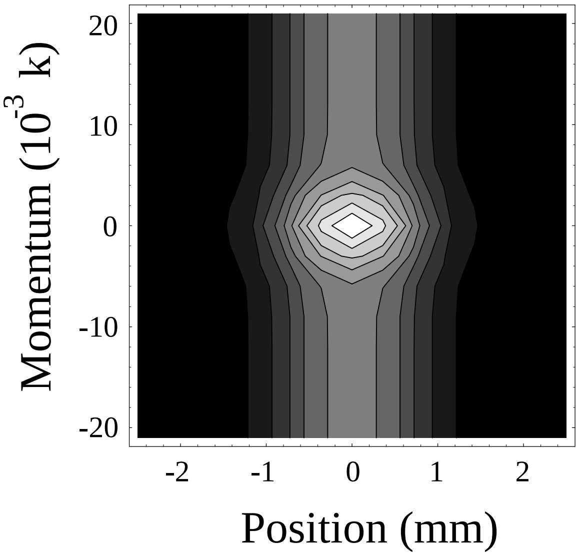

Figure 8.5: Theoretical optical phase space contours for backscattered light. $\Delta l' = 0.2$ mm, $\rho = 1.1 \times 10^{12}/\text{cm}^3$ (Linear scale).

and zero position represents the enhanced backscattering peak while the gray bands extending in momentum correspond to the diffuse background. This distribution qualitatively agrees with a theoretical treatment used to model enhanced backscatter. Figure 8.5 shows the theoretical optical phase space contours (Eq. 8.38) obtained for the same parameters as those used to collect the data shown in Fig. 8.4. The differences between the theoretical model and the experimental data become evident by examining the momentum distributions at zero position (Figure 8.6). In this plot the theoretical prediction (solid line) has a more prominent enhanced backscattering peak than the data (points). The theory and data agree more closely when the position integrated angular distributions are examined.

Enhanced backscattering is an effect observed in the momentum distribution of the backscattered light. For this reason, typical enhanced backscattering experiments employ position integrated momentum distributions to study the effect. Figure 8.7 presents the angular distribution obtained by integrating the optical phase space

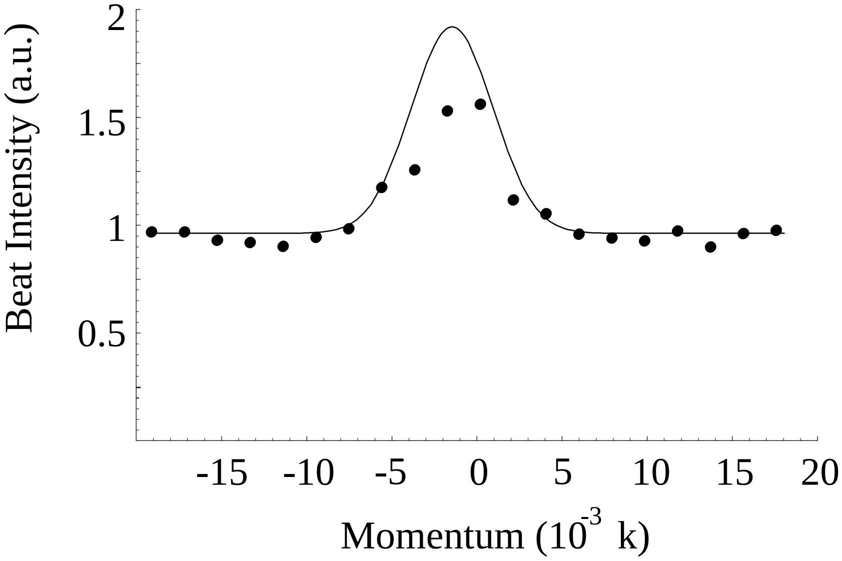

Figure 8.6: Measured optical phase space distribution for backscattered light at $x = 0$ with $\Delta l' = 0.2$ mm and $\rho = 1.1 \times 10^{12}/\text{cm}^3$. Solid line - theory; data - points.

distribution presented in Fig. 8.4 over position. This figure shows the measured angular distribution of light backscattered from a turbid sample of concentration $\rho = 1.1 \times 10^{12}/\text{cm}^3$ with an LO path delay, $\Delta l' = 0.2$ mm as compared to the theoretical prediction for the same parameters (solid line) as given in Eq. 8.39. This plot shows that here the theoretical model agrees more closely to the data than for the unintegrated case. The enhanced backscattering peak has a magnitude 1.6 times that of the background distribution. The peak is 3.9 mrad wide as it is measured in air. This corresponds to a width of 2.9 mrad within the medium ($n_o = 1.36$).

The treatment used to obtain the theoretical predictions for the enhanced backscattering is presented in detail in section 8.3. The theory makes use of the Gaussian-Schell model to describe the incident beam derived from the Anritsu SLD. The parameters of this model were found by replacing the scattering cell with a mirror and then applying the coherence characterization method described in Chapter 5. The

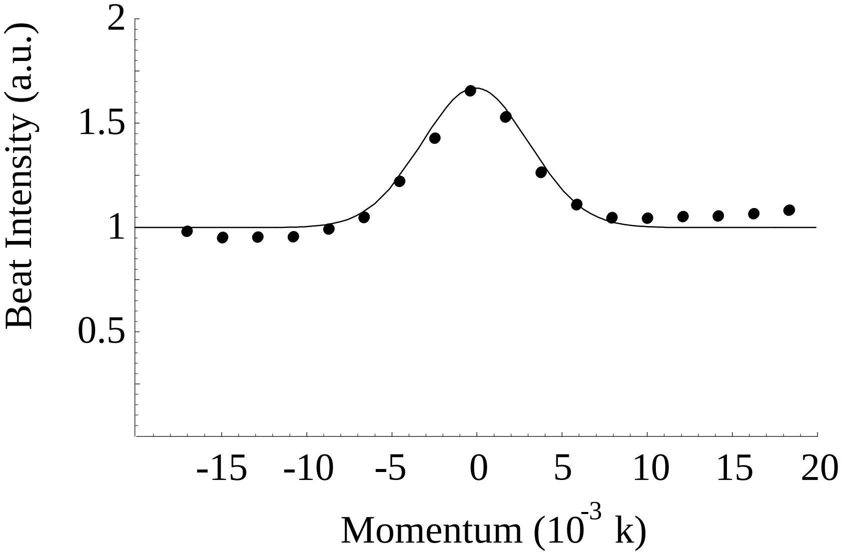

Figure 8.7: Measured angular distribution (position integrated) for backscattered light. $\Delta l' = 0.2$ mm, $\rho = 1.1 \times 10^{12}/\mathrm{cm}^3$.

Beam width, $2a$:	0.9 mm
Transverse coherence length, σ:	0.62 mm
Radius of wavefront curvature, R:	480 mm

Table 8.1: Summary of input beam coherence characteristics for backscattering experiments.

coherence properties of the beam are listed in Table 8.1. These properties differ from those listed for the Anritsu SLD in Table 5.2 as those measurements were made using the system configured for transmission measurements. In this experiment the system was configured to measure backscattering and thus the beam was not only shaped differently but passed through different optical elements than in the transmission configuration. Section 4.1.4 describes the differences between the transmission and backscattering measurement schemes in detail.

As a second example of enhanced backscattering, Figure 8.8 shows measured optical phase space contours for a LO path delay $\Delta l' = 0.6$ mm at the same concentration

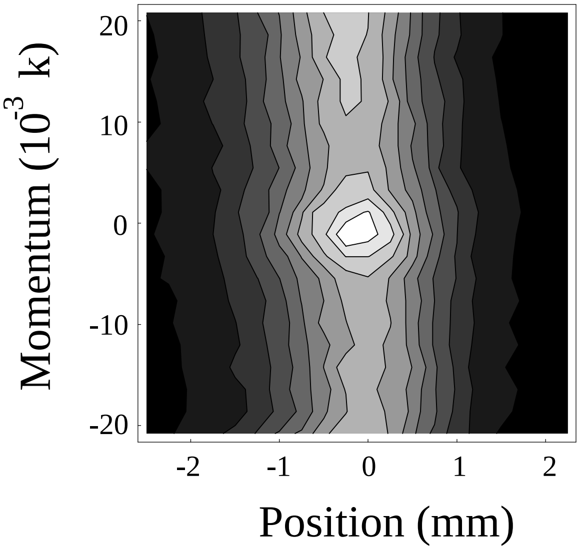

Figure 8.8: Measured optical phase space contours for backscattered light. $\Delta l' = 0.6$ mm, $\rho = 1.1 \times 10^{12}/\text{cm}^3$ (Linear scale).

($\rho = 1.1 \times 10^{12}/\text{cm}^3$). The enhanced backscattering peak is shown in this figure as the bright spot at zero transverse momentum and zero position. It is less prominent compared with the peak seen at shorter LO path delay (Fig. 8.4). The gray bands again correspond to the diffuse background light. This data is also in agreement with the theoretical model. For comparison, Figure 8.9 shows the theoretical distribution (Eq. 8.38) obtained using the same parameters as those for the distribution in Figure 8.8. While the theory also qualitatively agrees with the data at this path delay, examination of the angular distribution for zero position reveals the differences between the two. Figure 8.10 shows that the theory predicts a narrower more prominent peak than seen in the data. However, the position integrated measured angular distribution is seen to agree much more closely to the theory. Figure 8.11 presents the position integrated angular distribution for the optical phase space distribution presented in Figure 8.8. The solid line again represents the theoretical prediction as given by Eq. 8.39. In this plot, the enhanced backscattering peak is 1.34 times the

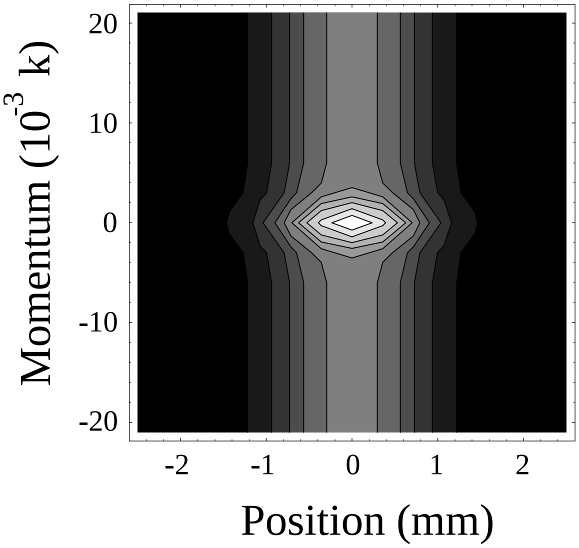

Figure 8.9: Theoretical optical phase space contours for backscattered light. $\Delta l' = 0.6$ mm, $\rho = 1.1 \times 10^{12}/\text{cm}^3$ (Linear scale).

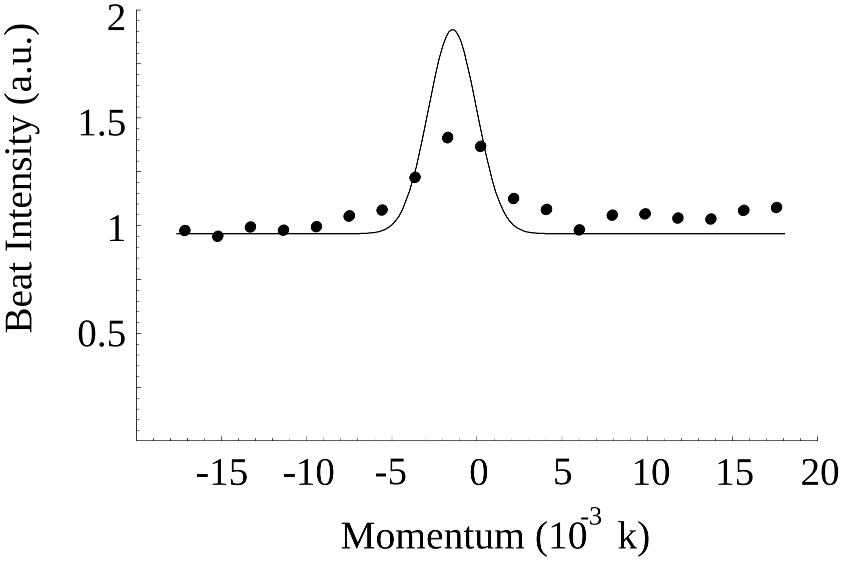

Figure 8.10: Measured optical phase space distribution for backscattered light at $x = 0$ with $\Delta l' = 0.6$ mm and $\rho = 1.1 \times 10^{12}/\text{cm}^3$. Solid line - theory; data - points.

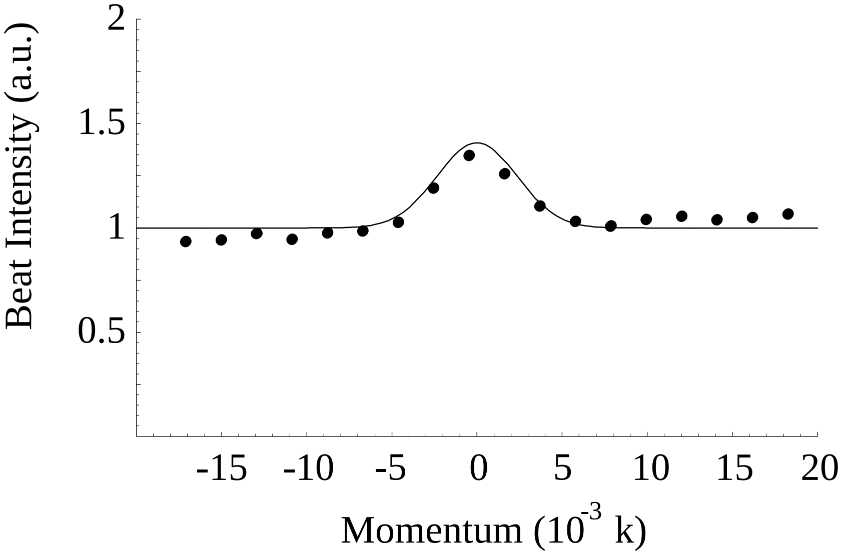

Figure 8.11: Measured angular distribution (position integrated) for backscattered light. $\Delta l' = 0.6$ mm, $\rho = 1.1 \times 10^{12}/\text{cm}^3$.

magnitude of the background light. The width of the peak is measured in air to be 3.1 mrad which corresponds to a width of 2.3 mrad within the medium.

8.2.2 Trends of the enhanced backscattering peak

Optical phase space distributions were measured for various LO path delays, ranging from 0 to 1 mm, for the turbid sample ($\rho = 1.1 \times 10^{12}/\text{cm}^3$). The fitted angular width and magnitude of the enhancement peak from the position integrated data yield good agreement to the theoretical model. Figure 8.12 shows the fitted momentum width as a function of photon path length within the medium (Table A.11). The widths are scaled to represent the angular width within the medium for comparison to the theoretical model (solid line). The theoretical curve shown here as given in Eq. 8.40 correctly models the trend in angular widths although predicts slightly broader peaks than those seen in the data. However the theoretical prediction shown is presented with no free parameters. If the value of a beam parameter, such as the radius of

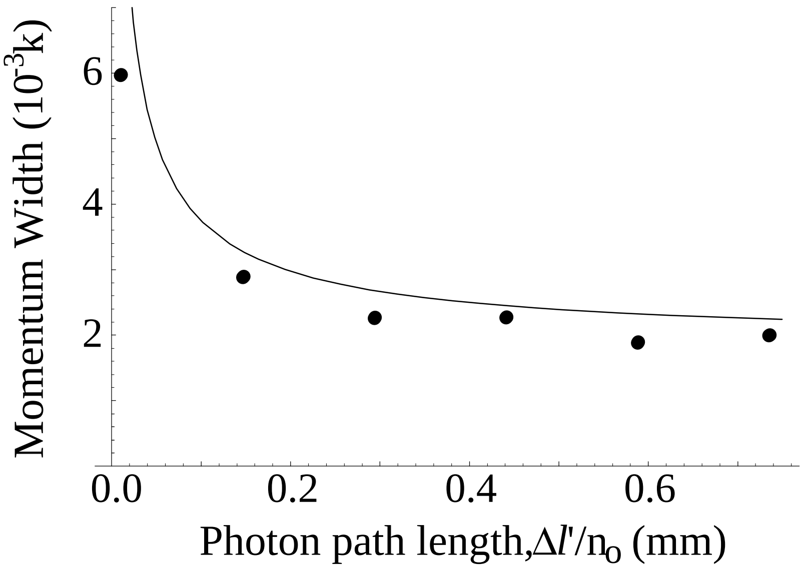

Figure 8.12: Fitted angular width of enhanced backscattering peak at various LO path delays, $\rho = 1.1 \times 10^{12}/\text{cm}^3$. Solid line- theory, points - data ($n_o = 1.36$).

curvature for the LO, is increased by 10% in the theory, the prediction and data are seen to agree even more closely. The data point at zero path delay does not agree with this model in either case. It is not expected to be correctly predicted because the theoretical model is based on a diffusion approximation which is invalid for short photon path length in the medium.

Further agreement between the data and the theoretical model is seen in a comparison of the predicted and measured peak heights. Figure 8.13 shows the magnitude of the enhanced backscattering peak as a function of photon path length within the medium (Table A.12). The magnitude has been normalized by the average magnitude of the diffuse background. The solid line represents the theoretical prediction as given by Eq. 8.41, again with no free parameters. It agrees well with the measured peak magnitudes with the exception of the data point at zero path delay. As noted previously, the theory is invalid for very short LO path delays.

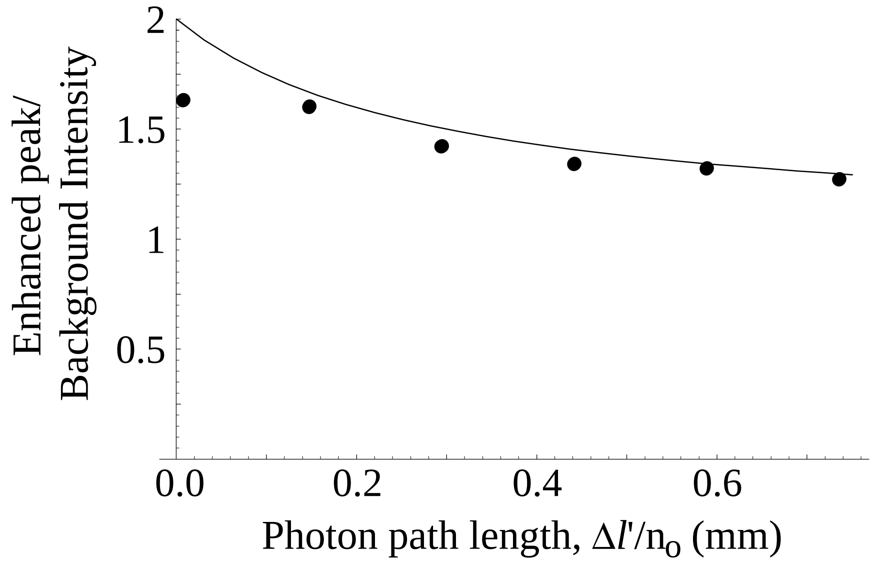

Figure 8.13: Fitted magnitude of enhanced backscattering peak at various LO path delays, $\rho = 1.1 \times 10^{12}/\mathrm{cm}^3$. Solid line- theory, points - data ($n_o = 1.36$).

8.3 Theory

In this section a theory is developed to explain the data shown in section 8.2. The theory is based on a treatment by Okamoto and Asakura [37] which examines the effects of partial spatial coherence on enhanced backscattering. The model developed here builds upon their work by adding time dependence so that the effects of temporal coherence are also included. The treatment begins by considering the field backscattered from a turbid medium. While Okamoto and Asakura give their result in terms of an intensity, this treatment casts the result in the form of a Wigner distribution so that the model can be compared with the experimental results.

8.3.1 Backscattering geometry

Figure 8.14 shows the geometry for the enhanced backscattering problem. In this geometry, a photon at frequency ν propagating with momentum $\mathbf{p}_o$ enters the scat-

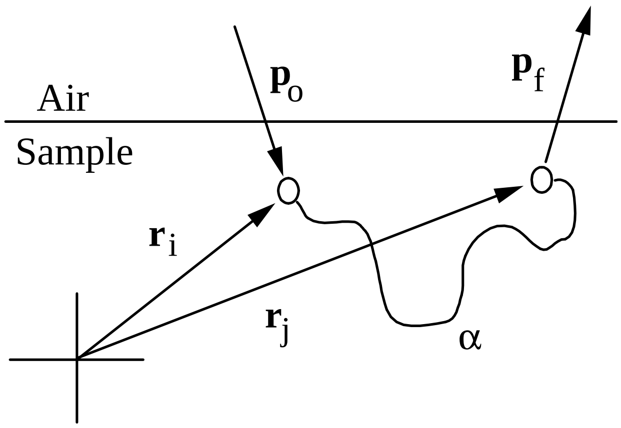

Figure 8.14: Geometry of the backscattering problem. $\mathbf{r}_i$ ($\mathbf{r}_j$) is the location of the first (last) scattering, $\mathbf{p}_i$ ($\mathbf{p}_j$) is the momentum of the photon as it enters (exits) the medium and α denotes the path a photon travels between the first and last scattering.

tering sample close to the point $\mathbf{r}_i$ where it first scatters. The photon travels along the path α until it exits the medium travelling in the direction $\mathbf{p}_f$ near the point of its final scattering $\mathbf{r}_j$. Summing such photons over all possible scattering paths within the medium results in a complex amplitude for the scattered field [37]

$$\mathcal{E}_{ij}(\mathbf{p}_o, \mathbf{p}_f, \nu) = \sum_{\alpha} a(\mathbf{p}_{o\perp}, \nu)\, p_{i\,j}(\alpha, \nu) \exp\left[i\left(\mathbf{p}_o \cdot \mathbf{r}_i - \mathbf{p}_f \cdot \mathbf{r}_j\right)\right], \tag{8.7}$$

where $a(\mathbf{p}_{o\perp}, \nu)$ is the angular spectrum of the incident field, and $p_{i\,j}(\alpha, \nu)$ is a complex probability amplitude which includes an implied phase shift for the path α. Its square modulus $|p_{i\,j}(\alpha, \nu)|^2$, is the probability density of a photon of frequency ν following the path α from $\mathbf{r}_i$ to $\mathbf{r}_j$.

To calculate the total field emerging with final momentum $\mathbf{p}_f$, all possible combinations of initial and final scattering positions as well as all incident directions, $\mathbf{p}_{o\perp}$, must be summed over. The amplitude of the field is thus given by

$$\mathcal{E}(\mathbf{p}_f, \nu) = \int d^2\mathbf{p}_{o\perp} \sum_{i,j} \mathcal{E}_{ij}(\mathbf{p}_o, \mathbf{p}_f, \nu), \tag{8.8}$$

where $\mathcal{E}_{ij}$ is given in Eq. 8.7. The total field with final momentum $\mathbf{p}_f$ is given by the summation of all frequency components

$$E(\mathbf{p}_f) = \int d\nu \, \mathcal{E}(\mathbf{p}_f, \nu) \, e^{-2\pi i \nu}. \tag{8.9}$$

8.3.2 Diffusive Propagation

For a sufficiently dense random medium, the probability of following a given path α, can be found by using the diffusion approximation to model the propagation. In this approximation, the photon density $\rho(\mathbf{r}, t)$ obeys the diffusion equation [38]

$$\frac{\partial \rho(\mathbf{r}, t)}{\partial t} = -D \nabla^2 \rho(\mathbf{r}, t), \tag{8.10}$$

where D is the diffusion constant. The diffusion constant is given by

$$D = \frac{1}{3} c' l^* \tag{8.11}$$

where $c' = c/n_o$ is the speed in the medium and l^* is the transport mean free path. The transport mean free path is related to the scattering mean free path l by

$$l^* = \frac{l}{(1-g)} \tag{8.12}$$

where g is the mean cosine of the scattering angle. The value of l^* for the backscattering experiments is given in Eq. 8.6 as $l^* = 53.1$ μm.

For the problem at hand, Equation 8.10 is subject to the boundary condition that the medium occupies the half space $z \geq 0$. This boundary condition does not demand that the density vanishes at $z = 0$, but rather at some position beyond the edge of the medium $z = -z_o$. The value of z_o, which represents the point outside of the medium at which the photon density vanishes is a matter of some debate. It is given by Akkermans [38] as

$$z_o = 0.7104...l, \tag{8.13}$$

where l is the scattering mean free path.

Using this boundary condition, the solution to Eq. 8.10 will be of the form

$$\rho(\mathbf{r},t) = \int_0^\infty dk_z \int d^2\mathbf{k}_\perp A(k_z,\mathbf{k}_\perp) \frac{e^{i\mathbf{k}_\perp\cdot\mathbf{r}_\perp}}{(2\pi)^2} \frac{2}{\pi} \sin\left[k_z(z+z_o)\right] e^{-\Gamma t}. \tag{8.14}$$

The parameter Γ can be found by inserting Eq. 8.14 into the diffusion equation (Eq. 8.10) and is given as

$$\Gamma = Dk^2. \tag{8.15}$$

The amplitude $A(k_z,\mathbf{k}_\perp)$ can be found by inverse transforming Eq. 8.14 with $t=0$. This yields the following expression:

$$A(k_z,\mathbf{k}_\perp) = \int_0^\infty dz' \int d^2\mathbf{r}'_\perp \rho(\mathbf{r}',0) \sin(k_z(z'+z_o)) e^{-i\mathbf{k}_\perp\cdot\mathbf{r}'_\perp}. \tag{8.16}$$

Reinserting this expression back into Eq. 8.14 yields

$$\begin{aligned} \rho(\mathbf{r},t) &= \int_0^\infty dz' \int d^2\mathbf{r}'_\perp\, \rho(\mathbf{r},0)\, \frac{1}{(4\pi Dt)^{3/2}} \exp\left(-\frac{(\mathbf{r}-\mathbf{r}')^2}{4Dt}\right) \\ &\times \left[\exp\left(-\frac{(z-z')^2}{4Dt}\right) - \exp\left(-\frac{(z+z'+2z_o)^2}{4Dt}\right)\right]. \end{aligned} \tag{8.17}$$

Thus the probability for propagation from $\mathbf{r}$ to $\mathbf{r}'$ in a time t is given by

$$\begin{aligned} P(\mathbf{r},\mathbf{r}',t) &= \frac{1}{(4\pi Dt)^{3/2}} \exp\left(-\frac{(\mathbf{r}-\mathbf{r}')^2}{4Dt}\right) \\ &\times \left[\exp\left(-\frac{(z-z')^2}{4Dt}\right) - \exp\left(-\frac{(z+z'+2z_o)^2}{4Dt}\right)\right]. \end{aligned} \tag{8.18}$$

8.3.3 Wigner distribution for enhanced backscattering

It is convenient to work with the Wigner distribution in terms of momentum space fields such as the one given in Eq. 8.9. It is given by [11]

$$W(\mathbf{x},\mathbf{p}) = \frac{1}{2\pi} \int d^3\mathbf{q}\, e^{i\mathbf{q}\cdot\mathbf{x}} \left\langle E(\mathbf{p}+\frac{\mathbf{q}}{2}) E^*(\mathbf{p}-\frac{\mathbf{q}}{2}) \right\rangle. \tag{8.19}$$

Expanding the field into its frequency components using Eq. 8.9, the Wigner distribution for backscattered light is given by

$$W_{back}(\mathbf{x}, \mathbf{p}_f) = \frac{1}{2\pi} \int d^3\mathbf{q} \int d\nu \, e^{i\mathbf{q}\cdot\mathbf{x}} \left\langle \mathcal{E}(\mathbf{p}_f + \frac{\mathbf{q}}{2}, \nu) \mathcal{E}^*(\mathbf{p}_f - \frac{\mathbf{q}}{2}, \nu) \right\rangle, \tag{8.20}$$

where the two integrals over frequencies have been reduced to a single integral by assuming that the $\mathcal{E}$'s are delta correlated in frequency. Using Eq. 8.8, the bracketed term in Eq. 8.20 is written as

$$\begin{aligned} &\left\langle \mathcal{E}(\mathbf{p}_f + \frac{\mathbf{q}}{2}, \nu) \mathcal{E}^*(\mathbf{p}_f - \frac{\mathbf{q}}{2}, \nu) \right\rangle = \\ &\left\langle \int d^2\mathbf{p}_{o\perp} \sum_{i,j} \mathcal{E}_{ij}(\mathbf{p}_o, \mathbf{p}_f + \frac{\mathbf{q}}{2}, \nu) \int d^2\mathbf{p}'_{o\perp} \sum_{l,m} \mathcal{E}^*_{lm}(\mathbf{p}'_o, \mathbf{p}_f - \frac{\mathbf{q}}{2}, \nu) \right\rangle. \end{aligned} \tag{8.21}$$

This can be rewritten as

$$\begin{aligned} &\left\langle \mathcal{E}(\mathbf{p}_f + \frac{\mathbf{q}}{2}, \nu) \mathcal{E}^*(\mathbf{p}_f - \frac{\mathbf{q}}{2}, \nu) \right\rangle = \\ &\int d^2\mathbf{p}_{o\perp} \int d^2\mathbf{p}'_{o\perp} \, \langle a(\mathbf{p}_{o\perp}, \nu) \, a^*(\mathbf{p}'_{o\perp}, \nu) \rangle \times \sum_{i,j} \left\langle \sum_{\alpha} |p_{i\,j}(\alpha, \nu)|^2 \right\rangle \\ &\times \left[\exp\left(i\mathbf{r}_i \cdot (\mathbf{p}_o - \mathbf{p}'_o)\right) \exp\left(-i\mathbf{q} \cdot \mathbf{r}_j\right) \right. \\ &\left. + \exp\left(i\mathbf{r}_i \cdot (\mathbf{p}_o + \mathbf{p}_f - \frac{\mathbf{q}}{2})\right) \exp\left(-i\mathbf{r}_j \cdot (\mathbf{p}_o + \mathbf{p}_f + \frac{\mathbf{q}}{2})\right) \right], \end{aligned} \tag{8.22}$$

by using Eq. 8.7 and making one key assumption. It is assumed that there is no correlation between scattering paths in the medium such that interference between photons travelling different paths cancel after averaging. This assumption is referred to as the weak disorder limit [37]. In this limit the only terms which contribute arise from self-interfering photons and time-reversed pairs. The self-interfering photons occur for $i = l$, $j = m$, and $\alpha = \alpha'$, while the time-reversed pairs occur for $i = m$, $j = l$, and $\alpha = -\alpha'$. This condition allows the sums over i, j and l, m and the implied sums over α and α' in Eq. 8.21 to be collapsed into a single sum over starting and ending points (i, j), and a single sum over paths (α).

For a completely uncorrelated medium, the probability of following a path from $\mathbf{r}_i$ to $\mathbf{r}_j$ depends only on the distance between the two points. In this situation, the term in Eq. 8.22 which governs the probability of scattering paths can be written as

$$\sum_{i,j} \left\langle \sum_{\alpha} |p_{i\,j}(\alpha, \nu)|^2 \right\rangle = \int d^2\mathbf{r}_i\, d^2\mathbf{r}_j P(|\mathbf{r}'|\,, t), \tag{8.23}$$

where $\mathbf{r}' = \mathbf{r}_i - \mathbf{r}_j$ and $d^2\mathbf{r}_i\, d^2\mathbf{r}_j P(|\mathbf{r}'|\,, t)$ is the probability of a photon entering the medium $\mathbf{r}_i$ and exiting at $\mathbf{r}_j$ as given by Eq. 8.18. Inserting this expression and Eq. 8.22 in Eq. 8.20 and carrying out some straightforward integrals yields

$$\begin{aligned} W_{back}(\mathbf{x}_\perp, z \;\; &= \;\; 0, \mathbf{p}_f) = \frac{1}{2\pi} \int d\nu \int d^2\mathbf{p}_{o\perp}\, d^2\mathbf{p}'_{o\perp}\, \langle a(\mathbf{p}_{o\perp}, \nu)\, a^*(\mathbf{p}'_{o\perp}, \nu) \rangle \\ &\times \int d^2\mathbf{r}_i\, d^2\mathbf{r}_j P(|\mathbf{r}'|\,, t) \times \Big[\delta(\mathbf{x}_\perp - \mathbf{r}_{j\,\perp}) e^{i\mathbf{r}_i \cdot (\mathbf{p}_o - \mathbf{p}'_o)} \\ &+ \delta\left(\mathbf{x}_\perp - \frac{\mathbf{r}_{i\,\perp} + \mathbf{r}_{j\,\perp}}{2} \right) e^{i\mathbf{r}_i \cdot (\mathbf{p}_o + \mathbf{p}_f)} e^{-i\mathbf{r}_i \cdot (\mathbf{p}_o + \mathbf{p}_f)} \Big]. \end{aligned} \tag{8.24}$$

This equation can be more elegantly written by changing variables:

$$\begin{array}{cc} \mathbf{r}' = \mathbf{r}_i - \mathbf{r}_j & \mathbf{p}' = \mathbf{p}_o - \mathbf{p}'_o \\ \mathbf{r} = \frac{\mathbf{r}_i + \mathbf{r}_j}{2} & \mathbf{p} = \frac{\mathbf{p}_o + \mathbf{p}'_o}{2} \end{array} \tag{8.25}$$

The delta functions now permit easy integration, which yields

$$\begin{aligned} W_{back}(\mathbf{x}_\perp, z \;\; &= \;\; 0, \mathbf{p}_f) = \frac{1}{2\pi} \int d\nu \int d^2\mathbf{p}_\perp\, d^2\mathbf{p}'_\perp\, \langle a(\mathbf{p}_\perp + \mathbf{p}'_\perp/2, \nu)\, a^*(\mathbf{p}_\perp - \mathbf{p}'_\perp/2, \nu) \rangle \\ &\times \int d^2\mathbf{r}' P(|\mathbf{r}'|\,, t) \left[e^{i\mathbf{x}_\perp \cdot \mathbf{p}'} + e^{i\mathbf{x}_\perp \cdot \mathbf{p}'} e^{i\mathbf{r}' \cdot (\mathbf{p} - \mathbf{p}_f)} \right]. \end{aligned} \tag{8.26}$$

The angular correlation function $\langle a(\mathbf{p}_\perp + \mathbf{p}'_\perp/2, \nu)\, a^*(\mathbf{p}_\perp - \mathbf{p}'_\perp/2, \nu) \rangle$, is the Fourier transform of the cross-spectral density

$$\langle a(\mathbf{p}_\perp + \mathbf{p}'_\perp/2, \nu)\, a^*(\mathbf{p}_\perp - \mathbf{p}'_\perp/2, \nu) \rangle = \int d^2\mathbf{x}_\perp\; d^3\mathbf{x}'_\perp\; \mathcal{W}(\mathbf{x}_\perp, \mathbf{x}'_\perp, \nu) \tag{8.27}$$

$$\times \exp\left[i\mathbf{x}_\perp \cdot (\mathbf{p}_\perp + \mathbf{p}'_\perp/2) - i\mathbf{x}'_\perp \cdot (\mathbf{p}_\perp - \mathbf{p}'_\perp/2) \right]$$

with $\mathcal{W}(\mathbf{x}_\perp, \mathbf{x}'_\perp, \nu)$ given in Eq. 5.2 as

$$\mathcal{W}(\mathbf{x}_\perp, \mathbf{x}'_\perp, \nu) \propto \exp\left[-\frac{\mathbf{x}_\perp^2 + \mathbf{x}'^2_\perp}{4a^2}\right] \exp\left[-\frac{(\mathbf{x}_\perp - \mathbf{x}'_\perp)^2}{2\sigma^2}\right] \exp\left[\frac{ik}{2R}(\mathbf{x}_\perp^2 - \mathbf{x}'^2_\perp)\right]. \quad (8.28)$$

In defining the cross-spectral density, the spatial intensity width, $2a$, the transverse coherence length, σ and the beam curvature, R, are introduced. These parameters are specified for the Anritsu SLD in Table 8.1.

Using Eq. 8.28 and Eq. 8.28, the Wigner distribution of the backscattered light can be written, after some straightforward integration, as

$$\begin{aligned} W_{back}(\mathbf{x}_\perp, z &= 0, \mathbf{p}_f) = \frac{1}{2\pi}\int d\nu \exp\left(-\frac{\mathbf{x}_\perp^2}{2a^2}\right)\int d^2\mathbf{p}_\perp \exp\left(-\frac{(\mathbf{p}_\perp - \frac{k}{R}\mathbf{x}_\perp)^2}{\left(\frac{1}{2a^2}+\frac{2}{\sigma^2}\right)}\right) \\ &\times \int d^2\mathbf{r}' P(|\mathbf{r}'|, t)\left[1 + e^{i\mathbf{r}'\cdot(\mathbf{p}-\mathbf{p}_f)}\right] \quad (8.29) \end{aligned}$$

For all points $\mathbf{r}_i$, $\mathbf{r}_j$ lying at the surface $z = 0$, the probability density of photon paths (Eq. 8.18) is given by

$$P(|\mathbf{r}'|, t) = \frac{1}{(4\pi Dt)^{3/2}} \exp\left(-\frac{\mathbf{r}'^2}{4Dt}\right)\left[1 - \exp\left(-\frac{(2z_o)^2}{4Dt}\right)\right], \quad (8.30)$$

where D is the diffusion constant as given in Eq. 8.11 and the parameter z_o is given in Eq. 8.13. Inserting Eq. 8.30 into the $\mathbf{r}'$ integral in Eq. 8.29 yields

$$\begin{aligned} \int d^2\mathbf{r}' P(|\mathbf{r}'|, t)\left[1 + e^{i\mathbf{r}'\cdot(\mathbf{p}-\mathbf{p}_f)}\right] &= \frac{1}{(4\pi Dt)^{3/2}}\left[1 - \exp\left(-\frac{(2z_o)^2}{4Dt}\right)\right] \quad (8.31) \\ &\times \int d^2\mathbf{r}' \exp\left(-\frac{\mathbf{r}'^2}{4Dt}\right)\left[1 + e^{i\mathbf{r}'\cdot(\mathbf{p}-\mathbf{p}_f)}\right]. \end{aligned}$$

After integration, this term becomes

$$\begin{aligned} \int d^2\mathbf{r}' P(|\mathbf{r}'|, t)\left[1 + e^{i\mathbf{r}'\cdot(\mathbf{p}-\mathbf{p}_f)}\right] &= \frac{1}{(4\pi Dt)^{1/2}}\left[1 - \exp\left(-\frac{(2z_o)^2}{4Dt}\right)\right] \\ &\times \left[1 + \exp\left(-Dt(\mathbf{p}-\mathbf{p}_f)^2\right)\right]. \quad (8.32) \end{aligned}$$

Thus, the form of the Wigner distribution is given as

$$\begin{aligned} W_{back}(\mathbf{x}_\perp, z &= 0, \mathbf{p}_f) \propto \exp\left(-\frac{\mathbf{x}_\perp^2}{2a^2}\right)\int d^2\mathbf{p}_\perp \exp\left(-\frac{(\mathbf{p}_\perp - \frac{k}{R}\mathbf{x}_\perp)^2}{\left(\frac{1}{2a^2}+\frac{2}{\sigma^2}\right)}\right) \quad (8.33) \\ &\times \frac{1}{(4\pi Dt)^{1/2}}\left[1 - \exp\left(-\frac{(2z_o)^2}{4Dt}\right)\right]\left[1 + \exp\left(-Dt(\mathbf{p}-\mathbf{p}_f)^2\right)\right]. \end{aligned}$$

After integration over $\mathbf{p}_\perp$ the distribution becomes

$$\begin{aligned} W_{back}(\mathbf{x}_\perp, z &= 0, \mathbf{p}_{f\perp}) \propto \frac{1}{(4\pi Dt)^{1/2}} \exp\left(-\frac{\mathbf{x}_\perp^2}{2a^2}\right)\left[1 - \exp\left(-\frac{(2z_o)^2}{4Dt}\right)\right] \\ &\times \left[1 + \frac{\frac{1}{Dt}}{\frac{1}{Dt} + \frac{1}{2a^2} + \frac{2}{\sigma^2}} \exp\left(-\frac{(\mathbf{p}_{f\perp} - \frac{k}{R}\mathbf{x}_\perp)^2}{\left(\frac{1}{Dt} + \frac{1}{2a^2} + \frac{2}{\sigma^2}\right)}\right)\right], \end{aligned} \tag{8.34}$$

which gives the form of the Wigner distribution emerging from the turbid medium.

8.3.4 Heterodyne beat signal

In order to compare the theoretical model to the experimental data, the Wigner distribution of the backscattered field (Eq. 8.34) must be convoluted with that of the LO. For computational simplicity, it is assumed that the LO has a sufficiently small coherence length to directly select the photon path length in the medium. Thus the Dt term in the distribution of backscattered light will be replaced by

$$Dt = \frac{1}{3}c'l^*t = \frac{1}{3}l^*\frac{\Delta l'}{n_o}, \tag{8.35}$$

where $\Delta l'$ is the path length difference between the LO and signal beams as given by Eq. 8.1 and $c't = \Delta l'/n_o$ is the corresponding path length within the medium. The phase space distribution of the LO is given by

$$\begin{aligned} W_{LO}\left(\mathbf{x}_\perp - d_x\hat{x}, \mathbf{p}_{f\perp} - \frac{k}{f_o}d_p\hat{x}\right) \propto \exp &\left(-\frac{(\mathbf{x}_\perp - d_x\hat{x})^2}{2a^2}\right) \\ \times \quad \exp &\left(-\frac{(\mathbf{p}_{f\perp} - \frac{k}{f_o}d_p\hat{x} - \frac{k}{R}\mathbf{x}_\perp - d_x\hat{x})^2}{\left(\frac{1}{2a^2} + \frac{2}{\sigma^2}\right)}\right), \end{aligned} \tag{8.36}$$

where the LO center momentum is varied by $\frac{k}{f_o}d_p$ and $2a$, R, and σ are the beam parameters for the Anritsu SLD as given in Table 8.1.

The convolution of the Wigner distributions for the LO and signal fields gives the heterodyne beat signal (Eq. 8.4):

$$\begin{aligned} S_B\left(d_x, \theta = \frac{k}{f_o}d_p, \Delta l'\right) &= \int d^2\mathbf{p}_{f\perp} \int d^2\mathbf{x}_\perp \\ & W_{LO}\left(\mathbf{x}_\perp - d_x\hat{x}, \mathbf{p}_{f\perp} - \frac{k}{f_o}d_p\hat{x}\right) W_{back}(\mathbf{x}_\perp, \mathbf{p}_{f\perp}, \Delta l'). \end{aligned} \tag{8.37}$$

Substituting Eq.'s 8.34, 8.35 and 8.36 into this equation and carrying out the $\mathbf{p}_{f\perp}$ and $\mathbf{x}_{\perp}$ integrals results in a mean square beat signal of magnitude

$$\begin{aligned} S_B\left(d_x, \theta = \frac{k}{f_o} d_p, \Delta l'\right) \;\propto\;& \frac{\pi^2}{2} \exp\left(-\frac{d_x^2}{4a^2}\right) \times \\ & \left[1 + \frac{1 + \left(\frac{1}{2a^2} + \frac{2}{\sigma^2}\right) \frac{l^*}{3} \frac{\Delta l'}{n_o}}{1 + \left(\frac{1}{a^2} + \frac{2}{\sigma^2}\right) \frac{l^*}{3} \frac{\Delta l'}{n_o}} \exp\left(-\frac{1}{a^4} \frac{(k\theta - \frac{k}{R} d_x)^2}{\left(\frac{1}{2a^2} + \frac{2}{\sigma^2} + \frac{3n_o}{l^* \Delta l'}\right)}\right)\right]. \end{aligned} \tag{8.38}$$

This theoretical model is seen to give good qualitative agreement with the data presented in section 8.2.

In backscattering experiments, it is useful to examine the angular distribution emerging from the medium. The angular distribution is found by integrating Eq. 8.38 over all LO center positions d_x. This yields a distribution of the form

$$\begin{aligned} S'_B\left(\theta = \frac{d_p}{f_o}, \Delta l'\right) \propto 1 \;\; &+ \;\; \frac{1 + \left(\frac{1}{2a^2} + \frac{2}{\sigma^2}\right) \frac{l^*}{3} \frac{\Delta l'}{n_o}}{1 + \left(\frac{4a^2k^2}{R^2} + \frac{1}{a^2} + \frac{2}{\sigma^2}\right) \frac{l^*}{3} \frac{\Delta l'}{n_o}} \\ &\times \;\; \exp\left(-\frac{(k\theta)^2}{\left(\frac{4a^2k^2}{R^2} + \frac{1}{a^2} + \frac{2}{\sigma^2} + \frac{3n_o}{l^* \Delta l'}\right)}\right). \end{aligned} \tag{8.39}$$

This model takes the form of a broad diffuse background (represented by the '1') and an enhanced backscattering peak which arises from coherent addition of time reversed photon paths. This distribution was used to plot the theoretical optical phase space distributions shown in Figures 8.5 and 8.9. The width of the backscattering peak scales with path delay $\Delta l'$ (Fig. 8.12) as

$$\theta_{1/e} = \frac{1}{k} \sqrt{\left(\frac{4a^2k^2}{R^2} + \frac{1}{a^2} + \frac{2}{\sigma^2} + \frac{3n_o}{l^* \Delta l'}\right)}, \tag{8.40}$$

while the magnitude of the peak compared to the diffuse background (Fig. 8.13) scales as

$$\frac{1 + \left(\frac{1}{2a^2} + \frac{2}{\sigma^2}\right) \frac{l^*}{3} \frac{\Delta l'}{n_o}}{1 + \left(\frac{4a^2k^2}{R^2} + \frac{1}{a^2} + \frac{2}{\sigma^2}\right) \frac{l^*}{3} \frac{\Delta l'}{n_o}}. \tag{8.41}$$

The trends in peak width and mangitude are in agreement with those seen in the experimental data shown in section 8.2.2.

8.4 Discussion

The Wigner distribution for light backscattered from a turbid medium is given by Equation 8.34 as

$$\begin{aligned} W_{back}(\mathbf{x}_\perp, z &= 0, \mathbf{p}_{f\perp}) \propto \frac{1}{(4\pi Dt)^{1/2}} \exp\left(-\frac{\mathbf{x}_\perp^2}{2a^2}\right)\left(1 - \exp\left(-\frac{(2z_o)^2}{4Dt}\right)\right) \\ &\times \left[1 + \frac{\frac{1}{Dt}}{\frac{1}{Dt} + \frac{1}{2a^2} + \frac{2}{\sigma^2}} \exp\left(-\frac{(\mathbf{p}_{f\perp} - \frac{k}{R}\mathbf{x}_\perp)^2}{\left(\frac{1}{Dt} + \frac{1}{2a^2} + \frac{2}{\sigma^2}\right)}\right)\right]. \end{aligned} \tag{8.42}$$

This distribution consists of two parts: a diffuse background and an enhanced backscattering peak. The diffuse background is represented by the first term (the '1') within the square brackets in Eq. 8.42. It has no momentum dependence, as expected for isotropic diffuse light. Its position dependence is due to the size of the input beam (given by the intensity width $2a$). The enhanced backscattering peak is represented by the second term within the brackets in Eq. 8.42. It arises from the coherent addition of time reversed photon paths within the medium. Examining the peak width and magnitude as a function of the photon path length can give physical insights into the propagation of optical coherence in a multiple scattering medium.

The shape of the enhanced backscattering peak is given in the Wigner distribution (Eq. 8.42) as

$$\exp\left(-\frac{\mathbf{x}_\perp^2}{2a^2}\right) \exp\left(-\frac{(\mathbf{p}_{f\perp} - \frac{k}{R}\mathbf{x}_\perp)^2}{\left(\frac{1}{Dt} + \frac{1}{2a^2} + \frac{2}{\sigma^2}\right)}\right). \tag{8.43}$$

For an input beam with no curvature ($R \to \infty$), the Wigner distribution factorizes into a gaussian position distribution and a gaussian momentum distribution. The position distribution reflects the size of the incident beam while the transverse momentum width is given by

$$|\mathbf{p}_{f\perp}|_{1/e} = \sqrt{\frac{1}{Dt} + \frac{1}{2a^2} + \frac{2}{\sigma^2}}, \tag{8.44}$$

where D is the diffusion constant, $2a$ is the $1/e$ intensity width of the input beam and σ is its transverse coherence width. Using Eq. 8.10, the product Dt can be rewritten as

$$Dt = \frac{1}{3}c'l^*t = \frac{1}{3}l^*\frac{\Delta l'}{n_o}, \tag{8.45}$$

where $c' = c/n_o$ is the speed of light in the medium, l^* is the transport mean free path (as given in Eq. 8.6) and $c't = \Delta l'/n_o$ is the photon path length in the medium. Using this expression, the transverse momentum width can be written as

$$|\mathbf{p}_{f\perp}|_{1/e} = \sqrt{\frac{3n_o}{l^*\Delta l'} + \frac{1}{2a^2} + \frac{2}{\sigma^2}}. \tag{8.46}$$

In this form, the momentum width is seen to depend on the coherent area of the input beam and the area of the diffusing light transverse to its direction of propagation, as discussed below.

The coherent area of the input beam is determined by the smaller of $2a$ and σ, i.e. if the beam is fully coherent ($\sigma > 2a$), the coherent area is limited by the beam size; but, for a partially coherent beam ($\sigma < 2a$), the transverse coherence width limits the coherent area. The spatial coherence manifests itself in the angular spectrum of the incident light. The angular divergence of a beam is inversely related to its transverse coherence length such that a beam with a high angular divergence will have low transverse spatial coherence. In the enhanced backscattering problem, a pair of photons sharing time reversed paths will only constructively interfere provided the starting points of both paths lie within the same coherence area. Thus, the coherence area influences the angular width of the backscattering peak through its relation to the angular spectrum of the incident light.

Once in the medium, the light undergoes diffusion due to multiple scattering. Its area transverse to the incident direction is given by Eq. 8.18 as $\sim Dt \propto l^*\Delta l'$, which grows with increasing photon path length, $\Delta l'$. As its area expands, the possible time reversed paths must correspondingly narrow in transverse momentum. Hence, the diffusive growth of the distribution also influences the width of the enhanced backscattering peak. However, as Eq. 8.46 shows, it is the smaller area which sets the width of the peak. For diffusive areas which are smaller than the coherence area of the incident beam, the angular width of the peak is seen to narrow as the reciprocal of the square root of the photon path length. However for very short photon path lengths, on the order of the mean free path l^*, the diffusion approximation is not valid and as expected, Eq. 8.46 does not accurately predict the width of the enhanced backscattering peak. Once the diffusive area grows larger than the coherence area of the incident beam, the beam characteristics become dominant and set a lower bound on the angular width of the enhanced backscattering peak.

The magnitude of the enhanced backscattering peak also offers insight on the propagation of coherence in a multiple scattering medium. According to Eq. 8.42, the enhanced backscattering peak at zero transverse momentum will have a magnitude above the diffuse background given by

$$height = \frac{\frac{1}{Dt}}{\frac{1}{Dt} + \frac{1}{2a^2} + \frac{2}{\sigma^2}} = \frac{\frac{1}{Dt}}{|\mathbf{p}_{f\perp}|^2_{1/e}}. \tag{8.47}$$

It can be related to the width of the enhanced backscattering peak using Eq. 8.44. The product Dt is again interpreted as the area of the diffusive distribution transverse to the incident direction for a given photon path length. Its reciprocal is related to the square of the corresponding angular width of the angular distribution. Thus the peak height can be seen as the ratio of the square of the angular width of the total diffusive distribution divided by the square of the angular width of the enhanced backscattering peak. This ratio decreases for increasing photon path lengths because the angular width of the diffusive distribution decreases more rapidly than the angular width of the enhanced backscattering peak which has a lower limit governed by the coherence properties of the input beam.

Including the beam radius of curvature, R in Eq. 8.42, in the Wigner distribution does little to the trends in the peak height and width discussed above. However, for a input beam with a small radius of curvature, corresponding to a strongly diverging beam for example, the Wigner distribution will have a strong correlation between position and momentum. This correlation becomes significant when one considers the means by which the backscattering is detected.

In our experiments, the backscattered distribution is measured via heterodyne detection which means the detected signal is the convolution of the backscattered and LO Wigner distributions (Eq. 8.4). For the backscattered light given by Eq. 8.42, the detected signal as a function of LO center position, momentum and path delay is given by Eq. 8.38 as

$$\begin{aligned} S_B(d_x, \theta &= \frac{d_p}{f_o}, \Delta l') \propto \frac{\pi^2}{2} \exp\left(-\frac{d_x^2}{4a^2}\right) \times \\ &\left[1 + \frac{1 + \left(\frac{1}{2a^2} + \frac{2}{\sigma^2}\right) \frac{l^*}{3} \frac{\Delta l'}{n_o}}{1 + \left(\frac{1}{a^2} + \frac{2}{\sigma^2}\right) \frac{l^*}{3} \frac{\Delta l'}{n_o}} \exp\left(-\frac{1}{a^4} \frac{(k\theta - \frac{k}{R} d_x)^2}{\left(\frac{1}{a^2} + \frac{2}{\sigma^2} + \frac{3n_o}{l^* \Delta l'}\right)}\right)\right]. \end{aligned} \tag{8.48}$$

In this expression the width of the enhanced backscattering peak is now given as

$$\left|\mathbf{p}'_{f\perp}\right|_{1/e} = \sqrt{\frac{3n}{l^* \Delta l'} + \frac{1}{2a^2} + \frac{1}{2a^2} + \frac{2}{\sigma^2}}. \tag{8.49}$$

The additional factor of $\frac{1}{2a^2}$ in this expression, compared to the $1/e$ momentum width of the Wigner distribution (Eq. 8.46), arises from convolution with the LO beam. The convolution of two gaussian distributions yields a broadened gaussian with a width given by the square root of the sum of the squares of the original distributions. Convolution with the LO also changes the height of the enhanced backscattering peak relative to the diffuse background:

$$height = \frac{\frac{3n}{l^* \Delta l'} + \frac{1}{2a^2} + \frac{2}{\sigma^2}}{\frac{3n}{l^* \Delta l'} + \frac{1}{a^2} + \frac{2}{\sigma^2}} = \frac{\left|\mathbf{p}_{f\perp}\right|_{1/e}^2}{\left|\mathbf{p}'_{f\perp}\right|_{1/e}^2}. \tag{8.50}$$

Instead of reflecting the ratio of the angular widths of the backscattering peak to the diffuse distribution within the medium, the peak height of the detected signal can be interpreted as relating the true angular width of the enhanced backscattering peak to the angular width of the peak when convoluted with the LO. The numerator in Eq. 8.50 gives the square of the width of the enhanced backscattering peak (Eq. 8.49) while the denominator gives the width of the convoluted distribution. This can be seen as the finite angular width of the LO detecting a portion of the diffuse background as well as the backscattering peak for the angle selected for detection. Thus the relative contrast of the peak is decreased . If the angular width of the LO is decreased (the $\frac{1}{2a^2}$ factor due to the LO is made small) then the peak height will be given as one. Thus, for the detected distribution, the characteristics of the backscattering peak with increasing photon path length reflect the measurement method in addition to the effects of coherence.

Most enhanced backscattering measurements examine the momentum distribution of the backscattered light by collecting light over a wide range of positions. In the heterodyne scheme, this can be duplicated by integrating the detected distribution over all possible LO positions. The resulting signal is given in Eq. 8.39 as

$$\begin{aligned} S'_B(\theta = \frac{d_p}{f_o}, \Delta l') \propto 1 \quad &+ \quad \frac{1 + \left(\frac{1}{2a^2} + \frac{2}{\sigma^2}\right)\frac{l^*}{3}\frac{\Delta l'}{n_o}}{1 + \left(\frac{4a^2k^2}{R^2} + \frac{1}{a^2} + \frac{2}{\sigma^2}\right)\frac{l^*}{3}\frac{\Delta l'}{n_o}} \\ &\times \quad \exp\left(-\frac{(k\theta)^2}{\left(\frac{4a^2k^2}{R^2} + \frac{1}{a^2} + \frac{2}{\sigma^2} + \frac{3n_o}{l^*\Delta l'}\right)}\right). \end{aligned} \tag{8.51}$$

Here the width of the backscattering peak is given by

$$\overline{|\mathbf{p}_{f\perp}|}_{1/e} = k\theta_{1/e} = \sqrt{\frac{3n}{l^*\Delta l'} + \frac{4a^2k^2}{R^2} + \frac{1}{a^2} + \frac{2}{\sigma^2}}, \tag{8.52}$$

while its height relative to the diffuse background is given by

$$height = \frac{\frac{3n}{l^*\Delta l'} + \frac{1}{2a^2} + \frac{2}{\sigma^2}}{\frac{3n}{l^*\Delta l'} + \frac{4a^2k^2}{R^2} + \frac{1}{a^2} + \frac{2}{\sigma^2}} = \frac{|\mathbf{p}_{f\perp}|^2_{1/e}}{\overline{|\mathbf{p}_{f\perp}|}^2_{1/e}}, \tag{8.53}$$

where $|\mathbf{p}_{f\perp}|_{1/e}$ is the angular width of the true backscattering distribution (Eq. 8.44). In both of these expressions, the wavefront curvature is seen to affect the measured characteristics of the backscattering peak. Upon integrating the detected signal over position, an additional factor of $\frac{4a^2k^2}{R^2} + \frac{1}{2a^2}$ arises in the measured angular width of the backscattering peak. This is partly a consequence of the correlation between position and momentum due to the curvature of the incident beam. Once the position dependence has been integrated out, the incident angular spectrum now depends on the entire extent of the wavefront rather than only the portion at a given position. In addition the angular spectrum of the LO is also broadened due to the integration. Convolution of the two broadened angular distributions results in the angular width given by Eq. 8.52.

The peak height (Eq. 8.53) is also affected by the wavefront curvature when the signal is integrated over position. In this case the peak height can be written as the ratio of the square of the angular width of the unintegrated backscattering peak distribution to the angular width of the position integrated distribution. Again, the LO momentum width measures a portion of the diffuse background in addition to the enhanced backscattering peak for the selected angle of detection. Hence, the maximum peak height is decreased relative to the diffuse background.

Finally, it is important to point out that this theory is based on diffusive propagation in the medium. While the nearly isotropic scattering and thick concentration serve to rapidly randomize the momentum distribution of the light in the medium, for short photon path lengths, this theory is not valid. The transition from ballistic light to diffusive propagation is an extremely interesting problem which warrants further study.

Chapter 9

Conclusions

This thesis has developed a heterodyne method for directly measuring optical phase space distributions, i.e. the joint position and momentum distribution of a light field. The utility of this method is demonstrated in studies of the propagation of light in multiply scattering media. These fundamental light scattering studies will aid in the development of novel biomedical optical imaging techniques, since many biological tissues predominantly scatter light rather than absorbing it.

The optical phase space distributions are measured using a novel heterodyne imaging scheme, implemented using either coherent or low coherence length light. By measuring the mean square heterodyne beat, the detected signal is given by the convolution of the Wigner distributions of the signal field and a reference field. Thus, optical phase space distributions are a form of smoothed Wigner distributions with the position and momentum resolution given by the diameter and diffraction angle of the reference field. The relationship between Wigner distributions and optical phase space distributions is important as it allows studies based on the measurement of optical phase space distributions to be interpreted in the language of Wigner distributions. As discussed in Chapter 3, the language of Wigner distributions is well suited for rigorous description of the heterodyne measurement methods employed in the light scattering experiments. Wigner functions correctly incorporate coherent and incoherent contributions to the beat power spectrum, including both ballistic and scattered light. Wigner distributions are shown to obey rigorous transport equations which are derived from the underlying wave equations. Thus, measurement methods based on Wigner distributions can be placed on a firm theoretical footing. In addition, the Wigner distribution is Fourier transform related to the two point coherence function of the light field and is therefore sensitive to its coherence properties. This sensitivity can be exploited to characterize light sources, as shown in Chapter 5.

The heterodyne imaging scheme developed to measure optical phase space distributions is presented in detail in Chapter 4. As with all heterodyne methods, the light field of interest is mixed with a strong reference field which is offset in frequency. Using Fourier optics, it is shown that by translating optical elements, namely a mirror and a lens, the center position and momentum of the reference field is varied, allowing the optical phase space distribution of the signal field to be mapped out in real time. The system is readily adapted for low coherence light by including a means of varying the path length of the reference field. A heterodyne beat is only produced when the signal and reference optical paths are matched to within the coherence length of the source. By scanning the path length of the reference field, the longitudinal coherence properties of the signal field are also probed. Finally, the detection apparatus, which converts the optical heterodyne beat signal to a voltage, permits measurements at the sub-femtowatt level. 10^{-16} watt signals are measured using input powers at the milliwatt level. This corresponds to a very high dynamic range of 130 dB.

The capabilities of the heterodyne imaging scheme are demonstrated in the variety of scattering studies presented in this thesis. Both coherent and low coherence sources are employed to study both transmission and backscattering from multiple scattering media. The transmission studies using the coherent helium neon laser presented in Chapter 6 show that multiple diffractive scattering in the forward direction can produce a narrow pedestal in the momentum distribution of the transmitted light which decays more slowly than the ballistic component. The data are well fit by a theoretical model that assumes the Wigner phase space distributions obey an approximate transport equation that is identical in structure to the usual transport equation for the specific intensity. By incorporating transverse momentum changes arising from multiple diffractive scattering and treating large angle classical scattering as a loss, the model shows very good agreement with the data. For thick biological samples, the diffractive pedestal becomes comparable in magnitude to the ballistic component. Thus, it can affect the apparent intensity of a probe beam compared to that expected for only exponential attenuation of ballistic light. This is consistent with an anomalous probe intensity observed in optical coherence tomography by Yadlowsky, et al. [20].

Low coherence length superluminescent diodes were used to conduct the transmission studies in Chapter 7. Employing a low coherence source permits selection of the photon path length within the medium, as a heterodyne beat is only produced when the signal and reference beams have equal path lengths. This effectively gives timing resolution inversely related to the bandwidth of the source. For the extended bandwidth superluminescent diode from Sarnoff labs used in some of the studies presented here, the timing resolution is as low as 25 femto-seconds.. This is comparable to the timing resolution of ultrafast pulsed lasers. The experimental data from the transmission experiments show it is possible to measure phase space distributions which are still narrow in momentum by detecting photons with a path length only slightly longer than that of the ballistic light. These narrow distributions represent low order scattering. Since these narrow distributions are transmitted through samples too dense for ballistic light to survive, they may be exploited to allow optical imaging through thick biological tissues. The studies with low coherence sources may have the greatest impact on the existing technology of optical coherence technology (OCT). Since OCT only uses spatial intensity measurement, additional information found in the momentum distribution and spatially varying phase of the light is neglected. While recovering all the position and momentum information present in the light field takes too long to be a viable medical diagnostic technique, employing optical phase space distributions can help in understanding light propagation in biological media and may lead to improvements in OCT imaging.

A low coherence light source was also used to conduct the backscattering study presented in Chapter 8. This study examined the coherent addition of backscattered light known as the enhanced backscattering effect. This phenomenon produces a narrow peak in the retroreflected direction of twice the magnitude of the broad diffuse background. By employing a low coherence length source, the backscattering peak can be dissected according to the length of the photon path within the medium. The data show that the backscattering peak narrows in momentum and decreases in magnitude with increasing photon path length. These trends can be explained using a theoretical treatment which treats the photon paths using a diffusion approximation, i.e. the photon transport is governed by the diffusion equation. Although the theory is based on the propagation of fields, the result is cast in the form of a Wigner distribution for comparison to the data. The treatment yields good agreement with the data only for non-zero photon path lengths. This is expected as the diffusion approximation does not correctly treat low order scattering. The trends in the characteristics of the backscattering peak were discussed with an emphasis on the relevant coherence areas contributing to the enhanced backscattering effect.

The studies presented in this thesis are preliminary investigations into the usefulness of the heterodyne imaging scheme for biomedical optical imaging. The heterodyne scheme offers several practical advantages such as a high dynamic range, and the ability to measure momentum distributions with high angular resolution. The method is particularly useful for examining the coherence properties of a light source as shown in Chapter 5. Detailed studies of light propagation in multiple scattering media are possible as the maximum amount of information present in a light field can be recovered using this method. These studies further the understanding of light transport in biological tissues by offering an ideal system which can be compared to theoretical treatments.

Future work using this system will focus on examining the light transmitted through different types of biological cells to determine if the phase space distributions can distinguish scattering media. Using a low coherence length source to measure phase space distribution adds timing resolution, which can be exploited to further contrast different types of cells by their optical scattering properties.

The relationship between optical phase space distributions and Wigner distributions presents a potential means of improving theoretical models of light transport in scattering media. Since the analysis based on the approximate transport for the Wigner distribution presented in Chapter 6 is equivalent to that based on the radiative transport equation for the specific intensity, it is similar to analyses presented in previous studies of small angle scattering [92]. However, when the Wigner distribution in the medium varies substantially over optical wavelength scales, the appropriate transport equation may be nonlocal, and the simple approximations used in the treatment presented here may break down [13]. Further inquiry into the failings of the approximate transport equation may also improve the resolution of biomedical optical imaging techniques.

Finally, additional inquiries are underway to examine the prospect of using multiple local oscillators to improve the resolution of the heterodyne imaging scheme. Currently, the position and momentum resolution form a minimum uncertainty product such that improvements in the position resolution come at the cost of decreased momentum resolution and vice versa. By using two local oscillators, one squeezed in position and one squeezed in momentum, it is believed that the signal beam can be recovered with a resolution beyond the limit imposed by the uncertainty product.

Appendix A

Tabular data

A.1 Intralipid transmission

Concentration (% of 10% solution)	Transmission
0	1.0
0.5	0.35
1.0	9.0×10^{-4}
1.5	2.3×10^{-5}
2.0	8.5×10^{-7}
2.5	2.0×10^{-8}
3.0	5.7×10^{-10}
3.25	1.8×10^{-10}
3.5	7.8×10^{-11}
3.75	5.5×10^{-11}
4.0	4.9×10^{-11}
4.5	3.7×10^{-11}
5.0	3.1×10^{-11}
5.5	3.1×10^{-11}
6.0	2.5×10^{-11}
6.5	2.3×10^{-11}
7.0	1.9×10^{-11}
8.0	1.5×10^{-11}
10.0	1.1×10^{-11}
12.0	7.8×10^{-12}
15.0	4.1×10^{-12}
20.0	2.1×10^{-12}
25.0	1.4×10^{-12}
30.0	9.0×10^{-13}
40.0	6.9×10^{-13}
50.0	2.5×10^{-13}

Table A.1: Data for Fig. 1.1 - Transmission through 1.3 cm of Intralipid solution

A.2 Coherent Source Transmission

Concentration (10^6/cm^3)	Pedestal Magnitude
0.202	4.8×10^{-5}
0.404	6.8×10^{-5}
0.521	3.5×10^{-5}
0.811	6.2×10^{-5}
2.03	1.6×10^{-5}
2.56	4.7×10^{-6}
3.08	1.8×10^{-6}
3.6	1.22×10^{-6}
4.0	0.95×10^{-6}
4.53	3.8×10^{-7}
5.13	1.26×10^{-7}
6.01	0.65×10^{-7}

Table A.2: Data for Fig. 6.8 - Amplitude of diffractive pedestal vs concentration

A.3 Broadband Source Transmission

Path delay, $\Delta l'$ (mm)	Momentum Width (k)
0	0.065
0.1	0.107
0.2	0.143
0.3	0.168
0.4	0.208
0.5	0.231
0.6	0.270
0.7	0.288
0.8	0.300

Table A.3: Data for Fig. 7.8 - Linear Momentum Growth

Path delay, $\Delta l'$ (mm)	Position distribution width (mm)
0	0.55
0.02	0.72
0.1	1.20
0.2	1.50
0.3	1.79
0.5	2.40

Table A.4: Data for Fig. 7.17 - Position Width Growth for $\rho = 1.2 \times 10^7/\text{cm}^3$

Path delay, $\Delta l'$ (mm)	Position distribution width (mm)
0	0.57
0.1	0.95
0.2	1.28
0.3	1.54
0.5	1.93

Table A.5: Data for Fig. 7.22 - Position Width Growth for $\rho = 1.5 \times 10^7/\text{cm}^3$

Path delay, $\Delta l'$ (mm)	Momentum distribution width (10^{-3} k)
0.05	48.4
0.1	76.7
0.2	84.5
0.3	124
0.4	158
0.5	153

Table A.6: Data for Fig. 7.28 - Transverse Momentum Width Growth for $\rho = 1.8 \times 10^7/\text{cm}^3$

Path delay, $\Delta l'$ (mm)	Position distribution width (mm)
0.05	0.65
0.1	0.96
0.2	1.16
0.3	1.57
0.4	1.74
0.5	2.0

Table A.7: Data for Fig. 7.29 - Position Width Growth for $\rho = 1.8 \times 10^7/\mathrm{cm}^3$

$\rho(10^7/\mathrm{cm}^3)$	"A" parameter (mm)
1.2	0.57
1.5	0.55
1.6	0.62
1.8	0.70
2.0	0.80

Table A.8: Data for Fig. 7.30 - Position Width Growth Model "A" parameter

$\rho(10^7/\mathrm{cm}^3)$	"B" parameter ($\mu\mathrm{m}^{-1}$)
1.2	0.034
1.5	0.022
1.6	0.018
1.8	0.015
2.0	0.013

Table A.9: Data for Fig 7.31 - Position Width Growth Model "B" parameter

$\rho(10^7/\text{cm}^3)$	"C" parameter (μm)
1.2	0
1.5	8
1.6	43
1.8	58
2.0	190

Table A.10: Data for Fig. 7.32 - Position Width Growth Model "C" parameter

A.4 Broadband Source Backscatter

Photon path length, $\Delta l'/n_o$ (mm)	Momentum Width (10^{-3} k)
0	5.96
0.15	2.88
0.29	2.26
0.44	2.26
0.59	1.88
0.74	1.99

Table A.11: Data for Fig. 8.12 - Momentum Width for Enhanced Backscattering Peak

Photon path length, $\Delta l'/n_o$ (mm)	Enhanced Peak Magnitude
0	1.63
0.15	1.60
0.29	1.42
0.44	1.34
0.59	1.32
0.74	1.27

Table A.12: Data for Fig. 8.13 - Peak Magnitude for Enhanced Backscattering Peak

Bibliography

[1] B. Chance. Optical Method. *Ann. Rev. Biophys. Chem.* 20:1-28, 1991.

[2] D. Delpy. Optical spectroscopy for diagnosis. *Physics World.* 7:34-9 1994.

[3] S. K. Gayen and R. R. Alfano. Emerging Optical Biomedical Imaging Techniques. In R.R. Alfano, and J. G. Fujimoto, editors, *OSA Trends in Optics and Photonics on Advances in Optical Imaging and Photon Migration*, Volume 2, pages 5-12. Optical Society of America, Washington, DC, 1996.

[4] L. Wang, P. P. Ho, C. Liu, G. Zhang, and R. R. Alfano. Ballistic 2-D Imaging Through Scattering Walls Using and Ultrafast Optical Kerr Gate. *Science* 253:769-71 1991.

[5] D. A. Benaron and D. K. Stevenson. Optical time-of-flight and absorbance imaging of biological media. *Science* 259:1463-5 1993.

[6] D. Huang, E. A. Swanson, C. P. Lin, J. S. Schuman, C. A. Puliafito, and J. G. Fujimoto. Optical coherence tomography. *Science*, 254:1178-81, 1991.

[7] J. A. Izatt, M. D. Kulkerni, K. Kobayashi, M. S. Sivak, J. K. Barton, and A. J. Welch. Optical Coherence Tomography for Biodiagnostics. *Optics and Photonics News*, 8(5):41-47, 65, 1997.

[8] J. A. Izatt, M. R. Hee, G. M. Owen, E. A. Swanson, and J. G. Fujimoto. Optical coherence microscopy in scattering media. *Opt. Lett.* 19, 590-2, 1994.

[9] A. Yodh and B. Chance. Spectroscopy and imaging with diffusing light. *Physics Today* 48(3):34-40, 1995.

[10] E. P. Wigner. On the quantum correction for thermodynamic equilibrium. *Phys. Rev.* 40:749-59 1932.

[11] M. J. Bastiaans. The Wigner distribution function applied to optical signals and systems. *Opt. Commun.* 25:26-30, 1978.

[12] M. Hillery, R. F. O'Connel, M. O. Scully, and E. P. Wigner. Distribution functions in physics: fundamentals. *Phys. Rep.* 106:121-67 1984.

[13] S. John, G Pang, and Y. Yang. Optical coherence propagation and imaging in a multiple scattering medium. *J. Biomed. Opt.* 1:180-91 1996.

[14] A. Wax and J. E. Thomas. Heterodyne measurement of Wigner phase space distributions in turbid media. In R.R. Alfano, and J. G. Fujimoto, editors, *OSA Trends in Optics and Photonics on Advances in Optical Imaging and Photon Migration*, Volume 2, pages 238-42. Optical Society of America, Washington, DC, 1996.

[15] M. Beck, M. E. Anderson, and M. Raymer. Imaging through scattering media using pulsed homodyne detection. In R. R. Alfano, editor, *Proceedings on Advances in Optical Imaging and Photon Migration*, Volume 21, pages 257-60. Optical Society of America, Washington, DC 1994.

[16] A. Schmidt, R. Corey, and P. Saulnier. Imaging through random media by use of low-coherence optical heterodyning. *Opt. Lett.* 20:404-6 1995.

[17] A. Ya. Polishchuk and R. R. Alfano. Fermat photons in turbid media: an exact analytic solution for most favorable paths - a step toward optical tomography. *Opt. Lett.* 19:1937-9 1995.

[18] L. T. Perelman, J. Wu, I. Itzkan, and M. S Feld. Photon migration in turbid media using path integrals. *Phys. Rev. Lett.* 72:1341-4 1994.

[19] L. T. Perelman, J. Wu, I. Itzkan, Y. Wang, R. R. Dasari, and M. S. Feld. Photon paths in turbid media: theory and experimental observation. In R. R. Alfano, editor, *Proceedings on Advances in Optical Imaging and Photon Migration*, Volume 21, pages 153-55. Optical Society of America, Washington, DC 1994.

[20] M. J. Yadlowsky, J. M Schmidt, and R. F. Bonner. Multiple scattering in optical coherence microscopy. *Appl. Opt.* 34:5699-707 1995.

[21] J. M. Schmitt, S. H. Xiang, and K. M. Yung. Speckle in Optical Coherence Tomography. *J. Biomed. Opt.* 4:xxx-xxx 1999.

[22] B. Crosignani, P. DiPorto, and M. Bertolotti. *Statistical Properties of Scattered Light*. Academic Press, New York, 1975.

[23] M. Kerker. *The Scattering of Light and Other Eletromagnetic Radiation.* Academic Press, New York, 1969.

[24] C. F. Bohren and D. R. Huffman. *Absorption and scattering of light by small particles.* Wiley, Interscience, New York, 1983.

[25] H. C. van de Hulst. *Light Scattering by Small Particles.* Dover, New York, 1957.

[26] A. Ishimaru, *Wave propagation and scattering in random media*, Vol. I,II. Academic, New York, 1978.

[27] A. Ishimaru. Theory and Application of Wave Propagation and Scattering in Random Media. *Proc. IEEE* 65:1030-61 1977.

[28] Y. Kuga and A. Ishimaru. Retroreflectance from a dense distribution of spherical particles. *J. Opt. Soc. Am. A* 8:831-9 1984.

[29] K. M. Watson. Multiple scattering of electromagnetic waves in an underdense plasma. *J. Math. Phys.* 10:688-702 1969.

[30] A. G. Vinogradov, Yu. A. Kravtsov and V. I. Tatarskii. Enhanced backscattering from bodies immersed in a random medium. *Izv. VUZ. Radiofiz.* 16:1064-70 1973.

[31] Yu. N. Barabanenkov, Yu. A. Kravtsov, V. D. Ozrin, and A. I. Saichev. Enhanced Backscattering in Optics. In E. Wolf, editor, *Progress in Optics*, Vol. XXIX, pages 67-190. Elsevier Science Publishers B. V., Amsterdam, The Netherlands, 1991.

[32] M. P. Van Albada and A. Lagendijk. Observation of Weak Localization of Light in a Random Medium. *Phys. Rev. Lett.* 55:2692-5 1985.

[33] P. E. Wolf and G. Maret. Weak Localization and Coherent Backscattering of Photons in Disordered Media. *Phys. Rev. Lett.* 55:2696-9 1985.

[34] R. Vreeker, M. P. Van Albada, R. Sprik and A. J. Lagendijk. Femtosecond Time-Resolved Measurements of Weak Localization of Light. *Phys. Lett. A*. 143:51-4 1988.

[35] K. M. Yoo. F. Liu and R. R. Alfano. Biological materials probed by the temporal and angular profiles of the backscattered ultrafast laser pulses. *J. Opt. Soc. Am. B* 7:1685-93 1990.

[36] M. Tomita and H. Ikari. Influence of finite coherence length of incoming light on enhanced backscattering. *Phys. Rev. B* 43:3716-9 1991.

[37] T. Okamoto and T. Asakura. Enhanced backscattering of partially coherent light. *Opt. Lett.* 21:369-71 1996.

[38] E. Akkermans, P. E. Wolf, R. Maynard and G. Maret. Theoretical study of the coherent backscattering of light by disordered media. *J. Phys. France* 49:77-98 1988.

[39] K. M. Yoo and R. R. Alfano. Time-resolved coherent and incoherent components of forward light scattering in random media. *Opt. Lett.* 15:320-2 1990.

[40] M. S. Patterson, B. Chance, and B. C. Wilson. Time resolved reflectance and transmittance for the non-invasive measurement of tissue optical properties. *Appl. Opt.* 28:2331-6 1989.

[41] K. M. Yoo, B. B. Das and R. R. Alfano. Imaging of a translucent object hidden in a highly scattering medium from the early portion of the diffusive component of a transmitted ultrafast laser pulse. *Opt. Lett.* 17:958-60 1992.

[42] J. Wu, Y. Wang, L. Perelman, I. Itzkan, R. R. Dasari and M. S. Feld. Time-resolved multichannel imaging of fluorescent objects embedded in turbid media. *Opt. Lett.* 20:489-491 1995.

[43] L. Wang, P. P. Ho, X. Liang, H. Dai, and R. R. Alfano. Kerr-Fourier imaging of hidden objects in thick turbid media. *Opt. Lett.* 18:241-3 1993.

[44] E. Arons, E. N. Leith, A. C. Tien, and R. Wagner. High-resolution optical chirped pulse gating. *Appl. Opt.* 36:2603-8 1997.

[45] Y. Q. Xiang, T. Raphan, X. Liang, L. Wang, P. P. Ho, and R. R. Alfano. Image-quality enhancement of objects in turbid media by use of a combined computational-photonics approach. *Appl. Opt.* 36:1045-53 1997.

[46] D. J. Hall, J. C. Hebden, and D. T. Delpy. Imaging very-low-contrast objects in breastlike scattering media with a time-resolved method. *Appl. Opt.* 36:7270-6 1997

[47] D. Grosenick, H. Wabnitz, and H. Rinneberg. Time-resolved imaging of solid phantoms for optical mammography. *Appl. Opt.* 36:221-31 1997.

[48] A. Joblin. Tumor contrast in time-domain, near-infrared laser breast imaging. *Appl. Opt.* 36:9050-7 1997.

[49] J. Chang, W. Zhu, Y. Wang, H. L. Graber, and R. L. Barbour. Regularized progressive expansion algorithm for recovery of scattering media from time-resolved data. *J. Opt. Soc. Am. A* 14:306-12 1997.

[50] J. C. Hebden, and S. R. Arridge. Imaging through scattering media by the use of an analytical model of perurbation amplitudes in the time domain. *Appl. Opt.* 35:6788-96 1996.

[51] J. C. Hebden, M. Tziraki, and D. T. Delpy. Evaluation of the temporally extrapolated absorbance method for dual-wavelength imaging through tissuelike scattering media. *Appl. Opt.* 36:3802-10 1997.

[52] S. K Gayen, M. E. Zevallos, B. B. Das and R. R. Alfano. Time-Sliced Transillumination Imaging of Normal and Cancerous Breast Tissues. In J. G. Fujimoto and, M. S. Patterson, editors, *OSA Trends in Optics and Photonics on Advances in Optical Imaging and Photon Migration*, Volume 21, pages 63-6. Optical Society of America, Washington, DC, 1998.

[53] H. Rinneberg, D. Grosenick, H. Wabnitz, H. Danlewski, K. Moesta and P. Schlag. Time-domain optical Mammography: results on phantoms, healthy volunteers and patients. In J. G. Fujimoto and, M. S. Patterson, editors, *OSA Trends in Optics and Photonics on Advances in Optical Imaging and Photon Migration*, Volume 21, pages 278-80. Optical Society of America, Washington, DC, 1998.

[54] M. A. O'Leary, D. A. Boas, B. Chance and A. G. Yodh. Refraction of Diffuse Photon Density Waves. *Phys. Rev. Lett.* 69:2658-61 1992.

[55] D. A. Boas, M. A. O'Leary, B. Chance and A. G. Yodh. Scattering and wavelength transduction of diffuse photon density waves. *Phys. Rev. E* 47:R2999-R3002 1993.

[56] J. M. Schmitt, A. Knüttel and J. R. Knutson. Interference of diffusive light waves. *J. Opt. Soc. Am. A* 9:1832-43 1992.

[57] B. J. Tromberg, L. O. Svaasand, T. T. Tsay and R. C. Haskell. Properties of photon density waves in multiple-scattering media. *Appl. Opt.* 32:607-16 1993.

[58] J. B. Fishkin and E. Gratton. Propagation of photon-density waves in strongly scattering media containing and absorbing semi-infinite plane bounded by a straight edge. *J. Opt. Soc. Am. A* 10:127-40 1993.

[59] A. Knüttel, J. M . Schmitt and J. R. Knutson. Spatial localization of absorbing bodies by interfering diffusive photon-density waves. Appl. Opt. 32:381-9 1993.

[60] M. A. O'Leary, D. A. Boas, B. Chance and A. G. Yodh. Experimental images of heterogeneous turbid media by frequency-domain diffusing-photon tomography. *Opt. Lett.* 20:426-8 1995.

[61] B. W. Pogue, M. Testorf, U. L. Osterberg and K. Paulsen. Development of quantitative imaging in frequency-domain diffuse optical tomography for breast cancer detection. In J. G. Fujimoto and, M. S. Patterson, editors, *OSA Trends*

in Optics and Photonics on Advances in Optical Imaging and Photon Migration, Volume 21, pages 245-50. Optical Society of America, Washington, DC, 1998.

[62] X. D. Li, J. P. Culver, T. Durduran, B. Chance, A. G. Yodh and D. N. Pattanayak. Diffraction Tomography with Diffuse Photon Density Waves: Clinical Studies and Background Subtraction. In J. G. Fujimoto and, M. S. Patterson, editors, *OSA Trends in Optics and Photonics on Advances in Optical Imaging and Photon Migration*, Volume 21, pages 281-3. Optical Society of America, Washington, DC, 1998.

[63] S. Fantini, S. A. Walker, M. A. Franceschini, A. E. Cerussi, J. Edler, K. T. Moesta, P. M. Schlag, M. Kaschke, and E. Gratton. Optical Characterization of Breat Tumors by Frequency-Domain Optical Mammography. In J. G. Fujimoto and, M. S. Patterson, editors, *OSA Trends in Optics and Photonics on Advances in Optical Imaging and Photon Migration*, Volume 21, pages 289-93. Optical Society of America, Washington, DC, 1998.

[64] D. Huang, E. A. Swanson, C. P. Lin, J. S. Schuman, W. G. Stinson, W. Chang. M. R. Hee, T. Flotte, K. Gregory, C. A. Puliafito, and J. G. Fujimoto. Optical Coherence Tomography. *Science* 254:1178-81 1991.

[65] E. A. Swanson, D. Huang, M. R. Hee, J. G. Fujimoto, C. P. Lin, and C. A. Puliafito. High speed optical coherence domain reflectometry. Opt. Lett. 17:151-3 1992.

[66] J. A. Izatt, M. R. Hee and G. M. Owen, E. A. Swanson and J. G. Fujimoto. Optical coherence microscopy in scattering media. *Opt. Lett.* 19:590-2 1994.

[67] G. J. Tearney, M. E. Brezinski, J.F. Southern, B. E. Bouma, M. R. Hee and J. G. Fujimoto. Determination of the refractive index of highly scattering human tissue by optical coherence tomography. *Opt. Lett.* 20:2259-61 1995.

[68] G. J. Tearny, B. E. Bouma, S. A. Boppart, B. Golubovic, E. A. Swanson, and J. G. Fujimoto. Rapid acquisition of *in vivo* biological images by use of optical coherence tomography. *Opt. Lett.* 21:1408-10 1996.

[69] G. J. Tearney, S. A. Boppart, B. E. Bouma, M. E. Brezinski, N. J. Weissman, J. F. Southern and J. G. Fujimoto. Scanning single-mode fiber optic catheter-endoscope for optical coherence tomography. *Opt. Lett* 21:453-5 1996.

[70] A. M. Sergeev, V. M. Gelikonov, G. V. Gelikonov, F. I. Feldchtein, R. V. Kuranov, N. D. Gladkova, N. M. Shakova, L. B. Snopova, A. V. Shakova, and I. A.

Kuzn. *In vivo* endoscopic OCT imaging of precancer and cancer states of human mucosa. *Opt. Express.* 1:432-40 1997.

[71] E. A. Swanson, J. A. Izatt, M. R. Hee, D. Huang, C. P. Lin, J. S. Shuman, C. A. Puliafito, and J. G. Fujimoto. In-vivo retinal imaging by optical coherence tomography. *Opt. Lett.* 18:1864 1993.

[72] J. W. Goodman. *Introduction to Fourier Optics.* McGraw-Hill, San Fransisco, 1968.

[73] A. Wax and J. E. Thomas. Optical heterodyne imaging and Wigner phase space distributions. *Opt. Lett.* 21:1427-29, 1996.

[74] M. G. Raymer, C. Cheng, D. M. Toloudis, M. Anderson, and M. Beck. Propagation of Wigner coherence functions in multiple scattering media. (private communication, 1995).

[75] C. Iaconis and I. A. Walmsley. Direct measurement of the two-point field correlation function. *Opt. Lett.* 21:1783-5, 1996.

[76] D. F. McAlister, M. Beck, L. Clarke, A. Mayer, and M. G. Raymer. Optical phase retrieval by phase-space tomography and fractional-order Fourier transforms. *Opt. Lett.* 20:1181-3, 1995.

[77] N. D. Cartwright. A non-negative Wigner-type distribution. *Physica* 83A:210-2 1976.

[78] H. P. Yuen and V. W. S. Chan. Noise in homodyne and heterodyne detection. *Opt. Lett.* 8:177-179 1983.

[79] H. Z. Cummins and H. L. Swinney. Light beating spectroscopy. In E. Wolf, editor, *Progess in Optics*, Volume VIII, Chap. 3, pages 133-200. North-Holland, New York, 1970.

[80] G. L. Abbas, V. W. S. Chan, and T. K. Yee. A dual detector optical heterodyne receiver for local oscillator noise suppression. *IEEE J. Lightwave Tech.* 3:1110-2 1985.

[81] V. J. Corcoran. Directional characteristics in optical heterodyne detection processes. *J. Appl. Phys.* 36:1819-25 1965.

[82] A. E. Siegman. The antenna properties of optical heterodyne receiver. *Appl. Opt.* 5:1588-94 1966.

[83] S. Cohen. Heterodyne detection: phase front alignment, beam spot size, and detector uniformity. *Appl. Opt.* 14:1953-9 1975.

[84] A. L. Migdall, B. Roop, Y. C. Zheng, J. E. Hardis, and Gu Jun Xia. Use of heterodyne detection to measure optical transmittance over a wide range. *Appl. Opt.* 29:5136-44 1990.

[85] G. R. Fowles. *Introduction to Modern Optics.* Dover, New York, 1975.

[86] A.M. Bacon. *Optical Dipole Noise.* PhD thesis, Duke University, 1995.

[87] L. Mandel and E. Wolf. *Optical Coherence and Quantum Optics.* Cambridge University Press, New York, 1995.

[88] A. Wax, S. Bali, and J. E. Thomas. Coherence Characterization of Broadband sources using Optical Phase Space Contours. submitted to *J. Biomed. Opt.*

[89] The idea of making measurements of Wigner distributions in this regime was suggested to us by Prof. R. J. Glauber, Harvard University, Dept. of Physics, Cambridge, MA 02138, private communication, 1996.

[90] Yu. N. Barabanenkov. *On the spectral theory of radiation transport equations.* Sov. Phys. JETP, 29:679-84, 1969.

[91] J. E. Thomas. Approximate Transport Equation for Wigner Distributions. January 1996. [unpublished].

[92] A. Zardecki and S. A. W. Gerstl, "Multi-Gaussian phase function model for off-axis laser beam scattering," *Appl. Opt.* 26:3000-4 (1987).

Biography

Adam P. Wax was born in New York City, New York on February 11, 1970. He grew up in the Long Island town of Great Neck, New York. He graduated from Great Neck South High School in 1988 where he served as student government president that same year. Shortly after graduation, he received the Nassau County Award for Academic Excellence and Community Service from the county executive. As a Physics major at the State University of New York at Albany, Adam distinguished himself as a top physics student and was elected to the Physics Honor Society, Sigma Pi Sigma. At SUNYA, Adam conducted an independent project determining the relative vapor pressures of volatile copper compounds for use as precursors in chemical vapor deposition in the laboratory of Professor Alain E. Kaloyeros. He continued his undergraduate education at Rensselaer Polytechnic Institute where he majored in Electrical Engineering. His academic success there led to his nomination to the EE honor society, Eta Kappa Nu. In 1993, he received dual bachelors degrees with *cum laude* honors: a B.S. in Physics from SUNYA and a B.S. in EE from R.P.I. In the fall of 1993, Adam enrolled in the graduate physics program at Duke University. His research at Duke University under the direction of Professor John E. Thomas explored the propagation of light in multiple scattering media for application to biomedical optical imaging. For this research, he received the Walter Gordy Fellowhip for work in optical physics. He received his A.M. in 1996 and his Ph.D. in 1999, both in Physics. In 1997, he was introduced to his future wife Jodi by his longtime friend Dave Trinin. Adam and Jodi will be married in June of 1999.

Publications

A. Wax, S. Bali and J. E. Thomas. Coherence Characterization of Broadband Sources Using Optical Phase Space Contours. Submitted to *J. Biomed. Opt.*, 1999.

A. Wax and J. E. Thomas. Measurement of Smoothed Wigner Phase Space Distributions for Low Coherence Light in Multiple Scattering Media. To appear in SPIE proceedings Vol. 3598, 1999.

A. Wax and J. E. Thomas. Measurement of Smoothed Wigner Phase Space Distributions for Coherence Tomography. In V. V. Tuchin, V. P. Ryabukho and D. A. Zimnyakov, editors, *Saratov Fall Meeting '98: Light Scattering Technologies for Mechanics, Biomedicine, and Material Science*, Proceedings of SPIE Vol. 3726, pp. 494-501. SPIE, Bellingham, Washington, 1999.

A. Wax and J. E. Thomas. Measurement of Smoothed Wigner Phase Space Distributions in Multiple Scattering Media. In J. G. Fujimoto and M. S. Patterson, editors, *OSA Trends in Optics and Photonics on Advances in Optical Imaging and Photon Migration*, Volume 21, pages 348-52. Optical Society of America, Washington, D. C., 1998.

A. Wax and J. E. Thomas. Measurement of Wigner phase space distributions for multiple small angle scattering in a turbid medium. *J. Opt. Soc. Am. A* 15:1896-1908, 1998.

A. Wax and J. E. Thomas. Wigner phase space distributions and optical coherence in turbid media. In *Conference on Lasers and Electro-Optics 1997*, Vol. 11, page 41. OSA Technical Digest Series, Optical Society of America, Washington, D. C., 1997.

A. Wax and J. E. Thomas. Optical heterodyne imaging and Wigner phase space distributions. *Opt. Lett.* 21:1427-29, 1996.

A. Wax and J. E. Thomas. Heterodyne measurement of Wigner phase space distributions in turbid media. In R.R. Alfano, and J. G. Fujimoto, editors, *OSA Trends in Optics and Photonics on Advances in Optical Imaging and Photon Migration*, Volume 2, pages 238-42. Optical Society of America, Washington, DC, 1996.

E.T. Eisenbraun, Bo Zheng, Hongwen Li, A. Wax, A.E. Kaloyeros, C. Dettelbacher, P.J. Toscano, N. Devashrayee, S.P. Murarka, J. Femi Olowolafe, F. Pintchovski. Selective and blanket low-temperature copper CVD for multilevel metallization in ULSI. *Advanced Metallization for ULSI Applications Proceedings of the Conference*, p. xv+580, 397-401. Matter Research Society, Pittsburgh, PA, 1992.

Presentations

“Measurement of Smoothed Wigner Phase Space Distributions for Low Coherence Light in Multiple Scattering Media,” A. Wax and J. E. Thomas, Photonics West, BiOS 99, San Jose CA, 1999, invited talk.

“Measurement of Smoothed Wigner Phase Space Distributions for Coherence Tomography,”, A. Wax and J. E. Thomas, Saratov Fall Workshop, Saratov, Russia, 1998, invited internet presentation, http://www.phy.duke.edu/∼awax/research/russia1.html

“Measurement of Smoothed Wigner Phase Space Distributions in Multiple Scattering Media,” A. Wax and J. E. Thomas, Advances in Optical Imaging and Photon Migration, Orlando FL, 1998.

“Wigner Phase Space Distributions and Optical Coherence in Turbid Media,” A. Wax and J. E. Thomas, Conference on Lasers and Electro-Optics, Baltimore MD, 1997.

“Heterodyne measurement of Wigner phase space distributions in turbid media,” A. Wax and J. E. Thomas, Advances in Optical Imaging and Photon Migration, Orlando FL, 1996.